ROLE OF COLLECTIVE EXCITATION IN HIGH ENERGY RADIATION INTERACTION WITH POLYCYCLIC AROMATIC HYDROCARBONS

A thesis submitted
in partial fulfillment for the degree of

Doctor of Philosophy

by

PREETI MANJARI MISHRA

Department of Physics

INDIAN INSTITUTE OF SPACE SCIENCE AND TECHNOLOGY
Thiruvananthapuram - 695547

JULY 2014

CERTIFICATE

This is to certify that the thesis titled **Role of collective excitation in high energy radiation interaction with polycyclic aromatic hydrocarbons** , submitted by **Ms Preeti Manjari Mishra**, to the Indian Institute of Space Science and Technology, Thiruvananthapuram, for the award of the degree of **Doctor of Philosophy**, is a bona fide record of the research work done by her under my supervision. The contents of this thesis, in full or in parts, have not been submitted to any other Institute or University for the award of any degree or diploma.

Dr Umesh R Kadhane
Supervisor
Department of Physics
Indian Institute of Space
Science and Technology
Thiruvananthapuram-695547
Kerala
India

Place: Thiruvananthapuram
JULY 2014

DECLARATION

I declare that this thesis titled **Role of collective excitation in high energy radiation interaction with polycyclic aromatic hydrocarbons** submitted in fulfillment of the Degree of Doctor of Philosophy is a record of original work carried out by me under the supervision of **Dr Umesh R Kadhane**, and has not formed the basis for the award of any degree, diploma, associateship, fellowship or other titles in this or any other Institution or University of higher learning. In keeping with the ethical practice in reporting scientific information, due acknowledgments have been made wherever the findings of others have been cited.

Preeti Manjari Mishra
SC10D018

Place: Thiruvananthapuram
JULY 2014

ACKNOWLEDGEMENTS

Completion of this doctoral thesis was possible with the support of several people. I would like to express my sincere gratitude to all of them.

I would like to express my special appreciation and utmost thanks to my supervisor **Dr. Umesh R Kadhane** for his valuable guidance, scholarly inputs, concise comments and consistent encouragement I received throughout the research work. It has been an honor to be his first Ph.D. student. This feat was possible only because of the unconditional support provided by Sir. A person with an amicable and positive disposition. Sir has always made himself available to clarify my doubts despite of his busy schedules. I consider it as a great opportunity to do my doctoral program under his guidance and to learn from his research expertise. Thank you Sir, for all your help and constant support. You have been a tremendous mentor for me. I would like to thank you for encouraging my research and for allowing me to grow as a research scientist. Your advice on both research as well as on my career have been priceless. The joy and enthusiasm you have for your research is always contagious and motivational for me, even during tough times in the Ph.D. pursuit. I am also thankful to you for introducing me to the experimental world and giving me an opportunity to place an example as a successful woman physicist and an experimentalist. At the end, I would like to express my gratefulness towards my guide who spent time and was always my support in the moments when there was no one to answer my queries.

I would also like to thank my Doctoral committee members, **Prof. Lokesh Tribedi, Prof. M. Krishnamurthy, Dr. S. Murugesh and Dr. Nirmala James**. I thank you

for letting my pre-synopsis viva voce exam be an enjoyable moment with enormous thoughtful questions, brilliant comments and suggestions which made me think even more and deeper about my research work. I specially thank Nirmala Madam for her moral support at the critical stages during my research.

I express my special gratitude towards our research collaborators **Prof. L Avaldi, Prof. K. C. Prince, Dr. P. Bolognesi, Dr. R. Richter, Dr. C. P. Safvan, Dr. J. Rajput, Dr. S. Vig** for the substantial help during the experiments and later in the analysis.

I thank **Dr. K. S. Dasgupta, Director**, for the academic support and the facilities provided to carry out the research work at the Institute. **Dr. Thomas Kurian, Dean, Research and Development, Prof. A. Chandrasekhar, Dean Academics**, has been very encouraging and supportive, and I express my gratitude to them. I also thank the Research council, IIST for their support at various phases of the Ph.D. program. I thank the Head of physics department, **Prof. C. S. Narayanamurthy** for providing the academic support as and when needed.

Some faculty members of the institute have been very kind enough to extend their help at various phases of this research, whenever I approached them, and I do hereby acknowledge all of them. I thank to **Dr. Sudheesh C** for introducing me to programming and **Dr. Naveen Surendran, Dr. Jinesh K. B., Dr. Jayanthi S. and Dr. Rakesh K Singh, Dr. A. Narayanan, Dr. S. Mandal, Dr. M. V. Ramana** for the friendly approach during the interaction and academic discussions.

I would especially thank the facilities and manpower provided by the institute which had played a great role during the Ph.D. tenure. I thank the **hostel staffs, canteen staffs, cleaning staffs, physicians, nurses, security**. All of you have been there to support me whenever I required, which had made my research comfortable at any time. No research is possible without the **library and laboratory facility**, the centre of learning resources. I take this time to express my gratitude to all the library staff and lab staff

of IIST for their services. I especially thank to the **atomic and molecular physics lab staff, chemistry lab staff, mathematics lab staff, IIST purchase and stores section** for their cooperation. I thank the staffs **Veena, Murthy, Sindhu, Deepthi, Viji, Remya, Anand, Jaysree R, Jaysri, Janma, Lekshmi, Anish, Karim, Sujith**. The thesis would not have come to a successful completion, without the help I received from the staff of the **High performance computing facility** of IIST. Nevertheless being a part of experimental work and developmental lab, I cannot stop myself from expressing my sincere acknowledgment to the **Machine lab staffs** of IIST and **Dr Vergheese**.

I also thank to my junior friends, the undergraduate students of IIST (**Vedant, Amit, Yogesh, Saiteja, Biswajit, Loveraj, Jaswanth, Prachi, Snehal and the 2010 Btech physical science batch**) and from other institute (**Salina, Neethu, Dhanya, Satwik, Najia**) for their active involvement and contribution in my research output and providing me a fun bunch with lots of enthusiasm. I will always remember the environment with full of academic discussions we had during the interaction with all of you. I thank **Loveraj** for the extensive help in MATLAB programming.

My time at IIST was made enjoyable in large part due to the many friends that became a part of my life. I would like to thank all of my friends and colleagues at IIST (**Anjali, Haripadmam, Jalaja, Remya, Kavitha, Sarika, Sara, Harsha, Sreenivasa, Richa, Ameya, Muthu, Bhaskar, Litesh, Rahul sir, Sarat sir, Arun, Narasimman, Roshina madam, Najeeb, Karthika, Resmi, Devi**, and many more) who supported me and incented me to strive towards my goal. I am grateful to **Rahul, Sanid, Dhanya** for the help whenever I needed.

The moral and academic support from my friends outside IIST is incredible. I thank my Masters course friends **Archana, Amita, Madhu, Minakhshi, Niru, Prachi, Shuvendu, Dibyakrupa, Maguni, Atul, Atulya, Sachi, Sameer, Niladri, Jeevan** and my degree course friends **Dipti, Sudeepa, Rajashree, Anupama, Salma, Sanjukta, De-**

vajani for the academic environment we had during our studies which had inspired me to explore this enchanting subject of physics and pursuit research in that. The group has been a source of friendships as well as good advice. I also thank all the friends I met in **SERC school-2013** at TIFR, for the nice moments during the school. I also thank **Bhargava, Rajesh, Umesh, Sairam, Mridula** and the other friends whom I met during my research period have helped me in many ways.

I am particularly indebted to few of my very close friends **Nigam, Dipti, Esani, Nirlipta, Monalisa, Renu** whose contribution had a lot of good impact on my career. I thank especially **Nigam** for the constant academic as well as non academic help and support I have received from him.

I am also grateful to some people whose help at my critical days of research was indeed a great favor to me. I thank people from my past institute IIT Madras where I started my research, **Prof. P. C. Deshmukh, Prof. Markandeyulu, Ranjit, Nibedita, Anuradha, Sunil, Gagan, Jobin, Manas, Zuby, Vivishek, Alak, Siji, Pramod, Ankita, Sreenath, Sandhya, Venkateswarulu** and many more.

I also devote my sincere thanks to my professors of Utkal University for their excellent teaching in MSc course. I thank **Prof. L. P. Singh, Prof. P. Khare, Prof. K. Maharana, Prof. S. Mohapatra, Prof. N. C. Mishra, Prof. D. K. Basa and the Physics department staffs** for the personal and scholarly interactions, their suggestions at various points. I will be grateful to you all for the knowledge you gave me and pave the path towards physics. My sincere thank goes to my high school and college teachers, who have developed me as a good person in the society.

A special thanks to my family which is negligible as compare to their contribution. Words cannot express how grateful I am to my **parents** for all of the sacrifices that you have made on my behalf. Your prayer for me was what sustained me thus far. I am very much indebted to my family who encouraged and helped me at every stage of my

personal and academic life, and longed to see this achievement come true. My sister **Pranati** has been one of my best friend all my life and I love her dearly and thank her for all her advice and support in my difficult days. I know I always have my family to count on when times are rough. The blessings of my elders, my grandparents, uncles, aunties and the good wishes from my cousins, friends have made the work fruitful.

I express my thank to **Mr. Vijayan Nandalan**, Division Head,SPT and DCTMD, ISRO for providing the facility support to conduct the collaborative work between IIST and ISRO on plasma thrusters.

The life at IIST in the God's own country, Kerala is indeed memorable due to the natural environment which is full of greenery and acted as a freshener for all type of worries. The campus on the hill with its beauty have always been attractive. I was very much privileged to learn from this institute, especially when I could personally witness the wonderful rocket launching view which is unforgettable for throughout the life.

Above all, I owe it all to Almighty God for granting me the wisdom, health and strength to undertake this research task and enabling me to its completion.

ABSTRACT

The work here is primarily associated with the understanding of structural and dynamical properties of few members of polycyclic aromatic hydrocarbons (PAHs), theoretically and experimentally under energetic radiation interaction. Influence of collective electronic excitations in this class of molecules while interacting with UV and FUV radiation as well as charged particle radiation is explored in this research work.

Ion-PAH collision using Electron Cyclotron Resonance source: Using Electron Cyclotron Resonance source at Tata Institute of Fundamental Research, Mumbai and Inter University Accelerator Center, New Delhi, the ion-PAH collision experiments were performed for the targets like naphthalene, fluorene with low energy (keV) projectiles (proton, helium, argon) of different charge state in coincidence. For 50 - 240 keV proton-naphthalene collision the mass spectra are obtained in two mode of detection using linear two field time-of-flight mass spectrometer for ion detection in coincidence with outgoing electrons and neutral projectile. Evaporation process like H loss, C_2H_2 loss and different fragments including up to triply charged parent intact molecular ion are visible in mass spectrum. Resonant capture process explained the independent nature of fragmentation yield in electron capture mode. The neutral evaporation process is used as the measure of internal energy. The detailed energetics of the ion-PAH collisions in the intermediate velocity regime and the importance of the collective excitation in this interaction is revealed. This is of great significance in the thermodynamics of interstellar medium in specific circumstances like supernova reverse shock region. We also observe a unique resilience toward fragmentation in such PAHs compared to other

type of organic molecules with structural similarity. Ions detected in multihit mode are used to obtain the kinetic energy released during the fragmentation process and infers about different dissociation pathways. The multifragmentation yields for electron emission mode is found to be decreasing with increase in projectile velocity. To reproduce this trend, *Monte Carlo* simulation within local density approximation were done and the electronic stopping is calculated. The theoretical cross sections obtained from this simulation matched well with the experimental results.

Photon-PAH collision by photoelectron spectroscopy using synchrotron source: The photoelectron spectroscopy studies as a function of photon energy were planned and performed for two PAH molecules namely, pyrene and fluorene. The aim is to investigate different coupling mechanisms between photoionization and electronic states of the molecule using synchrotron source facility at Elettra, Trieste, Italy. The multihit mode mass spectra and photoelectron spectra (PES) for a wide range of photon energy were recorded. The photoionization cross section is found to peak at collective excitation region around 17 eV for the outer valence band. The inner valance bands are found to be coupled with collective excitation feature more efficiently. The observed vibrational progressions were following the same trend for the whole photon energy range, indicating photon energy independent structural alteration post ionization. In addition to this to identify the correlation between photoelectron emission from a particular molecular orbital and the state of the residual ion, the photoelectron-photoion coincidence (PEPICO) measurement is performed. Near edge X-ray absorption fine structure (NEXAFS) data is taken at photon energy close to the *1s* edge of carbon atom to explore the inner shell molecular orbital structure.

For the present work, the Outer valence Green's function (OVGF) technique implemented in GAUSSIAN09 is used to reproduce the measured PES binding energies. The prominent peaks in the PES are identified according to their binding energy and

symmetry using OVGF calculations with a reasonable success. The PES is broadened due to Franck-Condon (FC) overlap of vibrational states. Using Hartree-Fock (HF) and Density functional theory (DFT), the Franck-Condon factors for vibrational progression in $D_0 \leftarrow S_0$ transition were calculated. The simulated results compare well with the experimental results.

Electron affinity calculation and its correlation to HOMA index: Adiabatic electron affinity (AEA) calculations are done using GAUSSIAN09 to understand the stability of PAH anions as well as the property of accommodating charges with the help of delocalization, geometry based aromatic index and structural character. Different levels of HF and DFT calculations are performed on few examples of PAHs and their anions. The calculated AEA matched well with the existing experimental values and also provide the AEA values for some PAHs which are not available in the literature. Presence of a cyclopenta ring is observed to enhance the AEA whereas sp^3 hybridized carbon atom decreases it. The electron density distribution over the anionic molecular volume is analyzed with the help of electrostatic potential maps and electron spin distribution. A geometry based aromatic index known as Harmonic oscillator model of aromaticity (HOMA) index is used to quantify the aromatic character.

Experimental setup developmental work: In order to study the molecules as well as its ions with kinematical correlations in the fragmentation process, an in house mass spectrometer setup is developed. The setup includes an electrospray ion source to produce molecular ions ranging from monomers to complex clusters by soft ionization method followed by an octupole ion guide to bring the ions from atmosphere to high vacuum region, multipole ion trap to thermalize the ions to a specific temperature by collisional cooling, and then an accelerating tube with a provision of pulsing the ion beam. The pulsed ion beam thus produced is made to collide with inert gas target

or irradiated with high intensity pulsed laser beam (UV to IR) of nanosecond width. The resulting fragmentation process is investigated using a parallel plate analyzer with a provision to detect neutral and ionic fragments in coincidence using position sensitive micro channel plate detectors. The ion-optics simulation is extensively done to obtain the optimized parameters and effect of electric field distortion due to mechanical defects for Wiley McLaren type time-of-flight mass spectrometer and parallel plate analyzer using SIMION 8.0. The mechanical drawings and fabrications are done for vacuum chambers, octupole ion guide, gauss tube for pulsed extraction of ion beam, parallel plate analyzer, detector mounting and other accessories using SOLIDWORKS. Position data is obtained from the detector and various calibrations and testing were performed using imaging mask to obtain detector resolution. The ultra high vacuum testing for chambers, electrical testing for power supplies and the testing for functionality of individual components, calibration and resolution measurement for detector are done. Using a penning ionization source, the functionality of parallel plate analyzer is tested. A fast multihit data acquisition time-to-digital converter (TDC) system of 50 picoseconds time resolution is established using NIM modules. The interfacing is done between the position sensitive detectors and the TDC using a MATLAB program. The full set up is tested and successfully gives mass spectrum at present for biomolecules.

TABLE OF CONTENTS

CERTIFICATE i

DECLARATION ii

ACKNOWLEDGEMENTS iii

ABSTRACT viii

LIST OF TABLES xvii

LIST OF FIGURES xviii

ABBREVIATIONS xxviii

1 INTRODUCTION 1

1.1 General introduction 1

1.2 Introduction to polycyclic aromatic hydrocarbons 2

1.3 Role of PAHs in interstellar space physics and chemistry 3

1.3.1 FUV photon interaction 4

1.3.2 Charge particle interaction 5

1.3.3 Cosmic rays interaction 6

1.4 Significance of PAHs on earth 7

1.5 Collective excitation in conjugated molecules 8

1.6 Laboratory studies for energetic radiation interaction with PAHs . . . 9

1.7 Thesis outline 11

2 EXPERIMENTAL WORK **13**

2.1 Ion-PAH collisions 15

2.1.1 Experimental details 16

2.1.2 Results and discussion 28

2.1.2.1 Intermediate velocity proton collision with naphthalene 28

2.1.2.2 Momentum correlation due to coulomb explosion of multiply charged species: identification of channels 42

2.2 Photoelectron spectroscopy for PAHs 47

2.2.1 Experimental details 48

2.2.2 Results and discussion 53

2.2.2.1 Photoelectron cross section measurements 53

2.2.2.2 PEPICO measurements 59

2.2.2.3 NEXAFS measurements 62

2.3 Conclusions 63

3 THEORETICAL WORK **66**

3.1 Introduction 66

3.2 Quantum chemistry calculations 68

3.2.1 Structure calculation for clusters 69

3.2.2 Electron affinity and proton affinity calculation for PAHs . . . 70

3.2.3 Outer valence Green's function method for photoelectron spectrum 82

3.2.4 Franck-Condon simulation for vibrational progression 89

3.3 *Monte Carlo* simulation for ion-molecule collisions 100

3.3.1 Local density approximation model 102

3.3.2 Computational details 103

3.3.3 Ion-PAH collisions 105

3.3.4 Ion-nucleobase collisions 117

3.4 Coulomb over-the-barrier model for electron capture 128

3.5 Conclusions 129

4 DEVELOPMENTAL WORK AND INSTRUMENTATION FOR MASS SPECTROMETER **132**

4.1 Schematic of the set up and its significance 132

4.2 Working principle and test results for individual components of set up 134

4.2.1 Electrospray ionization source 134

4.2.2 Octupole ion guide 139
4.2.3 14-pole ion trap 144
4.2.4 Gauss tube 147
4.2.5 Parallel plate electrostatic analyzer 150
4.2.6 Position sensitive microchannel plate detector assembly and testing 160
4.3 Data acquisition system 165
4.4 Interfacing of DAQ and time correlated pair of detectors 166
4.5 Preliminary results 168
4.6 Future aspects of the set up 169

5 SUMMARY AND OUTLOOK 173

5.1 Photoelectron spectroscopy 173
5.2 Study of highly charged ions interacting with PAHs 174
5.3 Excited state dynamics of PAHs and hybrid clusters 175

6 FUTURE PLANS 176

REFERENCES 178

A C PROGRAM FOR *MONTE CARLO* SIMULATION 214

B ELECTRON AFFINITY VALUES 219

C PROTON AFFINITY VALUES **222**

D OUTER VALENCE GREEN'S FUNCTION CALCULATIONS **223**

E FRANCK-CONDON FACTORS CALCULATIONS FOR VIBRATIONAL PROGRESSION **226**

F NON-INTRUSIVE DIAGNOSTICS FOR XENON ION THRUSTER **229**

LIST OF PUBLICATIONS **233**

LIST OF TABLES

2.1 Proton projectile detection efficiency for different energy. 26

4.1 Maximum counts recorded in TDC for different timeout. 168

B.1 AEA vaules in eV for different levels of calculations and experimental values 219

B.2 HOMA indices for individual rings 221

C.1 Proton affinity values (in kcal/mol) for PAHs at basis B3LYP/6-311++G(d,p) 222

D.1 OVGF calculation for pyrene 223

D.2 OVGF calculation for fluorene 225

E.1 Franck-Condon factors calculation for pyrene 226

E.2 Franck-Condon factors calculation for fluorene 227

E.3 Franck-Condon factors calculation for naphthalene 228

E.4 Franck-Condon factors calculation for anthracene 228

LIST OF FIGURES

1.1 A schematic view of cosmic life cycle (figure adapted from reference (Witt et al., 2004)). 4

2.1 Schematic picture for different post collisional processes. 15

2.2 ECR ion source at IUAC, New Delhi. 17

2.3 Schematic picture of the experimental set up for studying ion-naphthalene collision. 18

2.4 Mass spectra for different conditions. 20

2.5 Ion detection efficiency for different combination of mass and charge of molecular ion. 21

2.6 Mass spectrum for 100 keV proton projectile beam in electron capture mode showing H, 2H/H_2, C_2H_2 loss from naphthalene ion, multiply charged naphthalene ion and fragment ions. 29

2.7 Relative cross sections as a function of proton projectile energy for single, double, triple ionized naphthalene in EE (left) and EC (right) mode. The dashed line is guide to eye. 31

2.8 H and 2H/H_2-loss with respect to intact naphthalene molecular ion in capture mode. 32

2.9 Proportion of H and 2H/H_2-loss with respect to singly charged intact naphthalene molecular ion in capture mode (left) and proportion of C_2H_2 loss with respect to singly charged intact naphthalene molecular ion in both ionization and capture mode (right). The dashed lines are guide to eye. 34

2.10 Mass spectra of EE (left) and EC (right) mode normalized to parent single ionization peak area for all proton projectile energies. 37

2.11 (a) Energy level diagram for naphthalene target (obtained using DFT) and proton projectile, (b) Capture fraction (in percentage) for various molecules in collision with protons. 38

2.12 2D correlation diagram of first and second hit with the ToF mass spectra of singles overlaid for identification. 44

2.13 2D correlation diagram showing the possible m/q produced along with H^+. 44

2.14 Zoomed 2D correlation diagram showing the possible m/q produced along with H^+. 46

2.15 Different momentum correlated decay channels. (a) $CH_3{}^+$ (b) $C_2H_2{}^+$, (c) $C_3H_3{}^+$, (d) $C_4H_2{}^+$ loss region. 46

2.16 Schematic of experimental set up for PES experiment. Figure adapted from Nathan (June 2014) 49

2.17 ToF data for pyrene under 28 eV photon impact. 50

2.18 (a) Xenon Auger electron spectrum at 95.1 eV photon energy, (b) The efficiency variation for different CEMs as a function of photoelectron kinetic energy. 51

2.19 (a) Xe *5p* doublet for photon energy 27 eV, (b) Photon flux variation as a function of photon energy for individual CEMs. 52

2.20 (a) Integrated intensity and (b) branching ratio for various bands of pyrene. 55

2.21 (a) pyrene (b) fluorene PES at different photon energies scaled to the intensity of the HOMO band. 55

2.22 (a) Integrated intensity and (b) branching ratio for various bands of fluorene. 55

2.23 Pyrene (left) and fluorene (right) photoelectron spectra for different photon energy. 56

2.24 PEPICO data for fluorene. The numbers shows different m/q positions. 60

2.25 PEPICO measurements for fluorene at 40 eV photon energy for different CEMs. 61

2.26 C *1s* NEXAFS spectra for fluorene (left) and pyrene (right) for photon energy between 284 to 320 eV. 62

3.1 Optimized structure for clusters. Potential energy curve for the cluster: silver atom attached to corannulene (right side bottom). 70

3.2 The list of the selected examples: 1) Benzene, 2) Naphthalene, 3) Anthracene, 4) Tetracene, 5) Phenanthrene, 6) tetraphene, 7) chrysene, 8) Benzo[c]phenanthrene, 9) Pyrene, 10) Triphenylene, 11) 1,2,3,4-Tetrahydrochrysene, 12) 1,2,3,4,5,6-Hexahydrochrysene, 13) 4,5,9,10-Tetrahydropyrene, 14) 1,2,3,3a,4Hexahydropyrene, 15) Fluorene, 16) Acenaphthylene, 17) Acenaphthene, 18) 1H-Cyclopenta[I]phenanthrene, 19) Acephenanthrylene, 20) 4H-Cyclopenta[def]-phenanthrene, 21) 11H-Benzo[a]fluorene, 22) Aceanthrylene, 23) Fluoranthene, 24) Cyclopenta[hi]acephenanthrylene, 25) Cyclopent[fg]acenaphthylene, 26) Cyclopenta[cd]fluoranthene. The individual ring labels with alphabets are used in text. 73

3.3 Experimental vs. theoretical AEA (circles). Straight line drawn is with slope 1 and intercept zero for guide to eye. 75

3.4 Anionic electron spin distribution at B3LYP/6-31+G(d) level (difference of α and β electron density). 76

3.5 Electrostatic potential (ESP) mapped on to the total electron density distribution of anions. The red color indicates highest negative ESP. . 77

3.6 AEA (experimental and theoretical) vs. WAHOMA index, the line is a straight line fit to the theoretical calculations. 80

3.7 (a) Experimental PE spectrum of pyrene at 27 eV photon energy (outer valence band details in the inset) (b) OVGF calculations convoluted with 0.3 eV width Lorentzian and Gaussian (solid line). The bar graph shows the pole strength for a given binding energy peak. 87

3.8 (a) Experimental PE spectrum of fluorene at 27 eV photon energy (outer valence band details in the inset) (b) OVGF calculations convoluted with 0.3 eV width Lorentzian and Gaussian (solid line). The bar graph shows the pole strength for a given binding energy peak. 87

3.9 FC simulated spectrum for (a) optimized cation (solid) and cation at optimized neutral geometry (dashed) of fluorene for HWHM 50 cm^{-1}, (b) pyrene with and without polarization in the basis set. 93

3.10 Comparison of theoretically simulated spectra for different basis set and for different method of calculation. 95

3.11 Experimental PE spectrum comparison with theoretical vibrational progression showing CC stretch as dominant mode. Inset shows the TPES spectrum (Mayer *et al.* 2011). 96

3.12 Theoretical simulation of vibrational progression showing CC stretch as dominant mode. Inset shows the TPES spectrum (Mayer *et al.* 2011). 98

3.13 Mean energy loss calculation with naphthalene as target using *Monte Carlo* simulation for (a) randomly generated proton projectiles of different energies, (b) 50 keV proton projectile for random and plane wise impact. The numbers indicate electronic stopping value in eV for specific features, (c) randomly generated proton projectiles of different energies showing a comparison of with (solid line) and without (dotted line) inclusion of K-shell electron density, (d) randomly generated proton projectiles of different energies along Z-direction with naphthalene molecule placed in XY plane. 107

3.14 Contour plot for the calculated mean energy loss for random collision of 50 keV proton impinging on the naphthalene molecule placed in XY plane. The color scale represents the magnitude of electronic stopping. 110

3.15 (a) Mass spectra of EE mode normalized to parent single ionization peak area for different proton projectile energies (b) Relative experimental (black square) and theoretical (solid line) cross sections for multifragmentation. 110

3.16 Mass spectrum of EE (solid black) and EC mode (dashed red) normalized to C_7 mass region for 150 keV proton projectile. 114

3.17 (a) Mass spectrum for second hit in electron emission mode normalized to C_7 mass region for 75 keV He^+ (solid black) and He^{++} (dashed red) projectile (b) *Monte Carlo* simulation for mean energy loss calculation by randomly generated trajectories for He^+ (solid black) and He^{++} (dashed red) at 75 keV projectile energy. 115

3.18 *Monte Carlo* simulation for electronic stopping distribution for interaction of proton projectile of energy (a) 100 kev with PAHs, (b) 80 kev with naphthalene derivatives. 117

3.19 Schematic picture for five nucleobase adenine, cytosine, guanine (top three left to right), thymine, uracil and one PAH : naphthalene (bottom three left to right). The various atoms are shown as red (oxygen), blue (nitrogen), grey (carbon), white (hydrogen). 119

3.20 Mean energy loss curve for perpendicular impact of random straight trajectories of 80 keV proton in (a) Z, (b) Y, (c) X-direction with nucleobases placed in XY plane. 120

3.21 Contour plot for the calculated mean electronic energy loss for random collision of 80 keV proton in Z-direction with nucleobases placed in XY plane. 121

3.22 Mean energy loss calculation using *Monte Carlo* simulation for randomly generated (a) 80 keV and (b) 180 keV proton projectiles interacting with nucleobase targets and naphthalene. 122

3.23 Geometric cross sections obtained from *Monte Carlo* simulation of randomly generated classical trajectories of 80, 180, and 300 keV proton beam interaction with nucleobase electron density. 124

3.24 Experimental fragmentation cross sections comparison with theoretical calculations for 80 keV proton-nucleobases collision. 125

3.25 Experimental relative cross sections comparison with theoretical for proton-uracil collision at different projectile energy. 126

4.1 Schematic of the experimental set up at AMP Lab, IIST. 132

4.2 (a) Schematic of ESI source, (b) ESI source at AMP Lab, IIST. 137

4.3 Trajectory of ion inside an octupole when U=0 (left) U $\neq$ 0 (right) (Gerlich, 1992). 141

4.4 Octupole ion guide at AMP Lab, IIST. 143

4.5 RF power supply for the octupole ion guide. 144

4.6 Effective potential as a function of distance from centre for various multipole devices plotted using equation V*. 145

4.7 3D mechanical drawing for 14-pole ion trap with lens holders. 146

4.8 Circuit diagram for the HV pulser along with real Gauss tube. 149

4.9 HV pulser on the circuit board (left) and pulse shape shown on oscilloscope(right). 150

4.10 Parabolic trajectory of ion in electrostatic field between two plates. . . 151

4.11 Field lines inside the parallel plate analyzer with (a) 5, (b) 13 rectangular metallic frames between end plates. 153

4.12 Possible mechanical defects in parallel plate analyzer with total 13 plates while fabrication.(a) 2nd plate tilted by ϕ = 0.5 °, (b) 2nd plate tilted by θ = 1 ° in its own plane, (c) 7th plate is bent down by 4 mm vertical, (d) 7th plate is bent down by 8 mm vertical. 154

4.13 Simulation for the ions of different parameter entering parallel plate analyzer. The color part is showing the flying ions. 155

4.14 Mechanical drawings for (a)Laser interaction chamber attached to PPA chamber, (b)components of PPA: i)Ion beam entrance plate, ii)Middle plate, iii)neutral exit plate, iv)PPA support bracket, v & vi) spacer, vii) 45 ° holder for grounding mesh. 156

4.15 PPA chamber with pumping system attached (left), PPA inside chamber showing the 45 ° holder for grounding mesh allowing ion beam to enter at 45 ° (right top) and PPA (right bottom). 158

4.16 (a) Testing of PPA using a penning ion source, (b) current measurement as a function of scanning voltage on the spectrometer. 158

4.17 Delay line anode MCP detector mounted on spectrometer for charged particle detection and on a flange along the beam direction for neutral detection. 159

4.18 (a) Single MCP plate, (b) delay line anode structure, (c) electrical signal from DLD along two direction. Figures adapted from (DLD1, June 2014; DLD2, June 2014) 161

4.19 Pair of MCPs (chevron configuration) along with DLD as inset (Roent-Dek, June 2014) assembled on a CF160 flange (used for neutral particle detection. 163

4.20 Position image using radioactive source in 2D (left) and 3D (right). . . 164

4.21 Resolution measurement with stainless steel mask (0.5 mm holes). . . 164

4.22 Block diagram of data acquisition system. 164

4.23 Time measurement using various possible start (either from laser or pulsed beam) and stop signals (PSD) with TDC. 167

4.24 (a) Histogram for individual anode signal, (b) sum of anode signals obtained from TDC using MATLAB program 169

4.25 (a) Photograph of brass mask with 10 mm holes mounted on PSD (left) and position image obtained from TDC using MATLAB program with penning gauge as source of particles (right), (b) mass spectrum for glycine. 170

4.26 Laser for photoexcitation study (left) and typical output pulse energy (right). Figure adapted from (Laserdatasheet). 171

F.1 Breathing oscillation in FFT data of 18mN thruster at operation with Xe flow rate 1.2 mg/sec. 230

F.2 Line identification using OES data obtained from fibre optic spectrometer. 231

F.3 (a) Multispec data obtained using high sensitivity CCD camera with specific filters, (b) image converted to numbers showing the intensity profile of the plume coming from different elements within plasma. . 232

ABBREVIATIONS

AEA	Adiabatic electron affinity
AMP	Atomic and molecular physics
amu	Atomic mass unit
a.u.	Atomic unit
BE	Binding energy
BO	Born-Oppenheimer
C	Carbon
CEM	Channel electron multiplier
CFD	Constant fraction discriminator
CI	Capture ionization
CO	Carbon monoxide
COB	Coulomb over-the-barrier
DAQ	Data acquisition
DFT	Density functional theory
DIB	Diffuse interstellar band
DLD	Delay line anode detector
EA	Electron affinity
EC	Electron capture
ECR	Electron cyclotron resonance
EE	Electron emission
EELS	Electron energy loss spectroscopy
ESI	Electrospray Ionization

FC	Franck-Condon
FEL	Free electron laser
FFT	Fast Fourier Transform
FUV	Far ultraviolet
GTF	Gaussian type function
H	Hydrogen
He	Helium atom
HF	Hartree-Fock
HOMA	Harmonic Oscillator Model of Aromaticity
HOMO	Highest occupied molecular orbital
HT	Herzberg-Teller
IR	Infrared
ISM	Interstellar medium
IVR	Intravibronic rotational
KER	Kinetic energy release
LCAO	Linear combination of atomic orbital
LDA	Local (electron) Density Approximation
LUMO	Lowest unoccupied molecular orbital
MC	*Monte Carlo*
MCP	Microchannel plate
MCTDH	Multiconfiguration time-dependent Hartree
MO	Molecular orbital
MR	Membered ring
NEXAFS	Near Edge X-Ray Absorption Fine Structure
NIM	Nuclear Instrumentation Module
OES	Optical emission spectrum
OVGF	Outer valence Green's function

PA	Proton affinity
PAH	Polycyclic aromatic hydrocarbon
PDR	Photodissociation region
PE	Photoelectron
PEPICO	Photoelectron-photoion coincidence
PES	Photoelectron spectroscopy
PIMS	Photoionization mass spectrometry
PPA	Parallel plate analyzer
PSD	Position sensitive detector
SCF	Self consistent field
SOMO	Smallest occupied molecular orbital
STO	Slater type orbitals
TDC	Time-to-digital converter
TD-DFT	Time-dependent density functional theory
ToF	Time-of-Flight
ToFMS	Time-of-Flight mass spectrometer
TPES	Threshold photoelectron spectroscopy
UIR	Unidentified infrared
UV	Ultraviolet
Xe	Xenon
WAHOMA	Weighted average HOMA

CHAPTER 1

INTRODUCTION

1.1 General introduction

Atoms and molecules are the basic constituents of the world around us. Their fundamental properties are mostly governed by the quantum-mechanical nature of a phenomenon, which decide their role and their importance in our life. In fact some of them define the very existence of life as we know of. Thus it becomes greatly important to understand their behavior in a specific environment. Our understanding of matter is entirely dependent upon their response to external perturbations, be it heat, mechanical force, electromagnetic field etc. Investigation in to the nature of such responses has brought great innovation and improvement in our life as well as in our understanding of this universe. The quantum nature of the microscopic phenomenon brings about several experimental and theoretical challenges and interesting insights.

The microscopic studies of behavior of atoms and molecules are as old as the concept of atom itself in modern physics. A controlled and energetic perturbation is applied to a target system and its response is recorded and studied in great detail. This has been the philosophy of collision physics. With the advent of newer and more accurate perturbing and detecting tools, such investigations are taking up more and more challenging tasks and opening up new possibilities.

This work is one such attempt to unravel the subtle and intriguing effects of various quantum phenomenons vital to the definition of a molecular structure. Structural and dynamical investigation, both experimental and complimentary theoretical in nature,

is done for relatively large size of a family of molecules called polycyclic aromatic hydrocarbons (PAHs). These species are not just intriguing but also important in several aspects of modern science. They are model system which helps in designing the tools and methods, which on longer time scale can be applied to more complex and important systems like biomolecules, aggregates and clusters.

1.2 Introduction to polycyclic aromatic hydrocarbons

PAHs are a family of hydrocarbons consisting of molecules where carbon (C) atoms are arranged in a honeycomb lattice type structure of fused six-member aromatic rings with hydrogen (H) atoms located at the periphery of the ring. The smallest member of this family is benzene and the family expands by attaching more number of benzene rings linearly or otherwise. The three valence electron out of four of carbon atoms along with one of hydrogen undergo sp^2 hybridization and thus form covalent σ bonds with neighboring C or H atoms, resulting in a planar structure. The remaining valence electron of C atom is located in a *p*-orbital and is perpendicular to the plane. The superposition of the *p*-orbitals of adjacent C atoms forms π bonds and a delocalized electron cloud above and below the plane of the molecule. The inherent stability for PAHs and aromatic character is due to the existence of such a cloud of delocalized electrons (Eisenberg and Shenhar, 2012). Hence the aromaticity is lost only when the CC σ bonding is broken. The π electronic system also decides different important molecular properties such as color, magnetism, chemical reactivity of the system. Some PAHs are characterized by a peculiar property called Jahn-Teller distortion arising due to pseudo rotation as observed in C_{60} (Chancey, 1997).

A schematic picture for structure of different type of PAHs with different type of symmetry associated is given in Chapter 3. PAHs are classified into two main groups:

pericondensed PAHs (those who have a compact structure where C atoms are members of two or three separate rings, for example coronene). Further they are classified as centrally condensed, quasi-circular PAHs such as coronene and circum-coronene, where the central cycle is surrounded by a series of rings. These molecules are more stable because their structure allows complete electron delocalization and truly aromatic bonding between all adjacent carbon atoms. The second variety is the catacondensed PAHs where no C atom belongs to more than two rings, for example the linear chain PAHs like naphthalene, anthracene, tetracene or bent PAHs like phenanthrene, tetraphene, fluorene (Micelotta et al., 2009).

1.3 Role of PAHs in interstellar space physics and chemistry

In extraterrestrial environment, PAHs have been identified as an important and ubiquitous component of interstellar medium (ISM) and play a crucial role in interstellar physics and chemistry, in cosmic life cycle. These PAHs are predicted to be formed in the outflow of C rich asymptotic giant branch stars. By loosing the peripheral H-atom (see Chapter 2 for details), they become radical and more reactive to form clusters or large PAHs in space. They can be used as a diagnostic tracer of the environmental condition within astrophysical environment. PAHs in space are destroyed either by FUV photodissociation or by strong shock wave (200 km s^{-1}) driven by supernova explosions and are lost in ISM to become a part of ongoing star formation (Bakes and Tielens, 1998; Allamandola et al., 1985). Typically 1-10 % of the total carbon content in Galaxy is from PAHs with 15 - 500 C atoms (Allamandola et al., 1989) and are considered as the cosmically most abundant molecule after H and CO (Bakes et al., 2001). PAHs are also responsible for heating of ISM *via* photoelectric effect upon ionization

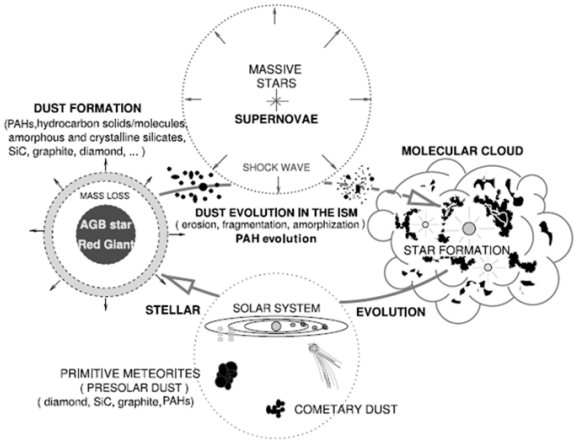

Figure 1.1: A schematic view of cosmic life cycle (figure adapted from reference (Witt et al., 2004)).

due to FUV impact and are applied to gas heating of photodissociation regions (PDRs) (Bakes and Tielens, 1994). They are also the cause of cooling of ISM *via* photoelectric ejection (Bakes and Tielens, 1994), IR emission (Tielens, 2008), collisional cooling with dust grains (Bakes and Tielens, 1998).

1.3.1 FUV photon interaction

PAHs are known to be efficient absorber of stellar UV photon. Upon absorption of a UV photon, PAHs becomes electronically excited and rapid statistically redistribution of the energy *via* intervibronic rotational (IVR) processes to vibrational degrees of freedom occurs over the available modes on timescales of order 10^{-12} - 10^{-10} s. Thus the PAHs in ISM gets de-excited either *via* emitting infrared photons (between 3.3 and 12.7 μm region) or loss of neutrals like H, H_2. The predominant de-excitation channel depends on the external environment and size of the molecule. For example on earth, it is mainly due to collisional de-excitation with ambient molecules. But in the collision-free en-

vironment of space, the IR fluorescence will be dominant mechanism (Tielens, 2005). These emission bands from PAHs are attributed as a primary contributor to the unidentified infra red (UIR) emission band of ISM. Because the laboratory measured IR spectra of PAHs resemble well with the IR bands from many interstellar objects ranging from HII region to galactic nuclei and entire galaxies obtained with the help of Spitzer Space Telescope (Tielens, 2005; Allamandola et al., 1999; Leger and Puget, 1984; Bakes and Tielens, 1998; Bakes et al., 2001). These UIR band appear at 3.3 (CH stretching mode), 3.4, 6.2, 7.7, 8.6 and 11.3 (CH out of plane bending) μm together with weaker feature at 5.6 and 6.95 μm. Hence the characteristic frequency of IR spectra of PAHs can be a tracer to identify a particular type or mixture of PAHs available in ISM (Allamandola et al., 1999; Tielens, 2008). This aspect is discussed in detail in section 3.2.4 of Chapter 3. Apart from this PAH cation is predicted as a possible carrier of UIR bands (Tielens, 2005). The charge state of PAHs are decided by the UV flux and ISM density because of ejection of electron and direct PAH-electron recombination (Bakes and Tielens, 1998). The interstellar abundance for PAHs was found to be 2×10^{-7} with respect to the molecular hydrogen (Allamandola et al., 1985). The i) low density of ISM, ii) no perturbation due to external environment to the isolated species, iii) evidence of ionic PAHs in ISM, compels one to study the ionized PAHs in gas phase under ultra high vacuum condition to simulate the ISM environment in laboratory which can help in understanding various UV photon-PAH interaction dynamics in ISM and the cause of stability of PAHs under such harsh medium.

1.3.2 Charge particle interaction

(a) Ion impact:

Interstellar supernova shock waves (0.1 - 1 keV) and hot post-shock gas (0.1 - 10 keV) (Micelotta et al., 2010) are consist of high energetic ions like H, He, C.

It was found that interstellar PAHs (50 C atoms) do not survive in shocks with velocities greater than 100 km s^{-1} and larger PAHs (200 C atoms) are destroyed for shocks with velocities $\geq$ 125 km s^{-1}. For shocks of in between range, because of incomplete destruction, the PAH structure is destroyed due to significant loss of C atoms from the skeleton. Considering the nuclear interaction, as compare to H and He, C does not contribute to PAH destruction much because of its low abundance (Micelotta et al., 2009). The destruction rate due to shock wave speed is same for molecules (of different masses) having same velocity & temperature profile (Micelotta et al., 2009). The destruction of PAHs due to ion impact may be modeled by an Arrhenius type reaction rate and the velocity of projectile decides the type of interaction, whether electronic or nuclear interaction.

(b) Electron impact:

The dissociation for PAHs in ISM due to electron impact can happen for velocities 2×10^3 km s^{-1} and 4×10^3 km s^{-1} for molecules with 50 and 200 C atoms respectively because larger PAHs require more energy deposition into the molecule for dissociation. These velocities correspond to electron temperatures of 10^5 K and 3×10^5 K, which are reached for shock velocities of approximately 100 and 150 km s^{-1}, respectively (Micelotta et al., 2009).

1.3.3 Cosmic rays interaction

Cosmic rays primarily consist of energetic particles like protons (1 - 10 GeV), 10 % He nuclei, and 1 % heavier element (carbon, oxygen etc.), electrons, gamma ray photons (Tielens, 2005). The heating and ionization of ISM gas is due to low energy cosmic rays which contribute considerably to energy density of ISM ($\approx$ 2 eV cm^{-3}). The cosmic ray ionization rate in ISM is measured to be $\approx 2\times10^{-16}$ (Tielens, 2005). The timescale

for PAH destruction by cosmic ray ions depends on the electronic excitation energy, the minimum cosmic ray energy and the amount of energy available for dissociation. Small PAHs are destroyed faster with He and the CNO group being the more effective projectiles. The shortest survival time that was found is $\sim 10^8$ yrs, which is comparable with the lifetime against destruction in interstellar shocks. For electron collisions, the lifetime is independent of the PAH size and varies with available cosmic ray energy and the threshold energy. The minimum lifetime in this case is 1.2×10^{13} yr (Micelotta et al., 2009, 2010).

1.4 Significance of PAHs on earth

On earth, PAHs are one of the most wide spread pollutant which are formed due to incomplete combustion of carbon rich fuels such as wood, coal, diesel, fat, tobacco, or incense, hence present in vehicular and industrial exhausts, cigarette smoke (Portella et al., 2005). The incomplete combustion of fossil fuels generates PAHs as a class of most spread mutagenic and carcinogenic particulate environmental pollutants. They are naturally present in crude oil and coal deposits, arising from chemical conversion of natural product molecules. These PAHs are identified as carcinogenic, mutagenic and teratogenic (Koper et al., 2002). Human body is contaminated through the skin absorption, inhalation, or food consumption. The contaminated skin on exposure to light (UV) or chemicals can cause mutagenic diseases like DNA single strand cleavage, oxidation of DNA bases and form DNA covalent adducts in human body (Yu, 2002). Because of multiple aromatic ring systems, these compound can absorb light energy in the UVA (320-400 nm) and for some in the visible region (400-700 nm) (Dabestani and Ivanov, 1999) forming reactive species. Therefore, a detailed mechanistic understanding on the photochemistry of PAHs is needed in order to determine the relationship between photo mutagenicity and structure of PAHs.

1.5 Collective excitation in conjugated molecules

Collective/plasmon excitation or giant resonance is a phenomenon involving the simultaneous coherent motions of the less tightly bound electrons in a system at a frequency far above the spectrum of the single particle excitation. The existence of the giant resonance phenomenon does not depend on the nature of the particles and the inter-particle forces. The necessary conditions are: the particles must be moving in a confining potential and the number of them should not be small. Different physical objects as nuclei, atoms, atomic clusters and condensed media, in all of them it is possible to excite collective states involving many particles. Such collective excited states were first discovered in nuclei (proton-neutron oscillation) (Baldwin and Klaiber, 1947) and were called giant dipole resonances (Kaplan, 1997, 1998). The energy of giant resonance peaks varies from $\approx$ 2 eV in metal clusters to $\approx$ 20 MeV in nuclei (on a range of 7 orders of magnitude).

Similar features observed in the case of graphite and graphene have been explained by Drude's model for electronic structure. In the case of C_{60} an analogous feature appears at about 21 eV with width 11.5 eV, close to the one observed in graphite at about 25 eV (Jochims et al., 1999). Considering the two dimensional structure of PAHs, this feature should be expected at about 17 eV (Jochims et al., 1999; Bertsch et al., 1991) and has been observed in electron energy loss spectroscopy studies of PAH films and photo ion yield studies in the gas phase (Jochims et al., 1999; Ling and Lifshitz, 1996). For other PAHs like phenanthrene, anthracene, fluoranthene, pyrene, triphenylene, plasmon resonance is observed in the range of 7 - 21.2 eV for gas phase VUV photoionization mass spectrometry studies (Jochims et al., 1997) and it was found that plasmon excitation leads to autoionization (Ling and Lifshitz, 1996). The positions and oscillator strengths of the π-π* transitions for different PAHs vary because of the difference in symmetry and molecular structure, but a very prominent broad feature at approximately

17 eV is commonly observed in all PAHs (Jochims et al., 1997, 1999). This feature can be attributed to collective or plasmon excitation as well as a mixture of various inner shell transition like σ-π*, π-σ* and σ-σ* transitions.

Collective excitation is shown to play a major role in the photoionization of PAHs (Jochims et al., 1997) and in ion collision with C_{60} (Kadhane et al., 2007). The chemistry of PAHs and fullerenes in natural environments may be closely related and PAHs can be viewed as small units of C_{60}, but the major difference lies in the dehydrogenation possibility due to presence of H-atoms in PAHs. It is now believed that ionized and dehydrogenated PAHs are responsible for the spectroscopic astrophysical observations and it is also shown that dehydrogenation leads to blue shift and broadness of π-π* resonance (Duley and Williams, 1981; Duley, 2006). Hence it is of great interest to study ionization and fragmentation of PAHs following plasmon excitation upon different collisional interactions: either due to photon or charge particle and correlate this relaxation mechanism to various post collisional effects in PAHs, which is the primary objective of this work.

1.6 Laboratory studies for energetic radiation interaction with PAHs

The low energy charge particle as well as FUV radiation interaction with PAHs is shown to be significant to understand various stellar environment processes and their dynamics (Postma et al., 2010). Similar studies performed at higher energy also can probe the structure of the matter into the microscopic details as well as explore a very different regime of physical phenomenons. Several laboratory studies have been carried out in past to understand the behavior of large molecules like PAHs upon energetic radiation interactions: photoionization and photofragmentation studies (Jochims et al.,

1997; West et al., 2012; Ling and Lifshitz, 1996), electron impact studies (Van Brunt and Wacks, 2004; Wacks and Dibeler, 2004) as well as the ion impact studies (Postma et al., 2010; Kadhane et al., 2003, 2007, 2009; Martin et al., 1998, 2012; Ławicki et al., 2011; Johansson et al., 2011; Holm et al., 2010).

The dynamics of ion-molecule collision is very complex as it involves numerous simultaneous processes such as direct (multiple) ionization, fragmentation, inner shell ionization preceding Auger effect, autoionization, transfer ionization and electron capture process. Generally, electron or photon impact mass spectroscopy measurements are dominated by single or multiple ionizations while fragmentation channels remain dormant. However, in ion-molecule collisions, fragmentation channels play a prominent role due to substantial energy deposition in electronic and vibrational modes. Therefore, theoretical modeling for such collision processes is a complex task and hence such studies depends mostly on experimental observations. Due to the broader energy deposition distribution in ion-PAH collision, they are difficult to investigate in terms of rate constants for various dissociative channels (Zettergren et al., 2007b,a; Tappe et al., 2002; Schlathölter et al., 1999a; Postma et al., 2010) and the energetics involved in that process is helpful for any conclusive fact to derive. Whereas in photon collision studies, the excitation energy of the systems upon photon absorption is well defined and gives a very accurate estimate of the appearance energy for a specific fragment. Because the photon interactions are governed by selection rules where the energy exchanged in either absorption or emission process occurs in a fixed quanta of hν. In this present work by realizing the complexity of interaction dynamics, simulation for ion-molecule collision is performed which can be applied to complex multielectron systems such as moderately large molecules and clusters.

Again the energy of the incident beam decides the interaction to be nuclear or electronic and hence the different path ways of reactions. The interactions of low velocity

and high charge state ions with PAHs (Ławicki et al., 2011; Johansson et al., 2011; Holm et al., 2010; Postma et al., 2010) show that the high impact parameter processes are dominated by multi electron transfer followed by coulomb explosion due to high projectile charge states. The low charge state projectile collisions, on the other hand, give rise to thermal excitation causing gentle fragmentation. The electronic stopping has been demonstrated as a prominent heating process responsible for (single and multiple) electron removal in low energy (keV) collision of He^{2+} ions with anthracene monomers (Postma et al., 2010).

Apart from the complexity in large molecules due to availability of large degrees of freedom for dissipation of energy deposited into it during the interaction, there are certain other excitation mechanisms also help PAHs to remain stable or change the post collisional property behavior. One such excitation is collective excitation which arises because of conjugation in ring of the PAHs (Bertsch et al., 1991; Ling and Lifshitz, 1996; Jochims et al., 1997). Due to the broad energy deposition this multiparticle excitation is mingled with other processes and difficult to isolate. The photoionization/fragmentation of PAHs have been studied rigorously (Jochims et al., 1997; West et al., 2012) showing the effect of collective excitation in the case of ionization of PAHs. For C_{60} also, this phenomenon (at $\sim$ 20 eV) is shown to affect the single and double ionization cross section (Tsuchida et al., 1998; Hertel et al., 1992; Kadhane et al., 2003, 2007) in the ion-C_{60} collision process and shows very weak projectile velocity dependence (Kadhane et al., 2007). Hence it is worth to study PAHs also because of structural similarity with C_{60}.

1.7 Thesis outline

The goal of the present work is to investigate the structural and dynamical property of the PAHs under photon and ion impact using several mass spectrometric techniques

and to understand the correlation between various molecular excitation mechanisms and relative stability of these molecules and their fragments.

In **Chapter 1**, a brief introduction to the significant role of PAHs in deciding the physics and chemistry of terrestrial and extraterrestrial environment is given. Apart from this several type of PAHs structure, symmetry is discussed in short with the detail understanding of a peculiar property associated with PAHs, i.e; collective excitation.

In **Chapter 2**, we discuss the experimental work carried out to study the photon and charge particle collision using photoelectron spectroscopy and mass spectrometric technique respectively for three different PAH molecules of different structure as well as symmetry. Various post collisional effects are discussed with the help energetics involved in the interactions.

Chapter 3 discusses the theoretical calculations performed using quantum chemistry and *Monte Carlo* simulation to validate or explain the experimental observations obtained from ion and photon impact experiments.

In **Chapter 4**, the developmental work conducted to establish a mass spectrometer set up at Atomic and Molecular Physics Laboratory, IIST, to perform in coincidence measurement for vibrationally cooled molecular ions in gas phase upon UV-IR photoexcitation under ultra high vacuum condition.

All parameters are in atomic units unless stated otherwise.

CHAPTER 2

EXPERIMENTAL WORK

Experimental study for collision of energetic radiation with molecule helps in understanding various post collisional processes like ionization, fragmentation, dissociation, electron capture (in case of ion impact). The photon induced excitations are governed by selection rules and the collision dynamics as well as consequences are different than the ion impact case. But for the ion impact studies the preference of one over the other process is primarily decided by the relative projectile velocity (v) in comparison with the target electronic orbital velocities (v_e) and the ratio of projectile charge (Z_p) to target nuclear charge (Z_t). However all the processes participate in the same collision process. Figure 2.1 shows schematic picture for different post collision processes. The energy deposition into the molecule due to coulombic interaction of charged projectile with target or electron capture by the ion projectile, leads to ionization/fragmentation/dissociation of target molecule. The kinetic energy released (KER) during this fragmentation/dissociation process is basically the conversion of potential energy stored as bond energy into kinetic energy of fragment ions upon dissociation (Mathur, 1993). Electron capture studies are also significant because electron capture by multiply charged ion has been proposed as a mechanism for generating ions in Earth's upper atmosphere (Prasad and Furman, 1975). Charge particle interaction with atom/molecule (other than PAHs) is extensively studied so far at various impact energy regime (Alvarado et al., 2007; Andersen et al., 1986; DuBois et al., 1984; de Barros et al., 2009; Browning and Gilbody, 1968; Champeaux et al., 2011; Chen et al., 2011; Coupier et al., 2002; Ptasińska et al., 2005; BoudaıÌĺffa et al., 2000; Abdoul-Carime et al., 2005; Märk, 2008). For PAHs such ion impact studies are so far limited to slow

and high velocity regime (Postma et al., 2010; Bordenave-Montesquieu et al., 2001; Wacks and Dibeler, 2004; Van Brunt and Wacks, 2004; Forsberg et al., 2013; Holm et al., 2010, 2012; Martin et al., 2012). To a large extent the structure and evolution of our macroscopic world is determined by the dynamics of many-electron processes using the wide applications in solid state physics, superconductivity and biological systems. But the theoretical investigations involve lots of difficulties and complexity (see Chapter 3) and are practically difficult to explain because of occurrence of several simultaneous processes. Also most of the theoretical calculations performed are photon energy independent above threshold, hence an experiment for a wide range of photon energy helps in exploring the behavior of the system as a function of photon energy. In addition to the above mentioned inelastic processes, collective or plasmon excitation in PAHs plays a significant role in these interactions, particularly in the ionization process, as shown by the photoionization studies (Jochims et al., 1997; Hertel et al., 1992). But this aspect has remained unexplored in collision with charged particle radiation. It is important to note that the influence of this plasmon resonance excitation in ion-PAH collisions other than C_{60} has never been investigated. Therefore post collision analysis of energy deposited in the target molecule in this velocity regime can shed light on understanding of such excitations and on the energetics of the collision process as well as the post collisional relaxation mechanisms. The present study for ion-PAH collision helps in understanding the physics behind the ionization and capture process by isolating them on the basis of electron emission or projectile neutralization. This interaction leads to various competitive collisional de-excitation/stable multiple ionized intact ion formation as well as multifragmentation of naphthalene, which are explained in detail in the following sections on the basis of energetics. In this regard such experimental investigations are found to be very useful which explores the microscopic property of molecules. To understand the behavior of the molecule of our interest (PAHs), we have performed the experiments for ion (for different charge state of different projectile) as

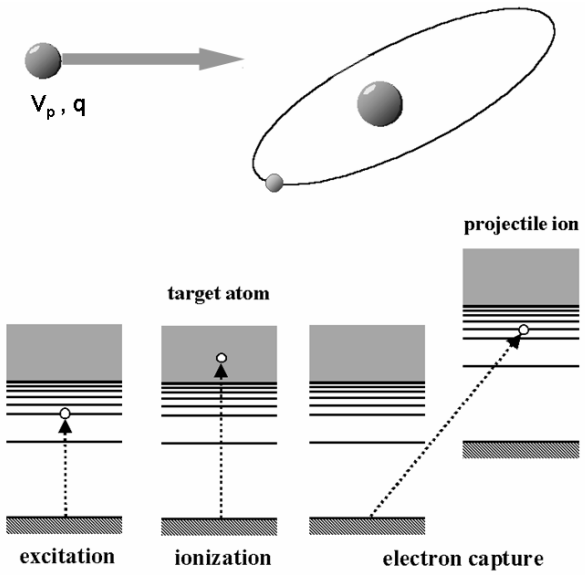

Figure 2.1: Schematic picture for different post collisional processes.

well as photon (for a wide range in UV) collision with PAHs. The significance and results of this studies is discussed in the following sections.

2.1 Ion-PAH collisions

Ion-PAH collisions at intermediate velocities (velocity comparable to less tightly bound target electron) presented in this work, are relatively complex due to competing magnitudes of ionization and electron transfer cross section in this regime. Interaction of intermediate velocity ($\sim$ 1 a. u.) protons with small PAH molecules enhances our understanding of the way low energy cosmic ray protons interact with PAHs in the interstellar medium, thus providing inputs to various models. The importance of collisions at relatively higher velocities ($\sim$ 1 a. u. or more) in the reverse shock of early stage of supernova remnants has been stressed by Postma et al. (2010). However, no laboratory measurements for PAHs have been carried out in this velocity regime whereas the

interaction of PAHs with electromagnetic radiation have been investigated numerous times. These include ionization and fragmentation of naphthalene by electron impact (Wacks and Dibeler, 2004; Van Brunt and Wacks, 2004). Recently, slow charge particle (velocity $v \ll 1$ a. u.) collisions with PAHs and their clusters leading to multiple ionization and fragmentation have been reported (Postma et al., 2010; Johansson et al., 2011; Ławicki et al., 2011; Holm et al., 2010; Seitz et al., 2011). The understanding of low energy collision processes is important because typical ionization cross sections of PAHs peak at about between 50 and 100 keV for proton projectiles (Rudd et al., 1985b) and $\sim$ 50 eV for electrons (Padovani et al., 2009). Due to broader energy deposition distribution in ion-PAH collision, they are difficult to investigate in terms of rate constants for various dissociative channels (Zettergren et al., 2007a,b; Tappe et al., 2002; Schlathölter et al., 1999a; Postma et al., 2010). Hence the present study which employs two distinct modes of ion detection helps in demarcating the energy deposition into the molecules (see later for a detail discussion). In addition to this the in coincidence measured multihit data identifies different dissociation pathways and provides information regarding the momentum associated with the fragmented ions. Such studies are existing in literature for small molecules (Bapat and Sharma, 2006; Bhatt et al., 2012; Rajput and Safvan, 2007; Martin et al., 1998) for which the degrees of freedom are less and hence the possible channels to be studied are less. For large molecules like PAHs, it becomes complex with several multiple processes together and the studies are so far very few (Rajgara et al., 2004; Reitsma et al., 2013).

2.1.1 Experimental details

The experiment was carried out at the Low Energy Ion Beam Facility, Inter University Accelerator Centre (IUAC), New Delhi, India, using an electron cyclotron resonance (ECR) ion source mounted on a high voltage deck. Proton (50, 75, 100, 120, 150, 180

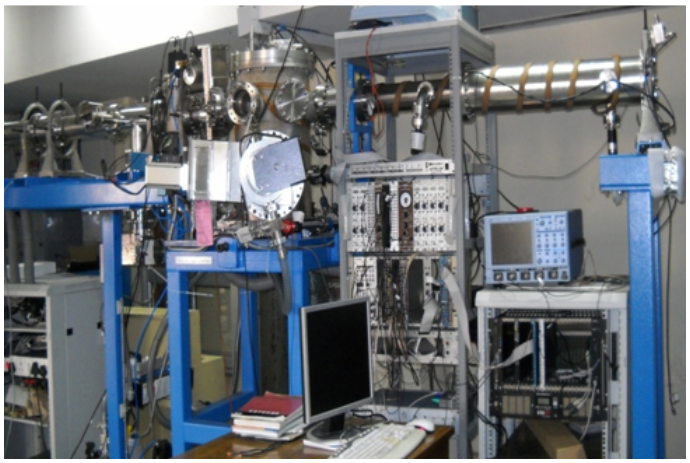

Figure 2.2: ECR ion source at IUAC, New Delhi.

and 240 keV), singly and doubly charged helium (75, 120, 150 and 240 keV), argon with positive charge state 1 - 4 (50, 100, 150 and 200 keV) beams were made to collide with naphthalene target. Naphthalene was effusing from a needle placed perpendicular to the projectile beam path in the collision chamber. The chamber pressure was 5 x 10^{-7} Torr during the experiment. The naphthalene sample was obtained from Sigma Aldrich with 98 % purity. Since the vapor pressure of naphthalene is 0.0817 torr at 22°C, no heating was required for evaporation. There was no contamination seen in the Time-of-flight (ToF) spectrum due to impurities in the sample.

Experimental set up: A linear two field ToF mass spectrometer (TOFMS) with a position sensitive microchannel plate (MCP) detector was used to detect the recoiled naphthalene ions after interaction with the proton beam. The electrons ejected in the process were extracted in an opposite direction to the ions and detected by a channeltron or channel electron multiplier (CEM) (denoted as CEM1). The neutralized projectile beam (as a result of electron capture process) was detected by a second channeltron (CEM2) placed in the path of the beam at a distance of 1.5 m from the collision chamber. Post collision, the charged projectiles were deflected away from this detector using an

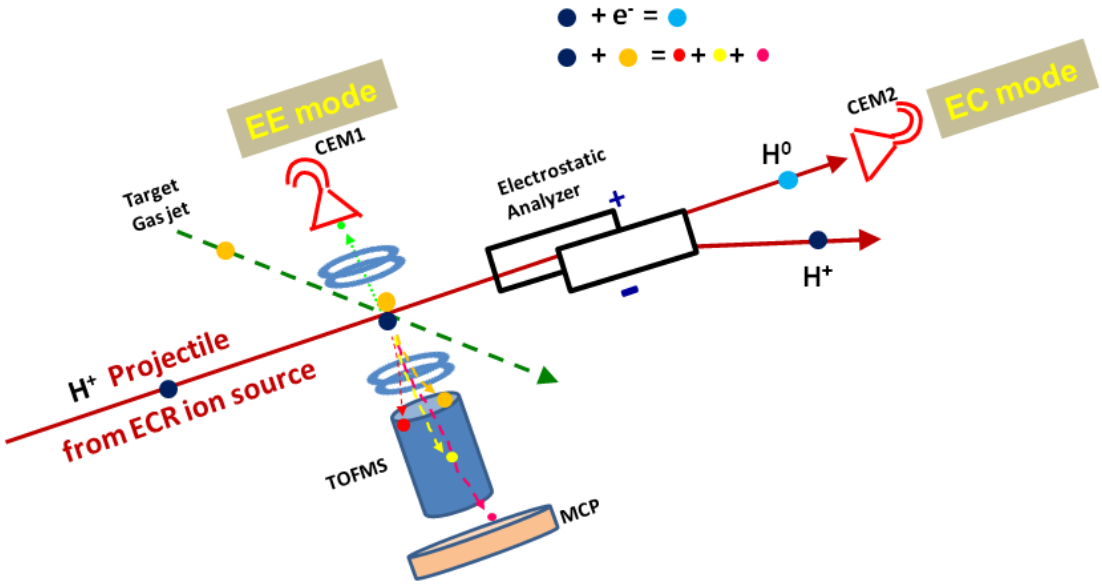

Figure 2.3: Schematic picture of the experimental set up for studying ion-naphthalene collision.

electrostatic deflector (see figures 2.2 and 2.3). There were three mode of detection used in the experiment. The start trigger for electron emission (EE) and electron capture (EC) modes of ion detection were taken from the ejected electrons and neutralized projectile beam, respectively (see equation 2.1 and 2.2). And a third mode was the "OR" mode of recoil ion detection where both the EE and EC mode were recorded simultaneously. Because in this mode the "OR" logic was implemented between both the possible start triggers. The stop signal was taken from the MCP detector. Multi coincidence measurements were carried out in both EE, EC and OR modes by a CAMAC based multihit data acquisition system (DAQ) employing LeCroy time-to-digital converter (TDC) (model 3377 TDC). The detailed layout of the experimental set up and DAQ is described in literature (De et al., 2006).

Multiple ionization events were analyzed using the yield of the respective ionization peaks in the presence or absence of electron and neutralized projectile coincidence.

These multiple ionization yields were used to extract the relative cross sections for ionization due to pure electron emission as well as by single capture along with electron emission. The double electron capture process for proton projectile is here neglected (Rudd et al., 1985b), which was the case shown by Tabet et al. (2010a) where the coincidence measurement of ions with H^- statistics is very poor for 80 keV proton beam interaction with nucleobase. Because at this velocity electron capture takes place in collision with small impact parameter than the relatively distant pure ionization collision. Therefore electron capture process is always accompanied by further excitation and ionization. It is also assumed that neutralization of beam due to capture of electron before collision is negligible which was verified by measuring the neutralization counts in the absence of target. Following pathways are considered for the experiment,
For EC mode:

$$H^+ + C_{10}H_8 \rightarrow H^o + ne^- + \text{(Parent ion / fragment ion)}, \tag{2.1}$$

For EE mode:

$$H^+ + C_{10}H_8 \rightarrow H^+/H^o + me^- + \text{(Parent ion / fragment ion)}, \tag{2.2}$$

where ($n \geq 0$ and $m \geq 1$)

Upon interaction with projectile, the target can undergoes following channels:

proton + $C_{10}H_8 \rightarrow (C_{10}H_8)^{n+}$ + ne^- [outer shell ionization]

$\rightarrow (C_{10}H_8)^{n+}$ + ne^- [inner shell ionization]

$\rightarrow$ [plasmon excitation]

$\rightarrow (C_{10}H_m)^{n+}$ + ne^- + mH/H^+ [neutral/ionic H-loss]

$\rightarrow (C_jH_k)^{n+}$ + $(C_pH_q)^{m+}$ + $(m+n)e^-$

[fragmentation with j+p = 10 and k+q = 8]

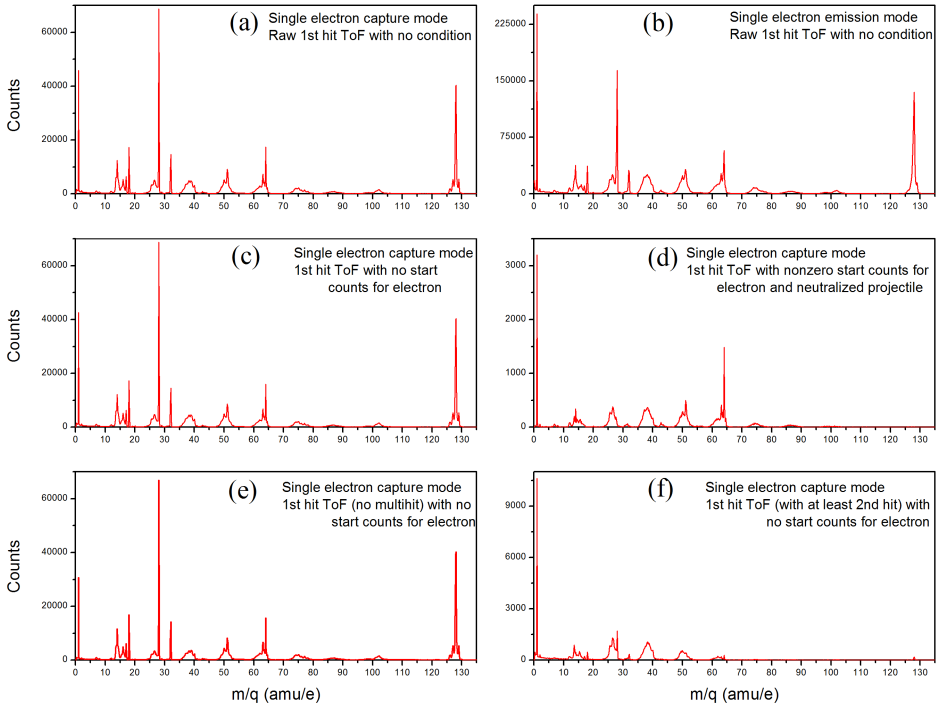

Figure 2.4: Mass spectra for different conditions.

Relative cross section calculation: The mass spectra were isolated according to the detection mode (see figure 2.4) in order to extract the relative experimental cross sections by appropriately correcting for the ion, electron and neutralized projectile detection efficiencies (the detailed procedure for efficiency calculation is given in following sections). The relative cross sections obtained from mass spectra are normalized to the electron (8%) and neutralized projectile beam detection efficiency (5-20%, depending on beam tuning condition) in EE and EC modes, respectively. The projectile detection efficiency as well as the target thickness and total beam flux were obtained for each projectile energy using the present experimental yields and previously published N_2 ionization and capture cross sections (Rudd et al., 1983). The ToF mass resolution ($\triangle$M/M) in case of EC mode was better than 1/128. However, in EE mode the resolution was poor due to slightly distorted start signal from the channeltron CEM1.

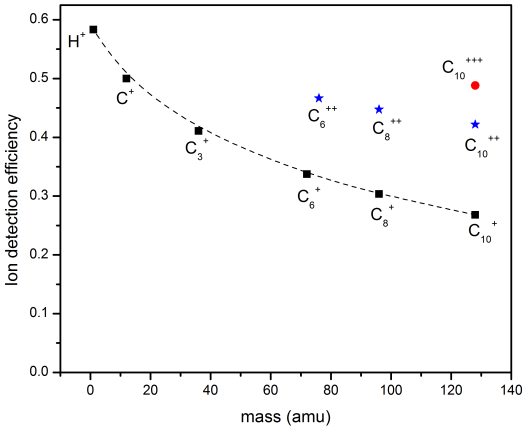

Figure 2.5: Ion detection efficiency for different combination of mass and charge of molecular ion.

A: Ion detection efficiency: The ion detection efficiency for the MCP detector has been obtained using an empirical model reported in literature (Krems et al., 2005). The detection efficiency is characterized by the following polynomial

$$\log[\eta] = A + B\chi + C\chi^2 + D\chi^3 + F\chi^4 \tag{2.3}$$

where $A = -0.257, B = 0.161, C = -0.239, D = -0.0184, F = -0.3,$
$\chi = \log\left[\frac{E}{M^{0.5}}\right]$

$E =$ impact energy in keV, $M =$ mass of ion in amu, η is the ion detection efficiency.

Using the above formula the cross sections are corrected for individual ion detection efficiency. Here the ToF contains two mesh along the flight tube path and we assume that the mesh transmission efficiency is independent of mass. Figure 2.5 shows the efficiency variation as a function of mass which tells that the absolute ion detection efficiency varies for a given mass with different charge state and also varies for different mass with same charge state.

B: Electron detection efficiency: Since we neglect contributions due to double capture, the double ionization of the target can occur either by transfer of one electron to projectile as well as emission of one electron, or by two electrons emission. Hence, by using the yields of dication with and without electron detection in EC mode, we have been able to determine the electron detection efficiency. The possibility of multiple electron detection (along with neutralized projectile detection probability in relevant cases) has been considered in efficiency correction for double and higher ionization relative cross sections. The procedure for calculation is the following:

Symbols used:

For EE process, it is required that at least one electron be detected for a start trigger

For EC process, it is required that a neutral projectile be detected for a start trigger

$N_t \times N_p$: target density times projectile density

ϵ_e : electron detection efficiency

ϵ_p : projectile detection efficiency

$\epsilon_{ion}{}^{+}$ and $\epsilon_{ion}{}^{++}$: singly and doubly charged molecular ion detection efficiency respectively

σ^i : single ionization cross section due to electron emission

σ^c : single ionization cross section due to electron capture

σ^{2i} : double ionization cross section due to electron emission

σ^{ci} : double ionization cross section due to electron capture and one electron emission

$(A_{Nph^+})_i$ and $(A_{Nph^+})_c$: single ionization experimental yield in EE and EC mode respectively

$(A_{Nph^{++}})_{ii}$: double ionization experimental yield in EE mode

$(A_{Nph^{++}})_{ic}$: double ionization experimental yield with electron detection in coincidence with neutral projectile in EC or neutral projectile detection in coincidence in EE mode

$(A_{Nph^{++}})_{c}$: double ionization yield in EC mode with no electron detected

Different types of processes:

1. Single ionization of parent molecule:

   (a) EE mode: $$(A_{Nph^{+}})_{i} = \sigma^{i} \times \epsilon_{e} \times {\epsilon_{ion}}^{+} \times N_{t} \times N_{p} \tag{2.4}$$

   (b) EC mode $$(A_{Nph^{+}})_{c} = \sigma^{c} \times \epsilon_{p} \times {\epsilon_{ion}}^{+} \times N_{t} \times N_{p} \tag{2.5}$$

2. Double ionization of parent molecule:

   (a) EE mode:

   i. $$(A_{Nph^{++}})_{ic} = \sigma^{ci} \times \epsilon_{e} \times \epsilon_{p} \times {\epsilon_{ion}}^{++} \times N_{t} \times N_{p} \tag{2.6}$$

   Equation 2.6 gives double ionization yield caused by one electron capture and one electron emission

   ii. $$\begin{aligned}(A_{Nph^{++}})_{ii} \quad &= [\sigma^{2i} \times (2\epsilon_{e} - {\epsilon_{e}}^{2}) \times {\epsilon_{ion}}^{++} \times N_{t} \times N_{p}] + \\ &[\sigma^{ci} \times \epsilon_{e} \times (1 - \epsilon_{p}) \times {\epsilon_{ion}}^{++} \times N_{t} \times N_{p}]\end{aligned} \tag{2.7}$$

   Where the $(2\epsilon_{e} - {\epsilon_{e}}^{2})$ term is the probability of detecting at least one electron out of the two emitted. The first term in equation 2.7 is due to pure double ionization, 2nd term is due to double ionization with no neutral projectile detection.

(b) EC mode

i. Double ionization by capture with electron detection in coincidence

$$(A_{Nph^{++}})_{ic} = \sigma^{ci} \times \epsilon_e \times \epsilon_p \times {\epsilon_{ion}}^{++} \times N_t \times N_p \tag{2.8}$$

The $(A_{Nph^{++}})_{ic}$ is obtained from first hit ToF values with neutral projectile detection (as well as electron is detected in the same event)

ii. Double ionization by capture with no electron detection

$$(A_{Nph^{++}})_{c} = \sigma^{ci} \times (1 - \epsilon_e) \times \epsilon_p \times {\epsilon_{ion}}^{++} \times N_t \times N_p \tag{2.9}$$

The $(A_{Nph^{++}})_{c}$ is obtained from first hit tof values with neutral projectile detection (no electron is detected in the same event)

Hence using equation 2.8 and 2.9 the electron detection efficiency is obtained as follows:

$$\epsilon_e = \frac{\tau}{1+\tau} \tag{2.10}$$

where $\tau = \frac{(A_{Nph^{++}})_{ic}}{(A_{Nph^{++}})_{c}}$

Since ϵ_e is independent of target and projectile, so this value can be used for any energy. So the mean value of ϵ_e for all projectile energy (ϵ_e = 0.08414) is used as the electron detection efficiency.

C: Projectile detection efficiency: The projectile detection efficiency depends on the energy of the projectile and on the other external experimental parameters. We have deduced it with the help background gas yield obtained under the constraint of the target experimental condition and electron detection efficiency. We follow the following nomenclature:

$(A_{N_2{}^+})_e$: Area of $N_2{}^+$ peak in EE mode with proton projectile and naphthalene target (while only electrons are detected)

$(A_{N_2{}^+})_p$: Area of $N_2{}^+$ peak in EC mode with proton projectile and naphthalene target (while only neutral projectiles are detected)

$$(A_{N_2{}^+})_e = \sigma^i \times \epsilon_e \times (\epsilon_{ion})_{N_2{}^+} \times ((N_t)_{N_2} \times N_p)_e \tag{2.11}$$

$$(A_{N_2{}^+})_p = \sigma^c \times \epsilon_p \times (\epsilon_{ion})_{N_2{}^+} \times ((N_t)_{N_2} \times N_p)_p \tag{2.12}$$

dividing equation 2.11 with 2.12 we get

$$\frac{(A_{N_2{}^+})_e}{(A_{N_2{}^+})_p} = \frac{\sigma^i}{\sigma^c} \times \frac{\epsilon_e}{\epsilon_p} \times \frac{((N_t)_{N_2} \times N_p)_e}{((N_t)_{N_2} \times N_p)_p} \tag{2.13}$$

In equation 2.13, the left-hand side is taken from the experimental data and the values for σ are taken from the published ionization and capture cross section for N_2 (Rudd et al., 1983). In this process it is assumed that the target density was in constant proportion to the N_2 and O_2 gas. This has been independently checked by comparing the yield ratios under identical experimental conditions at different times during the experiment.

Both EE and EC mode were performed simultaneously by using an "OR" condition between the respective start triggers to detect the ions. So for whole experimental duration, the product of target density and projectile density are same for a given projectile energy. So for these data sets

$$\frac{((N_t)_{N_2} \times N_p)_e}{((N_t)_{N_2} \times N_p)_p} = 1 \tag{2.14}$$

and using ϵ_e = 0.08414 and equation 2.13, we obtain the projectile detection efficiency as

$$\epsilon_p = 0.08414 \times \frac{\sigma^i}{\sigma^c} \times \frac{(A_{N_2{}^+})_p}{(A_{N_2{}^+})_e} \tag{2.15}$$

Table 2.1: Proton projectile detection efficiency for different energy.

Projectile Energy (keV)	ϵ_p
50	0.14826
75	0.20306
100	0.04686
150	0.16613

The cases for which we do not have such OR mode data set, the

$$\frac{((N_t)_{N_2} \times N_p)_e}{((N_t)_{N_2} \times N_p)_p} \neq 1 \tag{2.16}$$

For such cases:

$$(A_{Nph^{++}})_e{}^{ic} = \sigma^{ic} \times \epsilon_e \times \epsilon_p \times (\epsilon_{ion})_{Nph^{++}} \times (N_t \times N_p)_e \tag{2.17}$$

$$(A_{Nph^{++}})_p{}^{ic} = \sigma^{ic} \times \epsilon_e \times \epsilon_p \times (\epsilon_{ion})_{Nph^{++}} \times (N_t \times N_p)_p \tag{2.18}$$

where $(A_{Nph^{++}})_e{}^{ic}$ and $(A_{Nph^{++}})_p{}^{ic}$ are obtained from the data sets in EE and EC mode respectively with both electron and neutral projectile being detected.

dividing equation 2.17 with 2.18 we get

$$\frac{(A_{Nph^{++}})_e{}^{ic}}{(A_{Nph^{++}})_p{}^{ic}} = \frac{((N_t)_{N_2} \times N_p)_e}{((N_t)_{N_2} \times N_p)_p} = \Upsilon \tag{2.19}$$

using equation 2.13, we get

$$\epsilon_p = 0.08414 \times \upsilon \times \frac{\sigma^i}{\sigma^c} \times \frac{(A_{N_2{}^+})_p}{(A_{N_2{}^+})_e} \tag{2.20}$$

using equations 2.15 and 2.20, we get projectile detection efficiency (ϵ_p) for different projectile energy which are given in table 2.1.

Thus the projectile detection efficiency as well as the target thickness and total beam

flux were obtained for each projectile energy using the present experimental yields. The noticeable deviation of projectile detection efficiency for 100 keV proton projectile case as compared to the other cases could be an artifact of beam tuning. In the absence of absolute target density values, only the relative values of all cross sections for ionization, dissociation and multifragmentation channels could be estimated. The constant of proportionality needed to relate all the relative cross sections to their respective absolute cross sections, is a single common factor for EE and EC mode measurements. The overall target density fluctuations as well as errors in the efficiency are within 10 - 20% of the value in all cases except triple ionization where poor statistics leads to $\sim$ 30% error.

In figure 2.4 we have shown the mass spectra for different experimental mode of detection without any efficiency correction implemented. Raw data of first hit mass spectra with EE and EC mode is shown in figure 2.4 a and b respectively. Typically the number of events with more than one hit was at most 10% of the total recorded events and it also contains data with capture-ionization. The first hit mass spectra contain peaks form intact parent ions, residual ions with neutral loss (narrow peaks) as well as charged fragments produced in coulomb explosion of multiply charged ions (broad peaks). Generally in the present range of measurements, EE mode shows more yield for low mass fragments than the EC mode. The rest of the analysis discussed here is for only EC mode data. An additional condition in EC mode with no detection of accompanying electron shows very little difference between figures 2.4a and c (also in the case of figure 2.4e). This indicates that the events where neutralized projectile as well as emitted electrons being detected together are very few. Considering the fact that only single electron capture can be caused in these cases, it means that a large fraction of electrons are not detected. On the other hand when both neutralized projectile and emitted electrons are detected together we observe in figure 2.4d that the parent ion peak as well as C_2H_2 evaporation peak are excluded. Dication peak dominates the spectrum

with H^+ peak. Finally by demanding that at least two hits are produced in a given event, this condition removes contributions of all the intact ions and neutral evaporation ions from the spectra, except a small contribution from chance coincidence. Hence by putting such multi parameter conditions we can include or exclude specific contributions and thus estimate the yield due to pure ionization, pure capture and capture-ionization etc.

2.1.2 Results and discussion

2.1.2.1 Intermediate velocity proton collision with naphthalene

A. Single and multiple ionization: Figure 2.6 shows a typical mass spectrum observed in ion-molecule collisions, which is shown here for 100 keV proton impact on naphthalene in EC mode. This spectrum is enriched with sharp multiply ionized parent molecule M^{q+} (up to q = *3*), evaporation process like the loss of H, 2H/H_2, C_2H_2 and other broad fragmentation channels. The peaks at m/q of 129, 128, 127 and 126 correspond to (i) naphthalene isotopic peak with one ^{13}C, (ii) naphthalene with all ^{12}C, (iii) H-loss, and (iv) 2H or H_2 loss (from parent ion), respectively. The isotopic ratios for mass 128 and 129 are found to be consistent within the expected value of 11%. Single ionization is observed to be the most prominent channel followed by double ionization. Ionization of naphthalene up to charge state 3+ is observed but the intensity is low compared to multifragmentation channels.

In the dication region, the mass spectrum shows a composite peak with a sharp narrow peak overriding a broad feature. The peak at m/q of 64 can arise either due to a singly charged half mass peak or due to a doubly charged intact molecule. This ambiguity was resolved by comparing the area of the isotope peak at 64.5 mass (which gave the correct isotopic ratio) with the area of sharp peak at 64 alone, allowing us to

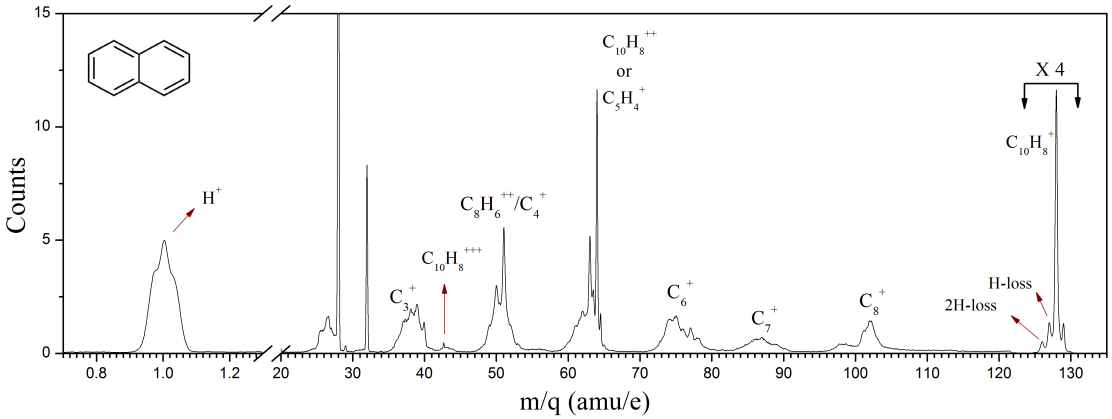

Figure 2.6: Mass spectrum for 100 keV proton projectile beam in electron capture mode showing H, 2H/H_2, C_2H_2 loss from naphthalene ion, multiply charged naphthalene ion and fragment ions.

conclude that the sharp peak structure is due to the dication species. The broad peak is likely to be due to the violent fragmentation of multiply charged species leading to singly charged $m/q \leq 64$ mass fragment. A clear difference in ionization mechanism was observed for naphthalene and nucleobase by comparing the double ionization yield upon collision with proton of same energy. The double ionization yield is much larger than the 2H/H_2 and C_2H_2 loss for naphthalene which is in contrast with collision of nucleobases with protons (in the same energy range) where the fragmentation channels dominate and multiple ionization is negligible (Tabet et al., 2010a). Considering that molecules like adenine (135 amu) and guanine (151 amu) are of the same mass range as naphthalene (128 amu) and have similar elemental composition, the electronic energy loss is also expected to be similar. Hence the difference in ionization can be due to the ability to accommodate excess charge without dissociation because of large delocalization of π electrons due to conjugation property in PAHs. This ability of accomodating excess charge in PAH rings is discussed in more detail in terms of electron affinity with the help of quantum chemistry calculations in Chapter 3. This is also well known in the case of C_{60} where metastable fullerenes with charge state up to 12+ have been de-

tected experimentally (Bhardwaj et al., 2003). The presence of hetero atom in the case of nucleobases may cause reduction in such delocalization, thus reducing the threshold energy for fragmentation compared to multiple ionization.

The mass spectra show a completely different behavior depending upon the mode of detection. We find that the double and triple ionization yields are higher in EE than in EC mode as shown in figure 2.7. Single and double ionization cross sections in EE mode are observed to be almost constant within error bars, whereas the corresponding cross sections in the (EC and CI) modes decrease with impact energy by about an order of magnitude. Several studies have shown that for collisions of proton with diatomic molecules (Rudd et al., 1985a), linear hydrocarbons (Janev et al., 2002) and nucleobases (Tabet et al., 2010a; Lekadir et al., 2009), the ionization cross sections in the present projectile velocity range, decrease by a factor of three. However, for C_{60} the cross sections increase slowly with energy (Tsuchida et al., 1998), approaching a constant value for energies larger than 100 keV. On the other hand capture cross sections show a drastic decrease with projectile velocity, as seen in all the above stated cases (except C_{60} where the relevant numbers are not available for comparison) (Janev et al., 2002; Tabet et al., 2010c; Lekadir et al., 2009; Rudd et al., 1985a; Gobet et al., 2004). Using the expression for calculating single ionization cross sections given by Stolterfoht et al. (1997) and binding energy values (obtained using DFT calculation), single ionization cross sections for naphthalene are calculated which also show a drop by factor of three. These observations, together with the fact that plasmon excitation plays a major role in single ionization of PAHs (Jochims et al., 1997; Ling and Lifshitz, 1996), indicate that plasmon resonance excitation could be the principal single ionization channel here (similar to the case of C_{60}). The decreasing behavior of single electron capture cross sections for parent ion are discussed in section 3.4 with the help of coulomb over-the-barrier model calculation.

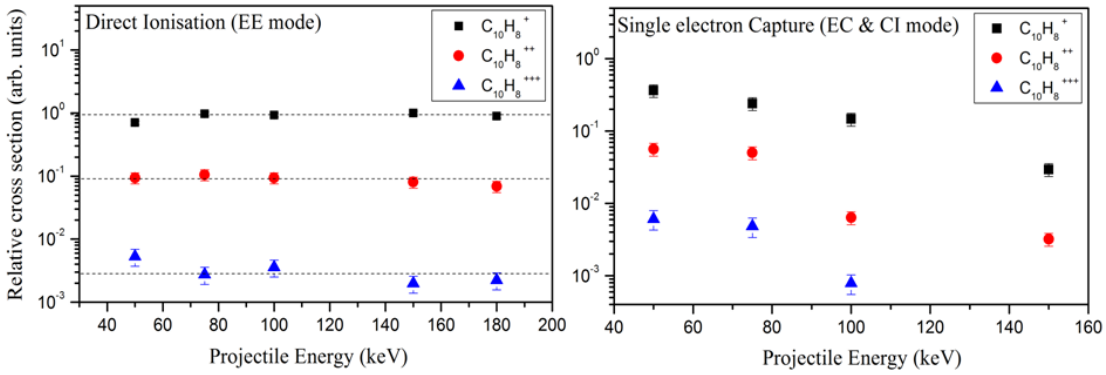

Figure 2.7: Relative cross sections as a function of proton projectile energy for single, double, triple ionized naphthalene in EE (left) and EC (right) mode. The dashed line is guide to eye.

B. H-loss, 2H/H_2-loss and C_2H_2 loss: Considering the time scale of geometry of the set up, the single ionization parent ion peak represents a low internal energy process. Apart from thermally colder ionization and violent fragmentation processes, the mass spectra in the present study is enriched with evaporation processes due to intermediate internal energy, which are primarily the neutral H-loss, 2H/H_2-loss and C_2H_2 loss for PAHs. By nature these are statistical processes and occur due to distribution of energy over the entire degrees of freedom in the full molecule leading to internal heating. Hence neutral loss population is a measure of temperature associated with the molecular ion. The FWHM corresponding to these peaks are comparable to intact singly charged molecular ion (see figure 2.8). These channels are well studied theoretically using Arrhenius law by Allain et al. (1996) as well as experimentally by Jochims et al. (1994). This kind of study is of significant in terms of the chemical balance studies in ISM. Vuong and Foing (2000) found that the PAHs tend to be dehydrogenated in diffuse cloud environments where the hydrogen density is about 0.1 - 100 cm^{-3} and the temperature is $\sim$ 100K. Larger PAH molecules (with more than 50 carbon atoms) have more degrees of freedom for storing the excess energy deposited by UV absorption. Hence,

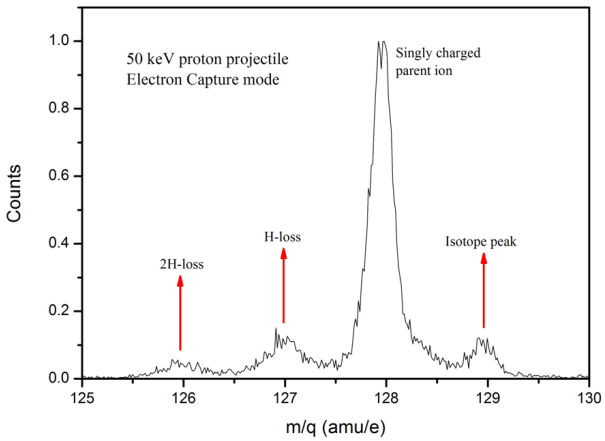

Figure 2.8: H and 2H/H_2-loss with respect to intact naphthalene molecular ion in capture mode.

they are less prompt to dehydrogenation even in low H-density regions of ISM (Vuong and Foing, 2000). By loosing H, 2H, these PAHs become more reactive and have high affinity for another radical PAHs and lead to formation of large PAHs in ISM. They also act as a catalyst/source for the formation of molecular hydrogen, the most abundant molecule in ISM (Tielens, 2008).

It is well-known that H-loss is a prominent evaporation mechanism by which the molecular ion of PAH can reduce its internal energy (Gotkis et al., 1993; Jochims et al., 1994). In the case of 2H or H_2 loss, it is not possible to distinguish between the two channels, i.e. whether the loss of H was sequential or simultaneous (in the form of molecular hydrogen). The latter is energetically favored but less probable at lower internal energy (Holm et al., 2011; Jolibois et al., 2005). Rousseau et al. (2012) have shown that when 11.25 keV He^+ ions collide with anthracene molecules, 2H/H_2 loss is much larger than H loss for single ionization. On the other hand, collision with Xe^{10+} beam at 360 keV produces anthracene ions with almost no 2H/H_2 loss and the fraction of H loss is very small. He^+ collision is expected to cause single ionization at a much lower impact parameter than Xe^{10+} collision. Hence the former projectile will deposit

more internal energy than the latter. Therefore, the dominance of 2H loss peak in He^+ collisions over H loss implies that this particular peak is not due to sequential H loss but a loss of molecular H_2. In other words, at lower internal energies, sequential double H loss mechanism is effective and at higher internal energies it is molecular H_2 loss mechanism. The trend is similar for coronene and pyrene (Ławicki et al., 2011). In the present case, the average electronic stopping is considerably less than those with lower velocities of He^+ ions discussed above. Hence the sequential loss of 2H is more likely than the loss of H_2.

Holm et al. (2011) have shown that with increasing charge state, the loss of charged species becomes energetically more probable. For naphthalene, it has been shown that for the charge state $q = 2$, the charged fragment evaporation becomes energetically comparable to neutral evaporation. The multi coincidence analysis in the present study shows that for H, 2H/H_2 loss peaks, there are no detectable charged fragments in coincidence. However, a detectable but week correlation channel between $C_2H_2{}^+$ loss in coincidence with $C_8H_6{}^+$ or more prominently with $C_8H_5{}^+$ fragment is observed. This is discussed in detail in section 2.1.2.2. Therefore, it can be concluded that even for doubly charged parent ion case, the charged fragment evaporation is not a favorable channel for naphthalene. As a result, the loss of H, 2H/H_2 and C_2H_2 can be considered as loss through evaporation of neutrals, predominantly.

In case of direct ionization mechanism (i.e. EE mode) the evaporation process C_2H_2 loss shows no dependence on impact energy and hence concludes in same amount of energy deposition (see figure 2.9). The single ionization peaks (which includes the H and 2H loss channels as well as an isotope peak) for the entire energy range under consideration overlap exactly, demonstrating the independence of projectile velocity in these channels. Due to poor resolution, the H and 2H loss channels are not plotted, but, since these channels are very sensitive to energy deposition, the energy deposition in EE

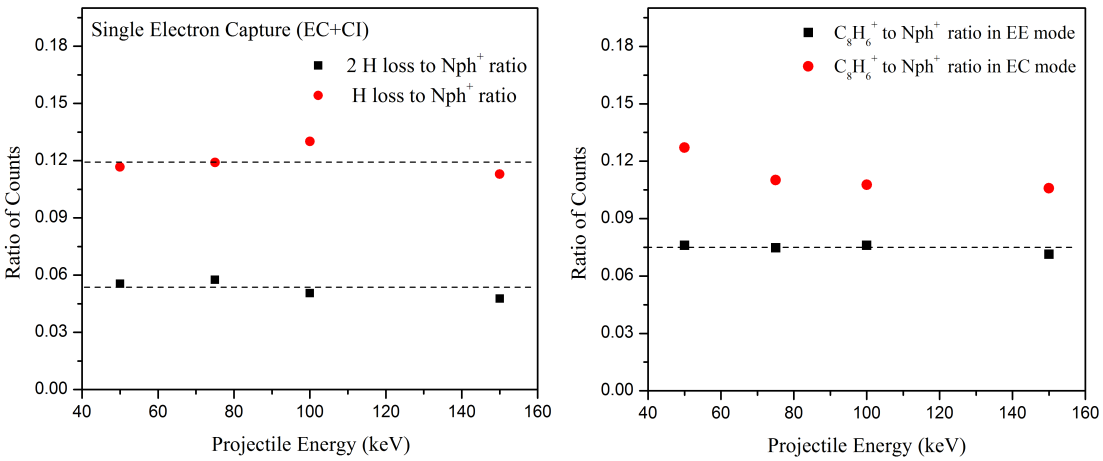

Figure 2.9: Proportion of H and $2H/H_2$-loss with respect to singly charged intact naphthalene molecular ion in capture mode (left) and proportion of C_2H_2 loss with respect to singly charged intact naphthalene molecular ion in both ionization and capture mode (right). The dashed lines are guide to eye.

mode should also be constant over the present velocity range, analogous to EC mode (figure 2.9 shows the constant nature of H and 2H loss channels for EC mode).

C. Internal energy deposition in EE and EC mode: For the de-excitation of PAHs, IR emission is expected to compete with other channels like H, $2H/H_2$ or C_2H_2 loss at a decay rate of 10^2 s^{-1}. At higher decay rates, the dissociation channels dominate (Allain et al., 1996). It has been shown both experimentally and theoretically that for naphthalene molecule at the appearance energy of the above mentioned loss channels, the decay rates are 10^4 s^{-1} or more (Jochims et al., 1994). The measured appearance energies are 15.41, 15.60 and 15.50 eV for H, H_2 and C_2H_2 loss, respectively (Jochims et al., 1994). Considering that the ionization potential is 8.12 eV, the minimum internal energy required for the above mentioned loss channels would be 7.40 eV, 7.59 eV and 7.49 eV, respectively with 0.11 eV average thermal energy. This is needed in order to

observe these channels in our experimental ToF range (which requires limiting decay rate of 10^5 s^{-1}). The other higher mass dissociation channels have appearance energy values close to (within few eV) the appearance energy of H, 2H and C_2H_2 loss channels (NISTe, June 2014). Therefore, at a higher internal energy, other dissociative channels will open up. This implies that the H, 2H/H_2 and C_2H_2 loss mass spectra are sensitive to internal energy variation in the present study ToF range (10 micro seconds). Consequently, any small change in the energy deposition close to the appearance energy will reflect in a large variation of H, 2H/H_2 and C_2H_2 loss yields in comparison to single intact ionization.

These decays have been modeled for naphthalene as an Arrhenius type of decay by Gotkis et al. (1993) using photoionization data. They have derived activation barriers as 4.23 and 4.6 eV for H and C_2H_2 loss, respectively. Ho et al. (1995) repeated these activation barrier measurements on naphthalene ions using two-photon absorption time-resolved photodissociation method and obtained values of 4.48 and 4.41 eV for H and C_2H_2 loss, respectively. On the other hand, Jochims et al. (1994) and Allain et al. (1996) have followed a simpler RRK approach with bond activation energies of 2.8 and 2.9 eV for H and C_2H_2 loss, respectively. The calculations are expected to be applicable to both forms of naphthalene, neutral and cationic, with identical decay parameters (Jochims et al., 1994). Recently West et al. (2012) have considered a much larger number of channels and accurately determined the Arrhenius parameters for the statistical dissociation of naphthalene monocation (West et al., 2012). To estimate the range of energy loss in the present case, we use the 0 K breakdown curves obtained by West et al. (2012) which have similar ToF time scale as in the present case. From these curves, we note that for the total energy deposition below 18 eV, C_2H_2 loss fraction is the same as H loss fraction. We find an analogous behavior for the EC mode, as shown in figure 2.9. In other words, most of the events leading to single ionization deposit energy less than 18 eV in EC mode. On the other hand, EE mode shows 30% less yield

of C_2H_2 compared to EC mode (see figure 2.9), implying that a significant fraction of collisions leading to single ionization involves energy deposition larger than 18 eV.

In the double ionization case, the loss of 2H/H_2 dominates over H loss corroborating the fact that double ionization requires lower impact parameter collisions compared to single ionization. This leads to higher amount of electronic energy loss. Also noteworthy is the observation that a large fraction of doubly charged naphthalene ions lose C_2H_2 giving rise to the sharp peak at m/q of 51. This peak is followed by another sharp peak corresponding to loss of (C_2H_2 + H_2). These observations are in agreement with the results obtained for ion-anthracene collision at lower energies (Martin et al., 2012). The measurements with anthracene have shown that loss of C_2H_2 dominates for internal energy less than 13 eV while sequential loss of H is the dominant mechanism at internal energies higher than 13 eV (Martin et al., 2012). These observations can be extrapolated to naphthalene considering the structural similarity. However, the lower degrees of freedom may lower the limiting values of the internal energy to less than 13 eV. Postma et al. (2010) have studied ion-anthracene collisions at lower energies using a reflectron ToF. Since a reflectron ToF compensates for the kinetic energy spread, it is not possible to distinguish if m/q of 76 is singly charged half or doubly charged fragment species after C_2H_2 loss (Postma et al., 2010). However, in our case, a clear difference in the peak shape helps in the identification.

D. Resonant electron transfer: Figure 2.10 shows the mass spectra of all the studied projectile velocities in EE and EC mode, normalized with parent single ionization peak area. The fragmentation yield behavior seen in EE mode will be discussed in detail in Chapter 3. In the EC mode, the change in cross section across energy is about an order of magnitude. However, on normalization with respect to the parent single ionization peak area for all the projectile energies (50-150 keV), the evaporation as well as multifragmentation channels overlap (see figure 2.10). It is therefore evident that the projectile

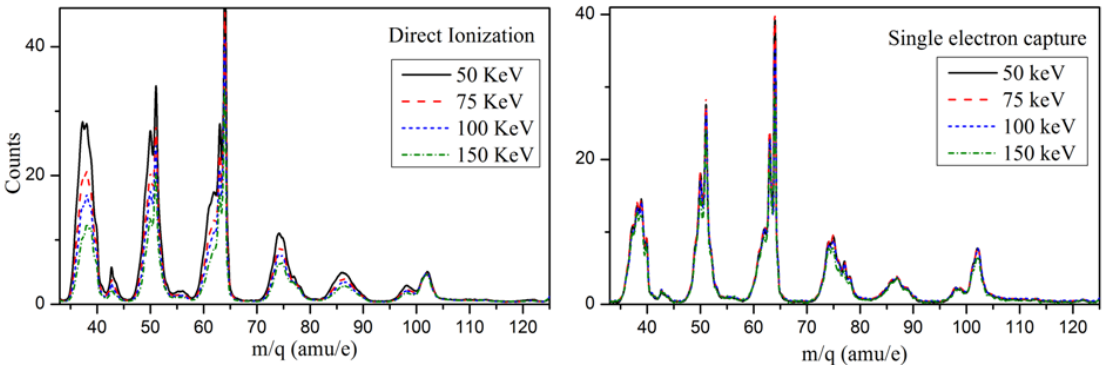

Figure 2.10: Mass spectra of EE (left) and EC (right) mode normalized to parent single ionization peak area for all proton projectile energies.

is depositing the same amount of energy in EC mode across the entire velocity range. This is explained on the basis of resonant or quasi-resonant electron transfer from target to projectile accompanied by electronic stopping (Postma et al., 2010; Alvarado et al., 2007). As mentioned earlier, singly ionizing events in EC mode lead to total energy deposition $<$ 18 eV. Structure calculations are performed for naphthalene using DFT at B3LYP/6-311g (2d,p) level with the help of GAUSSIAN09 (Frisch et al., 2009). The molecular orbitals (MOs) are calculated and their respective symmetries and binding energies were assigned. From figure 2.11a, it is seen that five MOs (with symmetries b_{2u}, b_{3g}, a_g, b_{1u} and a_g) with binding energies between 12 and 14 eV can possibly match the $n = 1$ bound state of the proton-electron system. A plot comparing the energy levels of the target (naphthalene) and projectile (proton) is shown in figure 2.11a, which shows that the electron is captured from the inner valence shell rather from HOMO. This fact is again in accordance with figure 2.11b which shows the singly charged naphthalene ions formed by EC process as a percentage of the total number of singly charged naphthalene ions produced in present study, i.e. [EC/(EC+EE)]*100 along with published values for other molecular targets: O_2, CH_4, CO_2 and uracil ($C_4H_4N_2O_2$) (Tabet et al., 2010a; Gobet et al., 2001; Rudd et al., 1983; Gobet et al., 2004; Luna et al., 2007).

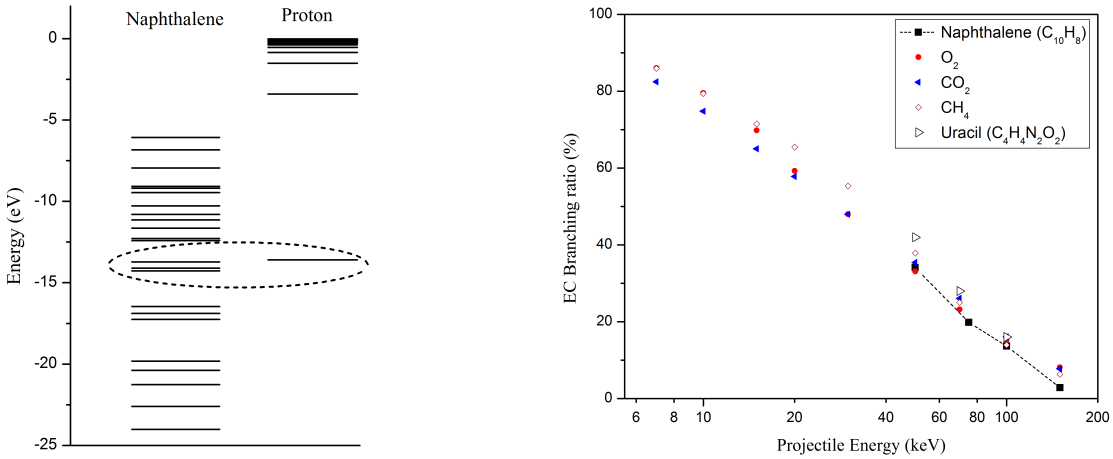

(a) Resonant transfer

(b) Capture fraction

Figure 2.11: (a) Energy level diagram for naphthalene target (obtained using DFT) and proton projectile, (b) Capture fraction (in percentage) for various molecules in collision with protons.

Note that, irrespective of size, composition and type of molecular target, the EC cross section decreases with increase in impact energy. Naphthalene also follows this trend fairly well. The highest occupied molecular orbital (HOMO) energy for such a variety of examples is different and the capture probability of the HOMO electron should also vary considerably. But the observed similarity in capture fraction indicates that the HOMO energy is not an appropriate parameter governing the contribution of EC and EE processes in proton collision with molecules.

From figure 2.11a, it is clear that the rearrangement following the capture will cause the internal energy to be elevated by about 6 eV. Since energy deposition for the resonant transfer is constant, the internal energy distribution is also constant. Comparing the relative yields of intact ions as well as H, H_2 and C_2H_2 loss species with the photoionization breakdown curves by West et al. (2012), it is observed that the internal energy after capture should be $\sim$ 7.5 eV. This is in agreement with the internal energy values

of $\sim$ 7.1 eV obtained by Gotkis et al. (1993). Therefore, to have the observed ratios of relative yields of the evaporation channels, the internal energy ought to be more than 8 eV. This implies that the capture process is accompanied by a considerable amount of electronic energy loss, $\sim$ 2 eV. The majority of events in EC mode therefore correspond to an energy loss that is limited to 14 - 16 eV, consistent with the upper limit of 18 eV.

E. Multifragmentation: Multifragmentation is usually followed by either dissociation of multiply charged ions (a violent process) or due to loss of neutrals, formation of metastable intermediates (which are thermally gentle process). The bonding in the molecule decides the shape of potential energy surface and hence decides the life time for dissociation. The multiply charged ions are unstable towards dissociation because of the coulomb repulsion which lifts the potential energy surface to continuum depending on the size of the molecules, hence dissociation is more prominent for small sized multiply charged molecules. But the large size for PAHs and the additional delocalization property (giving ability to accommodate extra charge within the molecule) produces local minima (metastable ion) through which the ion decay by tunneling process.

The fragment peaks containing C_6, C_7 and C_8 are broad indicating their origin to be multiply charged parent ion (see figure 2.6). This is over and above the overall widths due to variable number of H attached to such fragments. However, there are narrow features riding the broad peaks. These arise from the evaporation process of neutrals, e.g., one or two C_2H_2 fragments. This is also a prominent and well studied channel for PAHs (Holm et al., 2011). Therefore, the narrow features at m/q of 102 and 77 are attributed to the loss of C_2H_2 and (C_2H_2+C_2H), respectively. Both formation of metastable as well as loss of neutrals, are momentum correlated process because they are least thermally excited and associated with less number of charged fragments as product of the dissociation process. The kinetic energy release for these channels can be deduced using the correlation diagram, which is discussed later in detail.

Further, the C_7 mass fragments show no sharp features due to lack of evaporation or cold dissociative channel like acetylene loss in case of C_8. Prominent fragmentation peaks are observed at m/q positions of $C_nH_m{}^+$ (n =2, 3, 4, 5, 6, 7, 8 and m $\geq$ 0). Fragments with single C atom or with nine C atoms were negligibly small. All the fragmentation peaks were sufficiently broad to have substantial overlap with the adjacent mass value. This is because here the multiple ionization is followed by coulomb explosion giving rise to more than two ionic body fragmentation with high kinetic energy and hence their momentum correlation is complex in nature which is seen in section 2.1.2.2. This process is associated with low impact parameter collisions which leads to a substantial amount of energy transfer to the target. The overall observation is that for every C cluster fragment, i.e. $C_nH_m{}^+$, the yield is maximum for *m = 2* or *3*. A prominently sharp peak at m/q of 26.5 indicates doubly charged C_4H_5 fragment. Fragmentation of this high kinetic energy release type has been observed for proton-anthracene interaction by Postma et al. (2010). They have estimated an average energy loss of $\sim$ 58 eV for protons with energy 15 keV, leading to multi fragmentation. Their model shows a linear variation of average energy loss with projectile velocity. Although the model is for lower projectile velocities ($<$ 1 a. u.), we have used it in our case (for projectile velocity of 1.41 a. u.) in order to get an approximate value of energy loss. This corresponds to $\sim$ 116 eV. It is also assumed that the maximum cross section is offered by the molecule with its plane perpendicular to the beam. A detail theoretical analysis of this energy deposited into the molecule for different projectile energy and its effect on fragmentation distribution is discussed in Chapter 3. The fragmentation yields decrease considerably with increase in projectile velocity for EE mode. At 150 keV (highest projectile velocity), we find that the fragmentation yields approach the values in EC mode. Therefore, we anticipate a substantial variation in the energy deposition and consequently, in the overall decay rates. The ratio of multifragmentation peak areas is observed to vary by almost an order of magnitude in few cases, e.g., $C_2{}^+$. As discussed in previous sec-

tion that, though the C_2H_2 yields are constant across the energy range investigated here, the yields for EE mode are $\sim$ 30% lower than the EC mode when the corresponding intact parent single ionization peak areas are normalized (see figure 2.9). These lower C_2H_2 yields in EE mode, when considered with the breakdown curves by West et al. (2012), imply that for singly ionizing events, the energy loss distribution can be higher than 18 eV. However, it cannot be significantly higher lest H loss yield falls below 2H loss yields. It can, therefore, be concluded that energy loss from the projectile to the naphthalene target molecule occurs in two ways. First, there is a large impact parameter regime in which energy of $\sim$ 16 - 18 eV is deposited which leads to single ionization, sometimes followed by evaporation. The second process involves lower impact parameter collision process. Here, the projectile deposits higher energy into the target causing violent multifragmentation with substantial projectile velocity dependence.

F. Energetics of collective or plasmon excitation: Plasmon excitation was shown to influence the photoion yield for PAHs (Jochims et al., 1994). In the present proton-naphthalene collision experiment, it is observed that both the ionization (in EE mode) as well as evaporation processes (in EE and EC mode) are independent of projectile velocity. This constant nature of ionization cross section is attributed to plasmon excitation like the case for C_{60} (Kadhane et al., 2007). In addition, comparison of the present experimental yields from evaporation process (H-loss, 2H/H_2-loss and C_2H_2 loss) with the breakdown curves (West et al., 2012) indicate that the energy deposition peaks at $\sim$ 18 eV (where plasmon excitation peaks at 17 eV for PAHs with a FWHM of $\sim$ 7 - 8 eV). This signifies that, proton-naphthalene collisions at 1 a. u. velocity regime also show the influence of plasmon excitation followed by autoionization and subsequent evaporation, similar to the case of photoionization of naphthalene. As the plasmon peaks between 13 - 19 eV, it is expected that a substantial fraction of plasmon excited molecules should undergo evaporation after ionization. However, as the outgoing electron carries away

some of the kinetic energy, the net energy available for subsequent dissociation is lower than the difference between plasmon energy and ionization potential. Hence as compare to double ionization, the excited molecule prefers to de-excite via neutral loss (evaporation process). As shown in section C of 2.1.2.1, the H, 2H loss channels are very sensitive to energy deposition into the molecule and the yields are constant over the projectile energy like parent ionization peak, hence this evaporation process are due to again the large impact parameter interaction causing plasmon excitation.

As seen in section D of 2.1.2.1, the fragmentation yield are constant in electron capture case for all proton projectile energy unlike the electron emission case. This was explained in terms of the resonant capture of electron from inner valence shell of target to the proton projectile. From our photoelectron spectroscopy experiments (see section 2.2.2), it is seen that the plasmon excitation (for incident photon energy $\sim$ 16 - 18 eV) couples to inner valence shell. And the energy deposited in EC process is also overlapping in plasmon excitation region with capture of electron from inner valence shell. Hence both the processes quantitatively deposit the same energy into the molecule.

2.1.2.2 Momentum correlation due to coulomb explosion of multiply charged species: identification of channels

The ToFMS typically shows two types of peak: sharp singly (multiply) charged peak with no fragmentation or neutral evaporation and broader peaks due to violent explosion of multiply charged ions produced in the collision process. These ions have varying collection efficiency depending upon the configuration of the ToFMS and the kinetic energy imparted to them in the explosion process. Such variation can be seen as resolved forward-backward peaks with the actual m/q position in the middle of them or a very broad peak. In some cases if the decay process is slow enough, then there is a tail

also observed in the higher time scale of first ToF. Thus it becomes complex task to analyze such features in a simple ToF mass spectra. A much more useful technique is to use the multihit capability of the DAQ to record successive hits on the recoil ion detector for a given event. Eventually a two dimensional (2D) correlation graph can be made by plotting ToF of second fragment against the ToF of the corresponding first fragment. If the fragmentation or explosion process is a binary process (or produces many fragments but only two of them are ions), then their momenta will be equal and opposite. Such cases the 2D correlation diagram will show specific shape of the intensity island (figure 2.12 and 2.13).

Some features are immediately evident (figure 2.12), first are the blue streaks (vertical and horizontal) caused by chance coincidence. Several islands are seen which are correlated to a specific m/q pair produced in one event. If only those two are produced, they are seen as linear shaped islands with negative slope. Closer investigation also reveals more details of the energetics.

A. H^+ and $H_2{}^+$ loss channels: Energetic proton emission is known to be an important decay channel in de-excitation process of PAHs under certain environment of ISM. Also laboratory experiments shows the decays channels like H^+ and $C_2H_2{}^+$ ions loss from parent multiply charged PAHs (Holm et al., 2010, 2011). Figure 2.13 shows the regions where the first fragment is either H^+ or $H_2{}^+$. A large population of these ions is produced in coincidence with C_n fragments (*n = 2 - 8*). Note that though the coincidence is intense at C_8 mass fragment, the C_8H_6 fragment shows negligible population of H^+ correlation. Thus it can be stated safely that the H^+ or $H_2{}^+$ fragments are produced as an occasional by product of a violent coulomb explosion with no surprising results. What is indeed interesting is the observation of the coincidence in H^+ or $H_2{}^+$ correlation and H^+ and $C_{10}H_{8-x}$ (where x = 1 - 8) correlation. Both of these are shown in figure 2.14 in magnified form. This figure also shows concerted emission of H^+ and

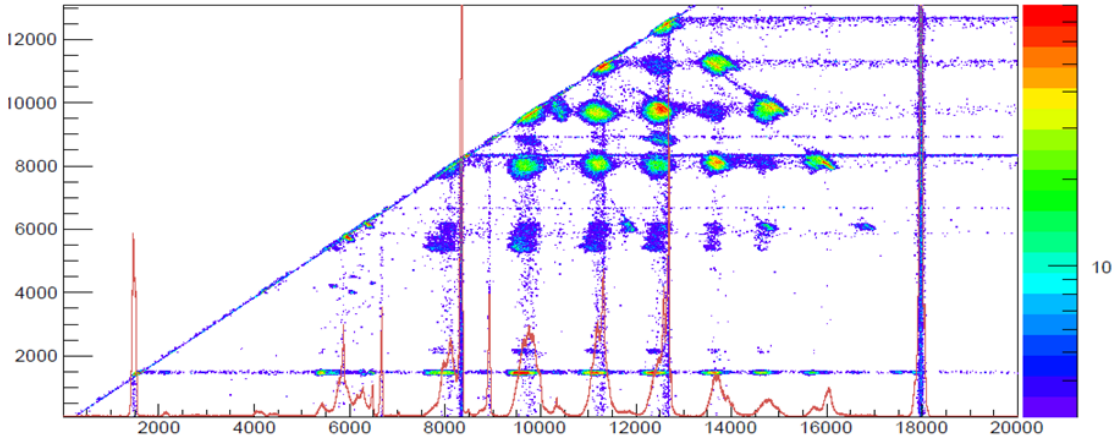

Figure 2.12: 2D correlation diagram of first and second hit with the ToF mass spectra of singles overlaid for identification.

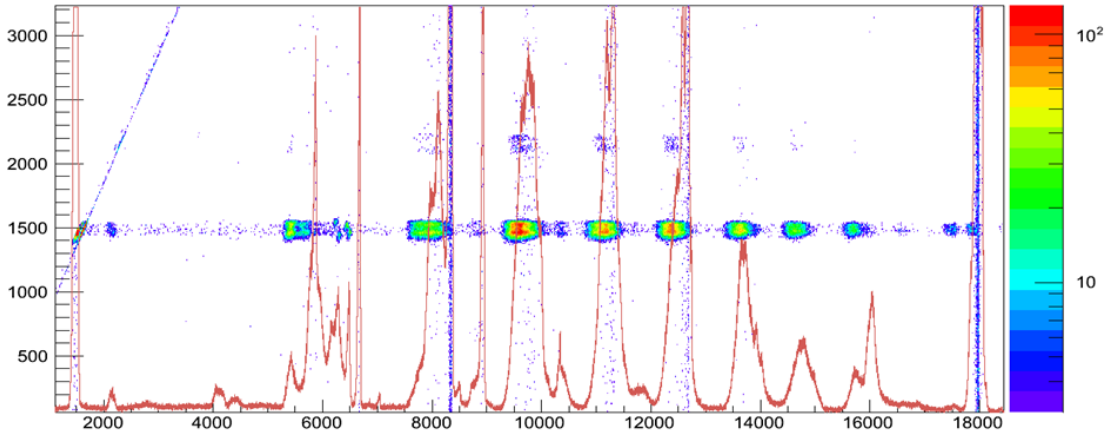

Figure 2.13: 2D correlation diagram showing the possible m/q produced along with H^+.

H_2^+ from the molecule leaving behind a neutral skeleton (though not all H may be lost). This indicates to the stability of the carbon backbone of PAHs. Similarly, the multiple H loss peak seen next to the parent ion peak shows decreasing intensity in the H^+ correlation up to the loss of 2H, then the intensity drops to almost zero for 3H and 4H loss and then it picks up again and a measurable intensity is seen even at the loss of all H species from naphthalene (figure 2.13).

B. Dication decay channels: The correlation diagram particularly in the heavy fragments region is dominated by dication decay, which can be ascertained by the observed momentum correlation (figure 2.15). First set of such correlations are observed in the CH_3^+ emission region (figure 2.15a). Loss of CH_3^+ channel for PAH dication (or higher charge states) is not reported before in literature. A clear channel is observed in coincidence with m/q = 113, 87 and 56.5 with additional neutral H-loss substructure in for 113 and 56.5 position. For m/q = 87 this substructure is much less or absent. The masses are attributed to $C_9H_5^+$, $C_7H_3^+$ and $C_9H_5^{++}$. The charge state of the last fragment decided by the slope of the correlation island. Particularly interesting observation is the tail observed in the higher time scale region of the first ToF for $C_7H_3^+$ and $C_9H_5^{++}$ fragments, indicating possible statistical nature of the H^+ loss process from a metastable multiply charged fragment.

A very prominent island is seen in correlated dissociation of dication to ($C_2H_2^+$ + $C_8H_{6-x}^+$) with x = 0 - 4 and $C_2H_3^+$ + $C_8H_{5-y}^+$) with y = 0 - 3. The loss of $C_2H_3^+$ appears to be a statistical process with decreasing correlation yield for increasing value of y. But the loss of $C_2H_2^+$ shows very different behavior. The most prominent channel for $C_2H_2^+$ loss is when x = 0 and to lower extent when x = 4 (figure 2.15b). The intermediate values of x are absent in the correlation. The island also shows a meta stable component being present. $C_3H_3^+$ region shows clear and prominent correlation with $C_7H_5^+$ and $C_7H_3^+$ (figure 2.15c). Thus the dication fragments either in binary man-

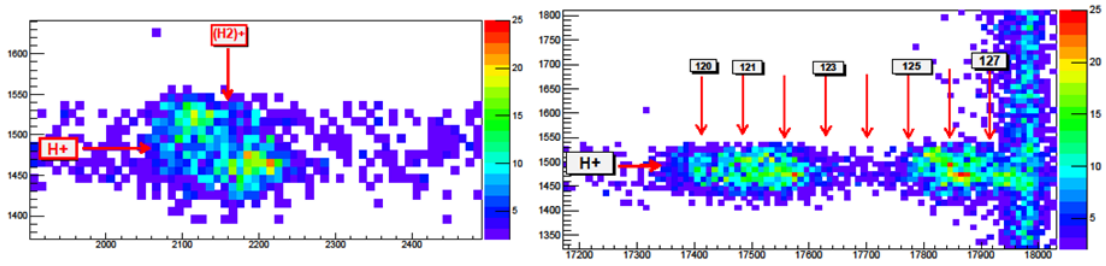

Figure 2.14: Zoomed 2D correlation diagram showing the possible m/q produced along with H^+.

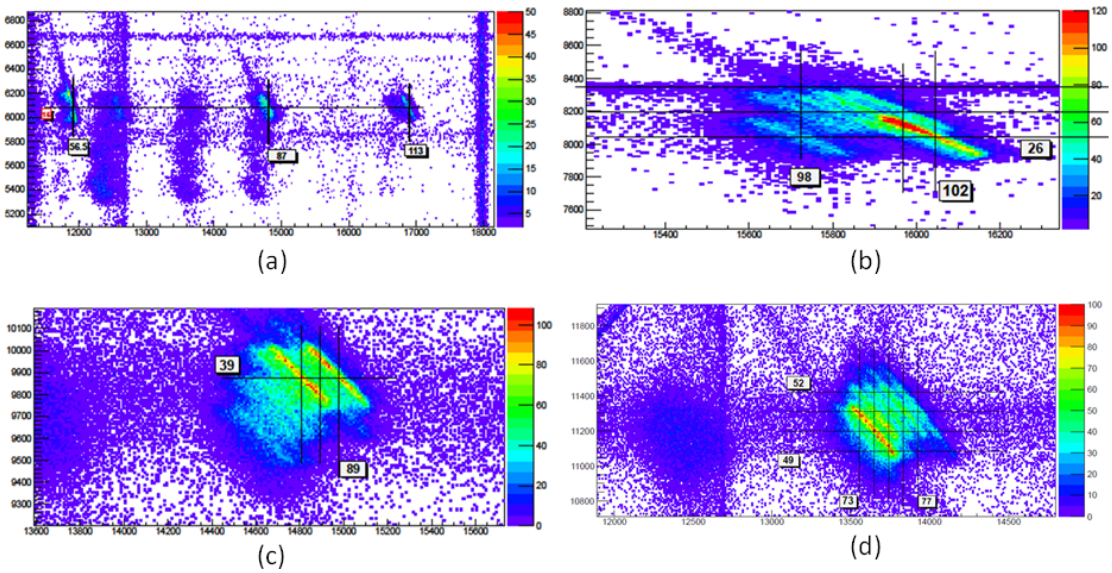

Figure 2.15: Different momentum correlated decay channels. (a) $CH_3{}^+$ (b) $C_2H_2{}^+$, (c) $C_3H_3{}^+$, (d) $C_4H_2{}^+$ loss region.

ner or prefers to lose H_2 neutral simultaneously or before coulomb explosion. Other breakup channels are observed but they are weak. Finally $C_4H_2^+$ (m/q = 50) loss is prominently correlated to $C_6H_2^+$ fragment (m/q = 74) (figure 2.15d). Other channels are less favored. Thus for this channel, loss of four neutral H are preferred either individually or in molecular form.

2.2 Photoelectron spectroscopy for PAHs

In section 2.1 we discussed the multi-fold aspect of ion-PAH collision and its consequences relevant to astronomical context by studying ion-naphthalene collision. In this section we will talk about the photon collision with two different PAHs namely pyrene and fluorene. It is worth to study the photon impact for these two molecules because, PAHs are known to be efficient absorbers of UV radiation particularly due to their π-π* transitions in the UV region, coupling electronic energy to vibrational energy and resulting in IR photon emission. In addition to this the radical cation of pyrene is thought to be responsible for major UV-Visible interstellar absorption bands (Salama and Allamandola, 1992a, 1993; Szczepanski and Vala, 1993; Parisel et al., 1992). Fluorene is also studied as a possible carrier for spectra of electromagnetic radiation from the ISM in terms of extinction coefficient (Yastrebov and Ivanov-Omskii, 2005). Because they contain multiple aromatic ring systems, these compounds can absorb light in the UV-A (320-400 nm) or the visible region (400-700 nm) (Dabestani and Ivanov, 1999) forming reactive species and causing damage to human metabolism along with DNA cleavage (Yu, 2002; Dong et al., 2000). Therefore, a detailed understanding of the photochemistry of PAHs is needed in order to determine the relationship between photo-mutagenicity, photo-stability and structure of PAHs. Fluorene and multilayered polymers of fluorene (polyfluorenes), moreover are particularly interesting systems for nano-electronics, optoelectronics and organic LEDs (Chen et al., 2008).

Photoelectron spectroscopy (PES) is a very well known and efficient approach to study the structural property of molecule with the help of electronic and vibronic state analysis. A typical photoabsorption spectrum of a PAH in the visible, UV and far UV regions is characterized by various molecular excitations starting from the outermost narrow π-π* excitations (at $\sim$ 7-8 eV) to the inner broad ones due to π-σ*, σ-π* and σ-σ* excitation (peaking at $\sim$ 17 eV). Jochims et al. (1999) have studied the photoion yield of several PAHs in the far UV region and observed that in spite of a substantial variation in the ionization potentials, the ion yield for single ionization almost always peaks at 17 eV. Photoelectron spectroscopy of PAHs was done mainly with He I and He II discharge sources in the seventies (Boschi et al., 1974; Schmidt, 1977; Klasinc et al., 1980). Theoretical investigations including the most recent ones (Deleuze, 2002) rely substantially on these old measurements. In the present study, synchrotron radiation has been used to investigate the systematic variation of the state selective PE cross sections over a wide range of photon energies, hence the in coincident measured recoil ion behavior is correlated with the corresponding outgoing electron and hence with the MO properties. This state selective photoemission intensities have never been measured for PAHs except benzene. In addition to this a detail study of photon energy dependence of PES for a wide range of photon energy in UV regime is performed for the first time for PAHs.

2.2.1 Experimental details

Experimental set up: The experiment was performed at the GASPHASE photoemission beam line at the Elettra-Sincrotrone Trieste laboratory, Trieste, Italy. The layout of beamline and details of experimental station have been described in detail in previous studies (Blyth et al., 1999; Plekan et al., 2008). Typical resolving power of the beamline is 2000 at the energies used here. The spectrometer was at magic angle with respect to

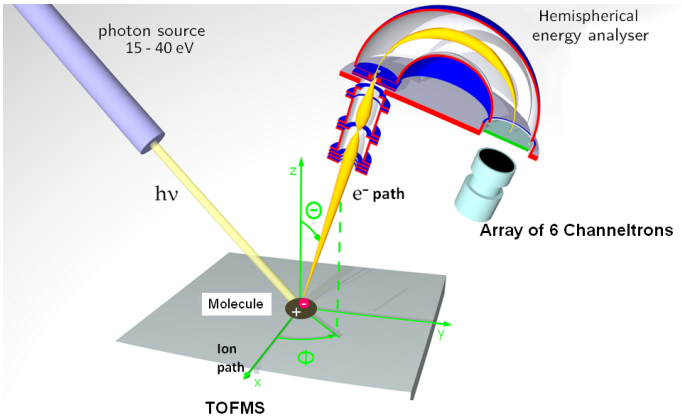

Figure 2.16: Schematic of experimental set up for PES experiment. Figure adapted from Nathan (June 2014)

polarization plane of the radiation ($54.7\,^{\circ}$), perpendicular to the direction of photon and molecular beam.

The photon beam crosses an effusive beam of the target molecules. Pyrene and fluorene were obtained from Sigma-Aldrich with $>$ 99 % purity. The target was placed in a copper container having a 3.3 cm length nozzle with opening of 3 mm. The container for pyrene was heated resistively to about $74\,^{\circ}\mathrm{C}$ which was kept constant with the help of a temperature controller. A ToF spectra taken from the same measurement (see figure 2.17) showed no trace of impurity or fragment peaks, so dissociation of the molecule from heating was insignificant. For fluorene the vapour pressure was high enough, so it did not require any heating. Xe flow was adjusted to maintain a constant chamber pressure while the full set of data for Xe was acquired. A hemispherical electron energy analyzer (150 mm mean radius) with six CEM detectors was used to measure the photoelectron (PE) spectra with a resolution down to 50 meV. The spectrometer acceptance angle is a cone of $\pm\,4\,^{\circ}$ with the axis of cone oriented at magic angle with respect to the direction of polarization. In this spectrometer the electrons are first accelerated and then decelerated within the spectrometer by varying the pass energy. The PE spectra were

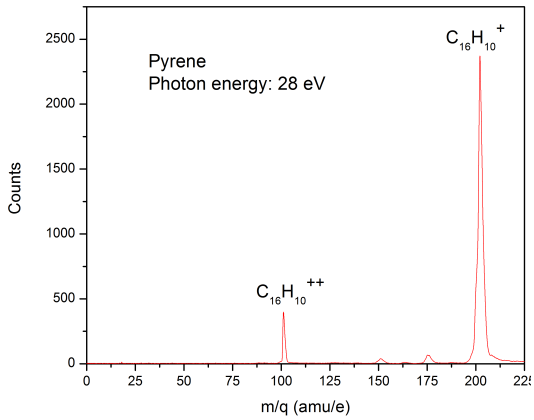

Figure 2.17: ToF data for pyrene under 28 eV photon impact.

recorded for a wide range of photon energies from 15 to 40 eV. In the case of pyrene, a data set at 95.1 eV also has been recorded.

To perform the state selective PES study, the photoelectron-photoion coincidence (PEPICO) measurements were also performed with the outgoing electron as start trigger. The corresponding ion was detected using a two field linear TOFMS followed by MCP detectors. The pusher, puller, drift tube of TOFMS are at 250V, -250V, 2500V. To measure the amount of chance coincidence, the ions were extracted in a pulsed manner using a pulse generator which was also used for random trigger generation. Near Edge X-Ray Absorption Fine Structure (NEXAFS) measurements were also done at photon energy between 284 and 320 eV for both the targets to probe the structural details. The photon energy resolution used in the experiment was 1/2000. The photon energy scale in the C *1s* edge NEXAFS spectra was calibrated using the known excitation energies of CH_4.

Normalization procedure for estimation of relative cross sections from PES: Xe Auger electron spectra were also recorded at 95.1 eV photon energy (see figure 2.18a) to obtain the transmission function of the spectrometer. Our measured intensity were nor-

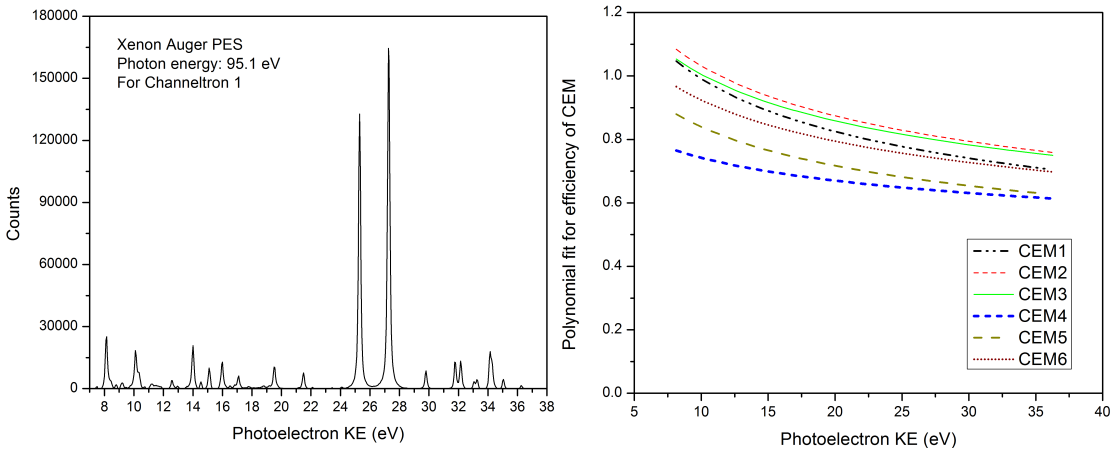

(a) (b)

Figure 2.18: (a) Xenon Auger electron spectrum at 95.1 eV photon energy, (b) The efficiency variation for different CEMs as a function of photoelectron kinetic energy.

malized to the Auger intensity distribution reported in previous investigations (Kivimäki et al., 1999) and the normalization factors were obtained. The spectrometer efficiency curve for each individual CEM was obtained by fitting a polynomial to these measured factors (see figure 2.18b). These polynomials were used to correct the yields for overall spectrometer efficiency.

The intensity of the photon beam was measured with a photodiode whose efficiency increases with photon energy. However due to the higher harmonic contribution at lower photon energy, a direct normalization of the data to the photodiode current was not possible. Therefore the measurements of the Xe ionization cross section were used to obtain the normalization to the photon flux. In order to extract the correct factor, the beam conditions at a given photon energy (i.e. entrance and exit slits, undulator gap etc.) were kept identical for all three targets namely Xe, pyrene and fluorene. Xe PE peak areas (see figure 2.19a as an example) measured in the present study (with spectrometer effi-

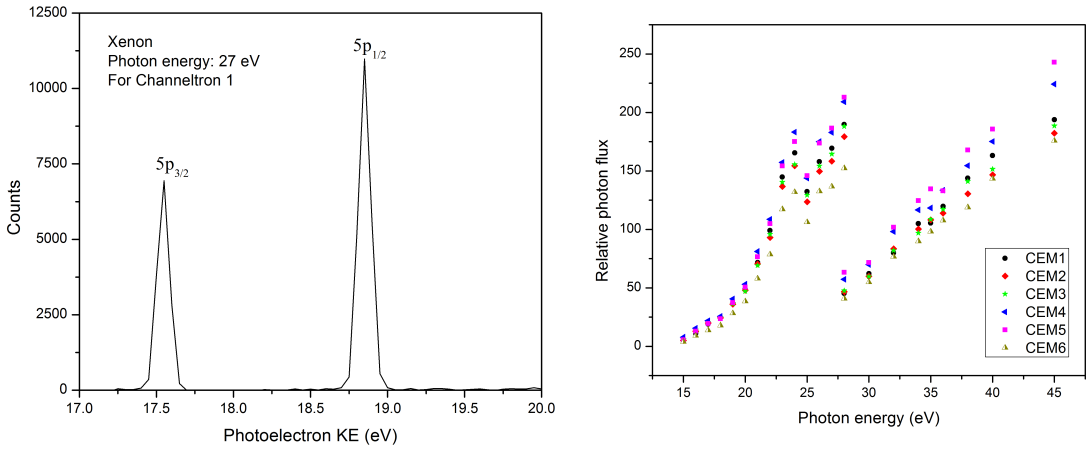

(a) (b)

Figure 2.19: (a) Xe *5p* doublet for photon energy 27 eV, (b) Photon flux variation as a function of photon energy for individual CEMs.

ciency correction incorporated as discussed above by using the polynomial expressions for individual CEMs) were compared with the previously published absolute cross sections for Xe *5p* photoionisation (Fahlman et al., 1984; Kutzner et al., 1989). This gives the number of photons or photon flux for each photon energy. This procedure was followed over the whole photon energy range studied. Figure 2.19b shows the photon flux variation as a function of photon energy for individual CEMs. The normalization factors obtained were used for normalizing the area obtained for pyrene and fluorene. The relative PE cross sections were finally obtained by including photon flux normalization and spectrometer efficiency correction (assuming constant target density). These relative cross sections are directly proportional to the absolute cross sections, by a constant factor unique for each target molecule.

2.2.2 Results and discussion

2.2.2.1 Photoelectron cross section measurements

The first ionization potential was estimated to be 7.436 eV $\pm$ 0.015 eV and 7.944 $\pm$ 0.055 eV for pyrene and fluorene, respectively. OVGF calculations are done to identify the prominent peaks in the PE spectrum according to their binding energy and symmetry, which is discussed in section 3.2.3 of Chapter 3 in detail. In the following sections of this chapter we discuss the experimental results and different aspects of PES studies for pyrene and fluorene and their comparison.

A. Pyrene PES: Integrated intensities of individual outer valence bands (see figure 2.20a) show a similar behavior over the entire photon energy range. All the bands show a peak at about 17 eV. This parallel trend for outer π orbital was theoretically predicted for the case of large polyene molecules by Carravetta et al. (1997), but calculations of the dynamics of the photoionization of PAHs have not been performed so far. In the absence of individual peak fits for the heavily overlapping bands in the inner valence region it is not possible to separate the individual trends. The overall shape is seen to evolve in the same way for the constituent bands, but there are a few bands within the inner valence region which show a slight variation in the cross section with respect to the nearby bands. It is observed that bands from VIII to X contribute strongly to the PE spectrum in the 16 to 27 eV photon energy range. These observations show no direct correlation with either π or σ characteristics of the MO.

PE spectrum with five different photon energies are plotted in figure 2.21a by scaling the data to the intensity of the HOMO band. The first five bands clearly show almost exact overlap. As Carravetta et al. (1997) have shown theoretically, the π orbital PE cross sections evolve similarly. On the other hand for the case of benzene (Baltzer et al.,

1997) particularly at lower photon energy the individual π MO cross sections show a different trend. Also noteworthy is the almost exact overlap of the full PE spectrum for 40 and 95.1 eV photon energy data. Only a small deviation is observed in the bands VI and VII.

B. Fluorene PES: Despite of the fundamental differences in the structure of the two molecules, such as symmetry, presence of sp^3 hybridized carbon and cyclopentane ring etc., the photon energy dependences are markedly similar. Figure 2.21b shows the evolution of PE spectrum of fluorene with photon energy. The outer four bands are seen to vary slowly compared to the inner valence bands as seen in the case of pyrene.

The areas under peak I, II and III are plotted along with the integrated area of the region from 10.50 to 12.97 eV in figure 2.22a. The relative intensities follow the same trend as seen in the case of pyrene. The outer bands display a plateau at around 17 eV irrespective of the type of MO involved. For the inner band, the peak appears to be at lower photon energy than for the outer bands, though the exact position can not be determined within the precision of the present measurements. The relative intensities follow the same trend beyond 27 eV for all the bands. The branching ratios (see figure 2.22b) show a similar behavior as pyrene. The outer bands contribute less in the lower photon energy than the inner ones up to 27 eV. Beyond that energy, the contributions stabilize and remain uniform up to the end of the photon energy range studied.

The scaled PE spectra in figure 2.21b show that in contrast to the outer valence bands which overlap at all photon energies, the inner valence bands show rapid variation in spite of the scaling to HOMO intensity. Unlike the case of pyrene where the rapid variation was observed only in the middle of the inner valence region by bands: VIII, IX and X. For fluorene this behavior is observed over the entire inner valence band, from band IV onwards. As a function of increasing photon energy, the contribution from

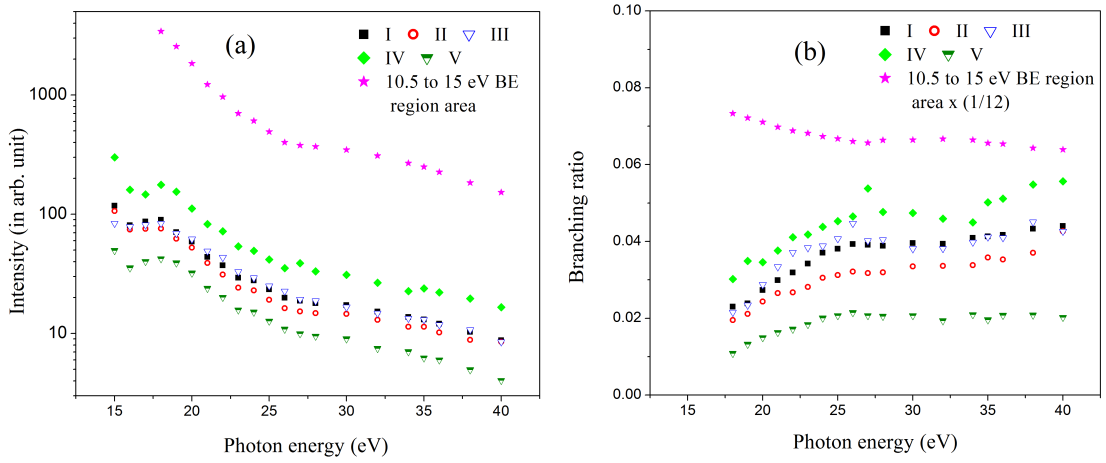

Figure 2.20: (a) Integrated intensity and (b) branching ratio for various bands of pyrene.

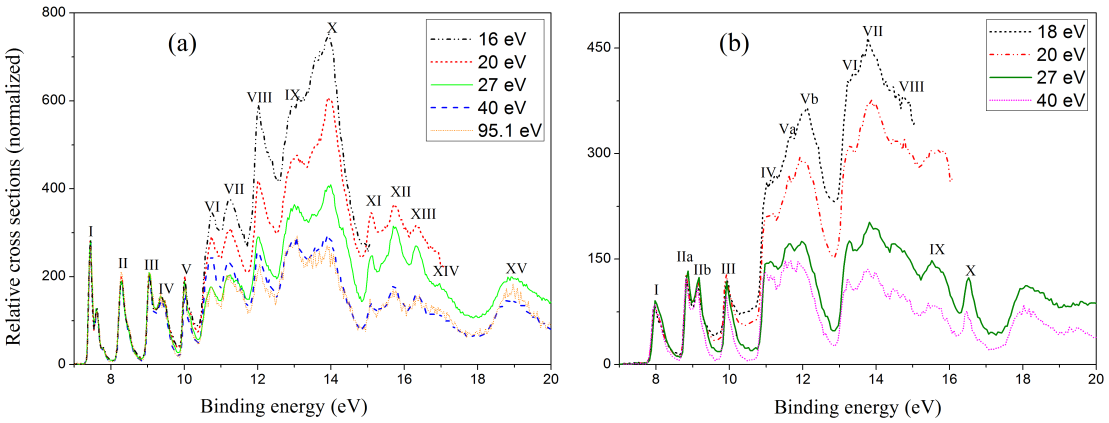

Figure 2.21: (a) pyrene (b) fluorene PES at different photon energies scaled to the intensity of the HOMO band.

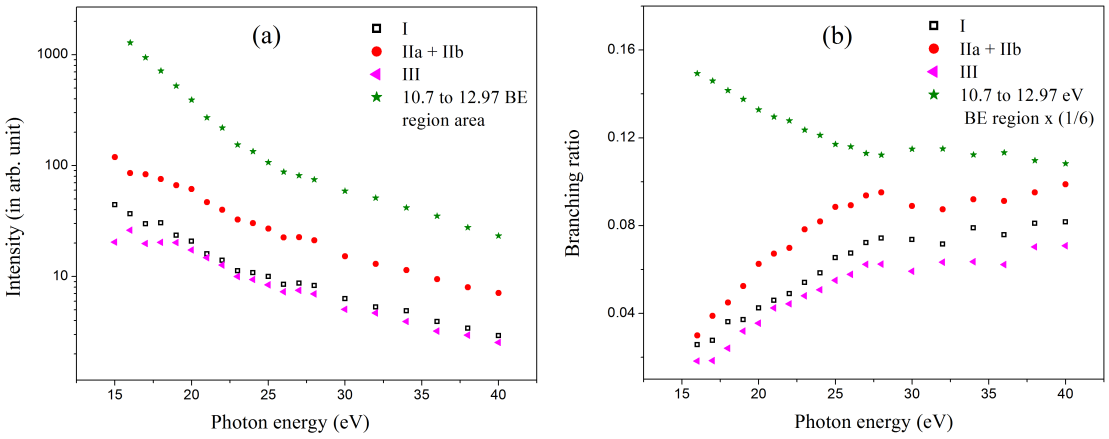

Figure 2.22: (a) Integrated intensity and (b) branching ratio for various bands of fluorene.

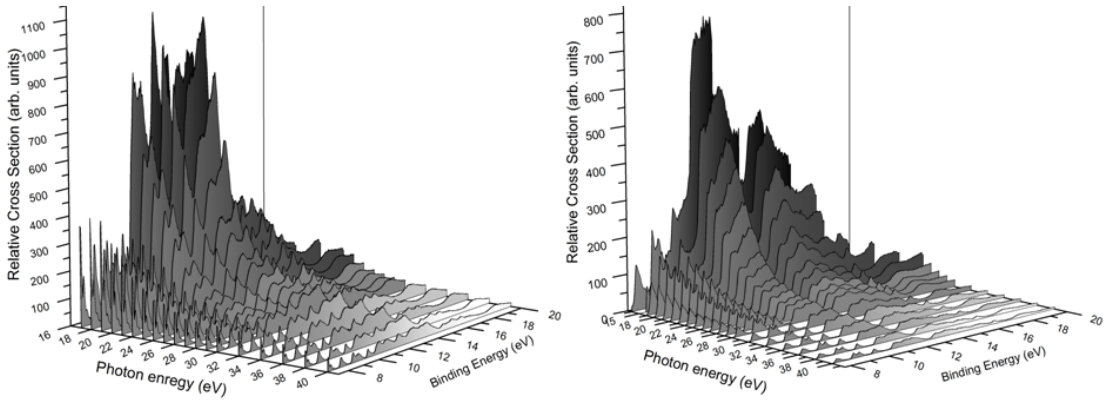

Figure 2.23: Pyrene (left) and fluorene (right) photoelectron spectra for different photon energy.

band V is seen to decrease faster than band IV. Whereas in the band V itself, band Vb decreases more rapidly than band Va. Among V, VII and VIII bands the VII band shows a faster decrease.

C. PES as a function of photon energy: Relative PE cross sections are plotted as a function of PE binding energy and photon energy in figure 2.23 for pyrene and fluorene. The measured cross sections for a given target molecule are proportional to the absolute cross section within a constant factor independent of binding energy and photon energy. The figure describe the systematic variation of the various bands as a function of the photon energy. They also show a pronounced intensity of the inner valence region at photon energy less than 27 eV. Above this energy all the features in the PE spectra evolve in a more uniform manner. The difference in the five outer valence bands for pyrene (three outer valence bands in fluorene) and the inner valence bands is very clear in the photon energy region below 27 eV. One prominent observation is the uniform variation of the cross section above 27 eV photon energy. This observation is discussed in more detail later.

Figure 2.21 shows the PE spectra scaled with respect to the HOMO intensity for the sake of comparison. A clear observation is that the first five (three) bands in pyrene (fluorene) overlap almost exactly over the entire photon energy range, but the inner valence bands show more drastic variation in the lower photon energy region, while past 27 eV the evolution follows the same trend as the re-normalized outer valence bands.

The relative intensities (see figures 2.20a and 2.22a) for the outer valence π MOs as a function of photon energy were obtained by determining the area under the peak after background subtraction. For the areas under peaks corresponding to IIa and IIb in fluorene (band III and IV in pyrene), asymmetric Lorentzian peak fits along with a first order polynomial (later is to incorporate background subtraction) were used. Since the confidence level for the separate fits of band IIa and IIb in the case of fluorene was not satisfactory, for these bands we report the sum of the intensities. For the peaks III and IV in pyrene the fits were satisfactory, so they are reported separately. For the broad feature (10.50 to 15.00 eV and 10.70 to 12.97 eV binding energy regions in PE spectra for pyrene and fluorene respectively) resulting from a severe mixing of π and σ MOs, the relative cross sections were obtained without any background subtraction. The branching ratios for the various bands shown in figures 2.20b and 2.22b were obtained by taking the ratio of the individual to total PE spectrum intensity.

D. Relative photoionization cross section and branching ratio as a function of photon energy: The similarity of the behavior of the PES data for pyrene and fluorene indicates that the evolution of PE cross sections is determined by similar processes. The enhancement in photoionization cross section around 17 eV photon energy (see figure 2.23) can be explained in terms of a plasmon-like peak resulting from a collective excitation of the valence electrons as already established for C_{60} (Korica et al., 2005; Bertsch et al., 1991) using synchrotron radiation (Ling and Lifshitz, 1996) and electron energy loss spectroscopy technique (Verkhovtsev et al., 2012). The most distinct char-

acteristic we observe is the peak of cross sections at around 17 eV particularly for the outer valance bands of pyrene (a plateau in the case of fluorene). The increase in inner valence band intensity indicates the proximity of a peak in absorption cross section, but does not show the exact energy of occurrence. This observation is in disagreement with a similar study of benzene by Baltzer et al. (1997) and Carlson et al. (1987). Due to the larger size of present molecules compared to benzene, it is expected that autoionization process plays a more important role in the far UV region for pyrene and fluorene as compared to benzene. It is known that the broad excitation region in PAHs is associated with plasmon-like excitations (Jochims et al., 1997). This excitation would then couple to various ionization channels. Thus the ionization cross section from a particular MO is due to the overall variation of the collective excitation cross section. The branching ratios shown in figures 2.20b and 2.22b also demonstrate the dominance of ionization from σ orbitals in the lower photon energy range, which decreases systematically up to 27 eV and remains constant afterwards. This is in contrast with the measurements for benzene (Baltzer et al., 1997) where the contribution from σ orbitals systematically grows with photon energy. Baltzer et al. (1997) have demonstrated that the inner valence bands contribute more with increasing photon energy whereas for pyrene and fluorene we observe opposite behavior in the studied photon energy range.

Normally an excitation of collective nature occurs well above the ionization threshold and is expected to couple to various ionization channels (Baltzer et al., 1997). Since this coupling will be weakly dependent on the photon energy, it is expected that the branching ratio of the PE intensities from various MOs will be constant. The other notable behavior is that in the region of the plasmon excitation the branching ratios of the outer valence bands are lower than the ones due to the inner valence and shakeup bands. Beyond the plasmon excitation region the behavior is same for both inner and outer band and they quantitatively display the same trend. This indicates that the plasmon excitation couples more efficiently to the inner valence bands (Jochims et al., 1997,

1999). It was also shown for coronene that the photoionisation cross section at 17.4 eV is primarily due to a giant resonance associated with σ and π electron plasmon excitation (Léger et al., 1989). This explanation of a signature of plasmon resonance in both pyrene and fluorene cross sections for a certain range of photon excitation needs improved theoretical modeling.

2.2.2.2 PEPICO measurements

The aim of this section is to understand the photodissociation/ photofragmentation in PAHs under UV excitation which is already studied for benzene using PEPICO technique (Boechat-Roberty et al., 2009). To identify the correlation between photoelectron emission from a particular MO and the state of the residual ion, the PEPICO measurements were performed. Such study is performed for biomolecules by Plekan et al. (2008, 2007) and not so far for PAHs to our knowledge. Upon removal of electron, the residual ion may remain in ground state or lifted to an excited state with a gain of internal energy, where both can be prone to fragmentation. Also there is a shifting of binding energy for MOs upon removal of electrons which again varies with different charge state, with a violation of Koopman's theorem (discussed in detail in section 3.2.3 of Chapter 3 with the help of OVGF calculations). As discussed in ion-PAH collision in above section, the possible ways in which molecule gets de-excited is either evaporation or fragmentation.

The PEPICO data was taken by pulsing the extraction voltage of linear ToF using a high voltage pulser. The high voltage pulser receives a trigger from an OR logic output of all the functioning CEMs (photoelectron detector). In addition to this one random pulse generator was also added to the input of OR gate. Since the synchrotron beam is ON continuously, the target molecules are also ionized continuously at random, therefore if the photoelectron produced is detected then it triggers the high voltage extraction and the corresponding recoil ion is detected and we get a genuine PEPICO counts. But

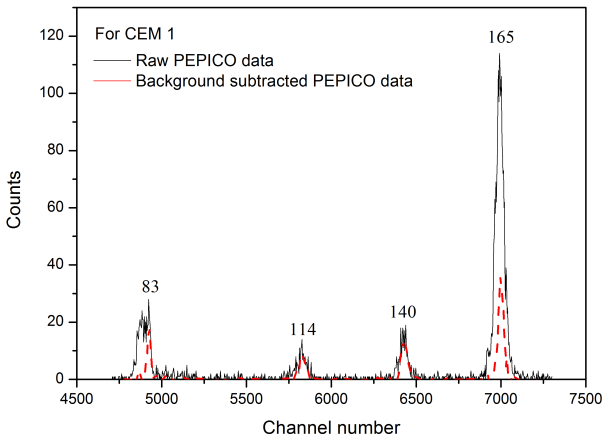

Figure 2.24: PEPICO data for fluorene. The numbers shows different m/q positions.

if there are some recoil ions present in the interaction region which are uncorrelated to this photoelectron, then we will detect an uncorrelated recoil ion but at the correct m/q position. Therefore the random pulse generator data helps us in estimating the contribution of such random correlation which can then be subtracted from the raw mass spectrum corresponding to a specific CEM. Incidentally since the random ions spend more time in the interaction region, they move away from the optimum interaction position in the mass spectrometer due to their drift velocities. Therefore such random contributions appear as a broad peak in the mass spectrum at a slightly lower m/q as compare to the genuine PEPICO mass peak. Thus by normalizing the random mass spectra to these broad peaks at the parent cation or parent dication peak position, we can do the background subtraction (see figure 2.24).

Since six CEMs are used in electron spectrometer, we can select multiple binding energy values of the orbital of origin and record the corresponding mass spectrum. Figure 2.25 shows one such data set taken at 40 eV photon energy and the corresponding binding energy values of 21.51, 22.01, 22.69, 23.19 eV. The corresponding subtracted mass spectra show mainly two channels: double ionization (at m/q 83) or single ion-

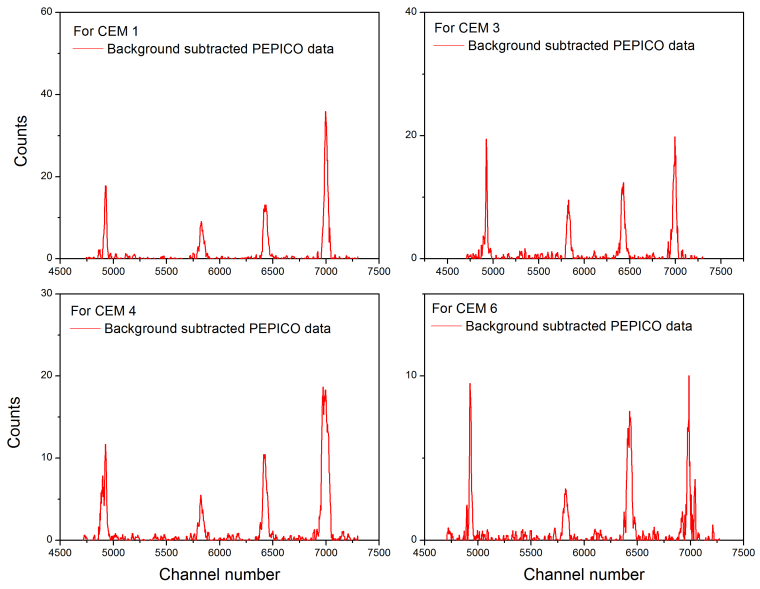

Figure 2.25: PEPICO measurements for fluorene at 40 eV photon energy for different CEMs.

ization followed by rapid evaporation of neutral fragments like H, H_2, C_2H_2, two C_2H_2 at m/q 165, 164, 140 and 114 respectively. Considering the fact that the first and second ionization potential of fluorene are 7.9 and 21 eV (Tobita et al., 1994), it is evident that an inner shell ionization will lead to substantial amount of deposition of energy. Since a large intensity of ions is observed at m/q near to 166, it is expected that at this amount of internal energy ($\sim$ 13.51 eV), it can be safely assumed that the parent ion would lose at least one H atom as a neutral fragment (West et al., 2012). The next energetically probable channel is the loss of one or two C_2H_2 fragments. An important observation made in figure 2.24 is that the random counts have a pronounced peak only at m/q 83 and 166. However the C_2H_2 loss show negligible intensity in the random mass spectrum. This is observed in all the CEM cases (not shown here).

Figure 2.25 shows the evolution of evaporative channels in comparison to double ionization channel with respect to the binding energy. Considering the broadness of

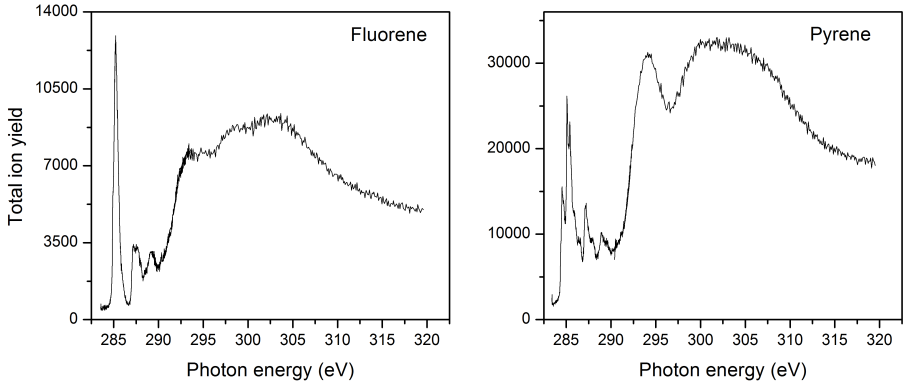

Figure 2.26: C *1s* NEXAFS spectra for fluorene (left) and pyrene (right) for photon energy between 284 to 320 eV.

the PES at these binding energy region (see figure 3.8a of Chapter 3), it is not possible to attribute these observation to a specific MO. A more detail though time consuming experimental investigation is needed to clearly identify the role played by the non statistical processes like electron-electron correlation, double ionization etc. in comparison with the statistical process like neutral evaporation. At present due to large random coincidence probability, we were compelled to keep the count rate very low. And at the same time, due to a large variation which can be done in operating parameters like photon energy and photoelectron energy, taking a complete set data in a very restricted time schedule of beam time is extremely difficult.

2.2.2.3 NEXAFS measurements

In section 2.2.2.2, the effect of outgoing electron from the inner most orbital on the residual ion is discussed. But sometimes this inner shell excitation leads to excitation of core electron to an empty state rather to a continuum. As a consequence, a fine structure is observed in the PES. Such NEXAFS measurements were performed at photon energy close to the *1s* or K - edge of carbon atom to explore the inner shell MO structure, elec-

tronic state property for unoccupied MOs and bands in molecules. The structures shown in figure 2.26 are due to transition from carbon *1s* electrons to unoccupied molecular states. The sharp structure in figure 2.26 are due to the transition from C *1s* to unoccupied MOs of π* symmetry, whereas broad bands are due to σ* resonance (Stöhr, 1992). The difference in intensity of π to σ* resonance peak for pyrene and fluorene suggests the difference in density of states for unoccupied MOs in both the molecule. Similar study is done for other linear PAHs, derivative of PAHs, mixture of PAHs where again the NEXAFS spectrum varies for all of them (Pereira Netto et al., 2005; Oji et al., 1998). To our knowledge it is the first time the NEXAFS spectrum for gas phase fluorene is reported in this work.

2.3 Conclusions

Ion-PAH collision: In contrast to many organic molecules, PAHs show resistance to fragmentation induced by energetic radiation. The present work explores this mechanism through collisions between energetic protons and naphthalene. The mass spectrum includes narrow peaks corresponding to singly, multiply ionized parent molecule or species with neutral fragment evaporation and broader peaks due to fragmentation of a multiply charged parent ion into charged fragments. The evaporation process is mainly H-loss or sequential emission of neutral H. But, for double ionization, H_2 loss is observed to be an important pathway compared to H loss due to higher internal energy deposition. Single and double ionization dominates over fragmentation yields unlike nucleobases which is a very important observation considering that the nucleobases and naphthalene are similar in structure and composition as far as electronic stopping is concerned. A substantial fraction of dications are seen to decay *via* 2H/H_2 loss or loss of C_2H_2 with a small fraction of $C_2H_2{}^+$ loss and no H^+ loss (in agreement with studies by Holm et al. (2010)). Whereas for single ionization the intact ion dominates over the loss

of H and C_2H_2 species. Triple ionization, although present, is noted to have relatively low yield.

Measured relative cross sections show that ionization in electron emission case dominates over electron capture case by a factor of three in the studied velocity regime. The cross sections for single ionization (in EE mode) and evaporation channels namely H, $2H/H_2$ and C_2H_2 loss are observed to be independent of projectile velocity (for both EE and EC modes). For C_{60}, it has been shown that plasmon or collective excitation process weakly depends on velocity but dominates the single and double ionization process in ion-C_{60} collisions. Thus, we conclude that for the single ionization of naphthalene, plasmon excitation has a significant influence. On the other hand, multifragmentation depends strongly on projectile velocity for EE mode, but independent for EC mode (explained by resonant electron transfer from inner valence shell). The transfer condition is satisfied for several molecular orbitals inferred from DFT calculations performed for naphthalene. Comparison of the breakdown curves obtained from photoionization studies estimates the energy deposition to be between 6 - 10 eV for EC events. The excess energy $>$ 2 eV is deposited by the electronic stopping of projectile.

The multihit data is used to analyze the momentum correlated fragments observed in the 2D correlation diagram and few of them are identified. The slope and the shape of the island in the 2D diagram decides the momentum associated during the fragmentation and the number of ionic partners involved in that. From these measurements the kinetic energy release during the fragmentation with the help of coulomb explosion model can be calculated.

Photon-PAH collision: A multi dimensional observation of the photoionization cross section of pyrene and fluorene using both the binding energy and the photon energy as variables was studied. The first ionization potential was estimated to be 7.436 eV

$\pm$ 0.015 eV and 7.944 $\pm$0.055 eV for pyrene and fluorene, respectively. The PES as a function of photon energy shows that the inner valence bands dominate in the lower photon energy range (below 27 eV) which is in contrast with the measurements for benzene. The cross sections for inner valence orbital display a peak for pyrene and a plateau for fluorene at 17 eV photon energy. This observation, along with the previously studied photoion yield studies and EELS studies, indicates that the collective excitation is responsible for this enhancement of the relative cross section for inner valence band.

To study the effect of outgoing electron from different states on the residual ion PEPICO experiment is performed. The PEPICO spectrum for 40 eV incident photon energy with an electron to be taken from inner shell shows two type of processes occurring in fluorene: double ionization of parent molecule and the evaporation (with loss of neutrals like H, H_2, C_2H_2 etc). It is seen that the deeper MO ionization leads to substantial energy deposition which has resulted in relative increase in the yield of H-loss mass. NEXAFS studies were performed at photon energy close to the *1s* edge of carbon atom to explore the inner shell molecular orbital structure by looking at the ion yield variation for different photon energy. Fluorene showed a very different NEXAFS spectrum than pyrene due to the structural difference.

CHAPTER 3

THEORETICAL WORK

3.1 Introduction

The theoretical study to explain the energetic radiation (ion or photon) interaction with molecule to a very good accuracy is difficult due to simultaneous involvement of several collisional processes during the experiment which are the results of the many body interaction process. These interactions play a major role due to multielectronic nature of the system and become essential to consider for large systems because of its dominance in the potential energy term of Hamiltonian. In addition to this for large molecules the experimental results become multidimensional in nature due to complexity in potential energy surface and associated many numbers of degrees of freedom ($3N - 6$ where N is the number of atoms in the molecule). Sometimes lack of symmetry adds more difficulty in numerical calculation and deriving analytical solution for any problem is practically impossible. Apart from these complications, the interaction sometimes leads to dynamical changes like alteration in geometrical coordinates upon removal or addition of an electron, hence the structure of molecule is significant in theoretical calculation and modeling. The stationary systems like atomic system for which the interaction potential is exactly known, can be explained with a very good precision by quantum mechanics. But for large systems like molecules (even the smallest molecule like H_2), the deduction of interaction potential becomes complicated due to involvement of many body system. The disagreement between theory and experiment can be attributed to this manybody aspects and the dynamics of the problem. The electronic wavefunction which decides various properties of diatomic molecule is a function of only one

internuclear coordinate, whereas for polyatomic systems, it is a function of several parameters simultaneously like bond distances, bond angles, dihedral angles of rotation. So a full theoretical treatment of polyatomic system numerically involves calculation of electronic wavefunction which depends on the above parameters and hence makes it difficult to calculate quantum mechanically. Thus a quantum chemical approach based on approximations helps in giving results with reasonable accuracy for nuclear coordinates, vibrational modes, potential energy surface and the electronic wavefunction. Whereas the statistical approach helps in determining various dynamical properties of the system like dissociation and fragmentation.

The topic of discussion in this section is to perform computational calculations (using quantum mechanics) and theoretical modeling (using statistical model) to validate the experimental results discussed in previous section and the domain of validity, applicability, computational difficulty for such calculations. We have done the theoretical calculation using both quantum chemistry calculation by GAUSSIAN09 (Frisch et al., 2009) and *Monte Carlo* (MC) simulation within Local density approximation (LDA) by a C program (see appendix A for the code). As discussed in the experimental section earlier, we have studied the ion as well as photon collision with PAHs. The ion impact results like ionization, fragmentation in the molecule are also dependent on the type of measurements (see section 2.1). A *Monte Carlo* simulation is performed to reproduce the observed fragmentation yield. On the other hand photon interaction with molecules gives PES in which the peaks represent the binding energy for MOs from where the measured electron is coming out. With the help of OVGF method the binding energy for different MOs are reproduced to a reasonable accuracy. Such interaction also alters the nuclear coordinates upon removal of electron, hence gives rise to vibrational transitions due to Franck-Condon overlap. The intensities as well as frequencies for different modes of vibration are identified with the help Franck-Condon factor calculation and compared with the observed experimental ones. In addition to experimental results

comparison, the gas phase properties calculations and structure calculation are also performed to obtain various stability parameters for several PAHs and PAH clusters.

3.2 Quantum chemistry calculations

As discussed above, the quantum mechanical calculations for structure and dynamics is critical to this work. The accuracy of these type of calculations depends on the proper choice of basis sets and methods implemented in GAUSSIAN09 (Frisch et al., 2009). The goal is to solve the time independent Schrödinger equation and to determine the electronic structure of atoms and molecules. There are different ways in quantum chemistry to find the molecular properties by finding solution to the Schrödinger equation: *ab initio* (Hartree-Fock self consistent, density functional theory), semiempirical method. The wavefunction obtained in HF method is not exact because it does not consider the instantaneous coulombic interactions between electrons. In addition to this HF has computational difficulty for achieving accuracy while using large basis sets for molecules where there are many atoms and electrons. In this regard, DFT is an approachable method where the input is a three dimensional quantity: the "electron probability density" which has no constraint due to permutation symmetry, unlike the trial wavefunction in HF method. So the electronic energy of the system is a functional of electron probability density where the later itself is function of spatial coordinates. As stated by P. Hohenberg and W. Kohn that the ground state energy and all other ground state electronic properties are uniquely determined by the electron density. Hence in DFT, there is a trial density function with a condition that energy functional of this density function cannot be less than the true ground state energy of the molecule. The electron density can be obtained from the set of one electron equations of a system consisting of non interacting electrons in an external potential with an assumption made by Kohn and Sham that this reference and real system have same electron density. This assumption leads to an

exchange-correlation potential which is derived from the exchange-correlation energy functional and the error in DFT comes from the approximate nature of this functional which are of two type: Local density and generalized gradient approximation (Atkins and Friedman, 2011; Levine, 2000). Hence DFT takes care of electron-electron correlation which is not the case in HF. Another reason of popularity of DFT than HF is its applicability on molecules of 100 atoms or above with significantly less consumption of time and comparable result with experimental one for systems involving d-block metals. DFT shows better agreement for vibrational frequency calculation than HF (Lee and Boo, 1996). Hence for our experimental result comparison with computationally calculated one for various experiments mentioned in Chapter 2, we have used DFT method and at some places shown the comparison of DFT to HF calculations.

3.2.1 Structure calculation for clusters

Due to their planar nature, PAHs have tendency to form clusters among themselves by van der Waals forces in ISM (Tielens, 2008). PAHs as large as ranging 50 - 400 C atoms are predicted to be present in ISM whose relative abundance is $\sim 3 \times 10^{-7}$ with respect to the most abundant molecule H_2 (Tielens, 2008). Quantum structure calculation is performed to obtain the optimized structure for clusters of following combination of molecule and atom: corannulene with water, coronene with water, corannulene with silver atom, silver atom sandwiched between two corannulene molecule (figure 3.1). These calculations are done using DFT at B3LYP/3-21G basis set to obtain the stability diagram for potential energy surface and nuclear coordinates with no symmetry constraints. These type of calculation helps in predicting the magic number for such stable cluster formation during the experiments. It is reported in literature that some of these clusters rapidly break by FUV absorption as reported by Rapacioli et al. (2006) for coronene cluster (two coronene molecule bonded by $\sim$ 1.3 eV). Figure 3.1 shows

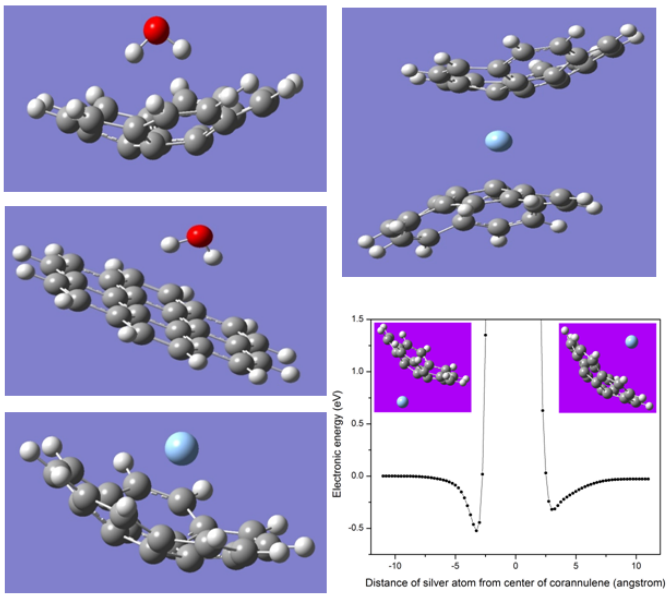

Figure 3.1: Optimized structure for clusters. Potential energy curve for the cluster: silver atom attached to corannulene (right side bottom).

the potential energy curve for the silver atom positioned above and below corannulene molecule, and it depicts that these clusters are stable enough. So the stability under UV-IR radiation impact in stellar medium can be studied in laboratory with the help of mass spectrometer set up developed in house (see Chapter 4).

3.2.2 Electron affinity and proton affinity calculation for PAHs

I. Electron affinity: The inherent structural attributes due to the carbon atoms make formation of large size PAHs possible and the strong delocalization of π-electrons leads to inherent stability (Eisenberg and Shenhar, 2012). The delocalization of electrons and spread of the wavefunction over several atoms in the molecule facilitates multiple ionization of the molecule as well as accommodation of extra electrons (Eisenberg and Shenhar, 2012). It has been seen that molecule like C_{60} can be experimentally detected

with charge states as high as +12 and as low as -2 in vacuum (Bhardwaj et al., 2003; Kadhane et al., 2009) (-3 in solution phase (Bühl and Hirsch, 2001)). Thus it is clear that the very nature of the π electronic structure of PAHs is an essential feature of these molecules and gives them the unique properties for which they occupy the center stage in several scientific investigations.

This section deals mostly with properties of anions of PAHs and additional gasphase property calculation for PAHs (see later). Anions of PAHs are less probable in ISM but are predicted to be present (Hudgins et al., 2000; Ruiterkamp et al., 2002). Apart from their own bio chemical significance, PAH anions are interesting systems to test the quantum mechanical structure calculations (Treitel et al., 2004). Starting from negative value in the case of benzene and naphthalene, the electron affinity (EA) roughly increases with the size of PAH (Rienstra-Kiracofe et al., 2002). This is clearly understandable on the basis of electron-electron interaction and resulting coulomb potential energy. The large delocalization of the electrons in the π-orbitals helps in accommodating an extra electron in the system (Koper et al., 2002). Many aspects of the MO calculations for PAH anions have been discussed in the literature (Treitel et al., 2004; Rienstra-Kiracofe et al., 2002; Modelli et al., 2006; Modelli and Mussoni, 2007; Malloci et al., 2007). Particularly interesting are the small size PAHs where the (smallest occupied molecular orbital) SOMO of the anion lies very close to zero or in a few cases negative with respect to the neutral energy. In such cases the diffuseness of the wavefunctions is needed in determination of adiabatic electron affinity (AEA) (Treitel et al., 2004; Modelli et al., 2006). Calculations at B3LYP level with 6-31+G(d) or better has been giving AEA values close to the experimental values in several of the small PAH cases (Modelli et al., 2006). Modelli and Mussoni (2007) have also shown for a very large set of PAHs that the HOMO and (lowest unoccupied molecular orbital) LUMO calculations at much lower level can give a satisfactory correlation with the experimental values of AEA and ionization energies. On the other hand aromaticity is a multidimensional feature (Krygowski and

Cyranski, 2001) and hence the quantification of it and correlation with any molecular feature is not simple. In this section the aromaticity is quantitatively compared with the help of a geometry based Harmonic Oscillator Model of Aromaticity (HOMA) index. The index is defined by Krygowski and Cyrański, and is known to be very effective, particularly for alternant PAHs (Krygowski and Cyranski, 2001). It reproduces the trend of reactivity of PAH molecules successfully (Portella et al., 2005).

The PAH molecules chosen for AEA calculation are of three variety as shown in figure 3.2. First group consists of all the PAHs starting with benzene and up to four aromatic six membered rings (6 MR) fused together in all possible configurations (1 - 10 in figure 3.2). The second variety are with the four 6 MR with at least two sp^3 hybridized C atoms (11 - 14 in figure 3.2). The final group consists of the molecules with at least one cyclopenta ring (5 MR), with or without a sp^3 hybridized C atom, fused to not more than three aromatic 6 MR (15 - 26 in figure 3.2). The groups are chosen to underline the effect of cyclopenta rings and aromaticity separately. Different criteria like comparison with experimental values of EAs, charge distribution on the anions and the aromaticity are used to compare the results and their implications. The second set of molecules are not as widely studied as regular PAHs. Partial hydrogenation of a PAH molecule is known to affect the reactivity and biological properties of the PAH significantly (Harvey, 1991). The addition of the hydrogen is associated with change of hybridization from sp^2 to sp^3 and hence induces non-planarity in the molecule. The reported work in this section demonstrates how systematically the increase in the hydrogenation can reduce the EA and in some cases decreases the electron delocalization between two aromatic rings in the same molecule causing a large reduction in the EA.

Computational details: The geometry optimization and vibrational frequency calculations are done using GAUSSIAN09 (Frisch et al., 2009) in steps starting from a very basic semi empirical to an efficient, more accurate and less time consuming DFT

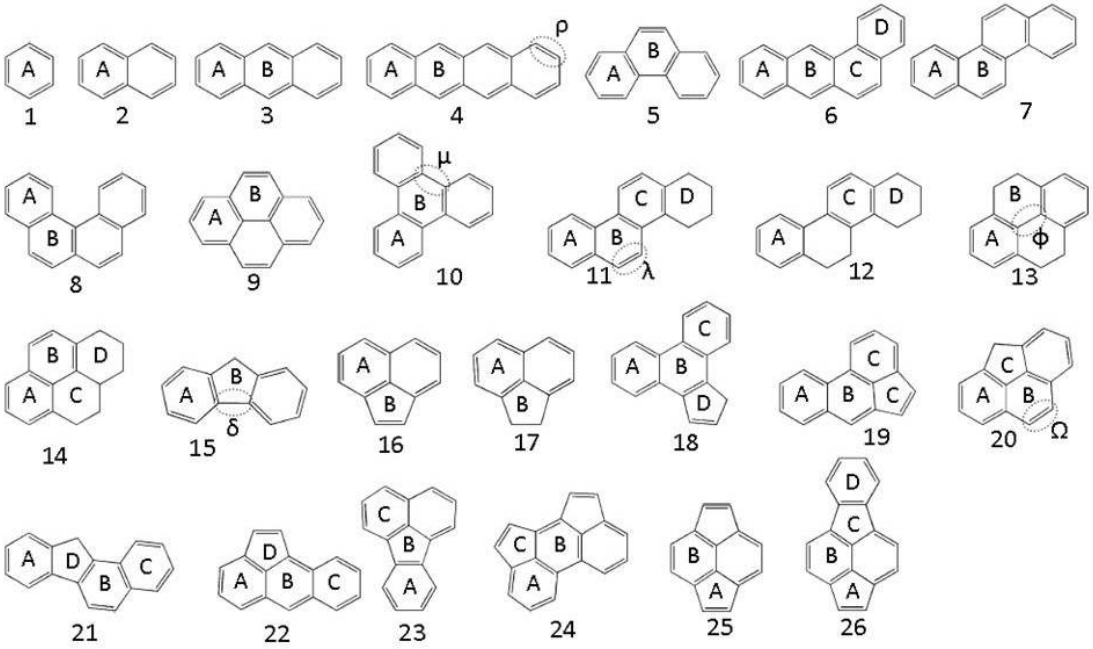

Figure 3.2: The list of the selected examples: 1) Benzene, 2) Naphthalene, 3) Anthracene, 4) Tetracene, 5) Phenanthrene, 6) tetraphene, 7) chrysene, 8) Benzo[c]phenanthrene, 9) Pyrene, 10) Triphenylene, 11) 1,2,3,4-Tetrahydrochrysene, 12) 1,2,3,4,5,6-Hexahydrochrysene, 13) 4,5,9,10-Tetrahydropyrene, 14) 1,2,3,3a,4Hexahydropyrene, 15) Fluorene, 16) Acenaphthylene, 17) Acenaphthene, 18) 1H-Cyclopenta[I]phenanthrene, 19) Acephenanthrylene, 20) 4H-Cyclopenta[def]-phenanthrene, 21) 11H-Benzo[a]fluorene, 22) Aceanthrylene, 23) Fluoranthene, 24) Cyclopenta[hi]acephenanthrylene, 25) Cyclopent[fg]acenaphthylene, 26) Cyclopenta[cd]fluoranthene. The individual ring labels with alphabets are used in text.

technique *via* HF method. DFT calculations are performed using B3LYP (which is a linear combination of HF exchange, Becke three-parameter exchange functional with Lee-Yang-Parr correlation functional). Optimized geometries and MOs are obtained with the help of various basis sets up to 6-311+G(d,p). Diffuse function is needed because to reduce the coulomb repulsion upon insertion of extra electrons into orbitals, the orbitals expand (Treitel et al., 2004) and diffuse function allows flexibility for the orbitals (Levine, 2000). Also for anions the calculation without diffuse function overestimates mutual electron repulsion (Clark et al., 1983), and gives false interactions of each electron with itself (Cole and Perdew, 1982). AEA was calculated by taking the difference of electronic energy of neutral and anion in their respective optimized geometry (without zero point energy and thermal corrections, these corrections are discussed in later sections). The output visualization and electron density distributions were obtained with the help of Gauss View 5.0 interface.

The relevance of diffused functions in the EA calculations of PAHs is a heavily discussed topic. After the work by Treitel et al. (2004), Modelli et al. (2006); Modelli and Mussoni (2007) and several others, it is clear that inclusion of diffuseness in the wavefunctions definitely improves the match between the calculated and experimental EAs. But at the same time using higher and higher basis with higher amount of diffuseness does not improve the results further. Changing the basis set from B3LYP/6-31+G(d) to B3LYP/6-311+G(d,p) increases the EA values systematically for all the PAHs by an average of about 50 meV with largest variation of approximately 68 meV and minimum being about 45 meV. Thus indicating absence of any molecular structure effects and could be an artifact of the diffuseness of the wavefucntion. Table B.1 in appendix gives the list of the AEA values calculated at all the basis sets and the experimental numbers wherever available. The calculated values at B3LYP/6-31+G(d) match qualitatively well with the experimental values as shown in figure 3.3. In the proceeding sections all the data discussed will be based on B3LYP/6-31+G(d) level calculations

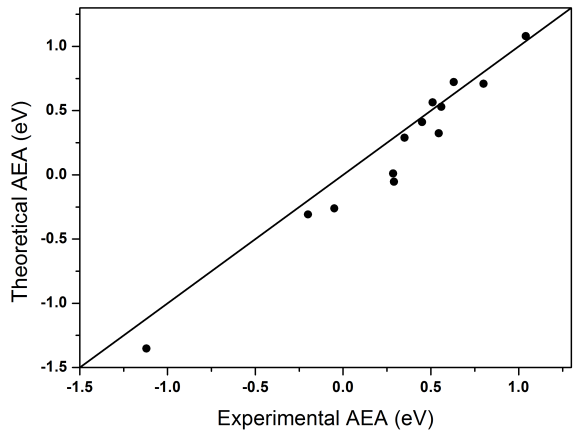

Figure 3.3: Experimental vs. theoretical AEA (circles). Straight line drawn is with slope 1 and intercept zero for guide to eye.

unless stated otherwise.

The computational results are analyzed using several criterion including $< s^2 >$, bond length changes, AEA values etc. Expectation value of s^2 is not a good measure for HF calculations. For DFT calculations in all the cases $< s^2 >$ are consistently between 0.75 and 0.77. Upon electron addition, for molecules with only conjugated 6 MR, maximum bond length decrease is observed in triphenylene of 0.0308 Å shown by μ in figure 3.2. Maximum increase of 0.0189 Å happens in tetracene shown by ρ. In the presence of sp^3 hybridized C atoms, ϕ labeled bond in 4,5,9,10 tetrahydropyrene shrinks by 0.0507 Å whereas expands by 0.0461 Å in 1,2,3,4 tetrahydrochrysene after reduction (shown by λ). For molecules with at least one 5 MR, it is observed that maximum decrease happened in fluorene is of 0.043 Å (shown as δ). Maximum increase of 0.053 Å happens in 4H-cyclopenta[def]-phenanthrene (shown by Ω). The zero point energy and thermal correction to the electronic AEA value is about 140 meV on an average for the examples with only 6 MR and no 5 MR present. The largest variation is shown by triphenylene of about 213 meV and smallest by benzene of about 75 meV. In case of the cylclopenta fused structures, the average increase is about 109 meV with minimum

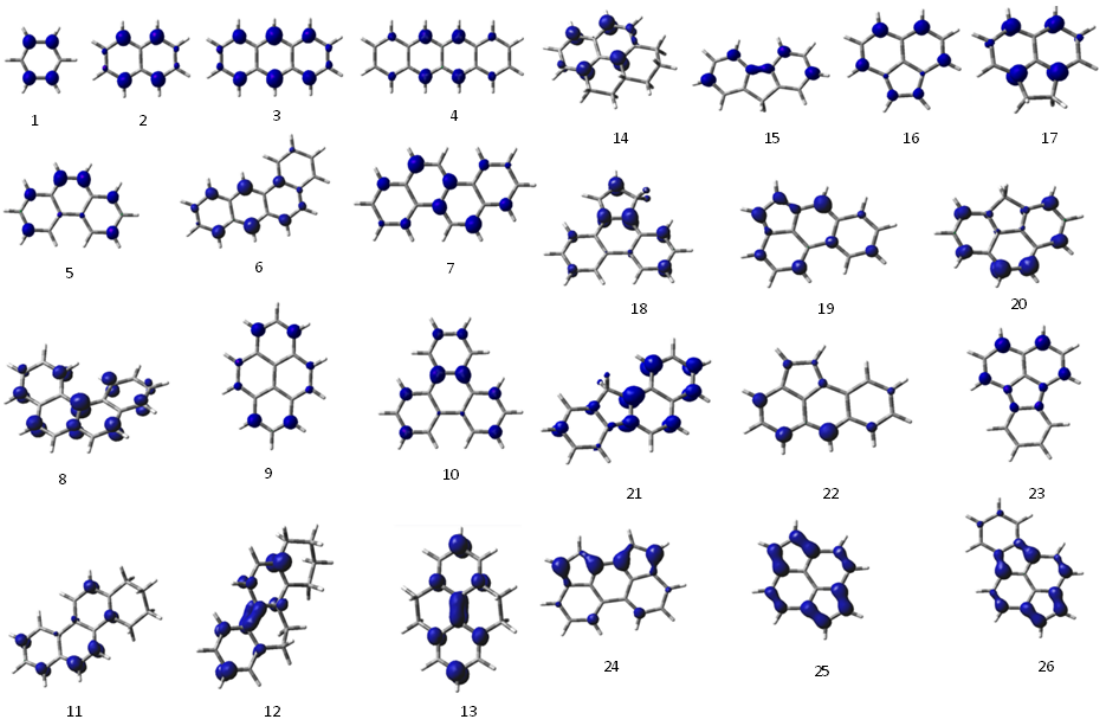

Figure 3.4: Anionic electron spin distribution at B3LYP/6-31+G(d) level (difference of α and β electron density).

increase for cyclopenta[fg]acenaphthylene of about 83 meV and largest increase in case acenaphthene of about 150 meV.

Electron density distribution: To understand the behavior of the various system under study the electron spin density distribution at a specific isovalue of the density are plotted in figure 3.4 and the electrostatic potential (ESP) mapped on the total electron density is shown in figure 3.5. The electron spin density distribution shows that the addition of an extra electron moves the excess electron density to the periphery of the molecule which is very much expected (Eisenberg and Shenhar, 2012). The sites of higher electron localization in the anions are indicated by the higher ESP value (by red color).

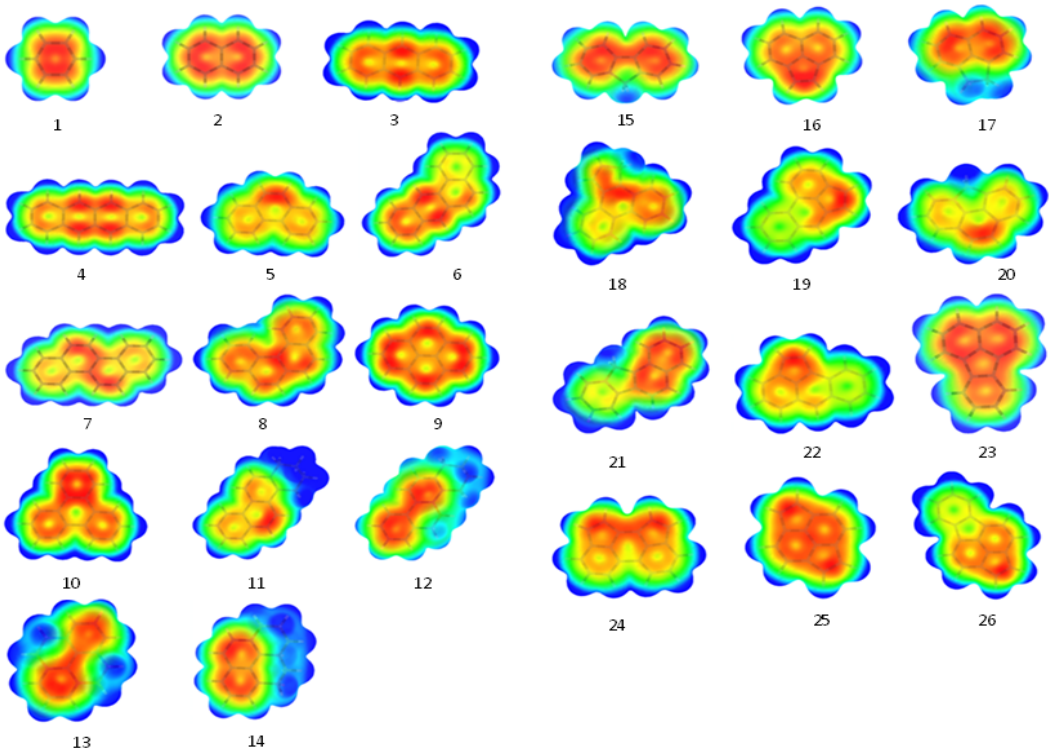

Figure 3.5: Electrostatic potential (ESP) mapped on to the total electron density distribution of anions. The red color indicates highest negative ESP.

A. For PAHs with only six member rings: Delocalization is understood to facilitate accommodation of extra electrons in the molecule leading to higher EA. Linear acenes show systematic increase of spin density on the inner hexa-rings as the chain length increases. Comparison of anthracene and phenanthrene shows that for the nonlinear PAH case, the electron density is less dispersed, thus increasing the electron-electron repulsion, hence making the system less stable for their anions. This fact can be seen from the calculated as well as experimental EAs. Higher concentration of electron density on the farthest six member rings lowers the energy for pyrene, hence higher EA is observed. Chrysene on the other hand shows the delocalization over the central CC bond retains a large fraction of the density. More details of this example are discussed in the next section.

The ESP mapped on the total electron density represents a picture consistent with the electron spin distribution. The red regions are the one where a test positive charge experience lowest potential indicating concentration of negative charge density. Most notable are chrysene and triphenylene (see table B.1 in appendix). In the former case the excess electron density is mostly concentrated on the common bond between the central rings. The outer rings carry much less density compared to the case of linear acenes. Whereas triphenylene showed a change in the symmetry of the SOMO of anion compared to the symmetry of LUMO of neutral (not shown here). It is possibly due to Jahn-Teller distortion (Townsend and Weissman, 1960) of the molecule which lifts the degeneracy causing change in the symmetry.

B. For PAHs with only six member rings and at least two sp^3 hybridized C atoms: These set of molecules underline the importance of aromaticity character on EA very strongly. As seen in figure 3.5 the cyclohexane rings are devoid of excess negative charge. The additional electron is accommodated in the delocalized structure over the aromatic rings. All the examples of this category clearly demonstrate that the excess electron is localized mostly on the aromatic site. Same is observed with electron spin density distribution (see figure 3.4).

C. For PAHs with at least one cyclopenta ring: Cyclopenta fused rings are known to increase the EA of the molecule compared to its counterpart without the cyclopenta ring (Todorov et al., 2008). Figure 3.4 compares the electron spin density distribution. The simplest case is fluorene in which the CC bond connecting the two aromatic rings (shown as δ in figure 3.2) bridges the delocalization and thus reducing the repulsion. The π electrons from the cyclopenta ring also play an important role in the increase of EA. As can be seen in the case of acenaphthylene and fluoranthene, the delocalization in the cyclopenta ring bridges the charge delocalization across the

molecule and hence increases EA. This fact is further substantiated by acenaphthene where the absence of double bond in the outer part of the ring reduces delocalization and EA substantially.

The ESP mapped electron density indicates the same behavior in figure 3.5. As noted before, fluorene shows the π delocalization bridge between the two aromatic rings. Acenaphthylene shows the concentration of the electron density over the cyclopenta ring and acenaphthene shows the absence of delocalization in the cyclopenta ring which moves the electron density away from the cyclopenta ring. Aceanthrylene, acephenanthrylene and cyclopenta[c d]fluoranthene retain the density distribution of acenaphthylene but the EA values differ a lot due to overall larger delocalization volume available. The presence of the cyclopenta ring in 4H-cyclopenta[d e f]-phenanthrene does not alter the distribution compared to phenanthrene. This may be due to the sp^3 hybridization of the C atom in the cyclopenta ring. A comparison of cyclopenta[c d]fluoranthene and fluoranthene indicates large change in the density distribution. The localization is observed to be more in the former case but still the electron affinity is higher by a large amount due to the additional cyclopenta ring. Cyclopenta[f g]acenaphthylene shows the domination of the cyclopenta rings structure and the same is true for the case of cyclopenta[h i]acephenanthrylene in electron density distribution.

Aromaticity index and Electron affinity: HOMA index as defined by Krygowski and Cyrański (Krygowski and Cyranski, 2001) is used to quantify the effect of aromaticity and identify the influence of the cyclopenta and cyclohexane ring fusion on the AEA of the PAHs. Equation 3.1 gives the expression used for calculation of HOMA index with α = 257.7 for CC bond so that in case of perfectly delocalized benzene structure the six member ring will have HOMA index of 1 and will be zero for hypothetical pure Kekule structure. n is the number of bonds considered

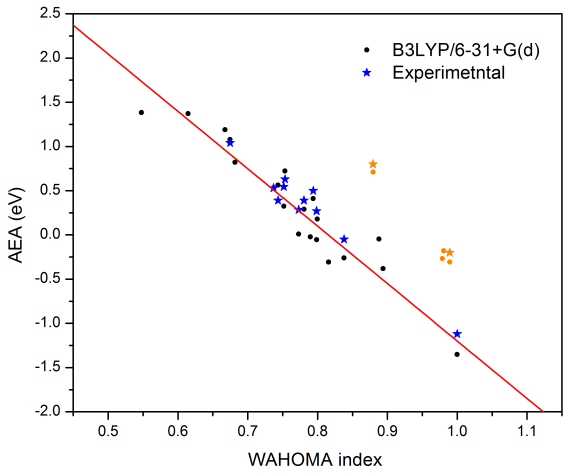

Figure 3.6: AEA (experimental and theoretical) vs. WAHOMA index, the line is a straight line fit to the theoretical calculations.

$$HOMA = 1 - \frac{\alpha}{n}(R_0 - R_i)^2 \tag{3.1}$$

Using equation 3.1, HOMA index is calculated for all the rings. All the cases the bond lengths as per B3LYP/6-31+G(d) calculation are used. Therefore the optimum CC bond length R_0 = 1.398 Å is used. Then for a given molecule we discard HOMA indices of all the rings which have at least one C atom with sp^3 hybridization. The rest of the values are summed and divided by the number of rings whose contribution is summed. This gives weighted average HOMA (WAHOMA) index of the molecule. Table B.2 in appendix lists all the calculated values of HOMA index for various rings as identified in figure 3.2 and the corresponding WAHOMA index values.

The effectiveness of this method is tested by plotting the experimental and theoretical (at B3LYP/6-31+G(d) level) AEA values against WAHOMA index. As can be seen from figure 3.6, a clear correlation between the WAHOMA and AEA is observed in both the cases. Most of the cyclohexane rings show large negative HOMA index which indicates the lack of delocalization due to sp^3 hybridization.

By design benzene structure gives highest HOMA index of 1 for the present level of calculation. For linear acenes as the length increases the HOMA index value decreases systematically with outer most rings having lower value than the inner aromatic rings. The trends and behavior of the HOMA index for various types of benzenoid family molecules are discussed in detail by Portella et al. (2005). The correlation of AEA with the HOMA is discussed in this work. If the electron spin density distribution and the ESP mapped density are compared then it is observed that the excess electron density is more prominent on the inner rings. This corroborate well with the HOMA index trend for linear acenes.

For the nonlinear acenes, cases with only 6 MRs we observe that whenever a given aromatic 6 MR shares its alternate bonds with two or three 6 MR then it causes higher amount of bond alternation in itself which leads to lower HOMA index for that ring. For example see the HOMA trend for individual rings in table B.2 in appendix for molecules numbered as 5, 6, 7, 8, 10 and 11.

For naphthalene the WAHOMA value is 0.838. Acenaphthylene gives value of 0.699 which is closer to anthracene, on the other hand acenaphthene gives a value of 0.894 which is higher than naphthalene. If we consider the WAHOMA index correlation with AEA then it can be expected that acenaphthene must have AEA closer or even lower than naphthalene and acenaphthylene must have AEA closer to anthracene. As can be seen from table B.1 in appendix that these trends are followed. Similar correlation can be seen for anthracene, phenathrene and their derivative.

Cyclopenta[f g]acenaphthylene and fluorene show a deviation from the trend in figure 3.6 (the former case not shown in the graph). This can be attributed to the stronger influence of the cyclopenta ring. As can be seen from the ESP distribution that both cases the 5 MR dominantly retains the electron density. 4,5,9,10-tetrahydropyrene and 1,2,3,4,5,6-hexahydrochrysene also show a large deviation which is difficult to ex-

plained on the basis of the HOMA index calculations.

In the case of cyclohexane fused PAHs, we note that for the case of 1,2,3,4,5,6-hexahydrochrysene and 4,5,9,10-tetrahydropyrene the individual HOMA values of the aromatic rings are greater than 0.9. Similarly in the case of fluorene and 11H-benzo[a]fluorene with sp^3 hybridized C atom containing cyclopenta ring, the aromatic rings have HOMA index values greater than 0.9. Thus it can be concluded that any ring (5 MR or 6 MR) lying in between a chain of aromatic rings and has a sp^3 hybridized C atom will reduce the delocalization and thus isolating the aromatic rings around it.

II. Proton affinity: It is very important to study the proton affinity (PA) for a molecule because proton transfer reaction plays a crucial role in many chemical transformations in chemistry and biochemistry (Stewart, 1985; Carroll, 2011). PA is directly correlated to the acidity and basicity, which is one of the fundamental properties of chemical systems (Finston and Rychtman, 1987; Pearson, 1987). The PA is defined by the enthalpy required to remove the proton from protonated molecule. For different PAHs and some organic molecules the PA value is calculated (see table C.1 in appendix) using *ab intio* measured SCF electronic energies (including the thermal energy) for protonated PAHs and PAHs with the help GAUSSIAN09. The basis set implemented was B3LYP/6-311++G(d,p) for geometry optimization and other thermo-chemistry calculation like zero point energies, vibrational and rotational energies.

3.2.3 Outer valence Green's function method for photoelectron spectrum

The photon interaction ionizes the molecule by removal of electron from different MOs and the distribution of the outgoing electron kinetic energy (which is related to the

binding energy of MO from which the electron is ejected) gives the PE spectrum. Such experiment for FUV radiation is performed for PAHs (see section 2.2) and in this section we discuss the theoretical analysis performed for PES. To a first approximation each peak in PE spectrum can be attributed to a MO, at least in the outer valence region. This type of analysis helps in understanding the electronic and bonding properties of the molecule. The PE spectrum of a molecule is typically associated with a broadening due to Franck-Condon overlap of vibrational states. The inner valence bands are characterized by satellite peaks due to configuration interaction between quasi-degenerate states with a single hole configuration in inner valence band and states with a configuration with two holes in an outer valence band along with one particle in an excited orbital. This strong interaction due to electron-electron correlation leads to redistribution of intensity over several satellite lines, which is a manifestation of the breaking down of molecular orbital picture of ionization (Schirmer et al., 1977; Cederbaum et al., 1977; Cederbaum and Domcke; Cederbaum et al., 1978). The Koopman's theorem which neglects the electron correlation energy in neutral as well as in ion and relaxation energy in ion, fails to explain the correct ordering of binding energy for MOs in ionic states. The Koopman's approximation up to some extent is valid for outer valence region but fails severely for the inner one. It is also been shown that low lying satellite lines appear in outer valence region are due to strong correlation effect in the inner valence region. It depends on size, symmetry and chemical properties of the molecule (von Niessen, 1991). All these indicate the failure of Koopman's approximation in predicting the accurate ionization energy and demand an advanced calculation which will take care of correlation as well as relaxation energy correction to represent the PE spectrum peak positions with a reasonable accuracy. Advanced calculations which take care of the electron-electron correlation as well as of the relaxation energy correction to represent the PES peak positions with a reasonable accuracy include techniques like configuration interaction, perturbation and Green's function methods (von Niessen, 1991). For a

reliable calculation of ionization energies and their relative intensities (pole strength), it is necessary to describe as accurately as possible the many-body effects that are very important in PE spectra.

The details of Green's function method are given in literature extensively (Cederbaum and Domcke; Schirmer and Cederbaum, 1978). The ionization energy and electron affinities are obtained by calculating poles and residues of Green's function using the Dyson equation which connects the Green's function with HF Green's function *via* a term called self energy potential. This is the exact potential seen by an electron due to the interaction with its surrounding. The computational method is called Outer valence Green's function methods (OVGF) in which there are approximations made to the one particle Green's function technique that is the self energy itself has poles and its perturbation expansion are justified only far away from poles where there is negligible satellite structure (i.e.; the outer valence region). This method is a perturbational expansion, exact to third order (in electron-electron interaction) like the advanced extended two particle hole Tamm-Dancoff approximation (2ph-TDA): ADC(3) calculation. It gives accurate results like ADC(3) calculations in the outer valence region, but not in the inner valence region where the satellite peaks start appearing, which can be described correctly to first order only (von Niessen, 1991). This is shown by Potts et al. (2003) for pyrimidine and purine where the many body Green's function calculations indicate that the molecular orbital picture of ionization is valid up to only $\sim$ 14.5 eV, whereas at higher binding energies the effects of electron correlation and relaxation needed to be taken into account. The higher order terms are approximated by renormalization procedure in this technique (Cederbaum, 1973, 1975). The outer valence band is accurately and reliably explained by OVGF calculated ionization energy and pole strength values because of direct relation between ionization from a particular MO and occurrence of a peak in PE spectrum. But OVGF becomes non reliable if ionization from a particular MO gives rise to significant satellite lines. For the present work we

have used the Green's function technique implemented in GAUSSIAN09 package. The prominent peaks observed in the experimental PE spectrum (section 2.2.2) are identified according to their binding energy and symmetry with the help of OVGF calculations. Our simulated spectrum using OVGF calculations reproduces the peaks in PES very well for outer valence region in terms of binding energy and relative intensity. This type of computational study for pyrene is extensively done by Deleuze (2002) with which our OVGF calculation matches very well. However to our knowledge for fluorene such comparison is not yet studied at this level of calculation.

Computational details: The ground state geometries of pyrene and fluorene were optimized with the constraint of D_{2h} and C_{2v} symmetry point groups (Jaffé, 1967), respectively, using DFT (Parr and Yang, 1989; Dreizler and Gross, 1990; Koch et al., 2001). We employed the B3LYP (Becke, 1993; Lee et al., 1988) and Dunning's correlation consistent polarized valence basis set of double zeta quality (cc-pVDZ) (Dunning Jr, 1989; Kendall et al., 1992), incorporated in the GAUSSIAN09 package for these calculations. OVGF calculations were carried out using Dunning basis set cc-pVDZ to predict molecular orbital ionization energies with respective pole strengths. We include all the orbitals in the calculation and the calculations are restricted to values of the ionization potential < 20 eV (Frisch et al., 2009).

Results and discussion:

A. The experimental and calculated PE spectrum for pyrene: The measured PE spectrum in the inner and outer valence region of pyrene at 27 eV photon energy is presented in figure 3.7, with the dominant peaks labeled with roman symbols. For the sake of convenience capital roman symbols are used while discussing experimental bands and small roman symbols in the context of theoretical bands. Figure 3.7b shows

the convoluted spectrum from the OVGF/cc-pVDZ calculations. A sum of Gaussian and Lorentzian functions with 0.3 eV widths is used for the convolution. Orbital symmetry assignments are made by comparing the binding energies of experimental and theoretical peaks obtained by OVGF calculations which are listed in table D.1 of appendix. The first ionization energy is found to be 7.436 eV $\pm$ 0.015 eV (I) which compares very well with the values obtained from REMPI-ZEKE and TPEPICO measurements: 7.426 eV and 7.415 eV respectively (Mayer et al., 2011). This HOMO band is accompanied by its vibrational progression which can be resolved up to 2 $\leftarrow$ 0 transitions. This is followed by a well isolated II band at 8.30 eV. The III and IV bands are observed to overlap and according to the OVGF calculations, originating from the π MOs b_{3u} (band iii) and a_u (band iv). Band IV shows much broader structure indicating possible coupling to other states leading to breakdown of the MO picture as ascribed by Deleuze (2002). Band V retains the sharp distribution with a poorly resolved vibrational substructure at 10.01 eV. The corresponding peak appears at 9.99 eV according to the OVGF calculations. The outer valence binding energies up to band V match with the OVGF calculations within 0.40 eV (see table D.1 of appendix).

From band VI onwards the individual MOs are very close in energy leading to a strong overlap of the bands. This scenario is made worse by the fact that strong electron-electron correlation effects lead to the mixing of several configuration with the redistribution of the intensity of the individual bands. This leads to severe broadening of the peak structure. Bands starting from VI to X mix very strongly and the OVGF results qualitatively match the peak positions of VIII, IX and X bands. Bands XI onward appear well separated and again match closely to the calculated band positions.

B. The experimental and calculated PE spectrum for fluorene: The PE spectrum for fluorene at 27 eV photon energy is presented in figure 3.8a. The assignment of the inner and outer valence MO has been done by comparing the theoretical binding

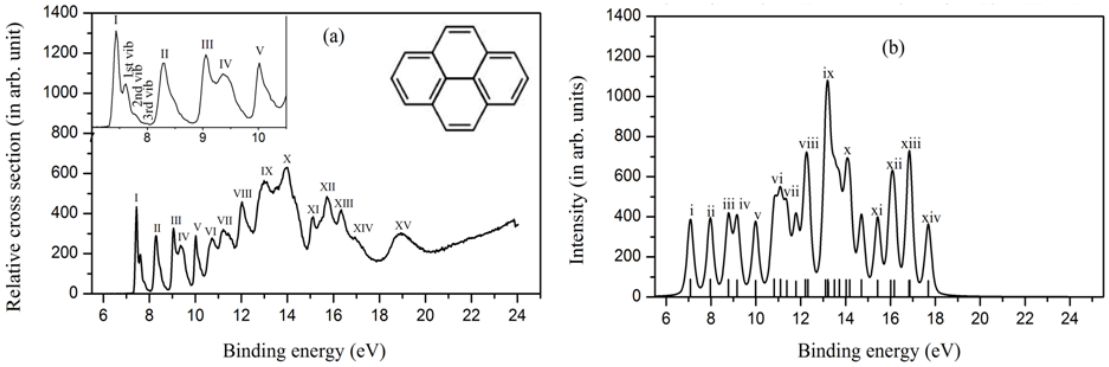

Figure 3.7: (a) Experimental PE spectrum of pyrene at 27 eV photon energy (outer valence band details in the inset) (b) OVGF calculations convoluted with 0.3 eV width Lorentzian and Gaussian (solid line). The bar graph shows the pole strength for a given binding energy peak.

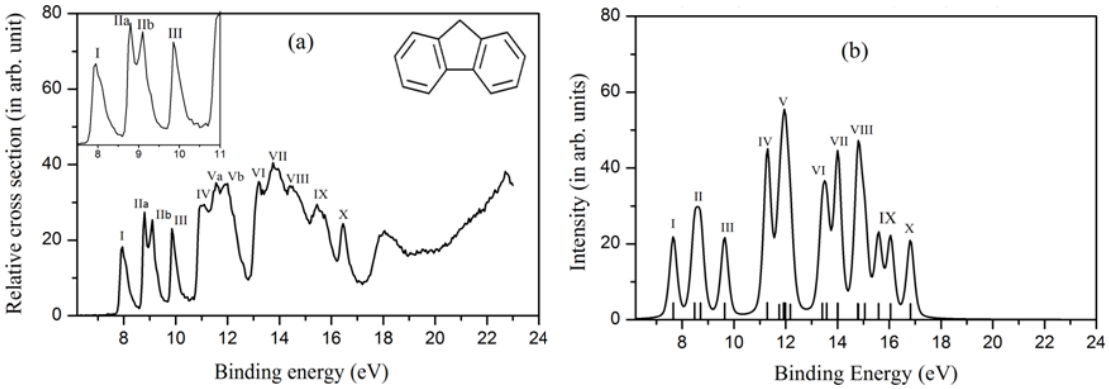

Figure 3.8: (a) Experimental PE spectrum of fluorene at 27 eV photon energy (outer valence band details in the inset) (b) OVGF calculations convoluted with 0.3 eV width Lorentzian and Gaussian (solid line). The bar graph shows the pole strength for a given binding energy peak.

energies (obtained from OVGF calculations, see table D.2 of appendix) with the measured PE spectrum binding energy. The figure shows qualitative agreement in energy as well as in intensity between theory and experimental PE spectrum. To our knowledge the theoretical fluorene PE spectrum has not yet been reported at this level of calculation. In figure 3.8a the outermost ionization line at 7.944 eV (I) originates from a π MO which is placed at 7.66 eV (i) by OVGF calculations (figure 3.8b). This peak is associated with poorly resolved vibrational transitions. The vibrational structure for fluorene is more complex due to its lower symmetry than that of pyrene where the bands are clearly resolved.

The well resolved lines at 8.80 eV (IIa) and 9.10 eV (IIb) compare well with the calculated band ii formed by two closely spaced MOs at 8.48 eV and 8.71 eV. Both MOs contribute with the same intensity in the experimental as well as theoretical PES. Band III at 9.85 eV matches well with the calculated band iii at 9.64 eV. This band is also accompanied by its vibrational progression. Band IV and following bands are well separated from band III. Band IV in PE spectrum can be attributed to a pair of MOs with almost identical binding energy originating from a_1 at 11.29 eV and b_2 at 11.28 eV (see table D.2 of appendix). Band V shows a complex substructure which can be attributed to the overlap of four MOs (v) as per OVGF with possible distortions due to shakeup processes. Band VI, VII and VIII appear to dominate the region experimentally as well as theoretically. Finally band IX and X come fairly close to the calculated values and also reproduce relative intensities with respect to preceding bands. Overall the structure observed experimentally is well reproduced as for the valence bands and the calculated band positions can be reliably associated with the measured positions.

In summary the outer valence region of our experimental PE spectrum for both pyrene and fluorene is reproduced in terms of binding energy within 0.4 eV or better with the present OVGF calculations at cc-pVDZ level. The overall agreement between

experimental and theoretical binding energy can be improved by extending the basis set in the calculations (Potts et al., 2003; Cederbaum et al., 1978, 1980). The difference due to basis set is estimated to be about 1 - 2 % by the comparison with the calculations done by Mayer et al. (2011) at cc-pVTZ level.

3.2.4 Franck-Condon simulation for vibrational progression

In this section, the theoretical calculations along with our laboratory experimental results for the vibrational progression seen in photoionization of two PAH molecules, pyrene and fluorene with photon energies between 15 and 40 eV (see section 2.2) is discussed. Experimental measurements provide necessary inputs to such theoretical models like nuclear coordinates, electronic energies and vibrational properties to a very good accuracy. These properties are essential for computing the multidimensional potential energy surfaces of the electronic states involved in the transitions. In addition, different modes of vibration give information about various types of CC and CH stretching/bending modes present in these PAHs. The strength of each mode, therefore, represents the probability of fragmentation or the breaking of a specific bond. Tan et al. (2011) recommend the use of vibronic oscillator strength instead of electronic oscillator strength to find interstellar abundance of PAHs as the latter underestimates the former by factor of 2.4. Hence it is useful to study the vibrational progression in PE spectrum.

The cationic forms of PAHs are believed to be a major carrier of the diffuse interstellar bands (DIBs) in the visible and near IR (Tielens, 2005). Some PAHs with five-membered rings like fluorene are found to be stable under stellar UV photons impact (Ekern et al., 1998). PAHs are believed to contribute to the IR emission features observed in the range of 700-3100 cm^{-1} (Duley and Williams, 1981; Leger and Puget, 1984; Allamandola et al., 1985, 1989; Léger and d'Hendecourt, 1985; Salama and Allamandola, 1992b). It is also well known that these infrared emission features are due

to the vibrational relaxation of UV-pumped PAHs (20 - 100 C atoms) (Leger and Puget, 1984; Allamandola et al., 1985, 1989). The most prominent IR emission bands are observed around 3030 cm^{-1} (CH stretch), 2941, 1613 cm^{-1} (CC stretch) and 1299, 1163, 885 cm^{-1} (CH out of plane bending) with weaker features detected at 1786 and 1439 cm^{-1} (Tielens, 2008). These spectral features vary from source to source as well as within the sources. The identification of a specific PAH and its proportion in a mixture of PAHs contributing to each band is an active area of research currently. To understand the contribution of PAHs to a particular emission band requires a knowledge of electronic and vibronic excitation energies of the individual PAH molecules as well as their oscillator strengths.

The vertical transition between neutral ground state to excited cationic vibrational state gives rise to vibronic progression in experimental PE spectrum due to a structural change. The individual transition intensity depends on the population of the initial state and the FC factor (i.e. the probability of transition). The simulation of vibronic spectra by computing overlap integrals (FC integrals) between vibrational wavefunction of electronic states involved in the transition becomes very challenging task for large molecules because of the steep increase in vibrational states with the size of the molecule. A literature survey shows that for simulation of spectra of significantly larger systems, so far, calculations of excited states have been carried out within time-dependent density functional theory (TD-DFT) (Scalmani et al., 2006; Furche and Ahlrichs, 2004; Hirata et al., 1999; Kokkin et al., 2007)) and resolution-of-the-identity approximation of coupled cluster theory (RI-CC2) (Köhn and Hättig, 2003). In addition to this, several studies investigate the vibronic transitions occurring between neutral and cationic ground electronic states for PAHs as well as other molecules (Oomens et al., 2001a,b; Piest et al., 2001; Kamisuki and Hirose, 2001; Itoh, 2005; Bini et al., 1998; Szczepanski et al., 2002). Here a vibrational assignment for the observed spectral features in simulated vibrational progression is carried out along with a description of bending and stretching

modes. A detail comparison of our theoretical results not only to laboratory experimental results but also with results from other theoretical methods is also discussed in later sections along with their astrophysical significance.

Computational details: The structure calculations were done using GAUSSIAN09 (Frisch et al., 2009). To reproduce correctly the band intensities and the extensive vibrational structure of the REMPI or Threshold photoelectron spectroscopy (TPES) type spectra, the equilibrium geometries, harmonic vibrational frequencies and normal modes in both the S_0 and D_0 electronic states for both the molecules were obtained. FC simulation is performed to calculate the vibronic spectrum of the $D_0 \leftarrow S_0$ transition at 318 K within the framework of Franck-Condon principle (Franck and Dymond, 1926; Condon, 1926, 1928) and Born-Oppenheimer (BO) approximation. The calculations were done using both HF and DFT methods to show the effect of inclusion of exchange interaction in DFT. Also the basis set dependence was studied for geometry and structure change upon removal of an electron which is significant for FC factor calculation. The structures were optimized at respective levels in which the FC factor calculations were done. The FC factors were also calculated while keeping the cationic nuclear coordinates identical to that of the neutral. This was done to check the significance of nuclear coordinate relaxation after ionization. We have used DFT at B3LYP for 6-311G and 3-21G basis sets, HF at 3-21G basis sets for both cation as well as neutral molecular geometry optimization. Different half widths at half maximum (HWHM) were used for theoretical convolution to reproduce the experimental spectrum qualitatively. No point group symmetry constraint was applied during the calculation. The inclusion of scaling factor (0.96) (Kamisuki and Hirose, 2001) for vibrational frequency calculation showed neither change in intensity nor change in peak position in the simulated spectrum. Hence the entire theoretical spectrum reported here are without any scaling factor.

According to the BO approximation, since the mass of the nuclei is significantly

larger than that of electrons, the nuclear coordinate remains constant during an electronic transition and is therefore a vertical transition. After completion of the vibronic transition, the nuclei adjust to the excited equilibrium bond length. The probability of these transitions is determined by the degree of overlap between the two wavefunctions describing the electronic states involved in the transition. The square of this overlap factor gives the FC factor for respective transitions. The present study deals with the FC factor calculation implemented in GAUSSIAN09 (Frisch et al., 2009) to simulate the resolved vibrational spectrum, is based on an integrated approach and is applicable for various targets ranging from small molecules in the gas phase to macrosystems in condensed phases, under the constraint of harmonic approximation with negligible nonadiabatic couplings (Barone et al., 2009). This simulation is within the frame work of FC and BO approximation where the Herzberg-Teller (HT) coupling (Herzberg and Teller, 1933) between electronic states due to the change in electronic potential energy as a function of nuclear coordinates is not considered by assuming that the cationic state is a ground state with a structural change upon photoionization. Hence the HT coupling is negligible for present study. Similar FC factor calculation studies for vibronic spectrum analysis using different theoretical methods and package have been done for different type of molecules including several PAHs (Bothe and Tainter, 2006; Dierksen and Grimme, 2005; Negri and Zgierski, 1994; Tan and Salama, 2005a,b; Meng and Meyer, 2013).

Results and discussion:

A. Simulation results: As stated above the change in geometry upon photoionization was seen for all the basis level of calculations by observing the geometrical coordinates like bond lengths and bond angles. This reflects into the FC overlap between the neutral and cationic ground state in a typical PE spectrum. Figure 3.9a shows the sim-

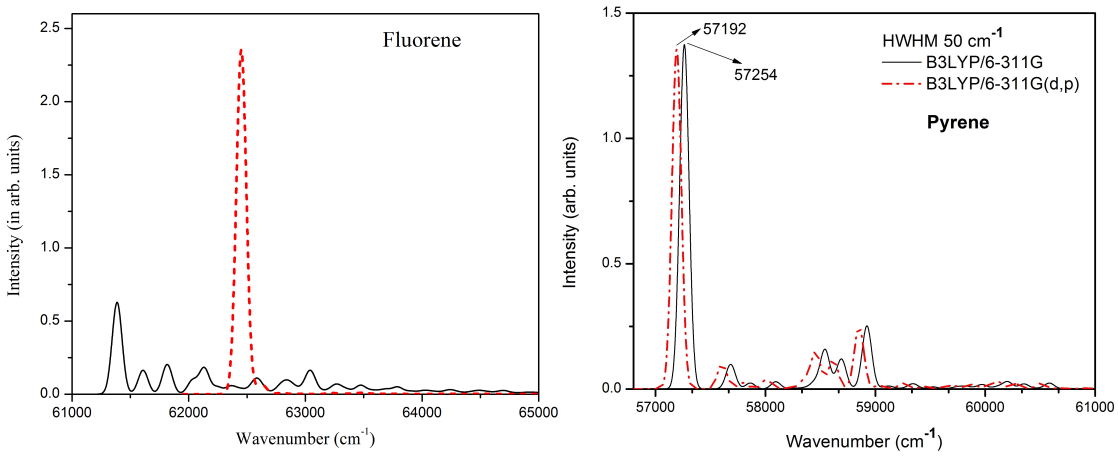

(a) (b)

Figure 3.9: FC simulated spectrum for (a) optimized cation (solid) and cation at optimized neutral geometry (dashed) of fluorene for HWHM 50 cm^{-1}, (b) pyrene with and without polarization in the basis set.

ulated vibrational spectrum calculated using B3LYP/6-311G functional with HWHM 50 cm^{-1} for fluorene as an example. As illustrated in figure 3.9a, the calculations are performed with unaltered coordinate for cation which shows that all the intensity concentrate in only $0 \leftarrow 0$ transition whereas the calculations with change in coordinate redistributes the intensity into the associated vibronic excitation.

The dependence of simulated spectrum on basis set did not show any significant difference within DFT calculation for B3LYP functional and 6-311G, 6-311G(d,p) basis sets, because the nuclear coordinates remain same. The effect of including diffuse functions or polarization functions does not improve the frequency in the case of, for example, acridine (Kamisuki and Hirose, 2001) whereas our simulation shows a linear shift of entire spectrum with intensity distribution unchanged (see figure 3.9b). (Tan and Salama, 2005a) have also shown that the vertical transition energy depends on the inclusion of polarization functions in calculation. But in our calculations, a marked dif-

ference in intensity as well as position of peaks is observed for the calculation done for both HF and DFT at the same basis level, which conveys that inclusion of exchange interaction (i.e.; DFT method) reproduces the vibrational structure both in qualitative and quantitative way efficiently (see figure 3.10). Because the vibrational mode calculation is done as a function of nuclear coordinate which depends on the potential used for the electron-electron interaction in above two methods and is proven to be influencing the vibrational mode calculation.

The theoretically calculated frequency for $0 \leftarrow 0$ transition at DFT level of calculation deviates from experimental value by 0.36 (0.34) eV for pyrene (fluorene) whereas for HF calculation this value is 1.5 (1.6) eV respectively. The experimental measurements match very closely to the highly accurate values obtained with REMPI-ZEKE and TPEPICO measurements (Mayer et al., 2011). However this deviation in band positions can be improved by employing advanced level of functional in DFT. It has been shown for phenanthrene (Piest et al., 2001) and fluoranthene (Bauschlicher Jr et al., 1999; Hudgins et al., 2000) cations that the disagreement between theory and experimental results is due to the difficulties in DFT calculated spectrum because of the strong perturbation of vibrational structure of ground cationic electronic state due to low-lying electronic states (Oomens et al., 2003). Also it has been shown that a match between theory and experiment can be achieved to a very good accuracy only by correcting the frequencies for anharmonicity (Barone et al., 2009; Oomens et al., 2001b). However our FC calculation does not take into account the anharmonicity factor because in case of photoionization the cation remains in low vibrational quantum number states and the harmonic approximation for potential remains valid. Whereas most of the study so far using ion mass spectroscopy rely on multiphoton absorption process (Zhang et al., 2008, 2010, 2011; Oomens et al., 2001a,b; Pitts and Knee, 1998) to produce a detectable signal, which makes the molecular ion to excite to a very large quantum number and therefore the structure calculations becomes more sensitive and demands the inclusion of anhar-

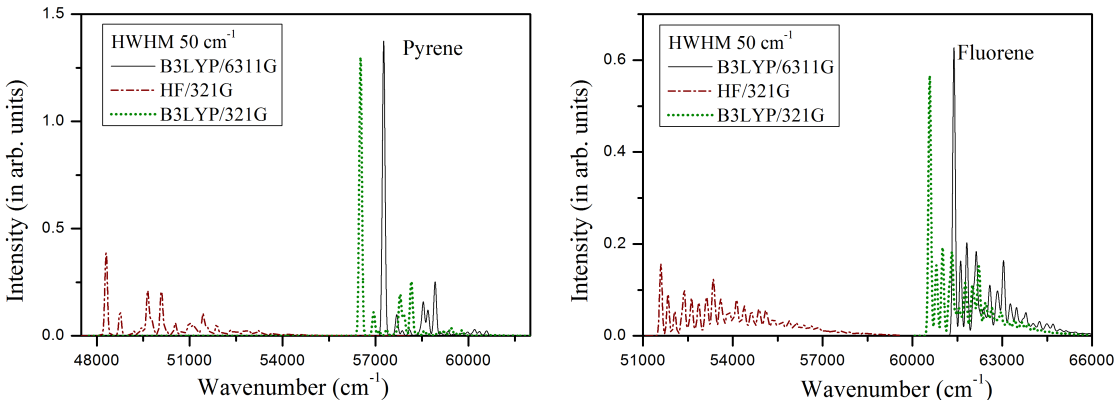

Figure 3.10: Comparison of theoretically simulated spectra for different basis set and for different method of calculation.

monicity factor to be considered. Such scenario is unlikely in real ISM environment, due to lack of such multiphoton sources as compare to the laboratory based IR sources. In addition to this Barone et al. (2009) have highlighted the fact that for a good match between theory and experiment the electronic transition should be computed within an accuracy of ~ 10 cm^{-1}.

Notably, the intensity of entire profile can be reproduced only by DFT method and is extremely poor for HF (see figure 3.10). Hence here after all the theoretical results for FC simulation reported are performed at B3LYP/6-311G unless otherwise stated.

B. Comparison of Simulated Results with Experimental PE spectrum: The vibrational progressions in HOMO band observed in the experimental PES (see section 2.2) are distinct in pyrene as compare to fluorene which can be attributed to difference in symmetry. The $1 \leftarrow 0$ and $2 \leftarrow 0$ transition intensity as compare to $0 \leftarrow 0$ transition intensity is observed to be photon energy independent (see section 2.2.2). The oscillator strengths for these vibrational transitions are well reproduced by our simulated FC factor with convolution of appropriate HWHM (470 cm^{-1}) (see figures 3.11a

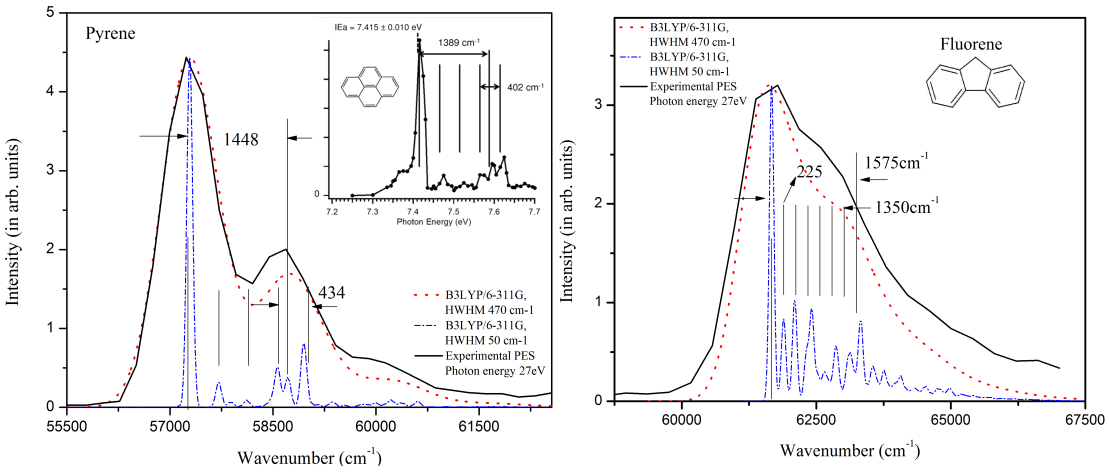

(a) Pyrene

(b) Fluorene

Figure 3.11: Experimental PE spectrum comparison with theoretical vibrational progression showing CC stretch as dominant mode. Inset shows the TPES spectrum (Mayer *et al.* 2011).

and 3.11b). The HWHM value is chosen empirically to match with experimental broadening. This broadening in experimental spectra is mainly caused by the instrumental resolution with a minor contribution from break down of BO approximation. For large molecules like PAHs and their ions, the BO approximation breaks down because of the large density of electronic states due to conjugated electronic system in small energy range. These compact energy states lead to strong perturbations such as vibronic and spin-orbit interaction which gives rise to the broadening of the spectrum.

In figures 3.11a and 3.11b the theoretically calculated vibration progression is shown along with the experimentally observed one for pyrene and fluorene in our experiment and they compare very well for the convoluted spectrum with HWHM 470 cm^{-1}. The oscillator strength for these vibronic transitions is well reproduced. Due to poor instrumental resolution in our experimental PE spectra ($\sim$ 50 meV), the vibrational progression as seen in TPES study by (Mayer et al., 2011) is not well resolved in our study. But

our FC simulation represents the TPES vibrational spectrum very well with a quantum of 434 cm^{-1} upto υ = 4 (Mayer et al., 2011) for pyrene. These represent the longitudinal stretching mode in plane of the molecular skeletal observed in (1+1′) REMPI-ZEKE experiment with $\upsilon_{13}(a_g)$ = 410 cm^{-1} (Zhang et al., 2010). In the simulated vibrational progression of pyrene, the most dominant component at 1448 cm^{-1} represents the CC trans-annular stretching in plane mode with a_g symmetry (Mayer et al., 2011) which is shown by Vala et al. (1994) in IR multiphoton absorption measurements at 1450 cm^{-1} and also visible in He I photoelectron spectrum at 1400 cm^{-1} (Boschi et al., 1972). The increase in intensity of υ = 4 and υ = 5 band is due to the influence of this strong component in PE spectrum.

Figure 3.11b shows vibrational progressions with quanta of 225 cm^{-1} for the theoretical spectrum convoluted with HWHM 50 cm^{-1} for fluorene. Like pyrene it does not show any longitudinal stretching mode of vibration. The dominant components in the theory spectrum are at 225, 450, 675 cm^{-1} band which represent the in-plane bending of hexagon rings, out of plane bending of carbon skeleton and CH bond respectively. The 1058 cm^{-1} band was observed neither by our simulation nor by the DFT calculation done by Oomens et al. (2001a) to produce the IR spectrum whereas experimentally it was observed prominently in free electron laser (FEL) experiment. The 1125 cm^{-1} component is due to antisymmetric breathing of the two aromatic rings and in-plane CH bending (Oomens et al., 2001a) which is at 1149 cm^{-1} position in multiphoton absorption experiment (Oomens et al., 2001a) and at 1100 cm^{-1} for He I PES studies on PAHs (Boschi et al., 1972). A strong and overlapping band in the CC stretch region near 1575 cm^{-1} is observed which appears at 1500 cm^{-1} in the multiphoton absorption experiments with intense narrow-band infrared light of a FEL (Oomens et al., 2001a), which is possibly arising from CC stretch/CH in plane bend modes . But our experimental spectrum for fluorene shows an agreement with the component at 1350 cm^{-1} which again represents the typical vibrational mode for PAHs corresponding to the CC trans-

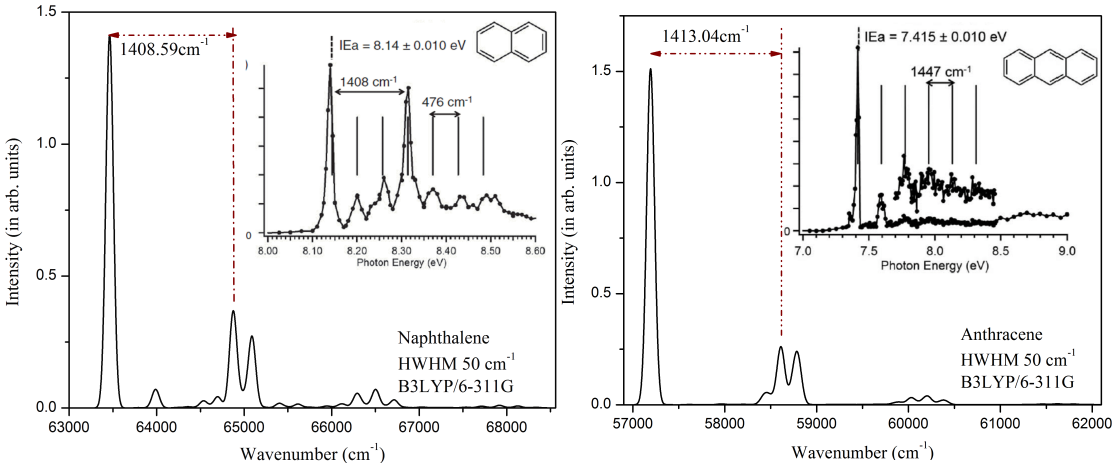

(a) Naphthalene (b) Anthracene

Figure 3.12: Theoretical simulation of vibrational progression showing CC stretch as dominant mode. Inset shows the TPES spectrum (Mayer *et al.* 2011).

annular stretching in-plane mode with a_g symmetry (Mayer et al., 2011). It is shown that unlike other PAH ions, the members of PAH family (particularly fluorene, fluoranthene) which contain five member ring show a strong absorption feature near 1000 cm^{-1} (Hudgins et al., 2000; Bauschlicher Jr et al., 1999; Oomens et al., 2001a) whereas for others it is around 1500 cm^{-1} (CC stretching and CH in-plane bending) and around 700 cm^{-1} (CH out of plane bending) (Oomens et al., 2003, 2001a). The two bands at 900 and 1125 cm^{-1} observed in our theory spectrum matches with the values reported by Oomens et al. (2001a) and is due to antisymmetric breathing of the two aromatic rings and in-plane CH bending, respectively.

The calculation is extended to two more planar PAHs namely naphthalene and anthracene. FC simulations have successfully reproduced the high resolution vibrational progression obtained from TPES results shown by Mayer et al. (2011). The intensity of bands is not mimicking well with the TPES results for naphthalene whereas anthracene

shows a very good agreement (see figures 3.12a and 3.12b). A CC-trans-annular stretching activity and skeletal longitudinal stretching at lower frequency (both the modes are characterised by in-plane mode of a_g symmetry) are observed for TPES (Mayer et al., 2011) and He I PES (Boschi et al., 1972) study for most of the PAHs. However Meng and Meyer (2013) have reported simulated vibrational spectrum with the help of multilayer multiconfiguration time-dependent Hartree (ML-MCTDH) as well as MCTDH method which reproduce the band position and intensity of gas phase PE spectra for naphthalene and anthracene very accurately.

C. Astrophysical Implications: In the stellar environment like reflection nebulae, planetary nebulae, HII region, active galactic nuclei, the PAHs do survive though continuously interacting with harsh UV radiation in the surrounding of stars and other nebulae. The photoexcited neutral as well as ionic PAHs can undergo relaxation *via* two channels: either by IR emission or by fragmentation. Since PAHs need very high internal energy for destruction ($\sim$ 10 eV for small PAHs (Allain et al., 1996)) and due to extremely low collision rate in ISM, the relaxation mechanism prefers the former path (Allamandola et al., 1989; Jochims et al., 1994). The IR emission obtained from NGC 7027 and Orion Bar nebulae is characterized by different excitation mode which is related to CC and CH stretching/bending modes of these molecules (Tielens, 2008; Snow et al., 1998). Among the PAH ions, the radical cations of naphthalene (Salama and Allamandola, 1992b, 1993; Szczepanski and Vala, 1993), anthracene (Szczepanski et al., 1993; Szczepanski and Vala, 1993), pyrene (Salama and Allamandola, 1992a, 1993; Szczepanski and Vala, 1993) and perylene (Szczepanski and Vala, 1993) have been found as strong candidates for the DIB carriers. The band widths of DIBs vary from 2 to 130 cm^{-1} (Tan and Salama, 2005b). Hence the distribution in band widths observed in DIB will provide the signature of specific PAH species. Laboratory IR spectroscopy studies have been done for cationic PAHs by several groups (Oomens et al., 2001a,b,

2003). Thus a detail theoretical and experimental study for UV photoionization helps in understanding the mechanism behind the stability and role of their photofragmentation dynamics in physics and chemistry of ISM. Also more experimental and theoretical work is needed on different PAHs. Therefore to mimic astrophysical relevant environment such as low density and high temperature, the gas phase study of molecules becomes essential. The thermodynamics and spectroscopic properties of PAH species have been studied for many years (Birks, 1970; Klessinger and Michl, 1995). Infrared spectroscopy for PAHs has been done in past by several experimental techniques like matrix isolation spectroscopy (MIS), infrared multiple-photon dissociation of trapped ions (MPD), dissociation spectroscopy of ionic PAH van der Waals clusters (VDW) and infrared emission (IRE). These IR bands were studied theoretically by including anharmonicity parameter by Oomens et al. (2003) and others (Barone et al., 2009).

3.3 *Monte Carlo* simulation for ion-molecule collisions

Theoretical calculation and modeling for the dynamics of ion-molecule collisions is very complex as it involves numerous processes occurring simultaneously such as direct (multiple) ionization, fragmentation, inner shell ionization preceding Auger effect, autoionization, transfer ionization and electron capture process. For intermediate velocity projectile collision, the energy deposited into the molecule due to a light ion like proton is dominated by electronic processes; the electronic stopping power is much larger than the nuclear one. In ion - molecule collision experiments, two things are not controlled: the impact parameter (distance of closest approach between the incident projectile and the target molecule) and the molecular orientation. And hence the site and amount of energy deposited into the molecule cannot be controlled experimentally. So the knowledge regarding amount of energy deposition can be obtained only from the degree of ionization/fragmentation of the target molecule. The projectile can transfer varied amount of

its kinetic energy depending on the nature of interaction whether direct ionization or electron capture or transfer ionization. The fragmentation dynamics depends upon the coulombic interaction between projectile and target, and hence on the energy transfer into the molecule. In collision induced dissociation, the energy gained by the system can only be determined by estimating the average energy deposited into the molecule unlike the photoionization mass spectrometry (PIMS) (Jochims et al., 2005), where the excitation energy of the systems upon photon absorption is well defined and gives very accurate estimate of the appearance energy of a specific fragment. Therefore, actual measurement of the initial internal energy of a fragmented system becomes a complex task in many experiments. For all atomic targets and few molecular targets such as C_{60}, the impact parameter treatment of energy loss is possible analytically due to spherical geometry (Kabachnik et al., 1997, 1998; Reinköster et al., 2001; Schlathölter et al., 1999a,b). However, this is difficult for non-spherical molecules like naphthalene, nucleobases etc. The motivation behind this work is to simulate the ion-molecule collision processes using existing theoretical framework that can be applied to complex multi-electron systems, such as moderately large molecules and clusters. To this end, we have implemented the *Monte Carlo* (MC) method in combination with the Local plasma or Local (electron) Density Approximation (LDA) to calculate the electronic energy loss. The LDA is a well known approach in stopping power for solid targets (Lindhard and Scharff, 1953; Lindhard and Winther, 1964).

The reported work in this section compares the fragmentation yields of our experimental results for naphthalene and the existing experimental results for nucleobases with the calculated electronic energy loss using LDA model (Lindhard and Winther, 1964). Although the impact of proton with fullerene and members of PAH family, namely anthracene has been studied (Reinköster et al., 2001; Postma et al., 2010; Martin et al., 2012; Bordenave-Montesquieu et al., 2001; Reinköster et al., 2003), we investigated the effect of such collisions on naphthalene to test the validity of LDA and electronic

stopping approximations. Naphthalene fragmentation yield trend is successfully reproduced with the help of our MC simulation within LDA and the calculations are extended to nucleobases. The ionization and fragmentation processes in the higher velocity ($v >$ 1 a. u.) are governed mainly by electronic energy loss when compared with the nuclear energy loss. Therefore, nuclear energy loss contribution is ignored in the reported calculations.

3.3.1 Local density approximation model

In the energy range under consideration, the recoil energy of the projectile is negligible compared to the net energy deposited in the molecule (Cocke and Olson, 1991). Therefore, to a good approximation, the energy loss of a projectile ion is equal to the energy deposited by it. In the present case, the target is considered equivalent to a free electron gas (Lindhard and Winther, 1964) and electronic energy loss is calculated by using LDA together with the linear response dielectric formalism (Lindhard and Winther, 1964). The LDA approach (Lindhard and Scharff, 1953) considers each volume element of the target at a given position "*r*" as an independent electron plasma of uniform density ρ = $\rho(r)$, where $\rho(r)$ represents the electron density of the molecule. The average energy loss is estimated using the stopping power of an electron gas and this loss is integrated over the path (Bonderup, 1967; Rousseau et al., 1971; Xu et al., 1984). The electron stopping power, in turn, is a function of $\rho(r)$ and v (velocity of ion). As LDA uses only the target ground state electron density, this approximation can be applied to molecules as well. Further, the projectile ion is equivalent to a point charge (Cocke, 1979) traveling with a constant velocity v through the electron gas of the target. We calculate the mean energy loss $E(b)$ (Lindhard and Scharff, 1953) of the projectile ion (where b is the impact parameter) as a line integral along the trajectory. This is because energy loss is considered as a statistical process according to the Russek-Meli-Cocke model (Cocke,

1979; Russek and Meli, 1970).

The total electronic stopping is given by

$$E(b) = \frac{4\pi {Z_1}^2}{v^2} \int_{-\infty}^{\infty} dz \rho(r) L(\rho(r), v) \tag{3.2}$$

where $L(\rho(r), v)$ is a function of $\frac{v}{v_f(r)}$ and the projectile of charge Z_1 is traveling along the Z-direction. $v_f(r)$ is the Fermi velocity for the local electron gas and is given by

$$v_f(r) = 3\pi^2 \rho(r)^{1/3} \tag{3.3}$$

3.3.2 Computational details

To estimate the energy transferred to the target molecule from the projectile ion due to coulombic interactions (in terms of electronic stopping), we have used the LDA model developed by Lindhard and Scharff (1953); Lindhard and Winther (1964) in our MC simulation. This model has also been used for ion-atom (Kabachnik et al., 1997) and ion-molecule collisions (Kabachnik et al., 1998). This analysis is applicable to a large energy range, several keV to several MeV per atomic mass unit (amu), where the collision time is shorter (10^{-16} - 10^{-17} s) than the vibrational or rotational time scales (10^{-13} s or longer) (Kabachnik et al., 1998; Rentenier et al., 2003). As a result, the simulation has been carried out for a fixed orientation of the molecule as well as for fixed internuclear coordinates, thus making it suitable for interpretation of the present experimental results. Kabachnik et al. (1998) have studied the variation in energy deposition as a function of orientation of the target molecule. They have also calculated the energy transferred to the molecule as a function of impact parameter for a fixed orientation. In our case, we have performed *Monte Carlo* simulations (see appendix A for the program) to incorporate the effect of all possible orientations. Since the projectile ions, particularly protons, have a high velocity and low charge state, the screening of the projectile

charge is not considered. The internuclear coordinates are taken from an optimized geometry. In addition, it is assumed that the removal of electrons is faster than the nuclear motion and slower than the collision time. Hence electronic stopping is considered as the main contributor to the energetics of the collision process. The amount of energy deposited into the molecule is the energy loss of the projectile with an approximation that the recoil energy of the projectile is negligible compared to the net energy deposited in the molecule (Cocke and Olson, 1991) under the studied projectile velocity regime. Thus the energy loss of projectile is considered to be equal to the energy deposited into the internal degrees of freedom of the target. The energy transferred leads to excitation and ionization of target molecules. Since numerous ionization and fragmentation channels are present, a statistical approach is more appropriate when compared to a detailed quantum-mechanical treatment of individual processes.

A wide range of projectile velocities (in intermediate range) are investigated here to estimate the energy deposited by the projectile ion in the molecule. A similar calculation using a different model has been carried out for anthracene (using only valence electrons) with H^+ and He^{2+} projectiles (few keV) (Postma et al., 2010). Similarly, for collision of fullerene with He^+ ion (Schlathölter et al., 1999a,b; Hadjar et al., 2000), an inelastic energy loss approach has been used.

Monte Carlo simulations were performed for random trajectories of projectile ions. The randomly generated trajectories pass through a non-uniform electron density distribution representing the target. In this LDA method, each volume element of the electron density contributes to the energy loss independently and the total energy loss is sum of all these contributions. We neglect the deceleration of projectile ions along their trajectories as well as the coulomb deflection of these ions in the field of the target nuclei.

We have considered the total electron density as the input for LDA model, rather than the density of the valence electrons alone as the magnitude of the projectile ve-

locity is close to that of the velocity of the inner most electron of the target molecule. The effect of this inclusion is briefly dealt with in section 3.3.3. The target electron density (for naphthalene and nucleobases as an additional test case) was determined quantum mechanically using the DFT in conjunction with B3LYP basis. This density was computed with the help of GAUSSIAN09 (Frisch et al., 2009). The geometry for naphthalene and nucleobases are optimized at the 6-311G (2d, p) basis set while incorporating the respective planar symmetry point group. The total electron density was computed using the same basis level. As a convention, we consider the plane of the molecule to be in XY plane, with the longer axis of the molecule in the X-direction.

In the MC simulations, two methods have been used in order to generate the random trajectories of the projectile: i) From all directions, to compare with and understand the experimental results, and ii) plane-wise, to understand the behavior of electronic stopping according to the elemental composition and geometry of the molecule. Simulations for a given collision system are performed for 10^7 random linear trajectories. The individual plane-wise interaction strongly correlates with the structure of the molecule (see figure 3.13b).

3.3.3 Ion-PAH collisions

Generally, electron or photon impact mass spectroscopy measurements on PAHs are dominated by single or multiple ionization while fragmentation channels remain dormant. On the other hand, in ion-PAH collisions, fragmentation channels play a prominent role due to substantial energy deposition in the electronic and vibrational modes. Therefore, theoretical modeling for such collision processes is a complex task. Electron impact studies on PAHs, in particular naphthalene (Wacks and Dibeler, 2004; Van Brunt and Wacks, 2004), have also been carried out. There has also been experimental investigation into interactions of low velocity and high charge state ions with PAHs other than

naphthalene (Postma et al., 2010; Ławicki et al., 2011; Holm et al., 2010; Johansson et al., 2011; Martin et al., 2012). In these cases, large impact parameter processes are dominated by multi-electron transfer followed by coulomb explosion. The low charge state projectile collisions, on the other hand, give rise to thermal excitation causing gentle fragmentation. Electronic stopping has been demonstrated as a prominent heating process responsible for (single and multiple) electron removal in low energy (keV) collision of He^{2+} ions with anthracene monomers (Postma et al., 2010). The proton-PAH collisions reported so far have been carried out at much lower projectile velocities ($v <$ 1 a. u.) (Postma et al., 2010; Ławicki et al., 2011). The velocity range probed here for proton projectile is from 1.41 to 2.68 a.u. (i.e. 50 to 180 keV).

***Monte Carlo* simulation results and discussion:**

A. Electronic stopping distribution: Figure 3.13a illustrates the electronic stopping for random linear trajectories of the projectile ions interacting with naphthalene electron density. The mean energy loss decreases with increasing projectile velocity. This explains our experimental mass spectrum fragmentation yield as a function of projectile velocity for direct ionization mode, as shown in figure 2.10. Figure 3.13b displays the simulated electronic stopping of 50 keV (v = 1.414 a.u.) protons impinging normal to the XY, XZ and YZ planes on the naphthalene molecule. The maximum stopping ($\sim$ 178 eV) is for collision along the longer axis of the molecule (i.e. YZ impact) although the theoretical cross section offered in this plane is minimum. The impact in the XY plane, on the other hand, offers $\sim$ 3 times lower electronic stopping than the former. However, the probability of higher energy loss decreases rapidly after a pronounced peak. This peak in the electronic stopping spectrum is due to a large number of trajectories experiencing similar electron density. This prominent energy loss value is the result of a specific range of v_f / v (where v_f is the Fermi velocity) occupying a

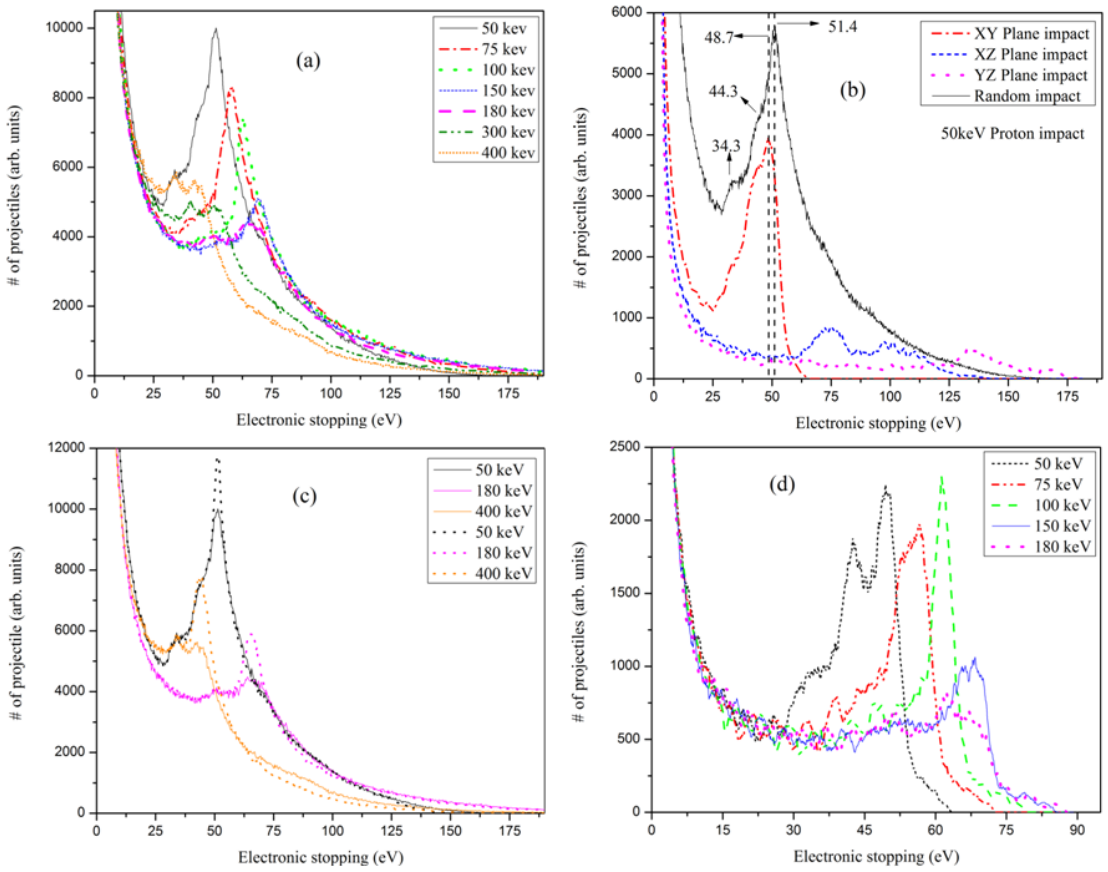

Figure 3.13: Mean energy loss calculation with naphthalene as target using *Monte Carlo* simulation for (a) randomly generated proton projectiles of different energies, (b) 50 keV proton projectile for random and plane wise impact. The numbers indicate electronic stopping value in eV for specific features, (c) randomly generated proton projectiles of different energies showing a comparison of with (solid line) and without (dotted line) inclusion of K-shell electron density, (d) randomly generated proton projectiles of different energies along Z-direction with naphthalene molecule placed in XY plane.

large area in XY plane. This varies with a change in the projectile velocity leading to a shift (and decrease) in the peak intensity for higher projectile velocities. However, the XY plane does not correspond to the maximum stopping because the mean electronic stopping is an integral of the projectile path for ions at all impact parameters *b* and orientations encountering the target. This also explains the maximum stopping appearing from the YZ plane impact. As an example, we consider here the energy loss from a 50 keV proton projectile. The distribution of impact energies in the XY, XZ and YZ planes are as high as 65, 143 and 183 eV, respectively. The energy loss peaks appear at 34, 42 and 49 eV for XY plane; 75 and 103 eV for XZ plane; and 136 eV for YZ plane (see figure 3.13b). The energy loss peaks for random trajectories are close to the peaks corresponding to the XY plane impact simulation as this plane offers the maximum geometrical area to the projectile ions. In addition, impact in this plane causes multiple peaks that can be attributed to a variation in electron density due to the contributions from CH and CC bonds in the molecule. The calculation with and without the inclusion of K-shell electron density is performed while maintaining the treatment of K-shell electron density in formulation identical to outer electron density as used within LDA. Exclusion of the *1s* electron density of carbon atoms causes a much sharper peak in the energy loss distribution (see figure 3.13c). This is because an interaction with these inner shell electron shifts some of the trajectory population from the peak region to the higher energy loss region in the rapidly falling part of the distribution.The broadening and shifting of peak positions in the electronic stopping curve from planar to random orientation is due to oblique trajectories. The distribution of electronic stopping for different velocities of proton projectile obtained from simulations (for impact in the XY plane) is shown in figure 3.13d. The energy loss peak shifts towards higher values of electronic stopping with increase in projectile velocity. The origin of the peaks in the spectrum can be explained on the basis of the following: (i) longer path integral of trajectories of those projectiles that interact with the valence electron density, spanning a

large fraction of molecular volume, (ii) short trajectories encountering a dense region that comprises a small fraction of molecule. Therefore, a change in velocity of projectile ions will lead to a change in intensity of the peak, particularly for the interactions with the valence electron density. Fast projectiles either need lower impact parameter collisions or longer interaction path compared to their slower counterparts to deposit a similar amount of energy into the molecule. The contour plot of electronic stopping for projectile impact normal to the molecular (XY) plane, with energy of 50 keV, is displayed in figure 3.14. The variation of energy loss over the total molecular volume due to non-uniform electron density is clearly discernible. Figure 3.14 also shows that the maximum electronic stopping is experienced by those projectile ions that encounter inner shell electrons where the electron density is relatively high around the carbon nuclei.

B. Comparison with fragmentation yield of proton-naphthalene collision: The yields of ionization/fragmentation peak in mass spectrum depend on the species, charge, and velocity of the projectile ions. The yield of fragments with smaller number of C atoms ($n < 5$) decreases with projectile velocity as the deposition of energy into the molecule is less (figure 3.15a). Similar conclusions have been drawn from the fragmentation distributions at low velocity (0.1 to 1 a. u.) He^+ - C_{60} collision (Schlathölter et al., 1999a) and proton-anthracene collision with $v < 1$ a. u. (Postma et al., 2010). The proton impact on naphthalene shows a disparity in fragmentation yields when compared with electron impact studies (Wacks and Dibeler, 2004; Van Brunt and Wacks, 2004). The only similarity with electron impact studies lies in the fact that a major part of ionization comes from singly charged parent ion and H^+ ion. But the number of ions formed due to the rupture of a ring and the subsequent loss of a neutral fragment is negligible in the case of electron impact (Wacks and Dibeler, 2004; Van Brunt and Wacks, 2004). Fragmentation being a violent process requiring much higher energy de-

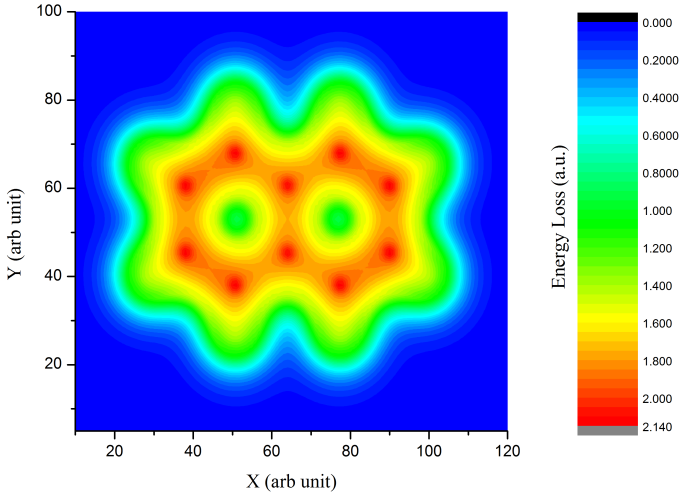

Figure 3.14: Contour plot for the calculated mean energy loss for random collision of 50 keV proton impinging on the naphthalene molecule placed in XY plane. The color scale represents the magnitude of electronic stopping.

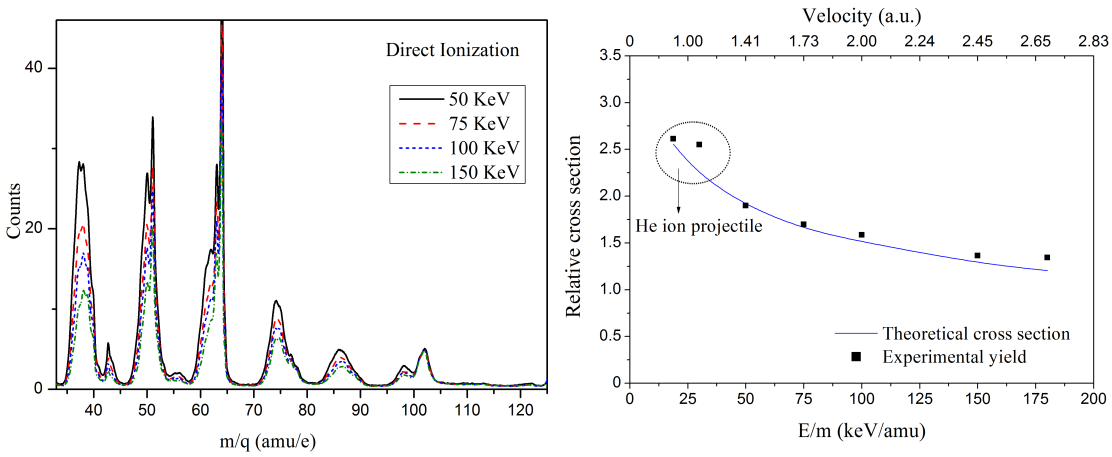

(a) (b)

Figure 3.15: (a) Mass spectra of EE mode normalized to parent single ionization peak area for different proton projectile energies (b) Relative experimental (black square) and theoretical (solid line) cross sections for multifragmentation.

position as compared to that of evaporation processes (discussed in section 2.1) which can be achieved by more localized energy loss to the target as the projectile traverses through the target volume. Of all the proton beam energies considered in our proton-naphthalene collision experimental study, the least fragmentation is due to the 180 keV proton beam as the energy deposited is the lowest. A careful comparison of yields of all the fragment ions at 180 keV proton collision with those of electron impact (Wacks and Dibeler, 2004; Van Brunt and Wacks, 2004) shows that, in our case, fragmentation yields are higher.

In this discussion, we scrutinize the behavior of fragmentation pattern for the electron emission mode over experimentally investigated proton projectile velocities (figure 3.15a) with the help of our MC simulations. The fragmentation yields observed in our naphthalene mass spectra decrease with increase in velocity (figure 3.15a), indicating a decrease in energy loss with increasing velocity. The fragmentation yields of high velocity interactions are analyzed on the basis of mean energy loss obtained from our MC-LDA simulations. As shown in figure 3.13a, the 50 keV proton projectile deposits the maximum energy in the molecule. Further, the decrease in energy loss with increase in projectile velocity is also observed in the simulations. Consequently, the probability of fragmentation decreases.

A comparison between experimental fragmentation yields and our simulations is shown in figure 3.15b. Measurements of photon impact with naphthalene show that the fragmentation is appreciable if the total energy deposited is in excess of 20 eV (West et al., 2012). Our MC-LDA simulated energy loss distribution shows a clear valley at $\sim$ 25 eV. Hence, we have selected 25 eV as a lower cut off to energy deposition that causes fragmentation. The fraction of trajectories in figure 3.13a depositing energy more than this value ($\sim$ 25 eV) is used to calculate the theoretical cross sections. The area under the peak has been obtained from the experimental mass spectrum. The fragmentation

yields have been estimated using equation 3.4, after normalization to the area under C_2H_2 loss and parent ion peaks while taking into account the ion detection efficiency.

The fragmentation yields were calculated from the area integrals as follows,

$$\sigma_f = \frac{\sum_{n=1}^{8} \int {C_n}^+}{\int {C_{10}}^+ + \sum_{n=1}^{8} \int {C_n}^+} \tag{3.4}$$

where σ_f is the total fragmentation yield, *n* is the number of carbon atoms, ${C_n}^+$ is the yield of the fragmented ion containing *n* number of carbon atoms (corrected for ion detection efficiency). No measurable contribution is seen from ${C_9}^+$ fragmentation channel. Since C_2H_2 evaporation is one of the lowest energy channel, it dominates over loss of single C fragment.

In our analysis, we have considered the nuclear energy loss or elastic terms to be negligible in the present system (Reinköster et al., 2001). From figure 3.15b, we see that model calculations agree very well with the experimental results. In order to understand this agreement, we consider alternative excitation mechanisms that can contribute to the experimental fragmentation yields. This is because the fragmentation could arise from multiple processes, like capture/ionization from carbon K-shell or coulomb explosion of multiply charged unstable cations. The capture/ionization from K-shell, however, is not feasible as the values of cross sections in the present velocity regime are negligible. The multiple ionization cross sections decrease by an order of magnitude or more as we go to successive ionization states (figure 2.7). As the single ionization or evaporation peaks are observed to be quite narrow, the broad fragmentation peaks (seen in figure 3.15a) have been used to estimate the fragmentation yields. These peaks have a major contribution from doubly charged cations. Therefore, the lower cut-off used to estimate theoretical cross sections from figure 3.13a match the energy favorably. Note that this cut off includes a double ionization threshold of 21.45 eV along with some excess energy to cause fragmentation. This explanation assumes that the lifetime of a

dication produced with negligible internal excitation is much larger than the present ToF range (Leach, 1989). Therefore, the sole process causing double ionization followed by fragmentation is the electronic energy loss that is well above the double ionization.

As reported in the past, collision of proton and He^{2+} (at few keV) with anthracene leads to substantial fragmentation with only $\sim$ 15 eV electronic stopping (Postma et al., 2010). On the other hand measurements of actual excess internal energy deposition by Martin et al. (2012) on anthracene shows that various evaporative processes dominate at 15 eV excess energy in the molecule whereas the multifragmentation contribute negligibly. It is well understood that such evaporative processes occur at much lower internal energy than the multifragmentation processes (section 2.1.2.1C). Our present simulation carried out with naphthalene shows that $\sim$ 52 eV internal energy is deposited for a 50 keV proton projectile (see figure 3.13a). This projectile energy (50 keV) gives the maximum fragmentation yield in our experiment (see figure 3.15a) among all the proton velocities. Further, we see fragments with higher m values in C_3H_m fragment yield, as these are highly influenced by variation in the internal energy deposition (see figure 3.15a) as compared to the H^+-anthracene collision system (Postma et al., 2010). Thus our results are more consistent with the actual energy deposition measurement (Martin et al., 2012) than the energy deposition simulated by Postma et al. (2010).

It has been shown by PEPICO experiments on naphthalene with photon energies up to 20 eV (West et al., 2012) as well as by PIMS for PAHs (Jochims et al., 1997), that 20 eV is the threshold for initiation of fragmentation in naphthalene. It has also been shown that single electron capture by proton projectile deposits $\sim$ 20 eV internal energy into naphthalene due to resonant capture of inner shell valence electron (with binding energy of 12 to 14 eV) to the *n = 1* state of the proton, and the excess energy due to electronic energy loss occurring concurrently (section 2.1.2.1D). Figure 3.16 shows that the electron emission mode deposits more energy than the single electron capture mode.

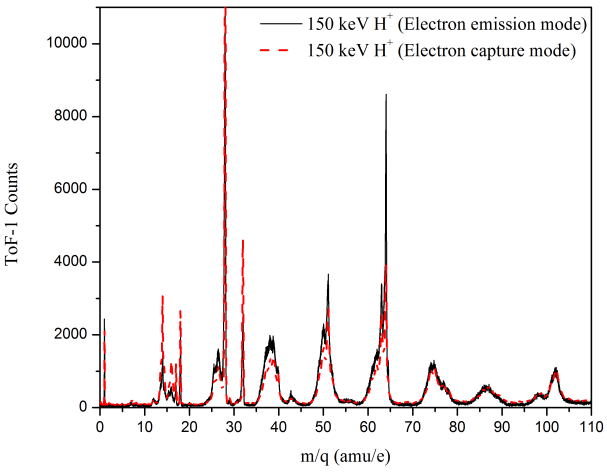

Figure 3.16: Mass spectrum of EE (solid black) and EC mode (dashed red) normalized to C_7 mass region for 150 keV proton projectile.

Thus the value predicted by our LDA based model ($\sim$ 52 eV) is consistent with the lower end of the internal energy deposition reported in the literature. The minor overestimation of energy loss could be because the screening of projectile nuclear charge by dynamic screening has not been considered in the present theoretical model (Kabachnik et al., 1997; Lindhard and Winther, 1964).

C. Comparison with fragmentation yield of He-naphthalene collision: effect of charge state equilibration: Here, we compare the experimental results on He-naphthalene collision (obtained from the same experimental set up with similar conditions for mode of detection as described in section 2.1.1) with electronic stopping results from LDA implemented MC simulations. Figure 3.17a displays the second hit of the mass spectrum normalized to a higher mass C_7 - peak yield in order to compare the fragmentation yields. Such a normalization is necessary as the fragmentation distribution shifts towards lower mass with increase in energy transfer to the molecule. This shift, therefore, would be independent of any efficiency correction or normalization. Further, energetic singly charged naphthalene ions could be produced by several active

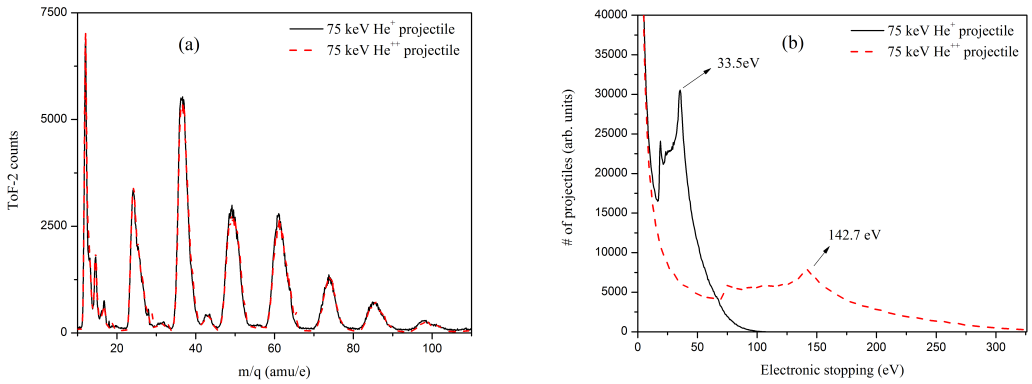

(a) (b)

Figure 3.17: (a) Mass spectrum for second hit in electron emission mode normalized to C_7 mass region for 75 keV He^+ (solid black) and He^{++} (dashed red) projectile (b) *Monte Carlo* simulation for mean energy loss calculation by randomly generated trajectories for He^+ (solid black) and He^{++} (dashed red) at 75 keV projectile energy.

channels (because of higher charge state and lower velocity projectiles). These, in turn, will contribute to the fragmentation yields. A comparison of second hit data excludes contributions from such processes. Therefore, we focus on the second hit data for the He-naphthalene collision analysis due to difficulties in normalization of first hit mass spectrum.

From figure 3.17a, we see that the fragmentation yield is independent of charge state for He projectile at 75 keV (0.866 a.u.). However, our model calculations for electronic stopping show $\sim$ 4 times more energy transfer to the molecule by He^{++} than by He^+ projectile (see figure 3.17b). This difference cannot be explained by a low velocity model using friction coefficient where the energy deposition scales linearly with velocity for proton collision with anthracene (Postma et al., 2010). The failure of high and low velocity models is due to comparable strengths of electron capture and ionization processes in the velocity regime close to $v = 1$ a. u. Close to this velocity, the modeling

of ion-molecule collisions becomes more complex and is not very reliable quantitatively. From an experimental point of view, the capture cross section for doubly charged projectile ions is higher than the ionization cross section in such case. Therefore, a He^{++} ion can capture an electron at substantially longer distance and result in a He^{+} projectile. The classical over-the-barrier (COB) model estimates the single electron capture distance to be 13.09 and 10.26 a.u. for He^{++} and He^{+}, respectively (Bárány et al., 1985). The latter is comparable to the experimentally observed dimension of naphthalene molecule of about 11.74 a.u. (Long et al., 2008). It has been shown that the total electronic stopping is the sum of electronic stopping obtained for different He charge states weighted by the equilibrium charge state distribution (Arnau et al., 1990). For 75 keV He ions, the equilibrium charge state distribution has almost equal contribution from neutralized and singly charged He ions with very small fraction in doubly charged form (Arnau et al., 1990; Peñalba et al., 1991). Rentenier et al. (2008) have studied the He^{++} collision with C_{60} at a wide range of energies (0.1 to 250 keV) and have explained the trend in cross sections. They show that the cross sections for the formation of He^{+} and He^{0} are comparable in magnitude. This cannot be explained by single and double electron capture alone and requires contribution from transfer ionization processes which are significant even at low impact energies. Therefore, a detailed analysis of fragmentation pattern of He interaction with naphthalene in the $v \sim 1$ a. u. regime is inexplicable solely on the basis of electronic excitation so far. This indicates that capture induced excitation of the molecule needs to be considered for a successful understanding of the fragmentation dynamics and energetics. At these impact energies, all electronic processes (electron capture, ionization, and excitation) are faster than fragmentation (Bréchignac et al., 2002).

D. Electronic stopping calculation for some more PAHs and their derivatives: Figures 3.18a and 3.18b shows the MC simulation result of mean electronic stopping

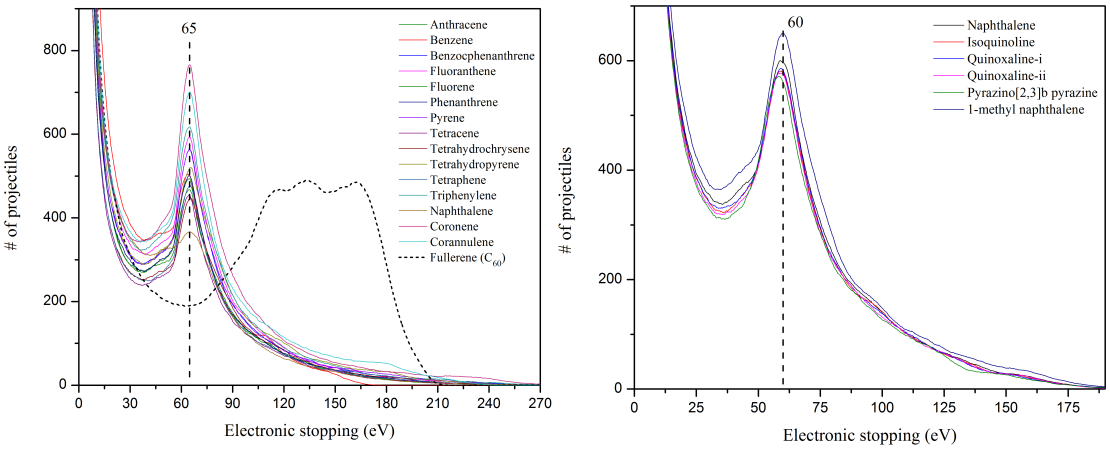

(a) (b)

Figure 3.18: *Monte Carlo* simulation for electronic stopping distribution for interaction of proton projectile of energy (a) 100 kev with PAHs, (b) 80 kev with naphthalene derivatives.

distribution for 10^6 randomly generated 100 keV proton trajectories interacting with different PAHs and PAH derivatives. As we see that the distribution varies only for C_{60}, which has very different symmetry (icosahedral) and structure than others.

3.3.4 Ion-nucleobase collisions

The radiation induced damages in biomolecules could be direct or due to the secondary particles like low energy secondary electrons and ions produced along the track of radiation during the interaction with target (Michael and O'Neill, 2000). It is shown that the single and double strand breaks in supercoiled DNA are caused by electrons between 3 and 20 eV (BoudaıÌĹffa et al., 2000). In addition to this the understanding of the energy deposition due to the projectile beam in the biological environment bears primary significance in medicine and more specifically in cancer therapy where the need of delivering highly localized doses using focused ion beams within tumors by avoiding damage to

the surrounding normal tissue is very crucial. In proton therapy, the incident energy ranges from 10 to 250 MeV and this beam experiences a severe deceleration within the target medium, and deposit a large dose at a given depth, in a well-defined volume, i.e. the so-called the Bragg peak. It is found that the 100 keV proton beam gives maximum stopping for liquid water which is used as a prototype for human cell (Ziegler and Biersack, 2000). 100 keV proton beam deposits the maximum energy with a Linear Energy Transfer (LET) of about 80 keV per micron (Le Padellec et al., 2008) and therefore gives maximum ionization cross section. Hence many experimental and theoretical investigations have been performed at kinetic energies in the keV range since these energies are relevant for the ion induced biological radiation damage in the region of the Bragg peak (De Vries et al., 2002; Coupier et al., 2002; De Vries et al., 2003b; Bacchus-Montabonel et al., 2005; Bacchus-Montabonel and Tergiman, 2006; Alvarado et al., 2006; Schlathölter et al., 2006; Bacchus-Montabonel et al., 2009). A simulation of proton-nucleobase collision is therefore essential to refine the best radiotherapy strategy. The literature is enriched with the experimental fragmentation studies for nucleobases using keV proton impact (Le Padellec et al., 2008; Coupier et al., 2002; Moretto-Capelle et al., 2007; Tabet et al., 2010a,c,d; Brédy et al., 2009), multicharged ion impact (Schlathölter et al., 2004; Manil et al., 2003; Brédy et al., 2005; Bernard et al., 2006; Agnihotri et al., 2012), 3 keV neutral fluorene impact for adenine (Chen et al., 2011), electron spectroscopy using keV proton impact (Moretto-Capelle and Le Padellec, 2006; Iriki et al., 2011a,b).

The present investigation is dedicated to proton interaction with the purine molecule adenine ($C_5H_5N_5$) and guanine ($C_5H_5N_5O$), and the pyrimidines cytosine ($C_4H_5N_3O$), thymine ($C_5H_6N_2O_2$) and uracil ($C_4H_4N_2O_2$) (see figure 3.19). We have here done the MC simulation within the frame work of LDA to calculate the mean electronic energy loss. To highlight some additional attributes, we have compared the result with the case of naphthalene. The geometric cross sections for a range of energy loss distribution were calculated using the above mentioned MC-LDA model. Our results are compared

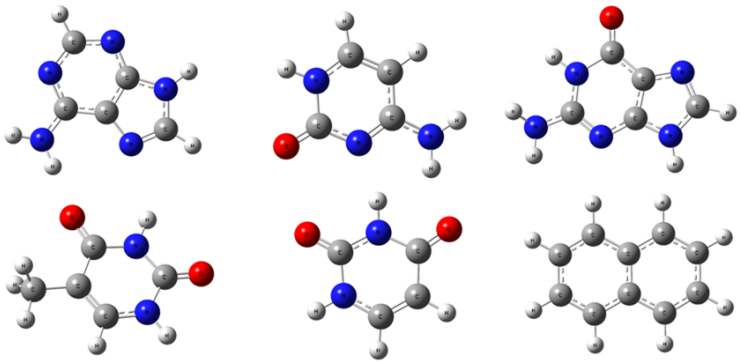

Figure 3.19: Schematic picture for five nucleobase adenine, cytosine, guanine (top three left to right), thymine, uracil and one PAH : naphthalene (bottom three left to right). The various atoms are shown as red (oxygen), blue (nitrogen), grey (carbon), white (hydrogen).

with other theoretical approach probed in past for nucleobases which are based on models like first-order Born approximation (CB1-CWB), continuum distorted wave-eikonal initial state (CDW-EIS), CTMC with classical over-the-barrier (CTMC-COB) (Champion et al., 2012; Galassi et al., 2012; Abbas et al., 2008; Lekadir et al., 2009).

***Monte Carlo* simulation results and discussion:** The energy transfer threshold for parent ionization is lower than dissociative ionization which is clear from photoionization and electron impact mass spectra (NISTe, June 2014). Hence increase in yield of fragmentation and relatively large number of low mass fragment ion yield in experimental mass spectrum gives evidence for higher energy deposition. In the following discussion, the deposited energy consumption by the photon emission or in the form of kinetic energy of emitted electron is neglected.

In figure 3.20 and 3.21 the results for electronic stopping due to straight impact of linear trajectories on XY plane of the molecule which offers the largest geometrical cross section to the projectile beam and also the perpendicular impact simulation for rest

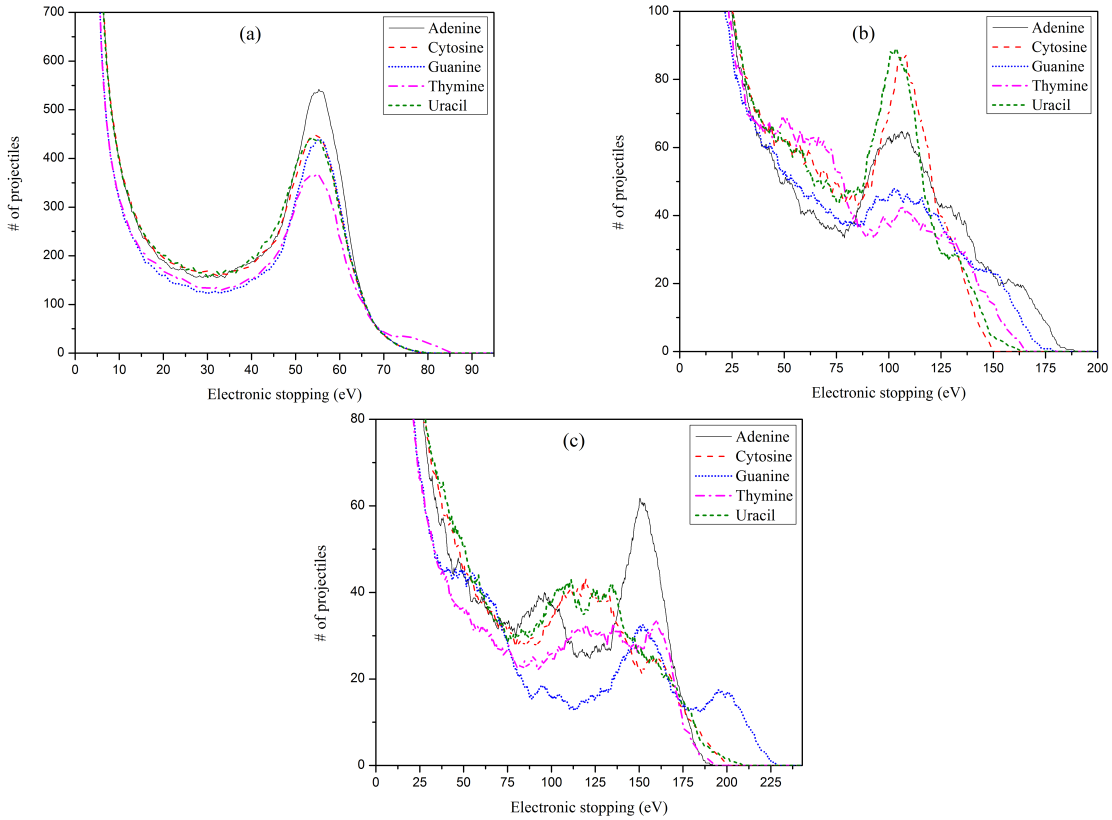

Figure 3.20: Mean energy loss curve for perpendicular impact of random straight trajectories of 80 keV proton in (a) Z, (b) Y, (c) X-direction with nucleobases placed in XY plane.

two planes are shown. Figure 3.21 shows the contour plots for energy loss distribution corresponding to the perpendicular impact of straight trajectories on molecular plane (i.e. XY plane). It is observed that there is a commonality among all the nucleobase as well as the individual plane impact simulation (see figure 3.20). The multiple peaks in a given spectrum are attributed to the different type of electron density experienced by the projectile over the molecular area. Out of which the peak with lowest energy loss arises from the interaction of projectiles with the electron density at the periphery of the molecule whereas the higher loss comes from the electron density near the nuclei. Since the core density is higher in magnitude and hence gives higher electronic

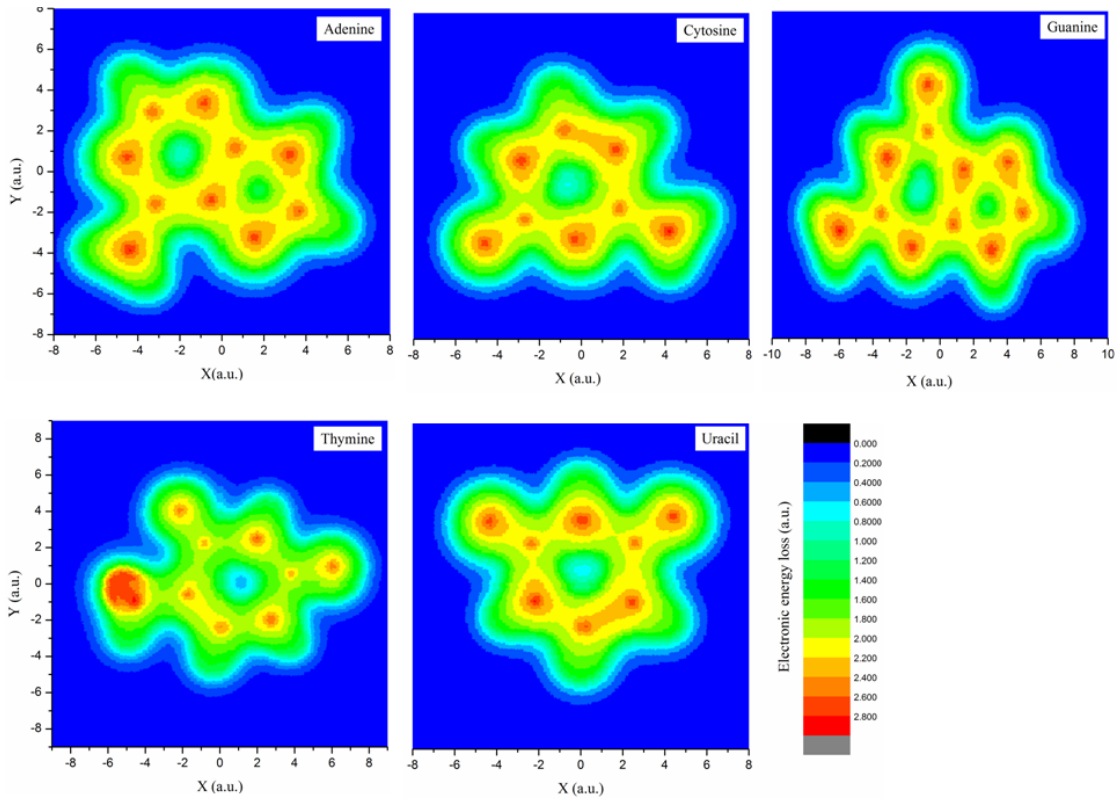

Figure 3.21: Contour plot for the calculated mean electronic energy loss for random collision of 80 keV proton in Z-direction with nucleobases placed in XY plane.

stopping. These correlations depict the major role of non-uniformity in electron density in determining the various features of electronic stopping curve. For example the second peak in XY plane impact electronic stopping curve (see figure 3.20) for thymine is explicitly from the methyl group associated with the molecule which gives the maximum stopping among all nucleobases. This feature is prominent in the contour plot for XY plane impact simulation (see figure 3.21). But to be noticed that thymine gives maximum stopping only for the perpendicular impact on XY plane simulation. This is due to the simultaneous contribution of two facts: non planarity of CH_3 group and the calculation of mean energy loss as a line integral of full length of projectile.

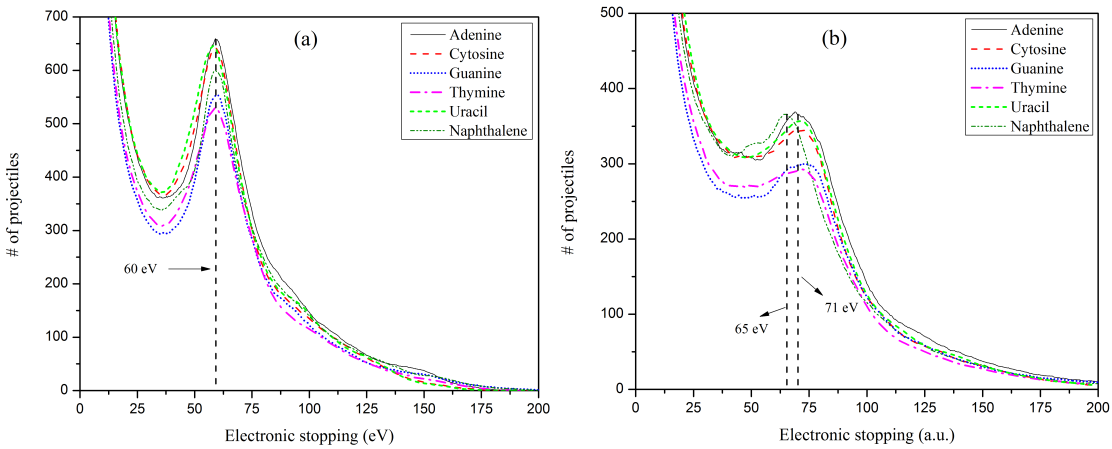

Figure 3.22: Mean energy loss calculation using *Monte Carlo* simulation for randomly generated (a) 80 keV and (b) 180 keV proton projectiles interacting with nucleobase targets and naphthalene.

Figure 3.22 illustrates the electronic stopping obtained for 10^6 random linear trajectories of the proton projectile ions of 80 keV and 180 keV on interaction with nucleobase electron density. The simulation shows that the peak in energy loss spectrum overlaps for all the five nucleobases and naphthalene for 80 keV proton projectile interaction whereas a shift in the peak is observed in the case of naphthalene for 180 keV proton projectile simulation. On the other hand, the trend in geometric cross sections is found to be independent of the projectile energy except a constant scaling factor for all the nucleobases. Naphthalene falls in the same trend, irrespective of its difference in composition than the nucleobases (see figure 3.23). Irrespective of difference in structure and symmetry of molecule, the most prominent stopping is same for all targets due to similar type of electron densities or bonds (though nucleobases involve the NH and NC as well as CO bonds). This effect is attributed to the relatively small change in fermi velocity distribution. The probability of higher energy loss decreases rapidly after a pronounced peak.

As discussed earlier, the peak in electronic stopping curve is due to a large number

of trajectories experiencing similar electron density and is a result of specific range of v_f / v where, v_f is the Fermi velocity (depends on electron density) and v is the projectile velocity. XY plane though, offers larger area, does not correspond to the maximum stopping because mean electronic stopping is an integral of the projectile path for ions at all impact parameters and orientations encountering the target. This also explains the maximum stopping appearing from the YZ plane impact. The multiple peaks can be attributed to different type of electron densities involved in the simulation (see later). Previously reported MC simulation for electronic stopping using Lindhard and Winther model (Lindhard and Winther, 1964) peaks at $\sim$ 80 eV for 100 keV proton impact on adenine (Moretto-Capelle et al., 2007) whereas for our simulation it peaks at $\sim$ 64 eV under same condition. This difference could be due to difference in calculated electron density which strongly shifts the position of the maximum, as noted by Ferrell and Ritchie (Ferrell and Ritchie, 1977). The proton collision study on PAHs in section A and B of 3.3.3 has shown that mean energy loss decreases with increasing projectile velocity and also there is a reverse in the shift of the peak energy loss after 150 keV for proton projectiles. This aspect is attributed to the change in parameter v_f / v. This parameter decides the maximum number of projectile experiencing a given type of electron density and hence the peak position. This explains the mismatch in peak position for naphthalene and other nucleobases at 180 keV proton projectile simulations.

The fragmentation yield of uracil induced by ion (De Vries et al., 2002, 2003b; Tabet et al., 2010a,c,d; De Vries et al., 2003a, 2004; Denifl et al., 2004; Imhoff et al., 2007; Schlathölter et al., 2006; Tabet et al., 2010b), electron (Coupier et al., 2002; Denifl et al., 2004; Imhoff et al., 2007; Feil et al., 2004) or proton (Le Padellec et al., 2008; Coupier et al., 2002; Tabet et al., 2010a,c,d,b) impact at different energies, as well as by photoionization (Imhoff et al., 2005) measurements indicate that dication of uracil is very unstable and lead to fragmentation (because the measured yield of multicharged ion is insignificant). Hence, indicating breaking of molecule as an alternative way of energy

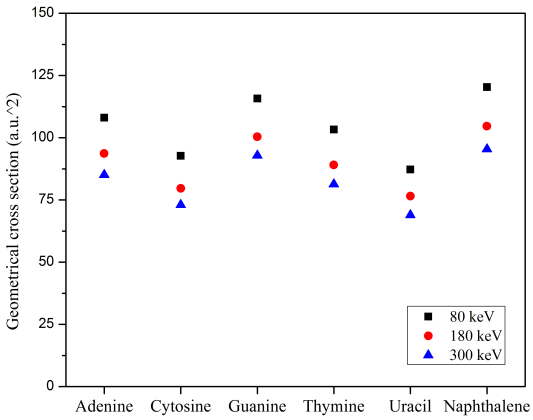

Figure 3.23: Geometric cross sections obtained from *Monte Carlo* simulation of randomly generated classical trajectories of 80, 180, and 300 keV proton beam interaction with nucleobase electron density.

dissipation (Agnihotri et al., 2012; Arani et al., 2012). The formation and subsequent instability of a doubly charged adenine molecule have been studied from two charged fragmentation correlation spectra by Moretto-Capelle et al. (2007). In contrast to these measurements, Alvarado et al. (2007) report the presence of doubly charged adenine in all of their ion and neutral impact studies. Further 100 keV (Le Padellec et al., 2008) and 80 keV (Tabet et al., 2010d) proton impact studies on uracil, cytosine and thymine also shows a scarcity of doubly charged parent ion in mass spectra and shows subsequent fragmentation. Whereas 100 keV proton-napthalene collision shows an intact dication with 33% yield and with measurable amount of trication (see section 2.1.2.1 and figure 2.6). The minimum amount of energy required for dications of nucleobase formation is $\sim$ 25 eV which is higher than the double ionization threshold for naphthalene (21.45 eV) (Holm et al., 2012). The appearance energy for fragments obtained from photofragmentation measurements for nucleobases are 11.56, 10.7, 10.95, 10.7, 16.67 eV for adenine, thymine, uracil, cytosine, guanine respectively (Jochims et al., 2005; Rice et al., 1965; Plekan et al., 2007). Hence fragmentation is appreciable if the total energy deposited is in excess of 12 eV at least, except for guanine which requires more

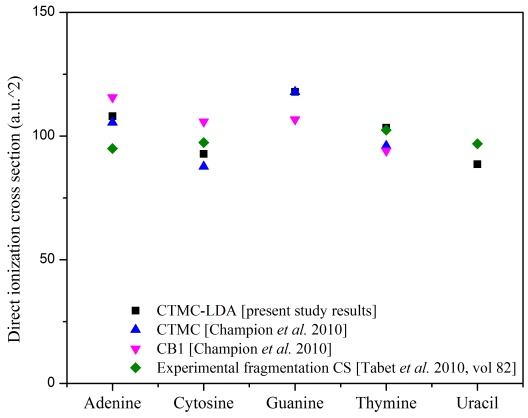

Figure 3.24: Experimental fragmentation cross sections comparison with theoretical calculations for 80 keV proton-nucleobases collision.

energy. Therefore we can put the single ionization threshold to be the lower limit for fragmentation yield in the energy loss spectrum to calculate the geometric cross section for fragmentation. The fraction of total number of trajectories depositing more than this value with respect to the total number of trajectories, is used to calculate the geometric cross sections.

Figure 3.24 shows the trend observed for experimental absolute fragmentation cross section in direct ionization process for different nucleobases (Tabet et al., 2010c) and a comparison with the trend shown by geometric cross section obtained from simulated energy loss spectrum. In the same figure different theoretical model calculation (Champion et al., 2010) are shown for comparison with experimental fragmentation cross section. The first ionization potential (IP) in the increasing order are for guanine (7.85 eV) $<$ adenine (8.3 eV) $<$ cytosine (8.45 eV) $<$ thymine (9.0 eV) $<$ uracil (9.2 eV) (Moretto-Capelle et al., 2007). And we have considered first IP as the threshold for fragmentation channels to open and hence among the studied molecules by Tabet et al. (2010d), adenine is more prone to fragmentation as well as ionization with less energy requirement. But the 80 keV proton impact studies by Tabet et al. (2010d) shows

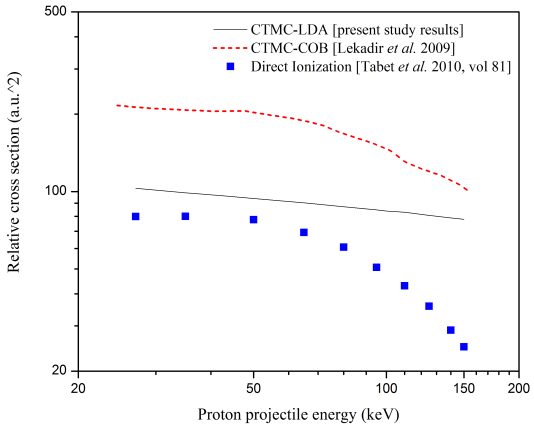

Figure 3.25: Experimental relative cross sections comparison with theoretical for proton-uracil collision at different projectile energy.

that the fragmentation ratio is greater for thymine as compare to adenine, cytosine, and uracil. This aspect is reproduced in terms of geometrical cross section (see figure 3.24). Fragmentation can be the important channel as a consequence of energy dissipation in thymine, though the threshold for fragmentation in thymine is higher among rest of the studied nucleobase. This is because of less degree of freedom available for thymine as compare to adenine for energy dissipation gained by coulombic interaction with projectile. Notably for all four nucleobases studied by Tabet et al. (2010c), the parent ions yield (given as a percentage of the total ion production) is greater for direct ionization (DI) than for electron capture (EC) process whereas fragmentation found to be more for EC process. This increase in fragmentation followed by electron capture as compared to direct ionization in 80 keV proton-molecule collisions is seen in nucleobases (Tabet et al., 2010d) and water (Gobet et al., 2001, 2004). However in general fragmentation yield for both direct ionization and capture process total is found to be much larger than the parent ion yield (Tabet et al., 2010c).

The experimental ionization cross section (including the contribution from both ionization as well as fragmentation) due to direct ionization process alone is considered

for a comparison with the geometrical cross section obtained from our *Monte Carlo* simulated energy loss curve for uracil (see figure 3.25). Figure 3.25 shows a relatively good agreement in the behavior as function of projectile energy for scaled experimental ionization cross section obtained in direct ionization process (Tabet et al., 2010a) with the theoretical geometrical cross sections upto 100 keV projectile energy. These experimental data (containing fragmentation as well as ionization yields) can be additionally contributed by the events from transfer ionization but do not contain the pure electron capture events at all, because these are exclusively obtained in coincidence with electrons emitted in the same event. The present simulation does not include electron capture and the transfer-ionization processes which are important channels at low projectile velocities. Hence the discrepancy between theory and experimental results is expected for low energy regime. But we observe an opposite behavior which demands a better theory simulation including other processes in addition to ionization for high projectile energy regime. This change in behavior of experimental cross section in contrast to theoretical models is very crucial to study because of the barrier around 100 keV which is the Bragg peak region and deals with maximum energy deposition during the cancer therapy. A classical *Monte Carlo* approach based on Coulomb over-the-barrier model has been used to calculate ionization as well as capture cross section in the identical systems presented here (Lekadir et al., 2009). This approach entirely depends upon the binding energy details of the target and disregards the structural and geometrical aspects all together. Our approach is more microscopic in this context due to the use of LDA method in the simulation. In figure 3.25 we plot our MC-LDA calculated geometrical cross sections along with the calculations by Lekadir et al. (2009) and experimental measurements by Tabet et al. (2010a). The cross sections in the whole reported range by Lekadir et al. (2009) were almost identical for all the nucelobases. Similar behavior is observed for our MC simulation results obtained from randomly generated 10^6 proton projectiles of different energy interacting with uracil electron density (see figure 3.25).

Our calculations are about factor of two smaller than that calculated by Lekadir et al. (2009). But the experimental cross sections are much larger by a factor as high as five. Moreover the trend followed by experimental curve is very different. Hence we suggest a better and more comprehensive experimental investigation can shade light on applicability of these two separate theoretical approaches.

3.4 Coulomb over-the-barrier model for electron capture

We have used the COB model at various occasions to estimate the capture cross section and capture distances for our experimental results. Considering the simplicity of this method the calculated numbers from this model were used qualitatively. As compare to pure ionization cross section single electron capture cross sections for parent ion are found to decrease with increase in projectile velocity $\sim v^{-4}$ (figure 2.7) which is slower than that from Bohr-Lindhard model (Bohr and Lindhard, 1954) where the cross sections should drop approximately v^{-7} as for sufficiently fast projectiles. It is important to note that such models assume the target to be either point-like or spherically symmetric. However, it is difficult to adopt such formalism here for the following reason. In the velocity regime under consideration, the capture distance is expected to be small, $\sim$ 11 a.u. for naphthalene as per COB estimate (Bárány et al., 1985). This is close to the actual molecular size of naphthalene, $\sim$ 11.71 a.u. (Long et al., 2008). Since naphthalene is planar, the assumptions about the target (point-like or spherically symmetric) do not strictly apply. Recently, Forsberg et al. (2013) have attempted to make a coulomb barrier model for large planar PAHs. However, this can only be applied in relatively simple cases, unlike naphthalene. Moreover, as shown in figure 2.11a, the active electron in the transfer process is from inner valence shell not from the HOMO. Therefore

the velocities in the present regime may not be high enough for Bohr-Lindhard scaling to be applicable.

3.5 Conclusions

Quantum structure calculations are performed for several PAHs as well as their clusters to identify the magic numbers and different stability parameters. For a selected set of PAHs and their derivatives Adiabatic electron affinity (AEA) values at B3LYP/6-31+G(d) level using DFT technique are obtained which are in agreement with the experimental values. Electron spin density distribution and electrostatic potential mapped energy plots showed the importance of delocalization to accommodate the excess electron. A correlation of experimental as well as theoretical AEA is observed with a very simple geometry based aromaticity index. A few deviations observed in the case of cyclopenta[fg]acenaphthylene and fluorene are explained on the basis of stronger influence of cyclopenta ring. The isolation of a 6 MR structure form the delocalization of rest of the molecule is found to be present in molecules where an aromatic 6 MR shares two or more alternate bond with other aromatic 6 MR. Aromaticity is a multidimensional character and hence its quantification is a complex task proven by the few deviations observed from the trend. In spite of this nature of aromaticity, we find a good correlation between the Weighted average of Harmonic Oscillator Model of Aromaticity index and AEA. In addition to this the gasphase properties like proton affinity and ionization potentials are also calculated for PAHs to use in experiments.

Outer valence Green's function technique is used to assign the symmetry and binding energy to MO observed in PE spectrum of pyrene and fluorene. UV photoabsorption causes ionization of PAHs which is followed by the structural alteration of cation and gives rise to the vibrational progression in PE spectrum. The observed vibrational pro-

gressions in experimental PES are well reproduced with the help of our Franck-Condon factors calculation for $D_0 \leftarrow S_0$ transitions using DFT method within harmonic approximation for a given HWHM. The Franck-Condon calculations for all the studied PAHs in the present work, showed CC trans-annular stretching in-plane mode with a_g symmetry as the dominant mode of vibration corresponding to $\sim$ 1400 cm^{-1} band. This is closed to the band observed in UIR bands of ISM where UV photoabsorption is a dominant excitation mechanism for PAHs. The formation of vibrationally excited cations during the process of UV photoionization will influence the IR bands seen in ISM. The appearance of band $\sim$ 1400 cm^{-1} in our Franck-Condon simulated spectrum for the all small PAHs, indicates PAHs as a possible carrier for UIR band. Since the UIR band is broad in nature and hence can be attributed to mixture of these small PAHs in both neutral and ionic form. The reliability of simulation results are confirmed with a good agreement of our experimental and simulation results with highly resolved Threshold photoelectron spectroscopy measured values.

Using Coulomb over-the-barrier model, the capture cross section and capture distance are found out for proton-naphthalene collision experiment. For non-spherical molecule the analytical impact parameter treatment of projectile energy loss is difficult due to the lack of symmetry and complex nature of the potential energy surface in such experiments. This is particularly the case at intermediate velocities and low projectile charge states, where the impact parameters of significance are comparable or smaller than the molecular dimensions. Hence, the molecule cannot be treated as a point target. This compels us to employ a *Monte Carlo* approach for such cases. Hence *Monte Carlo* simulation is performed for PAHs and their derivatives for randomly generated proton and He ion trajectories passing through a non-uniformly distributed electron density representing the molecular volume and the electronic energy loss distribution is estimated within local density approximation. The investigation for nucleobases is done in the Bragg peak regime of proton velocity ($\sim$ 100 keV). The observed decreasing trend

for fragmentation yield in our experiment of proton-naphthalene collision as a function of impact energy is reproduced with the theoretical cross section obtained from *Monte Carlo* simulation. The peak in distribution is decided by the orientation of the molecule as well as the charge and velocity of the projectile. Any non-planar feature like the one observed in case of thymine clearly provides a location for relatively higher energy deposition for all orientations. The model appears to overestimate the internal energy deposition. This may be corrected by including effects like projectile charge state screening. For a 75 keV He projectile, the fragmentation distribution in the mass spectrum is observed to be independent of the projectile charge state. This is attributed to electron capture at large distance before the projectile interacts with the target and equilibration of the projectile charge state. The theoretical cross sections obtained from our MC-LDA model for nucleobases were compared with another *Monte Carlo* approach using classical over the barrier model which purely involves binding energy of the target electrons and disregard the structural and geometrical aspects of the target. Our calculations match very closely to this model though it underestimates the values systematically. On the other hand experimental measurements on uracil give much higher absolute total ionization cross section surpassing the results by both models. Moreover, the experimental trend is much steeper at higher energy than both the model predictions. A more detailed experimental investigation with all the nucelobases as targets is in order to test the predictions and to find the appropriate region of applicability of these models.

CHAPTER 4

DEVELOPMENTAL WORK AND INSTRUMENTATION FOR MASS SPECTROMETER

To understand the correlation between various molecular excitation mechanism and relative stability of PAH molecules and their fragments upon photoexcitation or collisional dissociation, an in house mass spectrometer is built with several significant techniques integrated within it at Atomic and Molecular Physics (AMP) Laboratory, Indian Institute of Space Science and Technology. The detail lay out of the complete set up, individual component details and their test results are described in the following section.

4.1 Schematic of the set up and its significance

The experimental set up (schematic is shown in figure 4.1) consist of an ion source, pulsing device for ion beam, ion guide, parallel plate electrostatic analyzer, position sensitive detectors and a tunable nanosecond laser. In future this set up will be augmented

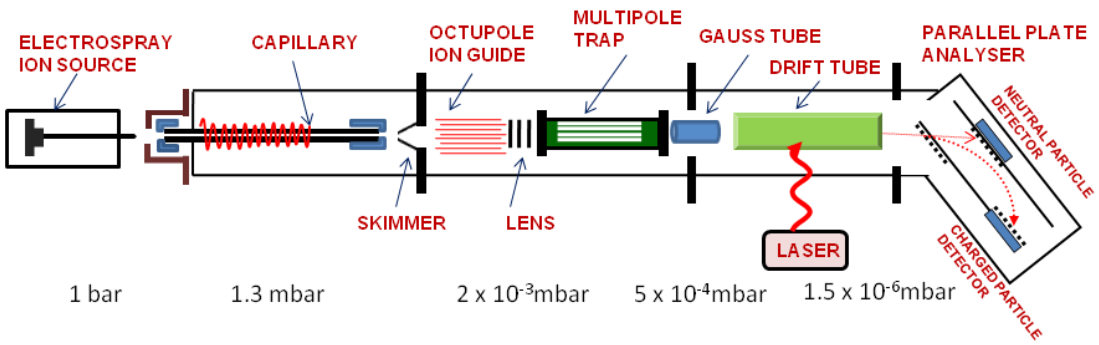

Figure 4.1: Schematic of the experimental set up at AMP Lab, IIST.

by an ion trap for storing of ions and by a collision cell for collisional dissociation with inert gas. The set up is capable of producing a wide variety of molecular ions of any polarity, starting from monomers to clusters (e.g; metal cluster, amino acid attached to water cluster, biomolecule cluster etc.). The hybrid molecules produced in the ion source after guided to an ultra high vacuum region will be stored in the ion trap for collisional cooling. The photodissociation or collision induced dissociation studies can be used to understand the stability, magic numbers for formation of cluster and fragmentation dynamics of molecular ions. This setup can be used to study the spectroscopic property of wide range of masses, 100 - 100000 amu, e.g.; PAHs, bio molecules like DNA as well as peptides, solvated molecules like amino acids with water or methanol molecules, water clusters and many other systems without any change in the setup because of the capability of the ion source producing intact large molecular ions without any dissociation. Hence it brings attention to study molecules significant to terrestrial as well as extraterrestrial environment. In addition to this ultra high vacuum also ensures the isolation of molecule under study from the undesired and uncontrollable effects of surrounding media. Such isolation assures that the measured effects in the experiment are purely resulting from the desired perturbation given as part of the experiment. Isolated molecules embedded in various matrices have a wide variety of applications like data storage media, fuel storage, drug delivery, smart sensors etc. due to the demand of miniaturization of electronic devices in today's world. In medical science it is essential to understand the response of biomolecules inside a living organism to external environment for drug delivery and discovery of compatible medicines. Not only in our terrestrial environment, in the extraterrestrial environment like ISM, PAH clusters are mediators of hydrogen molecule formation. Due to their planar nature, PAHs have tendency to form clusters among themselves by van der Waals forces (Tielens, 2008). PAHs as large as ranging 50 - 400 C atoms are predicted to be present in ISM whose relative abundance is $\sim 3 \times 10^{-7}$ with respect to the most abundant molecule H_2 (Tielens,

2008). Some of these clusters rapidly breaks by FUV absorption as reported by Rapacioli et al. (2006) for coronene cluster (two coronene molecule bonded by $\sim$ 1.3 eV). The stability of these clusters under UV-IR radiation impact in stellar medium can be studied with this mass spectrometer set up. From the above mentioned point of views, this setup therefore can be of interest to biochemists, biophysicists and chemical physics, astrophysics studies. Apart from the above versatile features, a complete kinematical study can be performed with this experimental set up *via* velocity-velocity correlation information of measured fragment ions in coincidence during a single collision event and hence can provide information regarding the stability or dissociation mechanism of the precursor ion.

4.2 Working principle and test results for individual components of set up

4.2.1 Electrospray ionization source

Prof. J. B. Fenn shared the Nobel prize in chemistry for the year 2002 for the discovery of this type of source for macro molecules which can be studied in gasphase. The initial development of the method is due to Malcolm Dole. Electrospray ionization (ESI) source: the "soft ionization" technique, produces the molecular ions in a very cold way which was very difficult earlier, as large molecules could not be vaporized without fragmentation or dissociation. The main hurdle in gaseous measurements is to build a setup which can provide the hybrid system in a suitable gaseous form or in the form of an ion beam. Laser desorption in such cases is one of the most widely used technique, but fails to produce good intensity of hybrid beams. It became possible to have a very good intense beam of molecules of biological, environmental and other interest with ESI. ESI

can produce inorganic to organic species, biomolecules, polymers etc. of very high molecular mass. The ion source due to its simplicity in construction and wide applicability, is used in many devices commercially (ESI1, June 2014). In this area of research, many different varieties of ESI are in use, some are available commercially and some are custom built to suit a particular type of investigation. Normally this device is coupled to a mass spectrometer and the parameters like relative abundance of different species after fragmentation, identification of the parent species, several possible fragmentation channels due to collision induced dissociation or photo induced dissociation are measured routinely (Lepère et al., 2007; Kadhane et al., 2008). ESI coupled to mass spectrometer is widely used in biochemical, biomedical, pharmaceutical and molecular physics research. ESI source is also being investigated to be used as rocket engines (ESI2, June 2014).

Working principle: The performance of ESI depends on multiple parameters simultaneously, like choice of solvent and concentrations of the analyte, choice of additives to enhance the polarity of solution, choice of the flow rates of the solution through the spray capillary (in the present work a hypodermic needle is used for this purpose), the electrical potentials applied to the spray capillary and the potentials of ion optical elements that are part of the mass analyzer. Proper choice of these parameters requires not only some understanding of conventional mass spectrometry but also of the electrospray mechanism with manual skill to find out right parameters for a given sample.

The basic principle behind the ESI is that highly charged droplets from solutions of nonvolatile solute species in volatile solvents might produce intact gaseous ions of those species (Fenn, 2002). To get the desired molecular ion or molecular ionic cluster using ESI, a solution is made composed of the desired molecule as solute, suitable solvent (proportionate mixture of methanol and deionized water or acetonitrile and deionized water), acetic acid (for protonation). The detail of this is discussed later. The solution

is sprayed in a regulated flow using a motor driven syringe pump which is connected to a hypodermic needle through a flexible glass syringe and tubing (see figure 4.2a). The voltage requirement to be applied to the needle depends on the separation between the needle tip and the grounded aluminum plate (capillary cap) on the glass capillary entrance surface. The polarity of the voltage applied to the needle with respect to the counter electrode (here the grounded capillary cap) decides the polarity of molecular ion to be thrown into the chamber. The ions enters the low pressure region from atmospheric zone through this glass capillary which is made up of quartz with aperture size 0.4 mm and length $\sim$ 200 mm (spanning atmosphere till low pressure region). A Wilson seal arrangement is used to take out the capillary for cleaning purpose without disturbing the rest of the set up.

The gas phase ions are formed from the ionic solution in the following sequential way on application of high voltage to the needle: i) The charged droplet is formed due to intense electric field near the region of needle tip and the interaction between the forces due to surface tension of the liquid and those due to the imposed field results in the formation of a conical meniscus at the needle tip which is known as Taylor cone. ii) The charged droplet shrinks due to evaporation of solvent and charge induced disintegration leading to small highly charged droplets. In addition to this as a result of another type instability called "Rayleigh instability" in which the interaction between viscosity and surface tension gives rise to varicose waves on the surface of such a liquid jet which grow in amplitude until they truncate the jet into a series of uniform droplets. iii) Ion separation due to coulombic repulsion which results in a divergent beam giving a conical "electrospray" of charged droplets.

All this occur in atmospheric region and then a fraction of ions are introduced into the vacuum ($\approx$ 1 mbar) region through the capillary of orifice 0.4 mm due to pressure gradient. For our case the capillary with 0.25 mm orifice gave very less current on

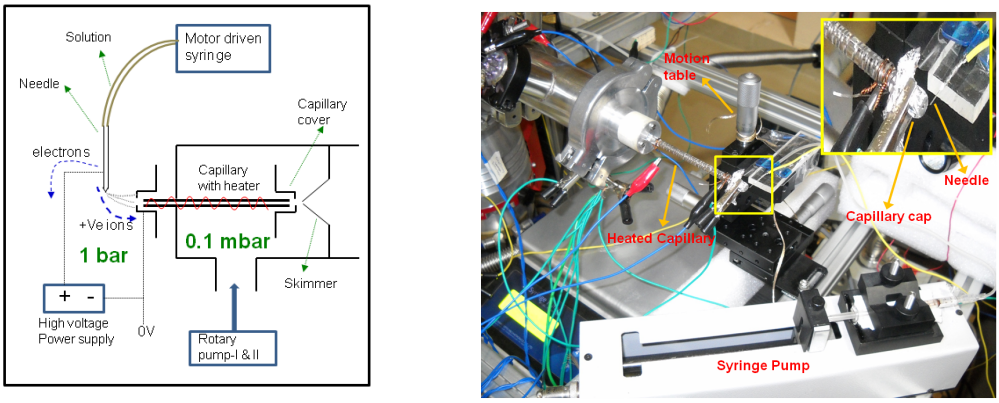

(a) (b)

Figure 4.2: (a) Schematic of ESI source, (b) ESI source at AMP Lab, IIST.

skimmer placed after the capillary cover inside the chamber. Hence to achieve low pressure and to compensate the larger aperture allowing more air into the chamber, this ion source chamber is pumped by two rotary pumps with total throughput 25 m^3/sec giving pressure $\approx$ 1 mbar. For this ion source, to avoid the water droplets entering capillary, an orthogonal ion extraction method is implemented. In addition to this, a nichrome wire wound around the capillary is used for heating of capillary which helps in evaporating the solvent molecules surrounding the solute molecular ions. The heating of capillary reduced the current on skimmer by 10 times. The ion currents depend strongly upon both the temperature of the emitter and the applied voltage to the tip. The currents are measured on skimmer. An electric field between the capillary cover at the exit surface and the skimmer cone accelerates the ions. The values of operational parameters for several test is given in following section.

Test results for ESI: The ESI is functioning and tested for PAHs as well as biomolecules. The nominal operating parameters to achieve maximum current on skimmer (thousands of picoampere) are the following:

i) Spray Solution: A small crystal of solute is dissolved in 50 % methanol and 50 % deionized water mixture solution. This solution is further added by 1 % acetic acid for protonation.

ii) Solution flow rate: 100 - 200 μlit per hour

iii) Syringe diameter: 5 mm

iv) Needle tip diameter: 300 micron

v) Needle tip bias: 2.5 - 3.0 kV (-Ve polarity)

vi) Needle to capillary cap separation: 2.0 - 3.0 mm

vii) Capillary cap (entrance of ion beam) bias: 0 V

viii) Capillary cover (exit of ion beam) bias: 30 - 35 V (-Ve polarity)

ix) Capillary heater bias (in atmosphere): 10 - 12 V (+Ve polarity)

x) Capillary heater bias (inside chamber): 7 - 8 V (+Ve polarity)

xi) Skimmer bias: 10 - 15 V (+Ve polarity); (when no current measurement on it)

The capillary cap is made of aluminum foil. The distance between the capillary cover and skimmer is kept 2 mm and the alignment is distorted slightly to avoid the inflow of air to the next chamber. The skimmer (with orifice 0.5 mm, made of aluminium) acted as a Faraday cup and the measured current is $\sim$ 2000 pA without heating and $\sim$ 200 pA with heating of capillary. The skimmer also helps in maintaining the vacuum in subsequent chambers and allows only the ions with less turbulence (caused due to bombardment of ions on skimmer surface). Figure 4.2b shows the existing ESI source in running mode. A test with five PAHs namely: naphthalene ($C_{10}H_8$), fluorene ($C_{13}H_{10}$), anthracene ($C_{14}H_{10}$), phenanthrene ($C_{14}H_{10}$), pyrene ($C_{16}H_{10}$) of equimolar

solution is performed and the current variation observed shows an increasing behavior with increase in molar mass of the molecule.

4.2.2 Octupole ion guide

The ion beam extracted from the ESI source enters the low vacuum region ($\approx 10^{-3}$ mbar) through the skimmer. After the skimmer, for guiding the ions to high vacuum region ($\approx 10^{-6}$ mbar) of the ion trap, an octupole ionguide is used.

Working principle: According to Earnshaw's theorem, static electric field cannot be used to trap charged particles because it produces a saddle point and cannot create absolute minima. This is the consequence of Laplace equation in charge free domain. But time varying field can produce two dimensional or three dimensional potential minima (Gerlich, 1992) in which ions can be trapped and guided. Hence with the help of time dependent radio frequency fields, ions are guided and trapped. This technique was first developed by Wolfgang Paul who shared the Nobel prize for this invention with Hans Dehmelt in 1989 (Paul, 1990).

The octupole ion guide is a device made of eight identical rods arranged in a symmetric way. Alternate rods are connected together and the two sets are connected to opposite phase of a RF power supply. The frequency and RF amplitude are adjusted such that the ion can guide through the setup.

Equations of motion of a two dimensional multipole device (Ghosh, 1995) with $2n$ number of electrodes ($n > 2$), are given by

$$\ddot{x} + \frac{q}{m}\left[\frac{(U + V\cos\Omega t)}{r_0} n \left(\frac{r}{r_0}\right)^{n-1} \cos((n-1)\phi)\right] = 0 \tag{4.1}$$

$$\ddot{y} - \frac{q}{m}\left[\frac{(U + V\cos\Omega t)}{r_0} n\left(\frac{r}{r_0}\right)^{n-1} \sin((n-1)\phi)\right] = 0 \tag{4.2}$$

where q is the charge of ion, m is the mass of ion, V is amplitude of RF voltage, U is the offset voltage, r_o is the inner radius of the device, r is the displacement of ion from the centre, ϕ is the azimuthal angle and Ω is the frequency of RF. These equations are non-linear and coupled, which cannot be solved analytically. Here the stability of ions depends on initial parameters like position, velocity etc. of ions (Gerlich, 1992). Unlike quadrupole mass filter (*n = 2*), multipoles with $n > 2$ are suitable for guiding, transporting and collimating ion beams, but they are generally not used for mass analysis (Gerlich, 1992) which is mainly done by the DC offset (U).

The time averaged energy of classical wiggling motion of the charged particle with respect to the field act as an effective potential V* and the force due to this potential helps in confining the particles.

$$V^*(r) = \frac{q^2 n^2 V^2}{4m\Omega^2 {r_0}^2}\left(\frac{r}{r_0}\right)^{2n-2} \tag{4.3}$$

To define the safe trapping of ions in higher order ($n > 2$) multipole traps, Gerlich (Gerlich, 1992) introduced a parameter η called adiabaticity parameter which is given by:

$$\eta = 2n(n-1)\frac{|q|V}{m\Omega^2 {r_0}^2}\left(\frac{r}{r_0}\right)^{2n-2} \tag{4.4}$$

From the above equation it is clear that η depends on the radius of the secular motion for $n > 2$. As shown by Gerlich (Gerlich, 1992), the micromotion and secular motion of ions remain independent of each other when $\eta < 0.3$ for $(r/r_0) < 0.8$. This approximation of $\eta < 0.3$ ensures the safe guiding and trapping of ions which does not depend on their initial conditions, but depends only on the transverse energy of the ions. The condition $\eta < 0.3$ is not a necessary condition, but only a sufficient one (Gerlich, 1992).

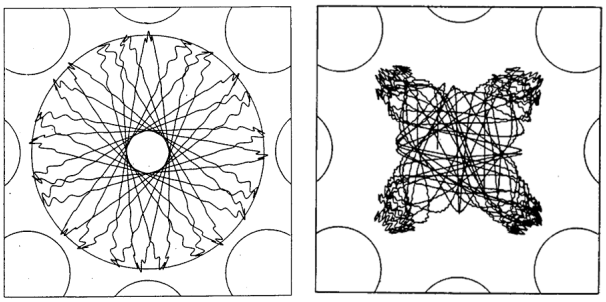

Figure 4.3: Trajectory of ion inside an octupole when U=0 (left) U $\neq$ 0 (right) (Gerlich, 1992).

There may be stable trajectory for some values of $\eta > 0.3$ and unstable for some $\eta < 0.3$ in the trap. But it is always good to keep of $\eta < 0.3$ for safe guiding and trapping. It is also shown that the amplitude of wiggling motion increases with increase in η.

The DC offset voltage (U) also effects the motion of ion inside the ionguide (see figure 4.3) as shown by Gerlich (Gerlich, 1992). The presence of hole in the centre is due to the conservation of angular momentum. The effective value of electric field is independent of azimuthal angle and hence the effective potential becomes rotationally symmetric. So the interaction between charged particle and RF field results in a central force. This is not the case when there is a superimposed static field created by U. The angular momentum is no longer conserved and the rotational symmetry is lost in this case, as shown in figure 4.3. Potential minima are obtained close to negative poles and ions avoid the positive poles (Gerlich, 1992).

Fabrication and test results for octupole ionguide: The geometry of the electrodes and their alignment with respect to central axis influences a lot the electric field inside the trap which is also seen by our simulation (Maryam, 2010). However for the guiding purpose the geometric precision is not so crucial as it is for mass filtering and trapping action. To form an effective potential as given in equation 4.3, the diameter of the elec-

trode (d) and inner radius (r_0) of the trap with $2n$ number of poles should be connected by the equation

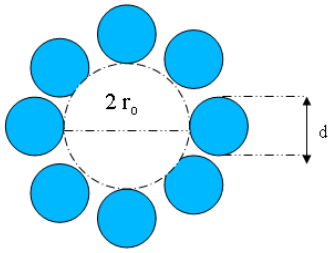

$$r_0 = \frac{(n-1) \times d}{2} \tag{4.5}$$

As octupole ion guide is a two dimensional device where the ions are free to move in the axial direction. Hence to focus the ion beam we have three circular plates with 10 mm hole acting as einzel lens with outer two electrodes being grounded permanently. So the AC field given to the eight rods confine the ions in the radial direction while axial motion is being controlled by the DC voltage applied to the lens. The octupole used here (see figure 4.4) is of dimension: rod length 150 mm, rod diameter 3 mm and the stainless steel rods are fixed on a teflon holder by maintaining the equation 4.5. It is fabricated in the institute machine workshop. The RF power is provided by a power supply made in house which is discussed in the following section. An extensive simulation is performed using an ion-optics simulation software called SIMION8 (Manura and Dahl, 2007) for this geometry and is described in a project report (Maryam, 2010). The initial conditions of ions like mass, charge, initial kinetic energy, initial position etc. and angle of projection of ions are defined using SIMION8 (Manura and Dahl, 2007). It also allows us to define ions singly or in a distribution. It is seen from the simulation (Maryam, 2010) that the stability of ions in the guide depends on the initial conditions as well as the parameters like amplitude and frequency of the RF field applied.

Making of RF power supply for octupole ionguide: Figure 4.5 shows the RF power supply made to provide both the RF amplitude (V) and RF frequency (Ω). The maximum RF amplitude applied through this is 600 V and the RF frequency ranges between

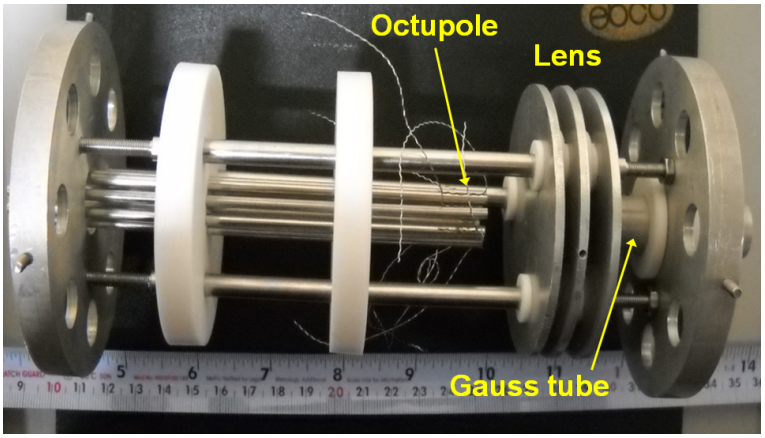

Figure 4.4: Octupole ion guide at AMP Lab, IIST.

600 KHz to 2.5 MHz (which are decided by the two type of inductor being used in the tank circuit). Within the same design, the provision of DC offset is also made. The circuit diagram is adapted from the work by Jones et al. (1997). The power supply gets power from the mains through a step down transformer and uses very robust pentode valves for running the circuit. An advanced version is under preparation to avoid the use of pentode valves which are commercially not available anymore in the market and for the miniaturization of the circuit. Shortest possible BNC cable are used to provide the output from the power supply to the rods of octupole. When not in use, the beam current measured on both the sets of rods together is $\sim$ 10 picoamperes.

The octupole ion guide functions at following parameter for the mass range 100 - 500 amu in the present set up:

i) RF amplitude: 400 V

ii) RF frequency: 1.5 MHz

iii) DC offset: 0 V

iv) Lens: 0 V:14 V (-Ve):0 V

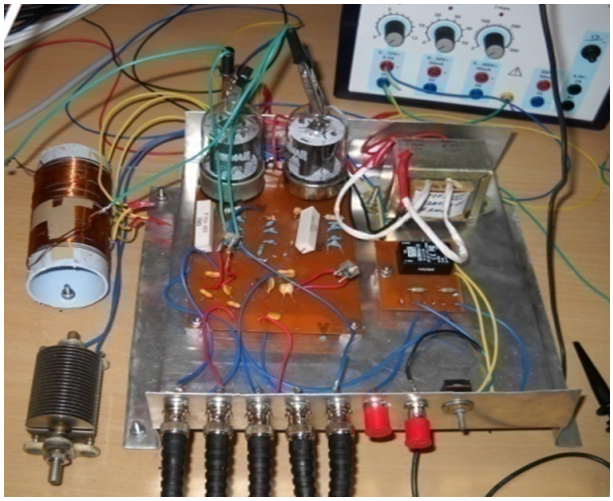

Figure 4.5: RF power supply for the octupole ion guide.

4.2.3 14-pole ion trap

Figure 4.6 shows that higher the order ($2n$) of trap device, the field free region approaches to box potential to a very good approximation (Gerlich, 1995) and near the electrodes, there is a very steep increase in effective potential which act as a barrier. As long as the ion is in the field free region, its energy is constant and there is no loss of ions due to RF heating. Because effective potential approximation will break down when the amplitude of micromotion (trajectories with frequency of the driving RF field) becomes higher than the secular motion (trajectories with relatively slower drift motion). Then the energy is exchanged between micromotion and secular motion, which will cause the increase of amplitude of secular motion and result in the loss of ions by colliding with the trap electrodes, called as "RF heating" (Wester, 2009). Hence such high field free multipole devices can be used for confining, storing, cooling of ions and precise measurement of different microscopic properties due to long storage time. Because in lower order multipole device, due to small field free region, the ions exchange energy upon interaction with the field (Gerlich, 1992), and hence cannot be used for collisional cooling. Due to large field free region in the centre, ions experience a reduced interac-

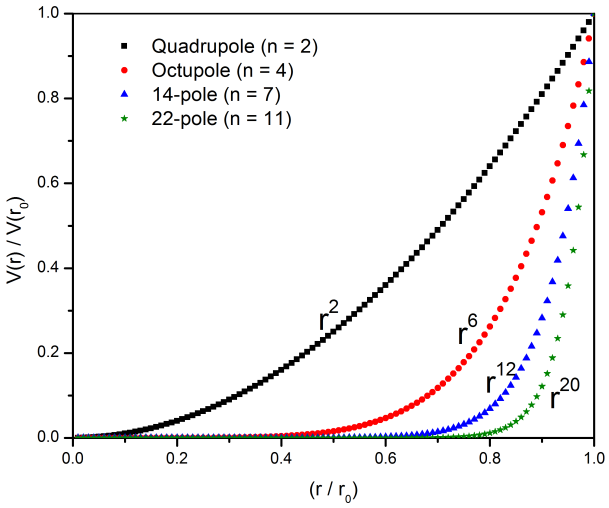

Figure 4.6: Effective potential as a function of distance from centre for various multipole devices plotted using equation V*.

tion time with the oscillating electric field (Otto et al., 2009). This allows one to obtain very low temperature and long storage time and therefore useful for measuring very small rate coefficients and vibrational ground state properties. The traps help us to do experiments on a single particle as well as on an ensemble of particles and therefore helpful for measuring individual properties and also ensemble properties (Jones et al., 1997). The disadvantage of higher order devices is that they are not very good mass filters unlike quadrupole. Multipole devices are used in many experiments where there is a need of precision spectroscopy, photoabsorption spectroscopy, photofragmentation spectroscopy, investigation of chemical reaction processes etc. This principle of handling ions also finds its importance in plasma physics, studying the properties of earth's atmosphere, interaction of electrons with microwave and laser fields etc (Gerlich, 1995). The method of trapping can be used to confine ions, clusters, electrons and charged microscopic particles using frequencies ranging from a few hertz to mega hertz (Gerlich, 2003).

The working principle and stable operation conditions are same as described above

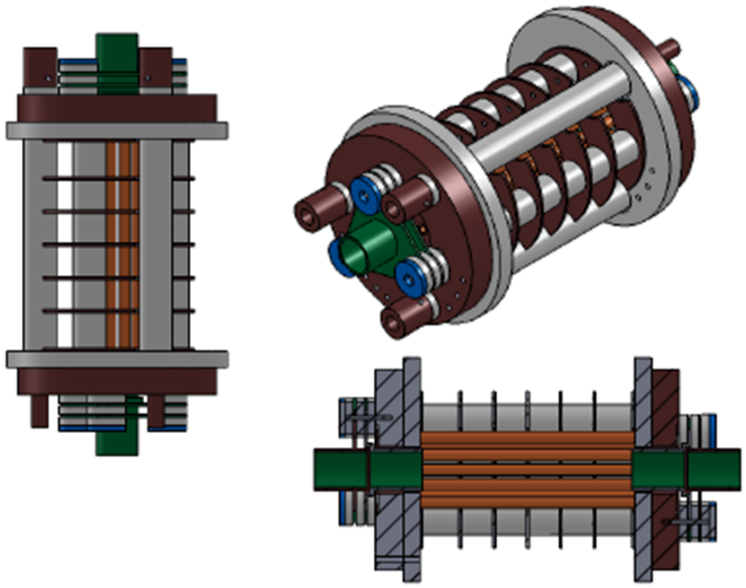

Figure 4.7: 3D mechanical drawing for 14-pole ion trap with lens holders.

for octupole ion guide and the optimum parameters are again derived using SIMION 8 simulation for the geometry and biasing condition (Maryam, 2010). The trap will consist of 14 stainless steel equal rods with alternate rods connected to opposite phase of RF. The similar type RF power supply mentioned above can be used for this purpose. Figure 4.7 shows the 3-dimensional mechanical drawing of 14-pole trap with lens holders using SOLIDWORKS software.The overall length of the trap with lenses is $\approx$ 80 mm with rod diameter 2 mm. The fabrication for this component is under progress.

Objective: This trap will be situated after the lens (see section 4.2.4) where the lens arrangement is followed by octupole ion guide. The studies involving reduced Doppler width in spectroscopy and population of internal states studies require lower energy ions (Otto et al., 2009). The purpose of this trap in future is to reduce the internal energy and translational energy of the molecular ions by colliding them with Helium buffer gas atoms (filled inside the trap) at a lower temperature. These ions will be thermalized to

the buffer gas temperature by undergoing repeated inelastic collisions with the buffer gas over a time period of about tens of milliseconds. We have adapted collisional cooling with light and inert gas for the following respective reasons: collision should only lead to loss of energy by ion and to avoid formation of background products by reaction with the excited ions (Gerlich, 1995). Helium is chosen because of its high vapor pressure at low temperature and light mass (Wester, 2009). Hence for collisional cooling high RF frequency, high mass ratio of ions and buffer gas and almost perfect trap geometry etc. are needed (Gerlich, 1992).

4.2.4 Gauss tube

The continuous ion source is pulsed with the help of a Gauss tube provided with high voltage pulse for a duration of hundreds of nanoseconds. The high voltage (V) requirement is to provide a known amount of high kinetic energy to the molecular ions which are cool down to vibrational ground state in the previous stage of set up (in ion trap) with the help of buffer gas cooling. The gauss tube is a cylindrical metallic tube. Hence the tube acts as a field free drift tube where the ions enter with a kinetic energy E,

$$E = qeV \tag{4.6}$$

where q = charge state of the ion, e = charge of an electron.
Hence the velocity of the ion is given by v

$$v = \sqrt{\frac{2qeV}{m}} \tag{4.7}$$

From equation 4.7, it is seen that for a given extraction field "V", the ions with a given value of $\sqrt{\frac{q}{m}}$ will have a given velocity and will take same time to be detected. This time t required to fly from extraction region to the detection region is known as

time of flight of ion.

$$t = A\sqrt{\frac{m}{q}} \tag{4.8}$$

where A is a constant and depends upon the geometry of the spectrometer and extraction field.

In a mass spectrometer, the goal is to find out the product masses after the intact molecular ion undergoes perturbations like photoexcitation (subject of current chapter), coulombic interaction (section 2.1), electromagnetic interaction (section 2.2). To achieve a good mass resolution (the largest mass, M, for which adjacent masses are well separated, i.e., that mass for which the time spread for ions just equals the time difference between the adjacent masses), the spatial and energy distribution of ions have to be minimum (Wiley and McLaren, 1955). The former is associated with the beam spread, but the later one is decided by pulse processing electronics. The width of the pulse decides the spread in energy. The pulsing is required to give a start trigger for measurement of the time-of-flight which gives the information for a mass to charge (m/q) ratio ion. Hence the requirement in accurate timing of signal becomes essential and demands for a fast switching, which is decided by the rise and fall time of the pulsing device.

Making of high voltage pulser for pulsing of ion beam: The high voltage pulser for pulsed extraction of ion beam is made in house. Figure 4.8 shows the circuit diagram for the HV pulser. The pulser on the circuit board is shown in figure 4.9 contains a transistor switch (Model number HTS 50 06) which consists of large number of MOSFETs in series and in parallel configuration controlled in a synchronized way by an external driving circuit. The control input circuit contains a TTL compatible control signal and 5 V DC bias. The impedance matching between switch, line and load is done by R_S. The transition time is decided by R_L. The R_B and C_B are added in the parallel to output to remove the noise.

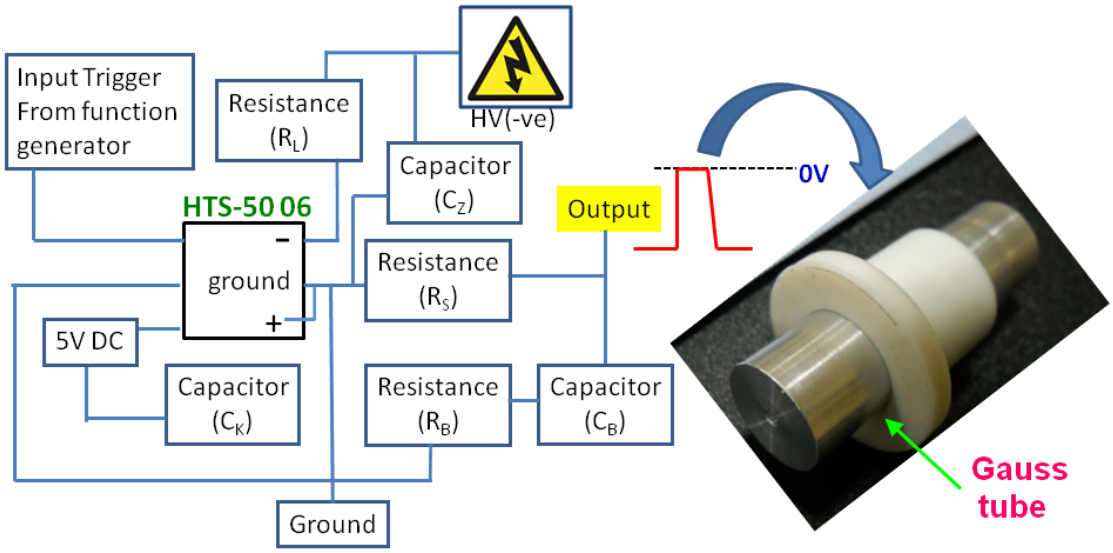

Figure 4.8: Circuit diagram for the HV pulser along with real Gauss tube.

Test results: Figure 4.9 shows the output pulse visualized on a oscilloscope. The spikes are due to the coupling capacitances between high voltage part and the control part. The switch has characteristic rise time 4 ns and width 150 ns. For our experimental set up the switch remains at -Ve high voltage for all the time and becomes 0V for 150 ns time interval. Hence the positive ions are extracted for 150 ns interval time with kinetic energy per charge state equal to the negative potential magnitude and the frequency at which the pulse is triggered. The following parameters are used for the test:

i) R_L = 1 kΩ

ii) R_S = 50 Ω

iii) R_B = 186 Ω

iv) C_B = 100 pF

v) C_K = 3.3 μF

vi) C_Z = 4700 pF (4 in series)

vii) High voltage = - 2000 V

Here the R_S consists of two 100 Ω resistors connected in parallel. The trigger input frequency is kept 100 Hz (duty cycle 50 %) with threshold for the TTL signal 3 V.

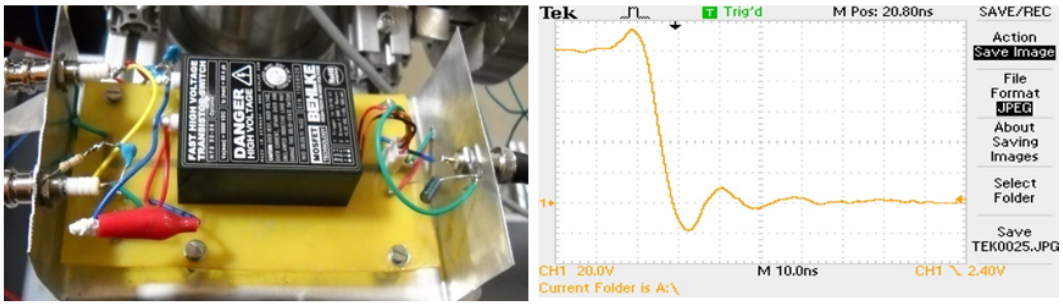

Figure 4.9: HV pulser on the circuit board (left) and pulse shape shown on oscilloscope(right).

The Gauss tube is made up of a cylindrical tube of length 50 mm with entrance opening 10 mm and exit opening 5 mm. The 40 lines per inch nickel wire mesh is mounted at the exit of gauss tube to maintain the field uniformity at the edge of the tube. This tube faces a ground plate with opening of 4 mm covered with a similar type of mesh for the same purpose. The gap between these two end is kept 5 mm because this is the distance a 2 keV ion of 100 amu travels in 150 ns time. For higher masses the distance traveled will be smaller. Figure 4.8 shows the Gauss tube with a teflon holder for electrical isolation.

4.2.5 Parallel plate electrostatic analyzer

Working principle: A Parallel plate analyzer (PPA) is an electrostatic energy analyzer which selects ions of a given energy-to-charge ratio depending on the electric field applied to it. It consists of a set of parallel plates separated by a distance and maintained at a specific potential difference. With respect to the entrance plate, the other plate(s) is biased to positive potential (for positive ions). The resultant component of electrostatic field between these plates and velocity of the ion causes the ion trajectories to travel in a parabolic path and finally the selected ions are detected using a detector placed at the

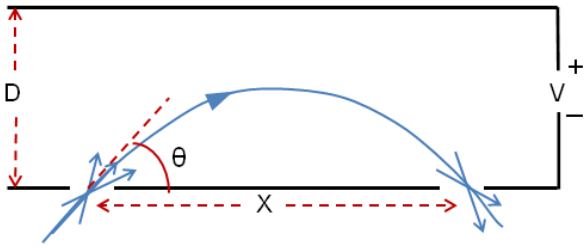

Figure 4.10: Parabolic trajectory of ion in electrostatic field between two plates.

exit of the analyzer. Due to the voltage configuration, only ions with a specific energy-to-charge ratio will enter the spectrometer. By varying the field between the charged plates, the entire spectrum of ion energies can be measured.

Let the distance between the plates be *D*, the horizontal range *x*, applied voltage *V*, *E* the incident energy of the ion, *q* the charge of the ion, ε is the electric field between the end plates of PPA and θ is the angle at which the ions enter the PPA.

The velocity in the X-direction ($v\cos\theta$) is constant because there is no acceleration in the horizontal direction. The displacement along this direction is:

$$x(t) = v\cos\theta t \tag{4.9}$$

While the motion along Y-direction is a parabolic trajectory because of the electrostatic field which gives an acceleration (vertical downward) to the particle $\frac{q\varepsilon}{m}$. The vertical component (in Y-direction) of the velocity changes linearly, because the acceleration due to field is constant. Hence the vertical displacement is:

$$y(t) = v\sin\theta t - \frac{q\varepsilon t^2}{2m} \tag{4.10}$$

The horizontal motion and the vertical motion are independent of each other. Combining equation 4.9 and 4.10, we get

$$y(x) = \tan\theta x - \frac{q\varepsilon}{2m(v\cos\theta)^2}x^2 \tag{4.11}$$

The above equation is equation for a parabola with $\theta, \varepsilon, m, q$ as constants.

The horizontal range R of the projectile is the horizontal distance the projectile has traveled when it returns to its initial height (i.e; y = 0).

Hence equating the equation 4.10 to zero, we get, time taken to reach the ground t = $\frac{2mv\sin\theta}{q\varepsilon}$. Using value of t in equation 4.9, we get the range (R) for the ions with same energy to charge ratio to travel:

$$x = R = \frac{mv^2}{q\varepsilon}\sin 2\theta \tag{4.12}$$

for θ = 45 °, R = $\frac{mv^2}{q\varepsilon}$ = $\frac{2E}{q\varepsilon}$ = $\frac{2Ed}{qV}$

Rearranging the above equation we get

$$\frac{E}{q} = \frac{R}{2d}V \tag{4.13}$$

where $\frac{R}{2d}$ is decided by the spectrometer geometry, and is a constant number. Hence for a given bias voltage V to the plate, the given ions of same $\frac{E}{q}$ are selected. In real situation the ion beam consists of a distribution of energy and the ions are oriented in all three possible direction. Hence for all this distribution we have done the ion optics simulation to decide the optimum parameters for the design of spectrometer as well as to achieve a good resolution (see the following section).

Ion-optics simulation for optimum parameters: In the present set up the pulsed molecular ion will be photo excited using a laser source to study the stability of molecular ions under UV and IR radiation impact. The energy deposited into the molecule under these excitation imparts momentum to different fragmented ions (formed as a result of interaction or excitation). Hence the fragments have momentum components in the direction other than the beam direction. This deviation from original direction could be in both azimuthal (θ) as well as elevation angle (ϕ) distribution. Hence to ac-

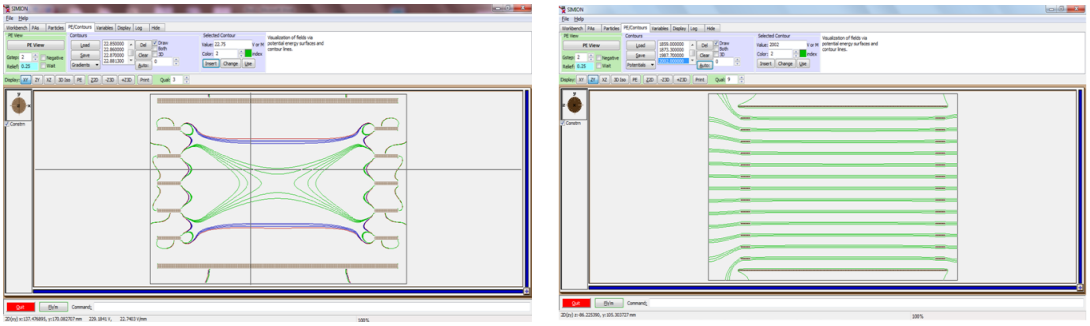

(a) (b)

Figure 4.11: Field lines inside the parallel plate analyzer with (a) 5, (b) 13 rectangular metallic frames between end plates.

commodate the full distribution and to detect them requires the spectrometer size to be large.

The deflection in the emitting angle (with respect to beam axis) decides the resolution and also provide information about the momentum imparted to it during the fragmentation. The deflection due to any other external source like non-uniformity in the field should be avoided. Since the energy resolution requirement makes the spectrometer large (range is larger) for our case, the gap between the end plates are large enough to introduce the fringe field inside the spectrometer and hence there is chance of ions getting deflected from their desired trajectories. For this purpose, to make the field uniform inside the spectrometer, a set of metallic rectangular frames are added in between the end plates. But the number of frames is decided by looking at the simulation results for the field lines. Figures 4.11a and 4.11b show the field lines between the plates using SIMION 8 and it is clearly shown by the simulations that the number of frames need to be higher to maintain better uniformity in the electric field inside the spectrometer. In this regard, a set of rectangular ring frames (for our case 13 frames separated by 8 mm) are put between the two end plates to keep the electric field uniform between them. The distortion in the field line is only outside the spectrometer as seen from simulations. To

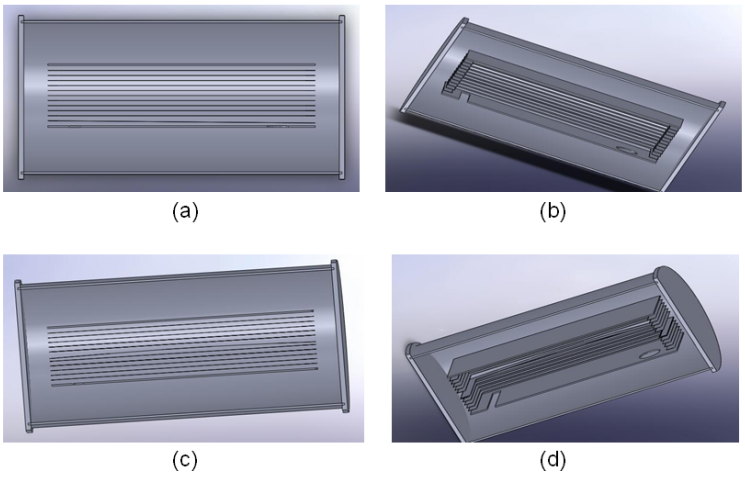

Figure 4.12: Possible mechanical defects in parallel plate analyzer with total 13 plates while fabrication.(a) 2nd plate tilted by $\phi = 0.5\,^{\circ}$, (b) 2nd plate tilted by $\theta = 1\,^{\circ}$ in its own plane, (c) 7th plate is bent down by 4 mm vertical, (d) 7th plate is bent down by 8 mm vertical.

have good mechanical strength and to avoid bending of plates, the thickness of plates are kept 2 mm. However our simulation for different type of mechanical defects (as shown in figure 4.12) showed no significant difference in field line uniformity. Hence for the fabrication purpose the tolerance values indicated in figure 4.12 are accepted.

The simulation for the resolution measurement of the spectrometer for different parameters with distribution like kinetic energy, azimuthal angle, elevation angle is shown in figure 4.13. The energy resolution is found to be 1/1000 for reasonably stable standard NIM power supplies and small acceptance beam entrance slit (width 1 mm).

Mechanical design and fabrication: As per the simulations for uniformity in electric field within spectrometer, resolution requirement, and enhancement in instrument detection efficiency, the mechanical design (see figures 4.14a and 4.14b) and fabrication for the PPA and its chamber is done (figure 4.15). The PPA plates are of length 640

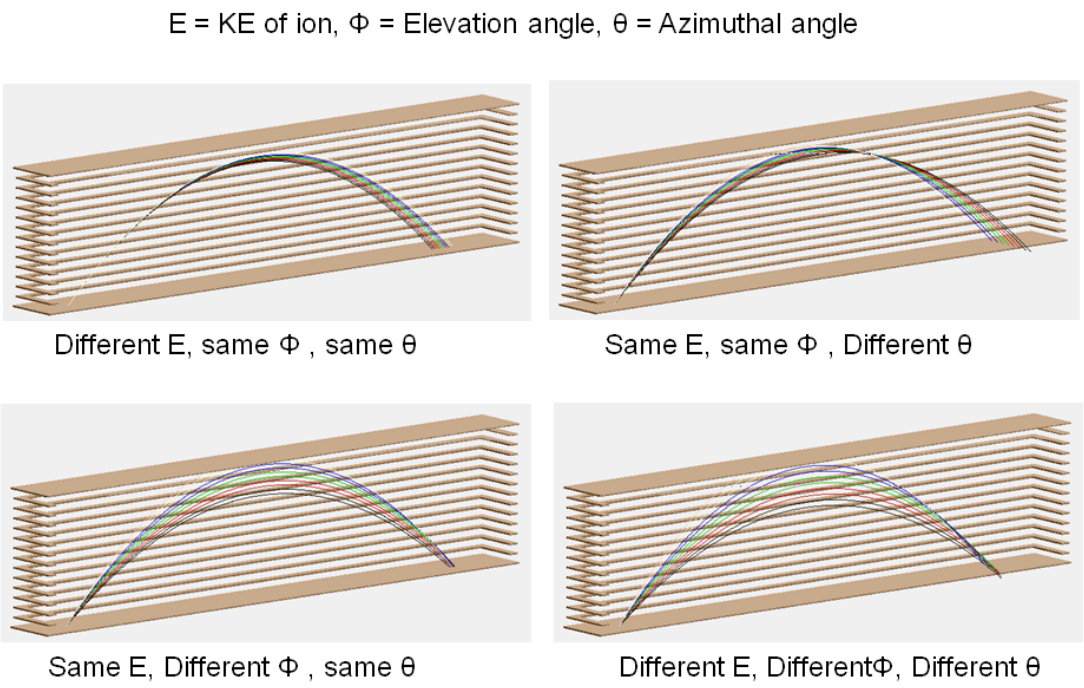

Figure 4.13: Simulation for the ions of different parameter entering parallel plate analyzer. The color part is showing the flying ions.

mm, thickness 2 mm and breadth 200 mm. The end plates are with width 4 mm. The full PPA set assembly is kept in a cylindrical chamber (see figure 4.15). The PPA and the chamber is made up of stainless steel. A 45 ° extension tube is added at the entrance opening of the spectrometer to provide a field free drift region with accurate alignment for the incoming ions. The spectrometer is mounted on an isolated tripod support with rotary feed through mechanism to align the spectrometer with the beam axis. The final alignment of the all the component is done with the help of a He-Ne laser. To avoid the fringe field due to the plate thickness at the entrance and exit, nickel wire mesh (40 lines per inch) is mounted at those places inside the spectrometer.

Test results: It is observed during the test that the reduction in the pressure with time was not exponential which can be attributed to the effect of leakage and out gassing. The

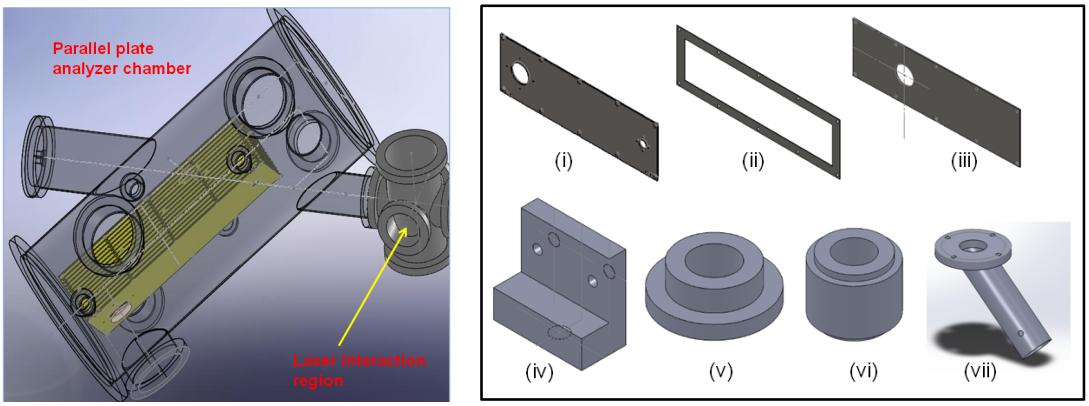

(a) (b)

Figure 4.14: Mechanical drawings for (a)Laser interaction chamber attached to PPA chamber, (b)components of PPA: i)Ion beam entrance plate, ii)Middle plate, iii)neutral exit plate, iv)PPA support bracket, v & vi) spacer, vii) 45 ° holder for grounding mesh.

PPA chamber was hence baked to outgas the chamber as much as possible. The chamber was heated up to a temperature of $70\,^{\circ}\mathrm{C}$ and the change in pressure were observed with the increase in heating and with time. This could be due to both out gassing and also increase in the kinetic energy of the gas inside the chamber. Since the baking tests were done at a pressure $\approx 10^{-7}$ mbar and considering the low density of particles inside the chamber at this pressure, the latter possibility can be ruled out.

A penning ion source is used to produce the atmospheric ions. To ensure that the ions are not deflected by the electric field due to the voltage applied to the PPA, before they enter the PPA, we use a hollow cylindrical tube (mounted at an 45 degree angle with respect to plane of the plates, see figure 4.15) to provide a field free path for the ions to enter the PPA. After the beam enters the spectrometer, the charged ions are deflected by the electric field and detected by a Faraday cup (a stainless steel plate for charge collection) for the first set of testing of parallel plate analyzer functioning (see

figure 4.16a for the experimental set up). Later these detection will be performed by using a delay line anode MCP detector (discussed later). Only ions of a specific energy to charge ratio are detected.

The 15 plates of spectrometer are connected to a voltage divider circuit (a resistance chain with 14 resistors in series) with each resistance of value 1 Megaohms (figure 4.15). The voltage divider circuit is tested for its high vacuum compatibility at high voltage condition. The current drawn from the power supply was observed to see if the resistances were still operational or any damage to the resistance chain has occurred. The pressure was observed to monitor the degassing process due to resistive heating of the chain. It is observed that at the maximum operating voltage of 3000 V, the pressure reached at a peak value of 1.6×10^{-6} mbar and dropped back to the initial pressure level (7.6×10^{-7} mbar). This increase in pressure is due to outgassing from the resistances. In addition to this, to maintain the field uniformity the resistance values for the resistors used in the voltage divider circuit are kept close as much as possible.

Depending on the kinetic energy of the ion E, (the bias potential on the ion source), the spectrometer pass energy (V) is selected by following the relation 4.13, which for our spectrometer geometry becomes

$$\frac{E}{q} = 1.81 \times V \tag{4.14}$$

where R = 500 mm and d = 138 mm

The tests are performed at ultra high vacuum condition ($\approx 10^{-8}$ mbar). This ensures a low density of molecules in the air so that the ions generated can be detected and analyzed without loss of energy due to collisions or interaction with other molecules. A set of two rotary pumps (throughput 20 m^3/hr) and two turbo molecular pumps (capacity 300 and 700 lit/sec) are used to achieve the required level of vacuum (nominal: 6.8×10^{-8} mbar, with ion source on: 1.0×10^{-5} mbar).

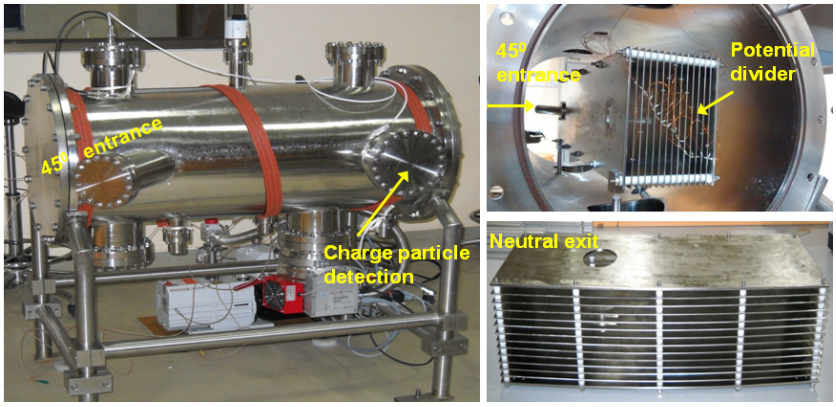

Figure 4.15: PPA chamber with pumping system attached (left), PPA inside chamber showing the 45 ° holder for grounding mesh allowing ion beam to enter at 45 ° (right top) and PPA (right bottom).

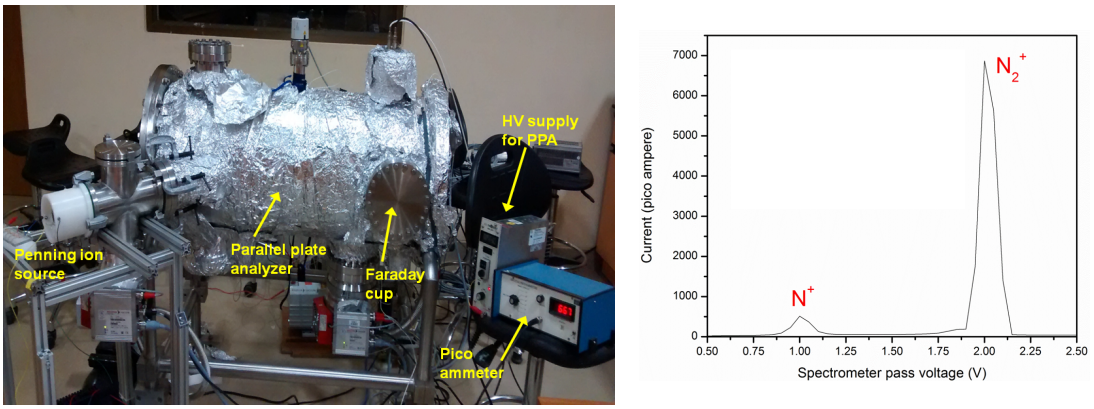

(a) (b)

Figure 4.16: (a) Testing of PPA using a penning ion source, (b) current measurement as a function of scanning voltage on the spectrometer.

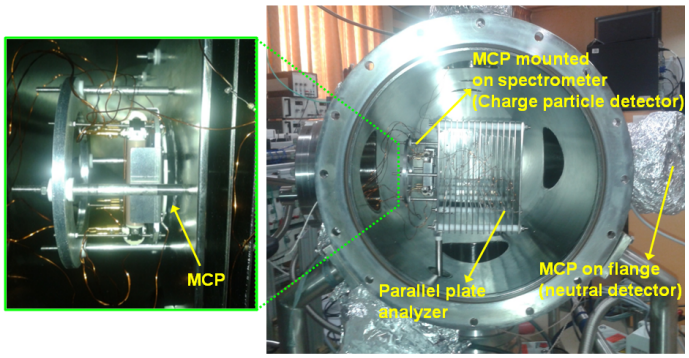

Figure 4.17: Delay line anode MCP detector mounted on spectrometer for charged particle detection and on a flange along the beam direction for neutral detection.

The ion source was operated at the total operating voltage of 4 kV. The produced ions are then accelerated towards the PPA chamber. The pass energy of the spectrometer or the voltage on the plates is scanned to obtain a significant current. For a given voltage, a given energy-to-charge ratio of ions will hit the Faraday cup by obeying the relation 4.14 and will give a peak in current measurement scan for those ions. The current measurement is performed using a pico ammeter. The scanning of voltage on plates (0.5 - 2.5 kV) results in two prominent peaks (see figure 4.16b) which corresponds to the singly charged molecular ions and atomic ion with energy $\approx$3.4 keV and $\approx$1.7 keV. The lower energy of the ions is because a small part of the voltage drop out of 4 kV is used to produce the plasma in the ion source. Since the ion source used here was a plasma ion source which uses atmospheric air which has nitrogen as the most abundant molecule, we attribute the peaks to singly charged nitrogen molecular and atomic ion, though in principle it scans for all the masses available in air with relative abundance. For this test we have discarded the possibility of doubly charged molecular ion formation due to high fragmentation probability.

In future plans, the experiments of coincidence measurement of neutral with ions de-

tection can be performed with this set up. In a fragmentation event, the charged fragment will be deflected and will travel a parabolic path to hit the MCP detector mounted on the spectrometer (figure 4.17). The neutrals formed in the same process travel straight along the beam direction and hit the second MCP detector (placed on a flange mounted on a port of PPA chamber along the path of the beam) (figure 4.17).

4.2.6 Position sensitive microchannel plate detector assembly and testing

Certain essential parameters for a detector system to be used in a mass spectrometer set up are:

1. Time resolution: The ability of detector to response fast enough to distinguish the particle which are hitting the detector in a very close time interval with respect to external trigger.

2. Spatial resolution: The ability to resolve the particle's position hitting the detector at different position.

3. Gain: It is the total number of secondary electrons generated for individual hit of ion.

4. Dark current: It is the electrical signal received in the external circuit when there is no particle hitting.

The MCP detector along with a delay line anode detector (DLD) system has the above parameters acceptable range for most of the molecular ion experiments. Hence these detectors are extensively used in mass spectrometer experimental set up. MCPs are widely used to detect electrons, ions, and photons. They are also used to measure

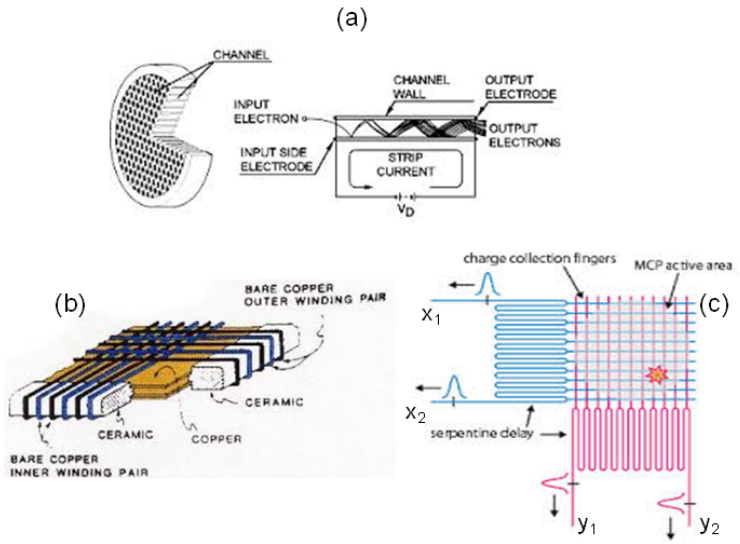

Figure 4.18: (a) Single MCP plate, (b) delay line anode structure, (c) electrical signal from DLD along two direction. Figures adapted from (DLD1, June 2014; DLD2, June 2014)

the ToF of ions with respect to an external trigger. These are disk shaped with several numbers of micrometer sized diameter holes arranged like an array and individual hole act as a CEM (figure 4.18a). The inner wall of these holes are coated with high resistive semiconductor material, so that the secondary emission of electron becomes easy and cascade of secondary electrons (10^6) are produced due to field emission from the channel walls when energetic ions hit the wall. For the present set up the diameter of each channel is 25 μm and ratio of length to diameter of the channel is 60. The MCP active diameter is 40 mm. The channel axis is kept at 8 $^\circ$ to minimize the loss of straight impinging ions onto the MCPs. In addition to this the pair of MCPs are arranged in chevron configuration. When particles hit MCP within a short period, the multi-hit detection capability of MCP enables it to deliver spatially and timely well-defined charge clouds for each particle.

A position sensitive detector typically comprises of MCPs with delay line anode (see inset of figure 4.19) such that the determination of fragment ion impact position (imaging) and fragment ion time-of-flight (timing) with respect to an external trigger is possible simultaneously. This anode is made up of crossed-wires in X and Y direction (figure 4.18b). Its position resolution is limited by the anode wire separation. In the present detector system it is 1 mm. Briefly, the delay line anode is two wires wound in a helical way over a copper plate supporting four ceramic holders placed at its four edges for electrical isolation. The wires are wound orthogonal to each other and thus covering XY plane (figure 4.18b). Thus there are four signals total. Each anode signal is again made to travel through a pair of wire twisted on each other. A small voltage difference (36 V) is applied between the twisted wires. This helps in better collection of charge cloud by one of the signal wire (figure 4.18c). The wire which is at high potential will always collect the electrons cloud with some noise but another wire will receive the noise signal. Hence the final output will be devoid of any noise when passed through a differential amplifier. An additional potential of 200 V is applied between the MCP and the delay line anode unit to accelerate the electron bunch to the delay-line anodes. Thus the incoming charge cloud from the MCP induces a differential signal on each delay line pair that propagates to the delay line ends where it is picked up by a fast differential preamplifier. To avoid noise, the signal is passed through a constant fraction discriminator. The amplifier and discriminator function for anode signal is performed by an unit called "ATR 19" (RoentDek, June 2014).

The detector is operated at pressure $< 2\times10^{-6}$ mbar. Typical voltage applied to the detector for the operations are
MCP front: -2100 V (23 μA)
MCP back: ground
Anode Reference: 200 V (0.05 μA)
Anode Signal: Anode Reference + 36 V

Figure 4.19: Pair of MCPs (chevron configuration) along with DLD as inset (RoentDek, June 2014) assembled on a CF160 flange (used for neutral particle detection.

Anode body: Ground

The position information from the detector is obtained by following method:

After the multiplication of electrons inside the channels of MCPs, the bunch of electrons hit the delay line wire in the form of a charge cloud, and two signals are produced from a short drop of voltage on each delay line wire. They propagate in both directions towards the ends of the line where impedance adjusted circuits pick it up for further processing. Hence there are four arrival times (x_1, x_2 and y_1, y_2) along the X-axis and Y-axis respectively (figure 4.18c). By measuring the difference between the signal arrival times on both ends of the delay line the position on anode where the particle has hit can be determined. The X and Y coordinates of a single event in time units can be calculated as (x_1-x_2, y_1-y_2) (figure 4.20). The precision in the position determination depends on the characteristic propagation time of the signal and the precision of the time measurement, but not on the length of the line.

The total propagation time along one wire is constant, $x_1 + x_2 = y_1 + y_2$. For data recording, the events which follow this condition are only taken into account. If more than one ion pulse strikes the MCP assembly, then each delay line produces a series

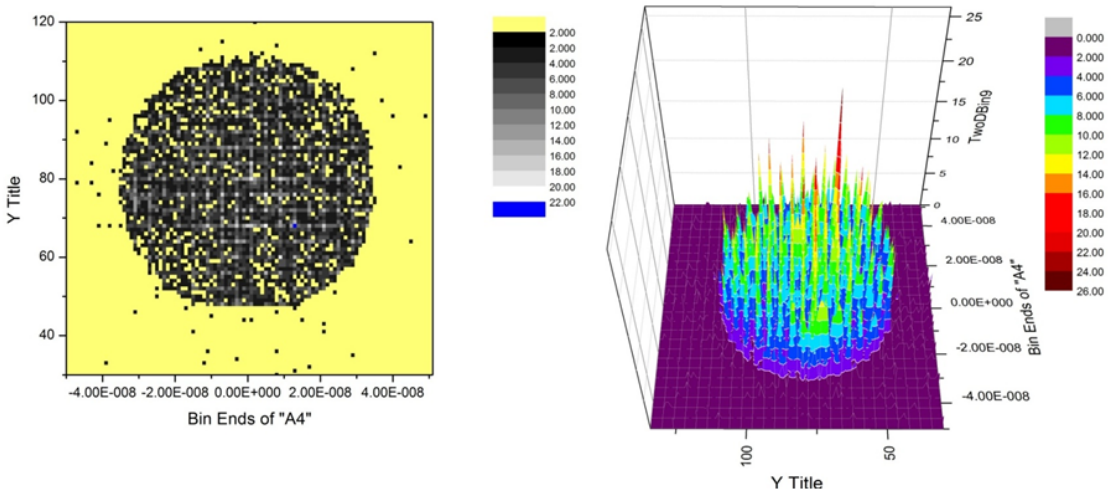

Figure 4.20: Position image using radioactive source in 2D (left) and 3D (right).

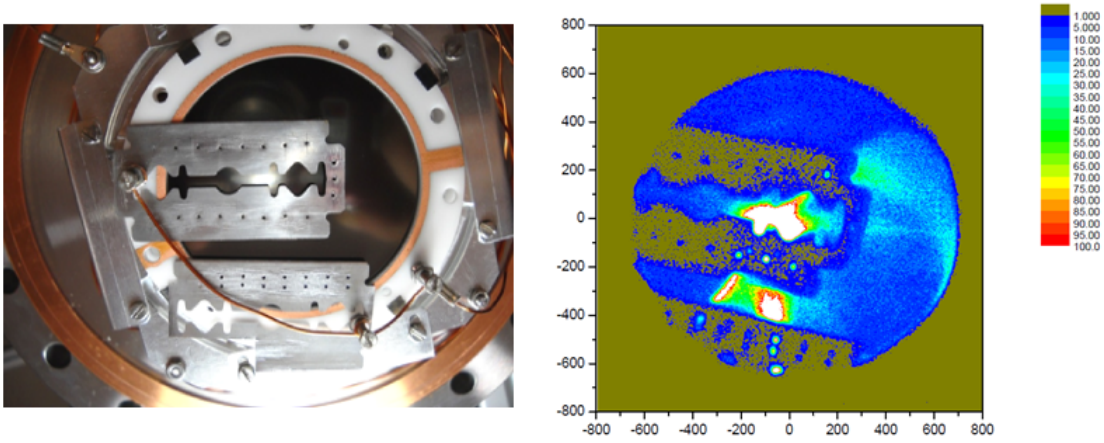

Figure 4.21: Resolution measurement with stainless steel mask (0.5 mm holes).

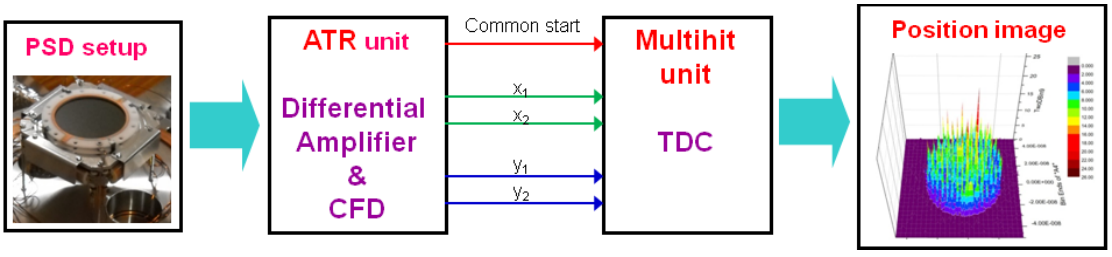

Figure 4.22: Block diagram of data acquisition system.

of pulses and the above criterion allows one to correctly assign individual pulses to individual ions, thereby distinguishing between true and false events. The ToF of the ion is determined from the flight time of the pulse recorded from the front plate of MCP with respect to an external trigger. The position resolution measurement for this detector system is performed up to an accuracy of 0.5 mm. This is done by using a stainless steel blade with 0.5 mm diameter holes with 1 micron tolerance in diameter. The figure 4.21 shows that 0.5 mm diameter corresponds to $\sim$20 ns in time unit.

4.3 Data acquisition system

Instead of using commercial off the self data acquisition (DAQ) electronics we have built our DAQ using various electronics modules as per our requirements. The details regarding specification for each module are discussed below. All the modules are Nuclear Instrumentation Module (NIM) based. Figure 4.22 shows the block diagram for our DAQ system.

Total 8 timing signal all together from delay line anode and a MCP signal are received from the detector. As discussed earlier the pair of anode signals are passed through the differentiator as a input which amplify the difference of signal giving a noise free output. Now these all four output signal from differentiator passes through the constant fraction discriminator (CFD). CFD reduces the time jitter and gives NIM signal of same amplitude. This is crucial because electrons cloud generated by MCP is not localized in time and has some spread in time. Also the all signal given by MCP does not have same amplitude. So CFD takes these signal as input signal, find the peak of signal and generates a NIM signal of -1 volt amplitude. Another function of CFD is to discriminate the true signal from noise by properly adjusting the threshold value. As noise signal amplitude will be always less than the true signal so the threshold value

should be set in such a way that it will not allow the noise signal to cross that threshold level but true signal can cross. But some time true signal is too low to cross the threshold and noise signal too high to block. So there will be some true signal loss in this case. In the present set up a unit named "ATR19" acts as both amplifier as well as CFD. Another important aspect is that since the interest is in measuring time-of-flight, hence the timing signals need to be very accurate, which can be provided by a NIM signal only with least jitter.

Time-to-digital converter (TDC) is a device which converts timing signal to digital values. It receives the NIM signal sent by the CFD. TDC requires fast rising edges with normed height which is provided by the CFD, a NIM pulse of normed height. The TDC here (Model: Agilent Acquiris) consists of 6 channels for input and one common trigger (figure 4.23 shows the TDC crate with two TDCs). The time measurement is done with respect to this common trigger. In this mass spectrometer set up, the common start trigger can be taken either from the ion beam pulser or laser ON time. The various possibilities of start and stop signal is shown in figure 4.23. Since the final objective is to measure in coincidence the neutrals and ions, we have two TDCs for two position sensitive detectors (PSDs). The 32 bit TDC used here has timing resolution 50 picoseconds with pulse pair resolution 10 ns and of unlimited multihit capability.

4.4 Interfacing of DAQ and time correlated pair of detectors

Hardware interfacing of detectors with TDC data acquisition software and real time processing of incoming data is done using a MATLAB program. The program generates the time and position information of incoming particle in real time and shows the histograms for different timing signals, histogram for x_1+x_2, y_1+y_2 and position image plot

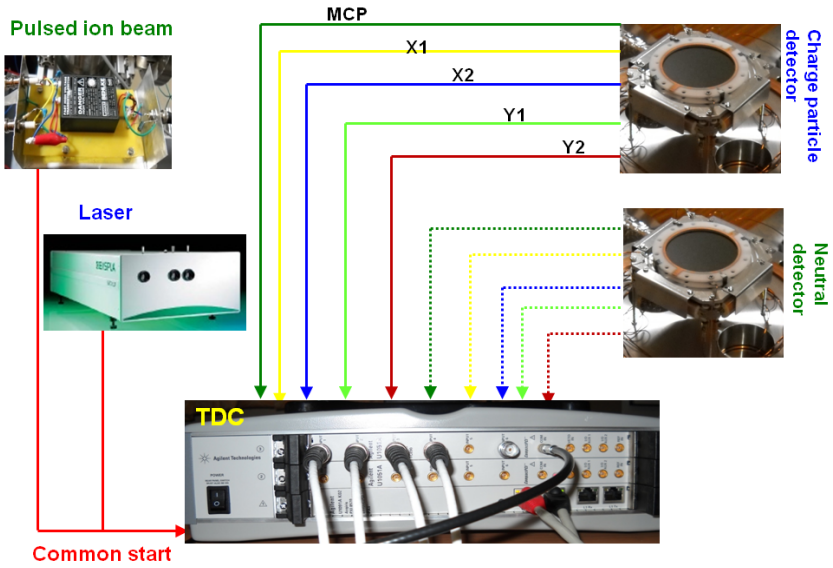

Figure 4.23: Time measurement using various possible start (either from laser or pulsed beam) and stop signals (PSD) with TDC.

in real time.

A function generator signal is used as an external trigger as well as stop for DAQ, to verify the validity of the program for different parameters like slope and frequency of the trigger, timing information, validation of the relation $x_1+x_2 = y_1+y_2$. The cable length for all the anode signals are same and are longer by 15 ns (10 feet long cable) than the MCP signal cable to provide sufficient delay in time between MCP front and the anode signals. The two important parameters associated with interfacing program are: "time out" and "number of counts" and these are correlated by a given relation:

time out $\geq$ number of counts x width of each pulse in common start

If number of counts for a given time out exceeds the maximum limit of counts then TDC does not give any data points for that data set. We have tested this relation with different frequency generated by a function generator keeping width of pulse 0.1 ms constant, the results are shown in table 4.1.

Table 4.1: Maximum counts recorded in TDC for different timeout.

Timeout (ms)	Maximum counts observed	Expected counts
10	100	100
20	209	200
30	299	300
40	390	400
50	499	500
60	599	600
70	698	700
80	809	800

For real signal analysis, using the program we have used a radioactive source (γ type, cobalt-60) kept outside the chamber facing the detector at an angle. The figures shown here are showing the data obtained using the MATLAB program with penning gauge as a source of particles (figures 4.24a, 4.24b and 4.25a). MCP front signal is used as a common start with four anode signals acting as stops and giving position information. As seen in figure 4.24b, the sum for anode signal in both direction comes $\approx$100ns.

Using two function generators, the start and stop signals were provided to both TDC (total 12 signals, 6 on each TDC) and the interfacing of both TDC DAQ software are performed and tested simultaneously using the MATLAB program for real time analysis as well as for multihit analysis.

4.5 Preliminary results

We have tested the set up using a biomolecule namely glycine ($C_2H_5NO_2$). Using the ESI, the glycine molecular ions were generated and then guided from atmospheric condition to vacuum region. The ion beams were extracted using the HV pulser and this pulser acts as a start trigger for time-of-flight measurement. Using a set of deflectors in both horizontal and vertical direction, the desired ions were deflected towards the

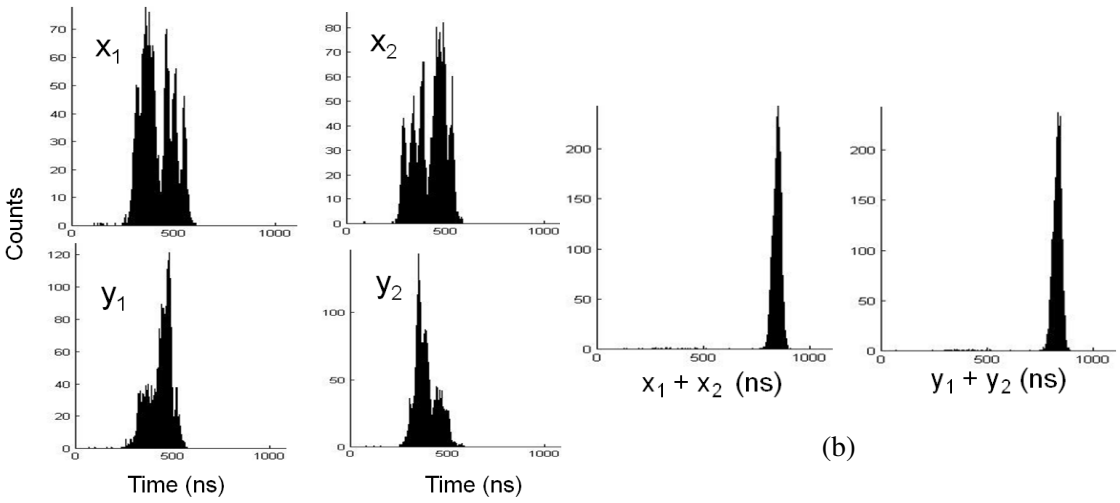

(a) (b)

Figure 4.24: (a) Histogram for individual anode signal, (b) sum of anode signals obtained from TDC using MATLAB program

MCP detector. This hit time is recorded as the stop signal. The pulses were provided to TDC after passing through differential amplifier and CFD. Using the MATLAB program the digital numbers were further processed to get the time-of-flight mass spectrum for glycine (figure 4.25b). In future the resolution has to be improved by improving the ion-optics for the beam to reduce the beam spread and divergence.

4.6 Future aspects of the set up

Cooling of ions inside ion trap: As discussed in "14 pole ion trap" section, to thermalize the molecular ions into vibrational ground state, the trap will be cooled with the liquid nitrogen and the molecular ions will be made to collide with inert gas.

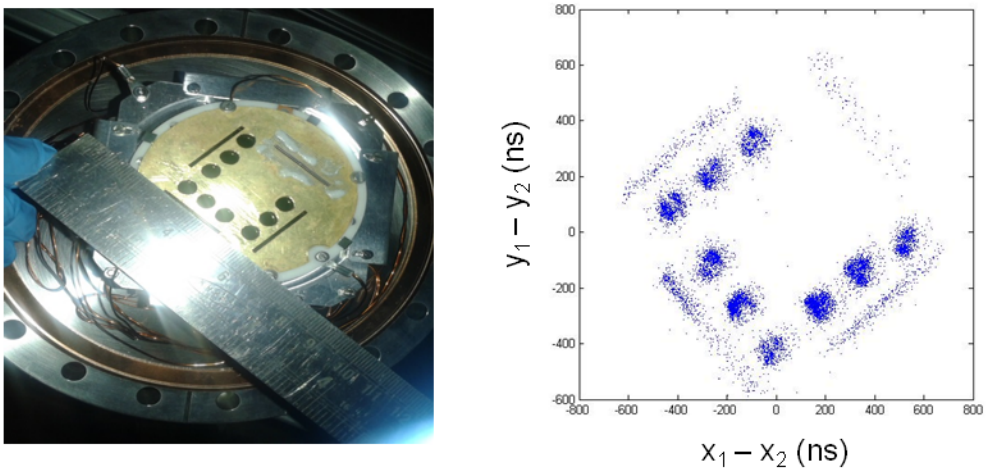

(a)

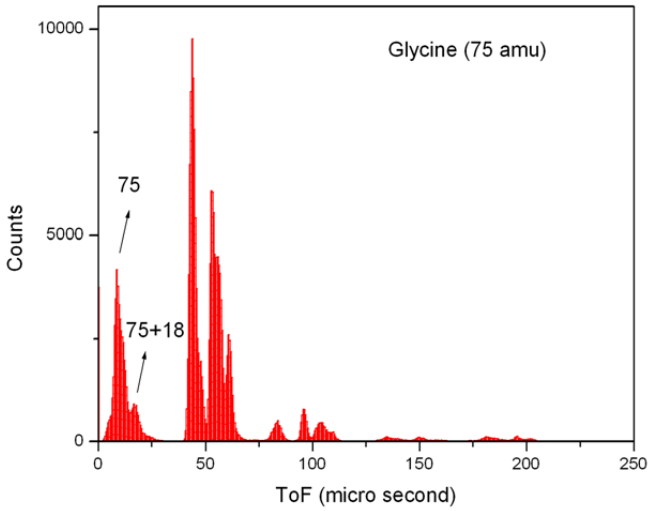

(b)

Figure 4.25: (a) Photograph of brass mask with 10 mm holes mounted on PSD (left) and position image obtained from TDC using MATLAB program with penning gauge as source of particles (right), (b) mass spectrum for glycine.

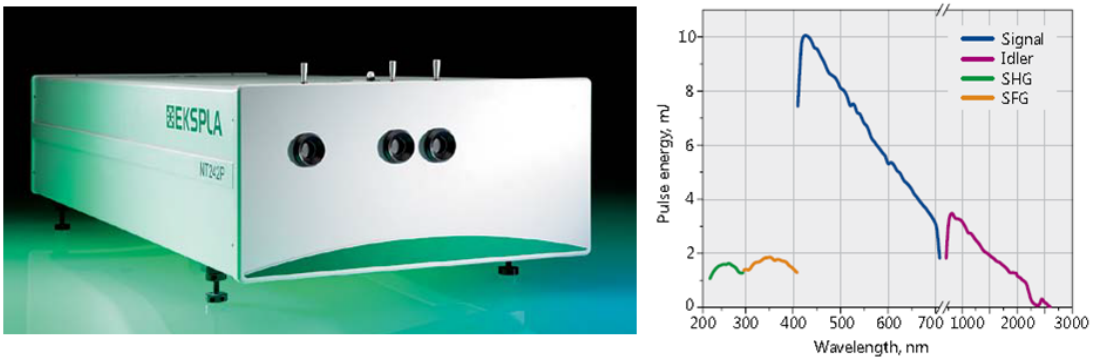

Figure 4.26: Laser for photoexcitation study (left) and typical output pulse energy (right). Figure adapted from (Laserdatasheet).

Laser induced photoexcitation: To understand the UV interaction dynamics of PAHs in ISM, the laser excitation study is proposed as a part of this mass spectrometer set up. The laser here used is a OPO based tunable one with wavelength regime UV to IR (210 to 2600 nm), Model: EKSPLA NT242P series. The laser has 10 mJ pulse energy, 100 Hz pulse repetition rate, 5 cm^{-1} line width, 3 - 6 ns pulse duration, beam diameter 4 mm.

The short duration of the laser pulse combined with mJ energy, when tightly focused in space, can result in sufficient amount of energy deposition into the molecule to excite them. In case of light-matter interaction, the phenomenon of quantization plays the role and deposits energy in quanta of $h\nu$. If the atom or molecule has energy levels separated by exactly $h\nu$, then the photon can be absorbed (or emitted) and the molecule can make a transition from one electronic state to another. This is the typical way of spectroscopy to probe the molecular structure as well as various dynamics as a consequence of electromagnetic interaction. Apart from this another approach to study such dynamics is to look into the residual ion(s) or neutrals formed after the interaction. This is the goal of the present experimental set up.

When a polyatomic molecule is exposed to electric fields of strength comparable to the intramolecular coulombic fields of the valence electrons, several valence electrons are stripped off. The resulting multiply charged complex is inherently unstable and eventually breaks apart into fragment ions and sometimes neutral along with the ions. We had already discussed another experimental way of producing such fragments in Chapter 2, i.e.; using energetic charge particle radiation (from ECR ion source). The dynamics of such interactions is governed by behavior of matter in strong field. The major parameters here are magnitudes, directional properties, and the time durations of the fields. Apart from this the time-dependent aspect of the field-target interaction is of special relevance to the molecules. Usually laser only provides the suitable time scales of interaction which are significant for molecules, whose typical rotational and vibrational time periods are tens of picoseconds and tens of femtoseconds, respectively. In the case of ion-induced fields, however, a beam of highly charged ions traverses a molecular dimension of a few angstroms in attosecond times. Hence in the later case essentially all internal degrees of freedom remain frozen during the interaction.

Ion-neutral in coincidence measurement: At a later stage the neutral and charged particle PSD detector will function together along with electrostatic analyzer to provide in coincidence measured data for single collision event in photon-molecule interaction. These data will be further processed using the MATLAB interfacing code to run both TDC software together in multihit mode. These measurements will provide the complete kinematical information (energy as well as momenta) for the fragment ions or neutrals associated with the dissociation mechanism upon laser interaction. The pulsed extraction of beam will provide the information for masses involved in the process.

CHAPTER 5

SUMMARY AND OUTLOOK

The main focus of this work has been the role of collective excitation in the high energy radiation interaction with PAHs. Various interesting and important conclusions have been drawn with the help of the mass spectrometric and electron spectroscopic techniques. In this process several data analysis techniques were used, particularly for the normalization process. Multicoincidence information in proton-PAH collision was used in an innovative manner to estimate various detection efficiencies in the absence of explicit measurement of the same. Similarly the photoelectron spectrometer efficiency was measured using Xe gas target data concurrently. An innovative method was used in the theoretical calculation of electron affinity to obtain the weighted average HOMA index to quantify the aromaticity in PAHs.

5.1 Photoelectron spectroscopy

Binding energy structure of a molecule can be explored very well with the help of PES. Two molecule from PAH family were investigated using synchrotron radiations. Using OVGF method, the MOs were identified as per their binding energy and symmetry. For complex molecules like PAHs, the PES is severely influenced by the electron-electron correlation effects leading to the breaking down of MO picture. In spite of the expected complications, the OVGF calculation reproduced the experimentally observed peaks in the PES to a reasonably good accuracy. For certain MOs, the vibrational progression is also visible in the PES, for which the Franck-Condon factors were calculated. These

calculations performed within DFT method could reproduce the positions as well as intensity of the vibrational progression for HOMO bands seen in pyrene and fluorene PES. This work also explores the significance of such vibrational progression in the context of UV induced IR fluorescence process in ISM. This work validates the theoretical tools used here which can be extended for other systems.

Rarely in the literature, a photon energy dependence of PES is reported for molecules. Often the theoretical tools also disregard this aspect. The basis of such simplification is the fact that beyond the ionization threshold, the outgoing electron rarely carries any other information. Collective excitation on the other hand is an intermediate process of photoabsorption as against direct photoionization. The present work demonstrates the coupling of collective excitation to the inner valence shell by systematically comparing the evolution of PES as a function of photon energy in FUV region.

5.2 Study of highly charged ions interacting with PAHs

Ion-PAH collisions have been very revealing in terms of role of collective excitation. This process supplements the other projectile energy loss mechanisms like nuclear and electronic energy loss. To a good extent the collective excitation is a special case of normal electronic stopping. The investigation presented here uses neutral evaporation and fragmentation as a measure of internal energy. A clear correlation is made between resonant electron transfer with small amount of electronic loss to the observed neutral evaporation rates. A similar comparison for the case of pure ionization process was correlated with the energetics of collective excitation.

The energetics of violent fragmentation has a more complex origin in the electronic energy loss process. Particularly so due to non-spherical nature of the target. This geometric nature is handled satisfactorily by doing *Monte Carlo* simulation within LDA

framework. In the intermediate projectile velocity with low charge state like proton. A comparison of these results with complementary measurements is reported in literature demonstrate the consistency of this simulation. The extension of this simulation to non-planar systems like nucleobases is also found to be qualitatively acceptable. But more investigation is needed theoretically as well as experimental to match the results quantitatively.

5.3 Excited state dynamics of PAHs and hybrid clusters

Production of molecular ions and their manipulation is of interest to study them in isolation. For such purposes an ion source with soft ionization technique is needed which is achieved by an ESI source. Here a developmental work is presented on such an ion source along with the design and fabrication of a ToF mass and momentum analyzer. This involves, pulsed extraction and acceleration of molecular ions produced *via* ESI with the help of RF ion guide and Gauss tube. These ions are then photoexcited using tunable laser and passed through a large parallel plate analyzer for momentum analysis.

CHAPTER 6

FUTURE PLANS

In many ways PAHs represent a model system to study the species with large delocalization. Clearly such investigation finds very close parallel to nanometers size metal clusters, an area which is emerging strongly due to its relevance in several applications. Similarly, biomolecular system are also finding more prominent place in molecular collision research. At this juncture, the method and understanding developed in this work can be easily extended to such systems. The following discussions take an overview of such possibilities and highlight the understanding emerged from this work.

PAH family is vast and certain structure attributes like presence of cyclopenta ring or one (or more) sp^3 hybridized carbon atoms substantially alters the electronic charge distribution on the molecule. This work has shown this effect in the case of the electron affinity of PAHs. For such cases it will be of great significance to measure the photoelectron spectrum. For anions of these molecules several such measurements have been attempted in past and still more study is needed. For neutrals these ionization energies lie in UV and FUV range. Such cases, synchrotron radiation based measurements will shade light on the state selective ionization processes. Break down of MO picture is an indicator of the strength of electron-electron coupling. This aspect also needs thorough investigation for PAHs as well as biomolecules. Strong theoretical models are very much desired for such results but they need to be validated experimentally.

Another aspect of PES is the PEPICO measurement. It is very informative to understand the secondary effects after the inner shell ionization. The assessment of fragmentation/dissociation/evaporation process for molecular targets is very much in need. One

such aspect studied here is the emission of neutral atomic and molecular hydrogen after the inner shell ionization in PAHs, which are used as a measure of internal energy and can very well be used for other systems. Such process is important for the abundance of molecular hydrogen as well as PAH cluster formation in ISM. Another system of great interest is nucleobase molecules. Their resistance to radiation damage is of central importance for the survivability of life on earth. Therefore a systematic measurement of dissociation dynamics under FUV radiation will be of great significance.

The intermediate velocity regime is rarely explored in ion-molecule collisions for relatively large molecular targets. Species like PAHs, metal clusters, biomolecules etc. will be interesting to study in this energy regime. The same energy range lies in Bragg peak region and hence acquires importance due to possible bio-medical effects. Charge particle interaction deposits energy in several modes of excitations which in turn exchange energy with each other post collision. The decay modes resulting from such interactions can be of statistical and nonstatistical by nature. The cases having competing rate constants for such processes will be interesting to study by ToF mass spectroscopy. Similarly resonant electron transfer process can be used to study the effect of electronic structure of target on its internal energy change. Systems with different target binding energy structures can be used to probe with proton and helium ion projectiles at intermediate velocities.

Electronic energy loss calculations using *Monte Carlo* simulation is another very powerful method devised in this work. A thorough validation of the results from this model is needed. Also the basic approach used here is LDA which in itself has a region of validity. These boundaries for validity need to be investigated for different molecular targets. Other possible energy loss formalisms can be readily incorporated in the same algorithm depending up on their validity and applicability as a function of projectile and target parameters.

The ability to form the clusters has made PAHs a very attractive proposition in ESI mass spectrometric studies. Computationally as well as experimentally such studies are done in past. But most of the studies have only demonstrated the existence of such clusters. More thorough investigation of their excited state properties is necessary to further understand them. An ESI based mass spectrometer equipped with a tunable fast laser provides such unique possibility.

REFERENCES

1. Abbas, I., Champion, C., Zarour, B., Lasri, B., and Hanssen, J. (2008). Single and multiple cross sections for ionizing processes of biological molecules by protons and α-particle impact: a classical Monte Carlo approach. *Physics in Medicine and Biology*, *53*, N41–N51.

2. Abdoul-Carime, H., Langer, J., Huels, M., and Illenberger, E. (2005). Decomposition of purine nucleobases by very low energy electrons. *The European Physical Journal D-Atomic, Molecular, Optical and Plasma Physics*, *35*, 399–404.

3. Agnihotri, A., Kasthurirangan, S., Nandi, S., Kumar, A., Galassi, M., Rivarola, R., Fojón, O., Champion, C., Hanssen, J., Lekadir, H. et al. (2012). Ionization of uracil in collisions with highly charged carbon and oxygen ions of energy 100 kev to 78 MeV. *Physical Review A*, *85*, 032711.

4. Allain, T., Leach, S., and Sedlmayr, E. (1996). Photodestruction of PAHs in the interstellar medium. I. Photodissociation rates for the loss of an acetylenic group. *Astronomy and Astrophysics*, *305*, 602–615.

5. Allamandola, L., Hudgins, D., and Sandford, S. (1999). Modeling the unidentified infrared emission with combinations of polycyclic aromatic hydrocarbons. *The Astrophysical Journal Letters*, *511*, L115–L119.

6. Allamandola, L., Tielens, A., and Barker, J. (1985). Polycyclic aromatic hydrocarbons and the unidentified infrared emission bands-Auto exhaust along the Milky Way. *The Astrophysical Journal*, *290*, L25–L28.

7. Allamandola, L., Tielens, A., and Barker, J. (1989). Interstellar polycyclic aromatic hydrocarbons-The infrared emission bands, the excitation/emission mechanism, and the astrophysical implications. *The Astrophysical Journal Supplement Series*, *71*, 733–775.

8. Alvarado, F., Bari, S., Hoekstra, R., and Schlathölter, T. (2006). Quantification of ion-induced molecular fragmentation of isolated 2-deoxy-D-ribose molecules. *Physical Chemistry Chemical Physics*, *8*, 1922–1928.

9. Alvarado, F., Bari, S., Hoekstra, R., and Schlathölter, T. (2007). Interactions of neutral and singly charged keV atomic particles with gas-phase adenine molecules. *The Journal of Chemical Physics*, *127*, 034301.

10. Andersen, L., Hvelplund, P., Knudsen, H., Møller, S., Elsener, K., Rensfelt, K.-G., and Uggerhøj, E. (1986). Single and double ionization of helium by fast antiproton and proton impact. *Physical Review Letters*, *57*, 2147–2150.

11. Arani, L. S., Mignon, P., Abdoul-Carime, H., Farizon, B., Farizon, M., and Chermette, H. (2012). DFT study of the fragmentation mechanism of uracil RNA base. *Physical Chemistry Chemical Physics*, *14*, 9855–9870.

12. Arnau, A., Pealba, M., Echenique, P., Flores, F., and Ritchie, R. (1990). Stopping power for helium in aluminum. *Physical Review Letters*, *65*, 1024–1027.

13. Atkins, P. W., and Friedman, R. S. (2011). *Molecular quantum mechanics*. (5th ed.). Oxford university press.

14. Azziz, Y. (2003). *Instrument development and plasma measurements on a 200-watt Hall thruster plume*. Ph.D. thesis Massachusetts Institute of Technology.

15. Bacchus-Montabonel, M., Łabuda, M., Tergiman, Y., and Sienkiewicz, J. (2005). Theoretical treatment of charge-transfer processes induced by collision of C^{q+} ions with uracil. *Physical Review A*, *72*, 052706.

16. Bacchus-Montabonel, M., and Tergiman, Y. (2006). Anisotropic effect in the charge transfer of C^{q+} ions with uracil. *Physical Review A*, *74*, 054702.

17. Bacchus-Montabonel, M., Tergiman, Y., and Talbi, D. (2009). Ab initio molecular treatment of charge-transfer processes induced by collision of carbon ions with 5-halouracil molecules. *Physical Review A*, *79*, 012710.

18. Bakes, E., and Tielens, A. (1994). The photoelectric heating mechanism for very small graphitic grains and polycyclic aromatic hydrocarbons. *The Astrophysical Journal*, *427*, 822–838.

19. Bakes, E., and Tielens, A. (1998). THE EFFECTS OF POLYCYCLIC AROMATIC HYDROCARBONS ON THE CHEMISTRY OF PHOTODISSOCIATION REGIONS. *The Astrophysical Journal*, *499*, 258–266.

20. Bakes, E., Tielens, A., and Bauschlicher Jr, C. W. (2001). THEORETICAL MODELING OF INFRARED EMISSION FROM NEUTRAL AND CHARGED POLYCYCLIC AROMATIC HYDROCARBONS. I. *The Astrophysical Journal*, *556*, 501–514.

21. Baldwin, G., and Klaiber, G. (1947). Photo-fission in heavy elements. *Physical Review*, *71*, 3–10.

22. Baltzer, P., Karlsson, L., Wannberg, B., Öhrwall, G., Holland, D., MacDonald, M., Hayes, M., and Von Niessen, W. (1997). An experimental and theoretical study of the valence shell photoelectron spectrum of the benzene molecule. *Chemical Physics*, *224*, 95–119.

23. Bapat, B., and Sharma, V. (2006). Mean kinetic energy of molecular fragment ions from time-of-flight and momentum analysis. *International Journal of Mass Spectrometry*, *251*, 10–15.

24. Bárány, A., Astner, G., Cederquist, H., Danared, H., Huldt, S., Hvelplund, P., Johnson, A., Knudsen, H., Liljeby, L., and Rensfelt, K.-G. (1985). Absolute cross sections for multi-electron processes in low energy Ar^{q+}- Ar collisions: Comparison with theory. *Nuclear Instruments and Methods in Physics Research Section B: Beam Interactions with Materials and Atoms*, *9*, 397–399.

25. Barone, V., Bloino, J., Biczysko, M., and Santoro, F. (2009). Fully integrated approach to compute vibrationally resolved optical spectra: from small molecules to macrosystems. *Journal of Chemical Theory and Computation*, *5*, 540–554.

26. de Barros, A., Lecointre, J., Luna, H., Shah, M., and Montenegro, E. (2009). Energy distributions of H^+ fragments ejected by fast proton and electron projectiles in collision with H_2O molecules. *Physical Review A*, *80*, 012716.

27. Bauschlicher Jr, C. W., Hudgins, D. M., and Allamandola, L. J. (1999). The infrared spectra of polycyclic aromatic hydrocarbons containing a five-membered ring: symmetry breaking and the b3lyp functional. *Theoretical Chemistry Accounts*, *103*, 154–162.

28. Becke, A. D. (1993). Density-functional thermochemistry. III. the role of exact exchange. *The Journal of Chemical Physics*, *98*, 5648–5652.

29. Bernard, J., Brédy, R., Chen, L., Martin, S., and Wei, B. (2006). Relative partial cross-sections and target fragmentation in ion-adenine collisions at 56keV. *Nuclear Instruments and Methods in Physics Research Section B: Beam Interactions with Materials and Atoms*, *245*, 103–107.

30. Bertsch, G. F., Bulgac, A., Tománek, D., and Wang, Y. (1991). Collective plasmon excitations in C_{60} clusters. *Physical Review Letters*, *67*, 2690–2693.

31. Bhardwaj, V., Corkum, P., and Rayner, D. (2003). Internal laser-induced dipole force at work in C_{60} molecule. *Physical Review Letters*, *91*, 203004.

32. Bhatt, P., Singh, R., Yadav, N., and Shanker, R. (2012). Formation, structure, and dissociation dynamics of CO_2^{q+} (q$\leq$3) ions due to impact of 12-keV electrons. *Physical Review A*, *85*, 042707.

33. Bini, R., Ebenhoch, J., Fanti, M., Fowler, P., Leach, S., Orlandi, G., Rüchardt, C., Sandall, J., and Zerbetto, F. (1998). The vibrational spectroscopy of $C_{60}H_{36}$: An experimental and theoretical study. *Chemical Physics*, *232*, 75–94.

34. Birks, J. B. (1970). *Photophysics of aromatic molecules*. London: Wiley Interscience.

35. Blyth, R., Delaunay, R., Zitnik, M., Krempasky, J., Krempaska, R., Slezak, J., Prince, K., Richter, R., Vondracek, M., Camilloni, R. et al. (1999). The high resolution gas phase photoemission beamline, elettra. *Journal of Electron Spectroscopy and Related Phenomena*, *101*, 959–964.

36. Boechat-Roberty, H. M., Neves, R., Pilling, S., Lago, A. F., and De Souza, G. G. B. (2009). Dissociation of the benzene molecule by ultraviolet and soft X-rays in circumstellar environment. *Monthly Notices of the Royal Astronomical Society*, *394*, 810–817.

37. Bohr, N., and Lindhard, J. (1954). Electron capture and loss by heavy ions penetrating through matter. *Det Kongelige Danske Videnskabernes Selskab Matematisk-fysiske Meddelelser*, *28*.

38. Bonderup, E. (1967). Stopping of swift protons evaluated from statistical atomic model. *Det Kongelige Danske Videnskabernes Selskab Matematisk-fysiske Meddelelser*, *35*, 1–19.

39. Bordenave-Montesquieu, D., Moretto-Capelle, P., Bordenave-Montesquieu, A., and Rentenier, A. (2001). Scaling of C_{60} ionization and fragmentation with the energy deposited in collisions with H^+, $H_2{}^+$, $H_3{}^+$ and He^+ ions (2-130 keV). *Journal of Physics B: Atomic, Molecular and Optical Physics*, *34*, L137–L146.

40. Boschi, R., Clar, E., and Schmidt, W. (1974). Photoelectron spectra of polynuclear aromatics. iii. the effect of nonplanarity in sterically overcrowded aromatic hydrocarbons. *The Journal of Chemical Physics*, *60*, 4406–4418.

41. Boschi, R., Murrell, J., and Schmidt, W. (1972). Photoelectron spectra of polycyclic aromatic hydrocarbons. *Faraday Discussions of the Chemical Society*, *54*, 116–126.

42. Bothe, J., and Tainter, C. (2006). An investigation in using Franck-Condon Factors to Simulate the Vibronic Spectrum of Iodine. *Journal of Physical Chemistry Lab*, *10*, 55–65.

43. BoudaıÌĹffa, B., Cloutier, P., Hunting, D., Huels, M. A., and Sanche, L. (2000). Resonant formation of DNA strand breaks by low-energy (3 to 20 eV) electrons. *Science*, *287*, 1658–1660.

44. Boyd, I. D., and Dressler, R. A. (2002). Far field modeling of the plasma plume of a Hall thruster. *Journal of Applied Physics*, *92*, 1764–1774.

45. Bréchignac, C., Cahuzac, P., Concina, B., Leygnier, J., Ruiz, L., Zarour, B., Hervieux, P., Hanssen, J., Politis, M., and Martín, F. (2002). Charge transfer and dissociation in collisions of metal clusters with atoms. *Physical Review Letters*, *89*, 183402.

46. Brédy, R., Bernard, J., Chen, L., Montagne, G., Li, B., and Martin, S. (2009). Fragmentation of adenine under energy control. *The Journal of Chemical Physics*, *130*, 114305.

47. Brédy, R., Bernard, J., Chen, L., Wei, B., Salmoun, A., Bouchama, T., Buchet-Poulizac, M., and Martin, S. (2005). Fragmentation of adenine induced by collision with slow F^{2+} ions. *Nuclear Instruments and Methods in Physics Research Section B: Beam Interactions with Materials and Atoms*, *235*, 392–396.

48. Browning, R., and Gilbody, H. (1968). Fragmentation of molecular gases by 5-45 keV protons. *Journal of Physics B: Atomic and Molecular Physics*, *1*, 1149–1156.

49. Bühl, M., and Hirsch, A. (2001). Spherical aromaticity of fullerenes. *Chemical Reviews*, *101*, 1153–1184.

50. Carlson, T. A., Gerard, P., Krause, M. O., Grimm, F. A., and Pullen, B. (1987). Photoelectron dynamics of the valence shells of benzene as a function of photon energy. *The Journal of Chemical Physics*, *86*, 6918–6926.

51. Carravetta, V., Yang, L., and Ågren, H. (1997). Partial channel photoionization cross sections of polyenes. *Physical Review B*, *55*, 10044–10050.

52. Carroll, F. A. (2011). *Perspectives on structure and mechanism in organic chemistry*. John Wiley & Sons.

53. Cederbaum, L. (1975). One-body Green's function for atoms and molecules: theory and application. *Journal of Physics B: Atomic and Molecular Physics*, *8*, 290–303.

54. Cederbaum, L., and Domcke, W. (). *Theoretical aspects of ionization potentials and photoelectron spectroscopy: A Green's function approach* volume 36. Wiley, New York.

55. Cederbaum, L., Domcke, W., Schirmer, J., and Von Niessen, W. (1980). Many-Body Effects in Valence and Core Photoionization of Molecules. *Physica Scripta*, *21*, 481–491.

56. Cederbaum, L., Schirmer, J., Domcke, W., and Von Niessen, W. (1977). Complete breakdown of the quasiparticle picture for inner valence electrons. *Journal of Physics B: Atomic and Molecular Physics*, *10*, L549–L553.

57. Cederbaum, L., Schirmer, J., Domcke, W., and Von Niessen, W. (1978). On the adequacy of the molecular-orbital picture for describing ionization processes. *International Journal of Quantum Chemistry*, *14*, 593–601.

58. Cederbaum, L. S. (1973). Direct calculation of ionization potentials of closed-shell atoms and molecules. *Theoretica Chimica Acta*, *31*, 239–260.

59. Champeaux, J.-P., Çarçabal, P., Sence, M., Moretto-Capelle, P., and Cafarelli, P. (2011). A simple 'statistical' approach for fragmentation studies of doubly ionized cytosine, thymine and uracil bases. *Journal of Physics B: Atomic, Molecular and Optical Physics*, *44*, 045205(6pp).

60. Champion, C., Galassi, M., Fojón, O., Lekadir, H., Hanssen, J., Rivarola, R., Weck, P., Agnihotri, A., Nandi, S., and Tribedi, L. (2012). Ionization of RNA-uracil by highly charged carbon ions. In *Journal of Physics Conference Series* (p. 012004). volume 373.

61. Champion, C., Lekadir, H., Galassi, M., Fojón, O., Rivarola, R., and Hanssen, J. (2010). Theoretical predictions for ionization cross sections of DNA nucleobases impacted by light ions. *Physics in Medicine and Biology*, *55*, 6053–6067.

62. Chancey, C. (1997). *The Jahn-Teller effect in C_{60} and other icosahedral complexes*. Princeton University Press.

63. Chen, E. S., and Chen, E. (2002). Electron-capture detector and multiple negative ions of aromatic hydrocarbons. *Journal of Chromatography A*, *952*, 173–183.

64. Chen, L., Brédy, R., Bernard, J., Montagne, G., Allouche, A., and Martin, S. (2011). Fragmentation of singly charged adenine induced by neutral fluorine beam impact at 3 keV. *The Journal of Chemical Physics*, *135*, 114309.

65. Chen, S.-A., Lu, H.-H., and Huang, C.-W. (2008). Polyfluorenes for device applications. In *Polyfluorenes* (pp. 49–84). Springer.

66. Clark, T., Chandrasekhar, J., Spitznagel, G. W., and Schleyer, P. V. R. (1983). Efficient diffuse function-augmented basis sets for anion calculations. III. The 3-21+G basis set for first-row elements, Li–F. *Journal of Computational Chemistry*, *4*, 294–301.

67. Cocke, C. (1979). Production of highly charged low-velocity recoil ions by heavy-ion bombardment of rare-gas targets. *Physical Review A*, *20*, 749.

68. Cocke, C., and Olson, R. E. (1991). Recoil ions. *Physics Reports*, *205*, 153–219.

69. Cole, L. A., and Perdew, J. (1982). Calculated electron affinities of the elements. *Physical Review A*, *25*, 1265.

70. Condon, E. (1926). A theory of intensity distribution in band systems. *Physical Review*, *28*, 1182.

71. Condon, E. U. (1928). Nuclear motions associated with electron transitions in diatomic molecules. *Physical Review*, *32*, 858.

72. Coupier, B., Farizon, B., Farizon, M., Gaillard, M., Gobet, F., de Castro Faria, N., Jalbert, G., Ouaskit, S., Carré, M., Gstir, B. et al. (2002). Inelastic interactions of protons and electrons with biologically relevant molecules. *The European Physical Journal D-Atomic, Molecular, Optical and Plasma Physics*, *20*, 459–468.

73. Dabestani, R., and Ivanov, I. N. (1999). A compilation of physical, spectroscopic and photophysical properties of polycyclic aromatic hydrocarbons. *Photochemistry and photobiology*, *70*, 10–34.

74. De, S., Ghosh, P., Roy, A., and Safvan, C. (2006). A setup for probing ion–molecule collision dynamics. *Nuclear Instruments and Methods in Physics Research Section B: Beam Interactions with Materials and Atoms*, *243*, 435–441.

75. De Vries, J., Hoekstra, R., Morgenstern, R., and Schlathölter, T. (2002). C^{q+}–induced excitation and fragmentation of uracil: effects of the projectile electronic structure. *Journal of Physics B: Atomic, Molecular and Optical Physics*, *35*, 4373.

76. De Vries, J., Hoekstra, R., Morgenstern, R., and Schlathölter, T. (2003a). Charge driven fragmentation of nucleobases. *Physical Review Letters*, *91*, 053401.

77. De Vries, J., Hoekstra, R., Morgenstern, R., and Schlathölter, T. (2003b). Multiple ionization and fragmentation of the DNA base thymine by interaction with C^{q+} ions.

The European Physical Journal D-Atomic, Molecular, Optical and Plasma Physics, *24*, 161–164.

78. De Vries, J., Hoekstra, R., Morgenstern, R., and Schlathölter, T. (2004). Ionization and fragmentation modes of nucleobases after collisions with multiply charged ions. *Physica Scripta*, *2004*, 336–339.

79. Deleuze, M. S. (2002). Valence one-electron and shake-up ionization bands of polycyclic aromatic hydrocarbons. II. Azulene, phenanthrene, pyrene, chrysene, triphenylene, and perylene. *The Journal of Chemical Physics*, *116*, 7012–7026.

80. Denifl, S., Sonnweber, B., Hanel, G., Scheier, P., and Märk, T. (2004). Threshold electron impact ionization studies of uracil. *International Journal of Mass Spectrometry*, *238*, 47–53.

81. Dierksen, M., and Grimme, S. (2005). An efficient approach for the calculation of Franck–Condon integrals of large molecules. *The Journal of Chemical Physics*, *122*, 244101.

82. DLD1 (June 2014). Microchannel plate (MCP) detectors. `http://www.atom.uni-frankfurt.de/research/coltrims/mcp/`.

83. DLD2 (June 2014). Molecular Photonics Group. `http://www.chem.queensu.ca/people/faculty/Stolow/Research/Facilities.html`.

84. Dong, S., Hwang, H.-M., Harrison, C., Holloway, L., Shi, X., and Yu, H. (2000). UVA light-induced DNA cleavage by selected polycyclic aromatic hydrocarbons. *Bulletin of environmental contamination and toxicology*, *64*, 467–474.

85. Dreizler, R. M., and Gross, E. K. (1990). *Density functional theory*. Springer-Verlag, Berlin Heidelberg, New York, 1990.

86. DuBois, R., Toburen, L., and Rudd, M. (1984). Multiple ionization of rare gases by H^+ and He^+ impact. *Physical Review A*, *29*, 70–76.

87. Duley, W. (2006). A plasmon resonance in dehydrogenated coronene ($C_{24}H_x$) and its cations and the origin of the interstellar extinction band at 217.5 nanometers. *The Astrophysical Journal Letters*, *639*, L59–L62.

88. Duley, W., and Williams, D. (1981). The infrared spectrum of interstellar dust-surface functional groups on carbon. *Monthly Notices of the Royal Astronomical Society*, *196*, 269–274.

89. Dunning Jr, T. H. (1989). Gaussian basis sets for use in correlated molecular calculations. I. the atoms boron through neon and hydrogen. *The Journal of Chemical Physics*, *90*, 1007–1023.

90. Eisenberg, D., and Shenhar, R. (2012). Polyarene anions: interplay between theory and experiment. *Wiley Interdisciplinary Reviews: Computational Molecular Science*, *2*, 525–547.

91. Ekern, S. P., Marshall, A. G., Szczepanski, J., and Vala, M. (1998). Photodissociation of gas-phase polycylic aromatic hydrocarbon cations. *The Journal of Physical Chemistry A*, *102*, 3498–3504.

92. ESI1 (June 2014). `http://www.spraybase.com/`.

93. ESI2 (June 2014). `http://web.mit.edu/aeroastro/labs/spl/research_ieps.htm`.

94. Fahlman, A., Krause, M. O., Carlson, T. A., and Svensson, A. (1984). Xe *5s, 5p* correlation satellites in the region of strong interchannel interactions, 28–75 eV. *Physical Review A*, *30*, 812–819.

95. Feil, S., Gluch, K., Matt-Leubner, S., Scheier, P., Limtrakul, J., Probst, M., Deutsch, H., Becker, K., Stamatovic, A., and Märk, T. (2004). Partial cross sections for positive and negative ion formation following electron impact on uracil. *Journal of Physics B: Atomic, Molecular and Optical Physics*, *37*, 3013–3020.

96. Fenn, J. (2002). Electrospray ionization mass spectrometry: How it all began. *Journal of Biomolecular Techniques: JBT*, *13*, 101–118.

97. Ferrell, T., and Ritchie, R. (1977). Energy losses by slow ions and atoms to electronic excitation in solids. *Physical Review B*, *16*, 115–123.

98. Fife, J. M. (1999). *Hybrid-PIC modeling and electrostatic probe survey of Hall thrusters*. Ph.D. thesis Department of Aeronautics and Astronautics, Massachusetts Institute of Technology.

99. Finston, H., and Rychtman, A. (1987). A New View of Current Acid–Base Theories, 1982.

100. Forsberg, B., Alexander, J. D., Chen, T., Pettersson, A., Gatchell, M., Cederquist, H., and Zettergren, H. (2013). Ions interacting with planar aromatic molecules: Modeling electron transfer reactions. *The Journal of Chemical Physics*, *138*, 054306.

101. Franck, J., and Dymond, E. (1926). Elementary processes of photochemical reactions. *Transactions of the Faraday Society*, *21*, 536–542.

102. Frisch, M. J., Trucks, G. W., Schlegel, H. B., Scuseria, G. E., Robb, M. A., Cheeseman, J. R., Scalmani, G., Barone, V., Mennucci, B., Petersson, G. A., Nakatsuji, H., Caricato, M., Li, X., Hratchian, H. P., Izmaylov, A. F., Bloino, J., Zheng, G., Sonnenberg, J. L., Hada, M., Ehara, M., Toyota, K., Fukuda, R., Hasegawa, J., Ishida, M., Nakajima, T., Honda, Y., Kitao, O., Nakai, H., Vreven, T., Montgomery, J. A., Jr., Peralta, J. E., Ogliaro, F., Bearpark, M., Heyd, J. J., Brothers, E., Kudin, K. N., Staroverov, V. N.,

Kobayashi, R., Normand, J., Raghavachari, K., Rendell, A., Burant, J. C., Iyengar, S. S., Tomasi, J., Cossi, M., Rega, N., Millam, J. M., Klene, M., Knox, J. E., Cross, J. B., Bakken, V., Adamo, C., Jaramillo, J., Gomperts, R., Stratmann, R. E., Yazyev, O., Austin, A. J., Cammi, R., Pomelli, C., Ochterski, J. W., Martin, R. L., Morokuma, K., Zakrzewski, V. G., Voth, G. A., Salvador, P., Dannenberg, J. J., Dapprich, S., Daniels, A. D., Farkas, ., Foresman, J. B., Ortiz, J. V., Cioslowski, J., and Fox, D. J. (2009). Gaussian 09 Revision D.01. Gaussian Inc. Wallingford CT 2009.

103. Furche, F., and Ahlrichs, R. (2004). Erratum:"Time-dependent density functional methods for excited state properties". *The Journal of Chemical Physics*, *121*, 12772–12773.

104. Galassi, M., Champion, C., Weck, P., Rivarola, R., Fojón, O., and Hanssen, J. (2012). Quantum-mechanical predictions of DNA and RNA ionization by energetic proton beams. *Physics in Medicine and Biology*, *57*, 2081–2099.

105. Gerlich, D. (1992). Inhomogeneous RF fields: a versatile tool for the study of processes with slow ions. *Advances in Chemical Physics*, *82*, 1–176.

106. Gerlich, D. (1995). Ion-neutral collisions in a 22-pole trap at very low energies. *Physica Scripta*, *1995*, 256–263.

107. Gerlich, D. (2003). Molecular Ions and Nanoparticles in RF and AC traps. *Hyperfine Interactions*, *146*, 293–306.

108. Ghosh, P. K. (1995). *Ion traps*. Clarendon press Oxford.

109. Gobet, F., Eden, S., Coupier, B., Tabet, J., Farizon, B., Farizon, M., Gaillard, M., Carré, M., Ouaskit, S., Märk, T. et al. (2004). Ionization of water by (20–150) keV protons: Separation of direct-ionization and electron-capture processes. *Physical Review A*, *70*, 062716.

110. Gobet, F., Farizon, B., Farizon, M., Gaillard, M., Carré, M., Lezius, M., Scheier, P., and Märk, T. (2001). Total, partial, and electron-capture cross sections for ionization of water vapor by 20–150 keV protons. *Physical Review Letters*, *86*, 3751–3754.

111. Goebel, D. M., and Katz, I. (2008). *Fundamentals of electric propulsion: ion and Hall thrusters* volume 1. John Wiley & Sons.

112. Gotkis, Y., Oleinikova, M., Naor, M., and Lifshitz, C. (1993). Time-dependent mass spectra and breakdown graphs. 17. Naphthalene and Phenanthrene. *The Journal of Physical Chemistry*, *97*, 12282–12290.

113. Hadjar, O., Földi, P., Hoekstra, R., Morgenstern, R., and Schlathölter, T. (2000). Z oscillations in ion-induced fullerene fragmentation. *Physical Review Letters*, *84*, 4076–4079.

114. Harvey, R. G. (1991). *Polycyclic aromatic hydrocarbons: chemistry and carcinogenicity*. CUP Archive.

115. Hertel, I., Steger, H., De Vries, J., Weisser, B., Menzel, C., Kamke, B., and Kamke, W. (1992). Giant plasmon excitation in free C_{60} and C_{70} molecules studied by photoionization. *Physical Review Letters*, *68*, 784–787.

116. Herzberg, G., and Teller, E. (1933). Schwingungsstruktur der elektronenübergänge bei mehratomigen molekülen. *Zeitschrift für Physikalische Chemie B*, *21*, 410.

117. Hirata, S., Lee, T. J., and Head-Gordon, M. (1999). Time-dependent density functional study on the electronic excitation energies of polycyclic aromatic hydrocarbon radical cations of naphthalene, anthracene, pyrene, and perylene. *The Journal of Chemical Physics*, *111*, 8904–8912.

118. Ho, Y.-P., Dunbar, R. C., and Lifshitz, C. (1995). CH Bond Strength of Naphthalene

Ion. A Reevaluation Using New Time-Resolved Photodissociation Results. *Journal of the American Chemical Society*, *117*, 6504–6508.

119. Holm, A., Zettergren, H., Gatchell, M., Johansson, H., Seitz, F., Schmidt, H., Rousseau, P., Ławicki, A., Capron, M., Domaracka, A. et al. (2012). Ionization and fragmentation of cold clusters of PAH molecules–collisions with keV ions. In *Journal of Physics: Conference Series* (p. 012051). IOP Publishing volume 388.

120. Holm, A. I., Johansson, H. A., Cederquist, H., and Zettergren, H. (2011). Dissociation and multiple ionization energies for five polycyclic aromatic hydrocarbon molecules. *The Journal of Chemical Physics*, *134*, 044301.

121. Holm, A. I., Zettergren, H., Johansson, H. A., Seitz, F., Rosen, S., Schmidt, H. T., Ławicki, A., Rangama, J., Rousseau, P., Capron, M. et al. (2010). Ions colliding with cold polycyclic aromatic hydrocarbon clusters. *Physical Review Letters*, *105*, 213401.

122. Hudgins, D., Bauschlicher, C., Allamandola, L., and Fetzer, J. (2000). Infrared spectroscopy of matrix-isolated polycyclic aromatic hydrocarbon ions. 5. PAHs incorporating a cyclopentadienyl ring. *The Journal of Physical Chemistry A*, *104*, 3655–3669.

123. Imhoff, M., Deng, Z., and Huels, M. A. (2005). Identification of ion fragments produced from thymine and deuterated thymine by low energy ion impact in films and electron impact in the gas phase. *International Journal of Mass Spectrometry*, *245*, 68–77.

124. Imhoff, M., Deng, Z., and Huels, M. A. (2007). Ionizing fragmentation of uracil and 5-bromouracil by electron impact in gas phase and hyperthermal Ar^+ ion irradiation in condensed phase. *International Journal of Mass Spectrometry*, *262*, 154–160.

125. Iriki, Y., Kikuchi, Y., Imai, M., and Itoh, A. (2011a). Absolute doubly differential cross sections for ionization of adenine by 1.0-MeV protons. *Physical Review A*, *84*, 032704.

126. Iriki, Y., Kikuchi, Y., Imai, M., and Itoh, A. (2011b). Proton-impact ionization cross sections of adenine measured at 0.5 and 2.0 meV by electron spectroscopy. *Physical Review A*, *84*, 052719.

127. Itoh, T. (2005). Franck-Condon analysis of the absorption and fluorescence spectra of all transα, ω-diphenylpolyenes with one to seven polyene double bonds. *The Journal of Chemical Physics*, *123*, 064302.

128. Jaffé, H. H. (1967). *Symmetry in chemistry*. New York: Wiley Publications.

129. Janev, R., Wang, J., and Kato, T. (2002). Charge exchange cross section database for proton collisions with hydrocarbon molecules. *Atomic and Plasma-material Interaction Data for Fusion*, (p. 129).

130. Jochims, H., Baumgärtel, H., and Leach, S. (1999). Structure-dependent photostability of polycyclic aromatic hydrocarbon cations: Laboratory studies and astrophysical implications. *The Astrophysical Journal*, *512*, 500–510.

131. Jochims, H., Rühl, E., Baumgärtel, H., Tobita, S., and Leach, S. (1994). Size effects on dissociation rates of polycyclic aromatic hydrocarbon cations: Laboratory studies and astophysical implications. *The Astrophysical Journal*, *420*, 307–317.

132. Jochims, H., Rühl, E., Baumgärtel, H., Tobita, S., and Leach, S. (1997). VUV peaks in absorption spectra and photoion yield curves of polycyclic aromatic hydrocarbons and related compounds. *International Journal of Mass Spectrometry and Ion Processes*, *167*, 35–53.

133. Jochims, H.-W., Schwell, M., Baumgärtel, H., and Leach, S. (2005). Photoion mass spectrometry of adenine, thymine and uracil in the 6–22eV photon energy range. *Chemical Physics*, *314*, 263–282.

134. Johansson, H. A., Zettergren, H., Holm, A. I., Seitz, F., Schmidt, H. T., Rousseau, P., Ławicki, A., Capron, M., Domaracka, A., Lattouf, E. et al. (2011). Ionization and fragmentation of polycyclic aromatic hydrocarbon clusters in collisions with keV ions. *Physical Review A*, *84*, 043201.

135. Jolibois, F., Klotz, A., Gadéa, F., and Joblin, C. (2005). Hydrogen dissociation of naphthalene cations: a theoretical study. *Astronomy and Astrophysics*, *444*, 629–634.

136. Jones, R. M., Gerlich, D., and Anderson, S. L. (1997). Simple radio–frequency power source for ion guides and ion traps. *Review of Scientific Instruments*, *68*, 3357–3362.

137. Kabachnik, N., Kondratyev, V., Roller-Lutz, Z., and Lutz, H. (1997). Multiple ionization of atoms and molecules in collisions with fast ions: Ion-atom collisions. *Physical Review A*, *56*, 2848–2854.

138. Kabachnik, N., Kondratyev, V., Roller-Lutz, Z., and Lutz, H. (1998). Multiple ionization of atoms and molecules in collisions with fast ions. II. Ion-molecule collisions. *Physical Review A*, *57*, 990–996.

139. Kadhane, U., Andersen, J. U., Bonderup, E., Concina, B., Hvelplund, P., Kirketerp, M.-B. S., Liu, B., Nielsen, S. B., Panja, S., Rangama, J. et al. (2009). Near-infrared photoabsorption by C_{60} dianions in a storage ring. *The Journal of Chemical Physics*, *131*, 014301.

140. Kadhane, U., Andersen, J. U., Ehlerding, A., Hvelplund, P., Kirketerp, M.-B. S., Lykkegaard, M. K., Nielsen, S. B., Panja, S., Wyer, J. A., and Zettergren, H. (2008). Photodissociation of protonated tryptophan and alteration of dissociation pathways by complexation with crown ether. *The Journal of Chemical Physics*, *129*, 184304.

141. Kadhane, U., Kelkar, A., Misra, D., Kumar, A., and Tribedi, L. C. (2007). Effect of giant plasmon excitations in single and double ionization of C_{60} in fast heavy-ion collisions. *Physical Review A*, *75*, 041201.

142. Kadhane, U., Misra, D., Singh, Y., and Tribedi, L. C. (2003). Effect of collective response on electron capture and excitation in collisions of highly charged ions with fullerenes. *Physical Review Letters*, *90*, 093401.

143. Kamisuki, T., and Hirose, C. (2001). Ab initio/density functional study of vibrational frequencies of acridine in the ground and excited states. *Journal of Molecular Structure: THEOCHEM*, *542*, 189–198.

144. Kaplan, I. (1997). Giant resonances in atoms, atomic clusters, fullerenes, condensed media, and nuclei. *Zeitschrift für Physik D Atoms, Molecules and Clusters*, *40*, 375–380.

145. Kaplan, I. (1998). Comparative discussion of the giant resonance phenomenon in nuclei, atoms, atomic clusters, and condensed media. *Czechoslovak Journal of Physics*, *48*, 763–768.

146. Kendall, R. A., Dunning Jr, T. H., and Harrison, R. J. (1992). Electron affinities of the first-row atoms revisited. Systematic basis sets and wave functions. *The Journal of Chemical Physics*, *96*, 6796–6806.

147. Kivimäki, A., Pfeiffer, L., Aksela, H., Nommiste, E., and Aksela, S. (1999). Intensities of the xenon $n_{4,5}oo$ Auger electron spectrum revisited. *Journal of Electron Spectroscopy and Related Phenomena*, *101*, 43–47.

148. Klasinc, L. et al. (1980). Photoelectron spectra of conjugated molecules. *Pure and Applied Chemistry*, *52*, 1509–1524.

149. Klessinger, M., and Michl, J. (1995). *Excited states and photochemistry of organic molecules*. VCH New York.

150. Koch, W., Holthausen, M. C., and Holthausen, M. C. (2001). *A chemist's guide to density functional theory* volume 2. Wiley-Vch Weinheim.

151. Köhn, A., and Hättig, C. (2003). Analytic gradients for excited states in the coupled-cluster model cc2 employing the resolution-of-the-identity approximation. *The Journal of Chemical Physics*, *119*, 5021–5036.

152. Kokkin, D. L., Reilly, N. J., Troy, T. P., Nauta, K., and Schmidt, T. W. (2007). Gas phase spectra of all-benzenoid polycyclic aromatic hydrocarbons: Triphenylene. *The Journal of Chemical Physics*, *126*, 084304.

153. Koper, C., Jenneskens, L. W., and Sarobe, M. (2002). Externally-fused cyclopenta moieties in non-alternant CP-PAHs act as *peri*-substituents. *Tetrahedron letters*, *43*, 3833–3836.

154. Korica, S., Rolles, D., Reinköster, A., Langer, B., Viefhaus, J., Cvejanović, S., and Becker, U. (2005). Partial cross sections and angular distributions of resonant and non-resonant valence photoemission of C_{60}. *Physical Review A*, *71*, 013203.

155. Krems, M., Zirbel, J., Thomason, M., and DuBois, R. D. (2005). Channel electron multiplier and channelplate efficiencies for detecting positive ions. *Review of Scientific Instruments*, *76*, 093305.

156. Krygowski, T. M., and Cyranski, M. K. (2001). Structural aspects of aromaticity. *Chemical Reviews*, *101*, 1385–1420.

157. Kutzner, M., Radojević, V., and Kelly, H. (1989). Extended photoionization calculations for xenon. *Physical Review A*, *40*, 5052–5057.

158. Laserdatasheet (). Http://www.ekspla.com/wp-content/uploads/2013/06/nt242p-series-nanosecond-tunable-dpss-lasers.pdf.

159. Ławicki, A., Holm, A. I., Rousseau, P., Capron, M., Maisonny, R., Maclot, S., Seitz, F., Johansson, H. A., Rosén, S., Schmidt, H. T. et al. (2011). Multiple ionization and frag-

mentation of isolated pyrene and coronene molecules in collision with ions. *Physical Review A*, *83*, 022704.

160. Le Padellec, A., Moretto-Capelle, P., Richard-Viard, M., Champeaux, J., and Cafarelli, P. (2008). Ionization and fragmentation of DNA, RNA bases induced by proton impact. In *Journal of Physics: Conference Series* (p. 012007). IOP Publishing volume 101.

161. Leach, S. (1989). Physical and chemical properties of polycyclic aromatic hydrocarbons. In *Interstellar Dust* (pp. 155–171). Springer.

162. Lee, C., Yang, W., and Parr, R. G. (1988). Development of the Colle–Salvetti correlation-energy formula into a functional of the electron density. *Physical Review B*, *37*, 785–789.

163. Lee, S. Y., and Boo, B. H. (1996). Density functional theory study of vibrational spectra of anthracene neutral and radical cation. *Bull. Korean Chem. Soc*, *17*, 755.

164. Léger, A., and d'Hendecourt, L. (1985). Are polycyclic aromatic hydrocarbons the carriers of the diffuse interstellar bands in the visible? *Astronomy and Astrophysics*, *146*, 81–85.

165. Leger, A., and Puget, J. (1984). Identification of the 'unidentified' IR emission features of interstellar dust? *Astronomy and Astrophysics*, *137*, L5–L8.

166. Léger, A., Verstraete, L., d'Hendecourt, L., Défourneau, D., Dutuit, O., Schmidt, W., and Lauer, J. (1989). The pah hypothesis and the extinction curve. In *Interstellar Dust* (pp. 173–180). Springer.

167. Lekadir, H., Abbas, I., Champion, C., Fojón, O., Rivarola, R., and Hanssen, J. (2009). Single-electron-loss cross sections of DNA and RNA bases impacted by energetic multicharged ions: A classical Monte Carlo approximation. *Physical Review A*, *79*, 062710.

168. Lepère, V., Lucas, B., Barat, M., Fayeton, J., Picard, V., Jouvet, C., Carcabal, P., Nielsen, I., Dedonder-Lardeux, C., Gregoire, G. et al. (2007). Comprehensive characterization of the photodissociation pathways of protonated tryptophan. *The Journal of Chemical Physics*, *127*, 134313.

169. Levine, I. N. (2000). *Quantum Chemistry*. (5th ed.). Prentice Hall (Upper Saddle River, NJ).

170. Lindhard, J., and Scharff, M. (1953). Energy loss in matter by fast particles of low charge. *Det Kongelige Danske Videnskabernes Selskab Matematisk-fysiske Meddelelser*, *27*.

171. Lindhard, J., and Winther, A. (1964). Stopping power of electron gas and equipartition rule. *Det Kongelige Danske Videnskabernes Selskab Matematisk-fysiske Meddelelser*, *34*.

172. Ling, Y., and Lifshitz, C. (1996). Plasmon excitation in polycyclic aromatic hydrocarbons studied by photoionization. *Chemical Physics Letters*, *257*, 587–591.

173. Long, C., Lu, J., Li, A., Hu, D., Liu, F., and Zhang, Q. (2008). Adsorption of naphthalene onto the carbon adsorbent from waste ion exchange resin: Equilibrium and kinetic characteristics. *Journal of Hazardous Materials*, *150*, 656–661.

174. Luna, H., de Barros, A., Wyer, J., Scully, S., Lecointre, J., Garcia, P., Sigaud, G., Santos, A., Senthil, V., Shah, M. et al. (2007). Water-molecule dissociation by proton and hydrogen impact. *Physical Review A*, *75*, 042711.

175. Malloci, G., Mulas, G., Cappellini, G., and Joblin, C. (2007). Time-dependent density functional study of the electronic spectra of oligoacenes in the charge states- 1, 0,+ 1, and+ 2. *Chemical Physics*, *340*, 43–58.

176. Manil, B., Lebius, H., Huber, B., Cormier, D., and Pesnelle, A. (2003). Fragmentation of thymidine and deoxyadenosine induced by slow multiply charged ions. *Nuclear Instruments and Methods in Physics Research Section B: Beam Interactions with Materials and Atoms*, *205*, 666–670.

177. Manura, D., and Dahl, D. A. (2007). SIMION 8.0 user manual, scientific instrument services, .

178. Märk, T. (2008). Cross section for single and double ionization of N_2 and O_2 molecules by electron impact from threshold up to 170 ev. *The Journal of Chemical Physics*, *63*, 3731–3736.

179. Martin, S., Chen, L., Brédy, R., Montagne, G., Ortega, C., Schlathölter, T., Reitsma, G., and Bernard, J. (2012). Statistical fragmentation of doubly charged anthracene induced by fluorine-beam impact at 3 keV. *Physical Review A*, *85*, 052715.

180. Martin, S., Chen, L., Denis, A., and Desesquelles, J. (1998). Production and asymmetric fragmentation of multicharged fullerene ions in Xe^{8++}–C_{60} collisions. *Physical Review A*, *57*, 4518–4521.

181. Maryam, N. K. (2010). *Design and Simulation of Octupole ion guide and 22-pole ion trap*. Masters of science dissertation Indian Institute of Technology, Madras.

182. Mathur, D. (1993). Multiply charged molecules. *Physics Reports*, *225*, 193–272.

183. Mayer, P. M., Blanchet, V., and Joblin, C. (2011). Threshold photoelectron study of naphthalene, anthracene, pyrene, 1, 2-dihydronaphthalene, and 9, 10-dihydroanthracene. *The Journal of Chemical Physics*, *134*, 244312.

184. Meng, Q., and Meyer, H.-D. (2013). A multilayer MCTDH study on the full dimensional vibronic dynamics of naphthalene and anthracene cations. *The Journal of Chemical Physics*, *138*, 014313.

185. Micelotta, E., Jones, A., and Tielens, A. (2010). Polycyclic aromatic hydrocarbon processing by cosmic rays. *arXiv preprint arXiv:1012.1599*, .

186. Micelotta, E. R. et al. (2009). *PAH processing in space*. Ph.D. thesis Leiden Observatory, Faculty of Science, Leiden University.

187. Michael, B. D., and O'Neill, P. (2000). A sting in the tail of electron tracks. *Science*, *287*, 1603–1604.

188. Modelli, A., and Mussoni, L. (2007). Rapid quantitative prediction of ionization energies and electron affinities of polycyclic aromatic hydrocarbons. *Chemical Physics*, *332*, 367–374.

189. Modelli, A., Mussoni, L., and Fabbri, D. (2006). Electron affinities of polycyclic aromatic hydrocarbons by means of B3LYP/6-31+G* calculations. *The Journal of Physical Chemistry A*, *110*, 6482–6486.

190. Moretto-Capelle, P., and Le Padellec, A. (2006). Electron spectroscopy in proton collisions with dry gas-phase uracil base. *Physical Review A*, *74*, 062705.

191. Moretto-Capelle, P., Le Padellec, A., Briere, G., Massou, S., and Franceries, F. (2007). Energetics and metastability of the adenine dication observed in proton-adenine collisions. *The Journal of Chemical Physics*, *127*, 234311.

192. Nathan, J. (June 2014). Photoemission spectroscopy. `http://en.wikipedia.org/wiki/User:Nathan_Johnson/photoemission_spectroscopy`.

193. Negri, F., and Zgierski, M. Z. (1994). On the vibronic structure of the absorption spectra of radical cations of some polycyclic aromatic hydrocarbons. *The Journal of Chemical Physics*, *100*, 1387–1399.

194. von Niessen, W. (1991). Application of a green's function method to the calculation of photoelectron spectra. *Butlletí de les Societats Catalanes de Física, Química, Matemàtiques i Tecnologia*, *11*, 227–262.

195. NISTa (June 2014). NIST Atomic spectra database. `http://www.nist.gov/pml/data/asd.cfm`.

196. NISTe (June 2014). NIST Chemistry WebBook. `http://webbook.nist.gov/chemistry/`.

197. Oh, D. Y. (1996). *Computational modeling of expanding plasma plumes in space using a PIC-DSMC algorithm*. Ph.D. thesis Massachusetts Institute of Technology, Dept. of Aeronautics and Astronautics.

198. Oji, H., Mitsumoto, R., Ito, E., Ishii, H., Ouchi, Y., Seki, K., Yokoyama, T., Ohta, T., and Kosugi, N. (1998). Core hole effect in NEXAFS spectroscopy of polycyclic aromatic hydrocarbons: Benzene, chrysene, perylene, and coronene. *The Journal of Chemical Physics*, *109*, 10409–10418.

199. Oomens, J., Meijer, G., and von Helden, G. (2001a). Gas phase infrared spectroscopy of cationic indane, acenaphthene, fluorene, and fluoranthene. *The Journal of Physical Chemistry A*, *105*, 8302–8309.

200. Oomens, J., Sartakov, B. G., Tielens, A., Meijer, G., and von Helden, G. (2001b). Gas-phase infrared spectrum of the coronene cation. *The Astrophysical Journal Letters*, *560*, L99–L103.

201. Oomens, J., Tielens, A., Sartakov, B. G., von Helden, G., and Meijer, G. (2003). Laboratory infrared spectroscopy of cationic polycyclic aromatic hydrocarbon molecules. *The Astrophysical Journal*, *591*, 968–985.

202. Otto, R., Hlavenka, P., Trippel, S., Mikosch, J., Singer, K., Weidemüller, M., and Wester, R. (2009). How can a 22-pole ion trap exhibit ten local minima in the effective potential? *Journal of Physics B: Atomic, Molecular and Optical Physics*, *42*, 154007.

203. Padovani, M., Galli, D., and Glassgold, A. (2009). Cosmic-ray ionization of molecular clouds. *Astronomy and Astrophysics*, *501*, 619–631.

204. Parisel, O., Berthier, G., and Ellinger, Y. (1992). New clues for ionized Polycyclic Aromatic Hydrocarbons as possible carriers of diffuse interstellar bands. *Astronomy and Astrophysics*, *266*, L1–L4.

205. Parr, R. G., and Yang, W. (1989). *Density-functional theory of atoms and molecules* volume 16. Oxford university press.

206. Paul, W. (1990). Electromagnetic traps for charged and neutral particles. *Review of Modern Physics*, *62*, 531–540.

207. Pearson, R. G. (1987). Recent advances in the concept of hard and soft acids and bases. *Journal of Chemical Education*, *64*, 561–567.

208. Peñalba, M., Arnau, A., and Echenique, P. (1991). Stopping power of carbon for helium. *Nuclear Instruments and Methods in Physics Research Section B: Beam Interactions with Materials and Atoms*, *56*, 352–354.

209. Pereira Netto, A., Skinner, R., Hollauer, E., and Rocco, M. (2005). Preliminary evaluation of inner shell spectroscopy as an analytical tool for the analysis of polycyclic aromatic compounds in environmental samples. *Revista Brasileira de Aplicações de Vácuo*, *24*, 104–109.

210. Piest, J. H., Oomens, J., Bakker, J., von Helden, G., and Meijer, G. (2001). Vibrational spectroscopy of gas-phase neutral and cationic phenanthrene in their electronic ground-

states. *Spectrochimica Acta Part A: Molecular and Biomolecular Spectroscopy*, *57*, 717 – 735.

211. Pitts, J. D., and Knee, J. (1998). Dynamics of vibronically excited fluorene-Ar_n (n= 4, 5) clusters. *The Journal of Chemical Physics*, *108*, 9632–9638.

212. Plekan, O., Coreno, M., Feyer, V., Moise, A., Richter, R., de Simone, M., Sankari, R., and Prince, K. (2008). Electronic state resolved PEPICO spectroscopy of pyrimidine. *Physica Scripta*, *78*, 058105.

213. Plekan, O., Feyer, V., Richter, R., Coreno, M., De Simone, M., and Prince, K. (2007). Photofragmentation of guanine, cytosine, leucine and methionine. *Chemical Physics*, *334*, 53–63.

214. Portella, G., Poater, J., Bofill, J. M., Alemany, P., and Sola, M. (2005). Local aromaticity of [n] acenes,[n] phenacenes, and [n] helicenes (n= 1-9). *The Journal of Organic Chemistry*, *70*, 2509–2521.

215. Postma, J., Bari, S., Hoekstra, R., Tielens, A., and Schlathölter, T. (2010). Ionization and Fragmentation of Anthracene upon Interaction with keV protons and α particles. *The Astrophysical Journal*, *708*, 435–444.

216. Potts, A., Holland, D., Trofimov, A., Schirmer, J., Karlsson, L., and Siegbahn, K. (2003). An experimental and theoretical study of the valence shell photoelectron spectra of purine and pyrimidine molecules. *Journal of Physics B: Atomic, Molecular and Optical Physics*, *36*, 3129–3143.

217. Prasad, S. S., and Furman, D. R. (1975). On the importance of doubly charged ions in the auroral ionosphere. *Journal of Geophysical Research*, *80*, 1360–1362.

218. Ptasińska, S., Candori, P., Denifl, S., Yoon, S., Grill, V., Scheier, P., and Märk, T.

(2005). Dissociative ionization of the nucleosides thymidine and uridine by electron impact. *Chemical Physics Letters*, *409*, 270–276.

219. Rajgara, F., Krishnamurthy, M., Mathur, D., Nishide, T., Shiromaru, H., and Kobayashi, N. (2004). Coulombic and non-coulombic fragmentation of highly charged benzene. *Journal of Physics B: Atomic, Molecular and Optical Physics*, *37*, 1699–1707.

220. Rajput, J., and Safvan, C. (2007). Kinetic energy distributions in ion-induced CO fragmentation: Signature of shallow states in multiply charged CO. *Physical Review A*, *75*, 062709.

221. Rapacioli, M., Calvo, F., Joblin, C., Parneix, P., Toublanc, D., and Spiegelman, F. (2006). Formation and destruction of polycyclic aromatic hydrocarbon clusters in the interstellar medium. *Astronomy and Astrophysics*, *460*, 519.

222. Reinköster, A., Siegmann, B., Werner, U., and Lutz, H. O. (2003). Ion-impact induced excitation and fragmentation of C_{60}. *Radiation Physics and Chemistry*, *68*, 263–267.

223. Reinköster, A., Werner, U., Kabachnik, N., and Lutz, H. O. (2001). Experimental and theoretical study of ionization and fragmentation of C_{60} by fast-proton impact. *Physical Review A*, *64*, 023201.

224. Reitsma, G., Zettergren, H., Boschman, L., Bodewits, E., Hoekstra, R., and Schlathölter, T. (2013). Ion–polycyclic aromatic hydrocarbon collisions: kinetic energy releases for specific fragmentation channels. *Journal of Physics B: Atomic, Molecular and Optical Physics*, *46*, 245201.

225. Rentenier, A., Bordenave-Montesquieu, D., Moretto-Capelle, P., and Bordenave-Montesquieu, A. (2003). Kinetic energies of charged fragments resulting from multifragmentation and asymmetric fission of the C_{60} molecule in collisions with monocharged ions (2–130 kev). *Journal of Physics B: Atomic, Molecular and Optical Physics*, *36*, 1585–1602.

226. Rentenier, A., Ruiz, L., Díaz-Tendero, S., Zarour, B., Moretto-Capelle, P., Bordenave-Montesquieu, D., Bordenave-Montesquieu, A., Hervieux, P.-A., Alcamí, M., Politis, M. et al. (2008). Absolute charge transfer and fragmentation cross sections in He_{2+}-C_{60} collisions. *Physical Review Letters*, *100*, 183401.

227. Rice, J. M., Dudek, G. O., and Barber, M. (1965). Mass spectra of nucleic acid derivatives. Pyrimidines. *Journal of the American Chemical Society*, *87*, 4569–4576.

228. Rienstra-Kiracofe, J. C., Tschumper, G. S., Schaefer, H. F., Nandi, S., and Ellison, G. B. (2002). Atomic and molecular electron affinities: photoelectron experiments and theoretical computations. *Chemical Reviews*, *102*, 231–282.

229. RoentDek (June 2014). Roentdek handels gmbh. `http://www.roentdek.com/`.

230. Rousseau, C., Chu, W., and Powers, D. (1971). Calculations of stopping cross sections for 0.8-to 2.0-MeV alpha particles. *Physical Review A*, *4*, 1066–1070.

231. Rousseau, P., Ławicki, A., Holm, A. I., Capron, M., Maisonny, R., Maclot, S., Lattouf, E., Johansson, H. A., Seitz, F., Méry, A. et al. (2012). Low-energy ions interacting with anthracene molecules and clusters. *Nuclear Instruments and Methods in Physics Research Section B: Beam Interactions with Materials and Atoms*, *279*, 140–143.

232. Rudd, M., Goffe, T., and Itoh, A. (1985a). Ionization cross sections for 10–300-keV/u and electron-capture cross sections for 5–150-keV/u $^3He^{2+}$ ions in gases. *Physical Review A*, *32*, 2128–2133.

233. Rudd, M. E., DuBois, R., Toburen, L., Ratcliffe, C., and Goffe, T. (1983). Cross sections for ionization of gases by 5-4000-keV protons and for electron capture by 5-150-keV protons. *Physical Review A*, *28*, 3244–3257.

234. Rudd, M. E., Kim, Y.-K., Madison, D., and Gallagher, J. (1985b). Electron production in proton collisions: total cross sections. *Reviews of Modern Physics*, *57*, 965–994.

235. Ruiterkamp, R., Halasinski, T., Salama, F., Foing, B., Allamandola, L., Schmidt, W., and Ehrenfreund, P. (2002). Spectroscopy of large pahs. *Astronomy and Astrophysics*, *390*, 1153–1170.

236. Russek, A., and Meli, J. (1970). Ionization phenomena in high-energy atomic collisions. *Physica*, *46*, 222–243.

237. Salama, F., and Allamandola, L. (1992a). Is a pyrene-like molecular ion the cause of the 4,430-å diffuse interstellar absorption band? *Nature (London)*, *358*, 42–43.

238. Salama, F., and Allamandola, L. (1992b). The ultraviolet and visible spectrum of the polycyclic aromatic hydrocarbon $C_{10}H_8{}^+$- Possible contributions to the diffuse interstellar bands and to the ultraviolet-visible extinction. *The Astrophysical Journal*, *395*, 301–306.

239. Salama, F., and Allamandola, L. J. (1993). Neutral and ionized polycyclic aromatic hydrocarbons, diffuse interstellar bands and the ultraviolet extinction curve. *Journal of the Chemical Society, Faraday Transactions*, *89*, 2277–2284.

240. Scalmani, G., Frisch, M. J., Mennucci, B., Tomasi, J., Cammi, R., and Barone, V. (2006). Geometries and properties of excited states in the gas phase and in solution: Theory and application of a time-dependent density functional theory polarizable continuum model. *The Journal of Chemical Physics*, *124*, 094107.

241. Schirmer, J., and Cederbaum, L. (1978). The two-particle-hole Tamm-Dancoff approximation (2ph-TDA) equations for closed-shell atoms and molecules. *Journal of Physics B: Atomic and Molecular Physics*, *11*, 1889.

242. Schirmer, J., Cederbaum, L., Domcke, W., and Von Niessen, W. (1977). Strong correlation effects in inner Valence Ionization of N_2 AND CO. *Chemical Physics*, *26*, 149–153.

243. Schlathölter, T., Alvarado, F., Bari, S., Lecointre, A., Hoekstra, R., Bernigaud, V., Manil, B., Rangama, J., and Huber, B. (2006). Ion-Induced Biomolecular Radiation Damage: From Isolated Nucleobases to Nucleobase Clusters. *ChemPhysChem*, *7*, 2339–2345.

244. Schlathölter, T., Hadjar, O., Hoekstra, R., and Morgenstern, R. (1999a). Strong velocity effects in collisions of He^+ with fullerenes. *Physical Review Letters*, *82*, 73–76.

245. Schlathölter, T., Hadjar, O., Manske, J., Hoekstra, R., and Morgenstern, R. (1999b). Electronic versus vibrational excitation in He^{q+} collisions with fullerenes. *International Journal of Mass Spectrometry*, *192*, 245–257.

246. Schlathölter, T., Hoekstra, R., and Morgenstern, R. (2004). Charge driven fragmentation of biologically relevant molecules. *International Journal of Mass Spectrometry*, *233*, 173–179.

247. Schmidt, W. (1977). Photoelectron spectra of polynuclear aromatics. V. Correlations with ultraviolet absorption spectra in the catacondensed series. *The Journal of Chemical Physics*, *66*, 828–845.

248. Seitz, F., Holm, A. I., Zettergren, H., Johansson, H. A., Rosén, S., Schmidt, H. T., Ławicki, A., Rangama, J., Rousseau, P., Capron, M. et al. (2011). Polycyclic aromatic hydrocarbon-isomer fragmentation pathways: Case study for pyrene and fluoranthene molecules and clusters. *The Journal of Chemical Physics*, *135*, 064302.

249. Snow, T. P., Le Page, V., Keheyan, Y., and Bierbaum, V. M. (1998). The interstellar chemistry of PAH cations. *Nature*, *391*, 259–260.

250. Stewart, R. (1985). *The proton: appellation to organic chemistry*. Academic, New York.

251. Stöhr, J. (1992). *NEXAFS spectroscopy* volume 25. Berlin: Springer-Verlag.

252. Stolterfoht, N., DuBois, R., and Rivarola, R. (1997). *Electron emission in heavy-ion-atom collisions, Springer Series on Atoms and Plasma*. Springer ,Berlin.

253. Szczepanski, J., Banisaukas, J., Vala, M., Hirata, S., Bartlett, R. J., and Head-Gordon, M. (2002). Vibrational and electronic spectroscopy of the fluorene cation. *The Journal of Physical Chemistry A*, *106*, 63–73.

254. Szczepanski, J., and Vala, M. (1993). Laboratory evidence for ionized polycyclic aromatic hydrocarbons in the interstellar medium. *Nature (London)*, *363*, 699–701.

255. Szczepanski, J., Vala, M., Talbi, D., Parisel, O., and Ellinger, Y. (1993). Electronic and vibrational spectra of matrix isolated anthracene radical cations: Experimental and theoretical aspects. *The Journal of Chemical Physics*, *98*, 4494–4511.

256. Tabet, J., Eden, S., Feil, S., Abdoul-Carime, H., Farizon, B., Farizon, M., Ouaskit, S., and Märk, T. (2010a). 20–150-keV proton-impact-induced ionization of uracil: Fragmentation ratios and branching ratios for electron capture and direct ionization. *Physical Review A*, *81*, 012711.

257. Tabet, J., Eden, S., Feil, S., Abdoul-Carime, H., Farizon, B., Farizon, M., Ouaskit, S., and Märk, T. (2010b). Absolute molecular flux and angular distribution measurements to characterize DNA/RNA vapor jets. *Nuclear Instruments and Methods in Physics Research Section B: Beam Interactions with Materials and Atoms*, *268*, 2458–2466.

258. Tabet, J., Eden, S., Feil, S., Abdoul-Carime, H., Farizon, B., Farizon, M., Ouaskit, S., and Märk, T. (2010c). Absolute total and partial cross sections for ionization of nucleobases by proton impact in the Bragg peak velocity range. *Physical Review A*, *82*, 022703.

259. Tabet, J., Eden, S., Feil, S., Abdoul-Carime, H., Farizon, B., Farizon, M., Ouaskit, S., and Märk, T. (2010d). Mass spectrometry (fragmentation ratios) of DNA base molecules

following 80keV proton impact with separation of direct ionization and electron capture processes. *International Journal of Mass Spectrometry*, *292*, 53–63.

260. Tan, X., Bernstein, L., Cami, J., and Salama, F. (2011). On estimating interstellar polycyclic aromatic hydrocarbon abundances with calculated oscillator strengths. *The Astrophysical Journal*, *728*, 62 (5pp).

261. Tan, X., and Salama, F. (2005a). Cavity ring-down spectroscopy and theoretical calculations of the S_1 ($^1B_{3u}$) $\leftarrow$ S_0 (^1A_g) transition of jet-cooled perylene. *The Journal of Chemical Physics*, *122*, 084318.

262. Tan, X., and Salama, F. (2005b). Cavity ring-down spectroscopy and vibronic activity of benzo [ghi] perylene. *The Journal of Chemical Physics*, *123*, 014312.

263. Tappe, W., Flesch, R., Rühl, E., Hoekstra, R., and Schlathölter, T. (2002). Charge localization in collision-induced multiple ionization of van der waals clusters with highly charged ions. *Physical Review Letters*, *88*, 143401.

264. Tielens, A. G. (2005). *The Physics and Chemistry of the Interstellar Medium*. Cambridge University Press.

265. Tielens, A. G. (2008). Interstellar polycyclic aromatic hydrocarbon molecules. *Annual Review in Astronomy and Astrophysics*, *46*, 289–337.

266. Tobita, S., Leach, S., Jochims, H., Rühl, E., Illenberger, E., and Baumgärtel, H. (1994). Single-and double-ionization potentials of polycyclic aromatic hydrocarbons and fullerenes by photon and electron impact. *Canadian Journal of Physics*, *72*, 1060–1069.

267. Todorov, P. D., Koper, C., van Lenthe, J. H., and Jenneskens, L. W. (2008). Gas phase adiabatic electron affinities of cyclopenta-fused polycyclic aromatic hydrocarbons. *Chemical Physics Letters*, *454*, 30–35.

268. Townsend, M., and Weissman, S. (1960). Possible Symptom of the Jahn-Teller Effect in the Negative Ions of Coronene and Triphenylene. *The Journal of Chemical Physics*, *32*, 309–310.

269. Treitel, N., Shenhar, R., Aprahamian, I., Sheradsky, T., and Rabinovitz, M. (2004). Calculations of PAH anions: When are diffuse functions necessary? *Physical Chemistry Chemical Physics*, *6*, 1113–1121.

270. Tsuchida, H., Itoh, A., Nakai, Y., Miyabe, K., and Imanishi, N. (1998). Cross sections for ionization and fragmentation of C_{60} by fast H^+ impact. *Journal of Physics B: Atomic, Molecular and Optical Physics*, *31*, 5383–5391.

271. Vala, M., Szczepanski, J., Pauzat, F., Parisel, O., Talbi, D., and Ellinger, Y. (1994). Electronic and Vibrational Spectra of Matrix-Isolated Pyrene Radical Cations: Theoretical and Experimental Aspects. *The Journal of Physical Chemistry*, *98*, 9187–9196.

272. Van Brunt, R. J., and Wacks, M. E. (2004). Electron-Impact Studies of Aromatic Hydrocarbons. III. Azulene and Naphthalene. *The Journal of Chemical Physics*, *41*, 3195–3199.

273. Verkhovtsev, A. V., Korol, A. V., Solov'yov, A. V., Bolognesi, P., Ruocco, A., and Avaldi, L. (2012). Interplay of the volume and surface plasmons in the electron energy loss spectra of C_{60}. *Journal of Physics B: Atomic, Molecular and Optical Physics*, *45*, 141002(6pp).

274. Vuong, M. H., and Foing, B. H. (2000). Dehydrogenation of polycyclic aromatic hydrocarbons in the diffuse interstellar medium. *arXiv preprint astro-ph/0010385*, .

275. Wacks, M. E., and Dibeler, V. H. (2004). Electron Impact Studies of Aromatic Hydrocarbons. I. Benzene, Naphthalene, Anthracene, and Phenanthrene. *The Journal of Chemical Physics*, *31*, 1557–1562.

276. West, B., Joblin, C., Blanchet, V., Bodi, A., SztaÌĄray, B., and Mayer, P. M. (2012). On the Dissociation of the Naphthalene Radical Cation: New iPEPICO and Tandem Mass Spectrometry Results. *The Journal of Physical Chemistry A*, *116*, 10999–11007.

277. Wester, R. (2009). Radiofrequency multipole traps: tools for spectroscopy and dynamics of cold molecular ions. *Journal of Physics B: Atomic, Molecular and Optical Physics*, *42*, 154001.

278. Wiley, W., and McLaren, I. H. (1955). Time-of-flight mass spectrometer with improved resolution. *Review of Scientific Instruments*, *26*, 1150–1157.

279. Witt, A. N., Clayton, G. C., Draine, B. T., Boogert, A., and Ehrenfreund, P. (2004). Astrophysics of dust, .

280. Xu, Y.-J., Khandelwal, G., and Wilson, J. (1984). Low-energy proton stopping power of N_2, O_2, and water vapor, and deviations from bragg's rule. *Physical Review A*, *29*, 3419–3422.

281. Yastrebov, S., and Ivanov-Omskii, V. (2005). Optical properties of interstellar medium. *Technical Physics Letters*, *31*, 878–880.

282. Yu, H. (2002). Environmental carcinogenic polycyclic aromatic hydrocarbons: photochemistry and phototoxicity. *Journal of Environmental Science and Health, Part C*, *20*, 149–183.

283. Zettergren, H., Schmidt, H. T., Reinhed, P., Cederquist, H., Jensen, J., Hvelplund, P., Tomita, S., Manil, B., Rangama, J., and Huber, B. A. (2007a). Even-odd effects in the ionization cross sections of $[C_{60}]_2$ and $[C_{60}C_{70}]$ dimers. *Physical Review A*, *75*, 051201(R).

284. Zettergren, H., Schmidt, H. T., Reinhed, P., Cederquist, H., Jensen, J., Hvelplund, P., Tomita, S., Manil, B., Rangama, J., and Huber, B. A. (2007b). Stabilities of multi-

ply charged dimers and clusters of fullerenes. *The Journal of Chemical Physics*, *126*, 224303.

285. Zhang, J., Han, F., and Kong, W. (2010). Zero Kinetic Energy Photoelectron Spectroscopy of Pyrene. *The Journal of Physical Chemistry A*, *114*, 11117–11124.

286. Zhang, J., Harthcock, C., Han, F., and Kong, W. (2011). Zero kinetic energy photoelectron spectroscopy of jet cooled benzo [a] pyrene from resonantly enhanced multiphoton ionization. *The Journal of chemical physics*, *135*, 244306.

287. Zhang, J., Pei, L., and Kong, W. (2008). Zero kinetic energy photoelectron spectroscopy of tetracene using laser desorption for vaporization. *The Journal of Chemical Physics*, *128*, 104301.

288. Ziegler, J., and Biersack, J. P. (2000). *SRIM software*.

APPENDIX A

C PROGRAM FOR *MONTE CARLO* SIMULATION

```
%%%%%%%%%%%%%%%%%%%%%%%%%%%%%%%%%%%%%%%%%%%%%%%%%%%%%
#include<stdio.h>
#include<stdlib.h>
#include<math.h>
#include<malloc.h>
#define pp 1000728 //pp =(Xmax*Ymax*Zmax)
#define s 123 // s=2*r
int main() {
 FILE *fpF3,*fpD,*fpF2;
int a,e,j,AA,BB,CC;
double r=87.0;//radius of sphere defining projectile volume
const double PI = 3.14159;
double p1,p2,q1,q2,zzz1,zzz2, x1,y1,z1,x2,y2,z2,theta1,phi1,theta2,phi2;
int x,y,z,Xtmax,Ytmax,Ztmax,Xmin,Ymin,Zmin,Xmax,Ymax,Zmax;
int xn,yn,zn,xxn,yyn,zzn,w,i;
float d,dr,m,c,xx,yy,zz,aa,bb,cc;
double density[pp];      double g[s];
double AAA[s],BBB[s],CCC[s],DDD[s],EEE[s],FFF[s];
double OMEGA[s],WWlsSq[s],WWlsSqdx[s];
double Vf[s],Wp[s],chiSq[s],Cchi[s],Lhv[s],dE[i],dEdx[i];
double WlsSq,WSq;
double b,zc,v,dx,E;
```

```
//b(impact parameter),zc(projectile charge)&v(projectile velocity)
int Xtmin=1; int Ytmin=1; int Ztmin=1;
Xtmax=123;Ytmax=113;Ztmax=72;// from gaussian output
zc=1.0;v=2.0;dx=0.184731;
fpD=fopen("inputdensity.txt","r");
for(i=0;i<=pp-1;i=i+1)
{fscanf(fpD,"%lf",&density[i]);}
fclose(fpD);
fpF3=fopen("outputdensity.txt","w");
a=1000000;\\event number
srandom(time(0));
for(e=1;e<=a;e++)      {x1=y1=z1=x2=y2=z2=0;
for (i=1;i<=s-1;i++)  {g[i]=0;}
zzz1=1.0*rand()/(RAND_MAX/2)-1;
theta1= 2.0*PI*rand()/RAND_MAX;
x1 = r* sqrt ((1-zzz1*zzz1)) * cos(theta1 * 180.0 / PI);
y1 = r* sqrt ((1-zzz1*zzz1)) * sin(theta1 * 180.0 / PI);
z1 = r* zzz1;
zzz2=1.0*rand()/(RAND_MAX/2)-1;
theta2= 2.0*PI*rand()/RAND_MAX;
x2 = r* sqrt ((1-zzz2*zzz2)) * cos(theta2 * 180.0 / PI);
y2 = r* sqrt ((1-zzz2*zzz2)) * sin(theta2 * 180.0 / PI);
z2 = r* zzz2;
//use setI(if Xtmax,Xtmin,Ytmax,Ytmin,Ztmax,Ztmin...all are odd)
//use set II if any one of the above is even, Xtmin,Ytmin,Ztmin
always odd as defined as 1, But remember that for example
if Xtmax is even, then choose both Xmin and Xmax from set II
//setI start
Xmin = -((Xtmax-Xtmin)/2); Xmax = ((Xtmax-Xtmin)/2);
```

```
Ymin = -((Ytmax-Ytmin)/2); Ymax = ((Ytmax-Ytmin)/2);
Zmin = -((Ztmax-Ztmin)/2); Zmax = ((Ztmax-Ztmin)/2); //setI ends
//setII start
Xmin = -((Xtmax-1-Xtmin)/2); Xmax = Xmin+(Xtmax-Xtmin);
Ymin = -((Ytmax-1-Ytmin)/2); Ymax = Ymin+(Ytmax-Ytmin);
Zmin = -((Ztmax-1-Ztmin)/2); Zmax = Zmin+(Ztmax-Ztmin);//setII ends

d=sqrt(((x2-x1)*(x2-x1))+((y2-y1)*(y2-y1))+((z2-z1)*(z2-z1)));
aa=(Xmax+Xmin)/2.0; bb=(Ymax+Ymin)/2.0; cc=(Zmax+Zmin)/2.0;
b=dx*(sqrt((((x2-aa)*(x2-aa))+((y2-bb)*(y2-bb))+((z2-cc)*(z2-cc)))
-(((((x2-x1)/d)*(x2-aa))+(((y2-y1)/d)*(y2-bb))+(((z2-z1)/d)*(z2-cc)))*
((((x2-x1)/d)*(x2-aa))+(((y2-y1)/d)*(y2-bb))+(((z2-z1)/d)*(z2-cc))))));
for(j=1;j<=s;j=j+1)
{x = x1 + j*((x2-x1)/d);
y = y1 + j*((y2-y1)/d);
z = z1 + j*((z2-z1)/d);
if((x>=Xmin)&&(x<=Xmax)&&(y>=Ymin)&&(y<=Ymax)&&(z>=Zmin)&&(z<=Zmax)){
w=(z-Zmin+1)+((y-Ymin)*(Zmax-Zmin+1))+((x-Xmin)*(Ymax-Ymin+1)
*(Zmax-Zmin+1));
g[j] = density[w-1]; }
     else {g[j]=0.0;} goto BB; BB:; }
E=0.0; WlsSq=0.0;
for(i=1;i<=s;i=i+1)
{  if (g[i]>0.0)  {
double L = 1.0/3.0; double M = 1.0/2.0;
Vf[i]=pow(((3.0*3.143*3.143)*g[i]),L);
Wp[i]=pow((4.0*3.143*g[i]),M);
if(v<=Vf[i]) {
chiSq[i]=1.0/(3.143*Vf[i]);
```

```
AAA[i]=0.5/(pow((1.0-(chiSq[i]/3.0)),2.0));
BBB[i]=log((1.0+0.666*chiSq[i])/chiSq[i]);
CCC[i]=(1.0-(chiSq[i]/3.0))/(1.0+0.666*chiSq[i]);
Cchi[i]=AAA[i]*(BBB[i]-CCC[i]);
Lhv[i]=1.05*Cchi[i]*(pow((v/Vf[i]),3.0));
//Lhv[i]=0.0;
//defined to have only high velocity regime energy loss
FFF[i]=pow((v/Vf[i]),2.0);
OMEGA[i]=(1.0/(1.0+sqrt(13.0*chiSq[i])))*(FFF[i]); }
if(v>Vf[i]) {
chiSq[i]=1.0/(3.143*Vf[i]);
DDD[i]=log((2.0*v*v)/Wp[i]);
EEE[i]=pow((Vf[i]/v),2.0);
Lhv[i]=DDD[i]-0.6*EEE[i]-0.214*EEE[i]*EEE[i];
//Lhv[i]=0.0;
//defined to have only low velocity regime energy loss
FFF[i]=pow((v/Vf[i]),2.0);
OMEGA[i]=1.0+((0.2+(sqrt(chiSq[i])/1.732))*(EEE[i])*(log(FFF[i])));}
dE[i]=(4.0*3.143*zc*zc*g[i]*Lhv[i])/(v*v);
dEdx[i]=dE[i]*dx;//each cell length (of total cube) is dx
E=E+dEdx[i];
if(OMEGA[i]>=0.0) {
WWlsSq[i]=(4.0*3.143*zc*zc*g[i]*OMEGA[i]);
WWlsSqdx[i]=WWlsSq[i]*dx;
WlsSq=WlsSq+WWlsSqdx[i];//straggling within Lindhard-Scharff model
WSq=WlsSq+(E*E);// including bunching correction }}}
fprintf(fpF3,"%e\n",E); } fclose(fpF3); return 0; }
% Program ends here.
```

APPENDIX B

ELECTRON AFFINITY VALUES

Table B.1: AEA vaules in eV for different levels of calculations and experimental values

No[a]	HF	B3LYP				Experimental value[b]	WA HOMA
	6-311+G(d,p)	6-31G	6-31G(d)	6-31+G(d)	6-311+G(d,p)		
1	-2.136	-2.123	-2.103	-1.353	-1.290	-1.12[c]	1.000
2	-1.257	-0.774	-0.767	-0.260	-0.199	-0.05	0.838
3	-0.496	0.100	0.107	0.530	0.589	0.53	0.737
4	0.075	0.692	0.699	1.080	1.140	1.04	0.675
5	-0.969	-0.515	-0.503	-0.054	0.006	0.27	0.799
6	-0.366	0.145	0.157	0.564	0.625	0.39	0.743
7	-0.607	-0.124	-0.116	0.290	0.345	0.32	0.781
8	-0.561	-0.111	-0.095	0.323	0.386	0.545	0.752
9	-0.526	0.006	0.003	0.411	0.466	0.5	0.794
10	-0.931	-0.469	-0.447	0.011	0.070	0.285	0.773
11	-0.954	-0.474	-0.451	-0.023	0.034		0.790
12	-1.217	-0.771	-0.723	-0.268	-0.217		0.979
13	-1.059	-0.650	-0.608	-0.179	-0.122		0.981
14	-1.384	-0.810	-0.777	-0.308	-0.260		0.816
15	-1.226	-0.834	-0.809	-0.308	-0.243	-0.2	0.989
16	0.032	0.261	0.252	0.709	0.761	0.8[d]	0.699
17	-1.374	-0.904	-0.882	-0.380	-0.324		0.894

No[a]	HF	B3LYP				Experimental value[b]	WA HOMA
	6-311+G(d,p)	6-31G	6-31G(d)	6-31+G(d)	6-311+G(d,p)		
18	-0.787	-0.262	-0.258	0.178	0.227		0.799
19	0.248	0.403	0.400	0.822	0.874		0.682
20	-0.988	-0.514	-0.495	-0.048	0.013		0.888
21	-0.780	-0.294	-0.281	0.157	0.213		0.888
22	0.732	0.788	0.777	1.190	1.241		0.668
23	-0.047	0.288	0.292	0.722	0.779	0.63	0.753
24	0.496	0.986	0.972	1.371	1.418		0.615
25	0.309	0.961	0.945	1.379	1.422		0.404
26	0.414	0.983	0.978	1.384	1.434		0.548

[a] 1)Benzene, 2)Naphthalene, 3)Anthracene, 4)Tetracene, 5)Phenanthrene, 6)tetraphene, 7)chrysene, 8)Benzo[c]phenanthrene, 9)Pyrene, 10)Triphenylene, 11)1,2,3,4-Tetrahydrochrysene, 12)1,2,3,4,5,6-Hexahydrochrysene, 13)4,5,9,10-Tetrahydropyrene, 14)1,2,3,3a,4Hexahydropyrene, 15)Fluorene, 16)Acenaphthylene, 17)Acenaphthene, 18)1H-Cyclopenta[I]phenanthrene, 19)Acephenanthrylene, 20)4H-Cyclopenta[def]-phenanthrene, 21)11H-Benzo[a]fluorene, 22)Aceanthrylene, 23)Fluoranthene, 24)Cyclopenta[hi]acephenanthrylene, 25)Cyclopent[fg]acenaphthylene, 26)Cyclopenta[cd]fluoranthene; [b] (Modelli and Mussoni, 2007); [c] (Rienstra-Kiracofe et al., 2002); [d] (Chen and Chen, 2002).

Table B.2: HOMA indices for individual rings

	Molecule	A	B	C	D	WAHOMA
1	Benzene	1.000				1.000
2	Naphthalene	0.838				0.838
3	Anthracene	0.707	0.798			0.737
4	Tetracene	0.627	0.723			0.675
5	Phenanthrene	0.910	0.576			0.799
6	Tetraphene	0.777	0.829	0.434	0.933	0.743
7	Chrysene	0.892	0.669			0.781
8	Benzo[c]phenanthrene	0.872	0.631			0.752
9	Pyrene	0.908	0.679			0.794
10	Triphenylene	0.935	0.287			0.773
11	1,2,3,4-Tetrahydrochrysene	0.909	0.595	0.865	-2.637	0.790
12	1,2,3,4,5,6-Hexahydrochrysene	0.988	-1.310	0.969	-2.673	0.979
13	4,5,9,10-Tetrahydropyrene	0.981	-1.242			0.981
14	1,2,3,3a,4,5-Hexahydropyrene	0.836	0.796	-1.977	-2.686	0.816
15	Fluorene	0.989	-0.738			0.989
16	Acenaphthylene	0.892	0.314			0.699
17	Acenaphthene	0.894	-2.100			0.894
18	1H-Cyclopenta[I]phenanthrene	0.904	0.599	0.895	-0.705	0.799
19	Acephenanthrylene	0.891	0.578	0.939	0.319	0.682
20	4H-Cyclopenta[def]-phenanthrene	0.947	0.770	-0.998		0.888
21	11H-Benzo[a]fluorene	0.988	0.844	0.831	-0.701	0.888
22	Aceanthrylene	0.815	0.819	0.666	0.370	0.668
23	Fluoranthene	0.955	0.263	0.897		0.753
24	Cyclopenta[hi]acephenanthrylene	0.950	0.598	0.288		0.615
25	Cyclopenta[fg]acenaphthylene	0.022	0.786			0.404
26	Cyclopenta[cd]fluoranthene	0.156	0.827	0.023	0.905	0.548

APPENDIX C

PROTON AFFINITY VALUES

Table C.1: Proton affinity values (in kcal/mol) for PAHs at basis B3LYP/6-311++G(d,p)

Molecule	Experimental value	Theoretical value (Kapinus *et al.* 2004)	Our calculation
Benzene	179.3	182.19	181.59
Naphthalene	191.9	196.20	195.55
Anthracene	209.7	200.80	200.19
Ethene	162.6	167.61	165.36
Ethane	142.5	134.15	137.83
Propyne	178.8	181.59	179.24
Propene	179.6	186.71	184.81
Butane		157.56	155.42
Pentane		158.32	160.20

APPENDIX D

OUTER VALENCE GREEN'S FUNCTION CALCULATIONS

Molecular orbital calculations with OVGF estimates of binding energy and pole strength using cc-pVDZ basis in comparison with experimentally measured binding energy. Capital roman symbols are used to label experimental bands.

Table D.1: OVGF calculation for pyrene

MO	Type	Koopman theorem value (eV)	OVGF (eV)	Pole strength	label used in figure	Experimental binding energy (eV)
$2b_{1g}$	π	7.03	7.08	0.89	I	7.43
$2b_{2g}$	π	8.07	7.97	0.88	II	8.30
$3b_{3u}$	π	9.36	8.78	0.88	III	9.05
$1a_{u}$	π	9.86	9.17	0.86	IV	9.38
$2b_{3u}$	π	10.97	9.99	0.83	V	10.01
$9b_{3g}$	σ	12.57	10.82	0.89	VI	10.73
$1b_{1g}$	π	12.62	11.38	0.83		
$14a_{g}$	σ	12.92	11.09	0.89		
$1b_{2g}$	π	13.40	11.79	0.79	VII	11.21
$10b_{2u}$	σ	14.09	12.21	0.88	VIII	12.02
$12b_{1u}$	σ	14.14	12.32	0.88		
$8b_{3g}$	σ	14.91	13.10	0.87	IX	13.01
$1b_{3u}$	π	15.16	13.23	0.76		
$11b_{1u}$	σ	15.18	13.21	0.88		
$9b_{2u}$	σ	15.32	13.50	0.87		

Continuation of Table D.1

MO	Type	Koopman theorem value (eV)	OVGF (eV)	Pole strength	label used in figure	Experimental binding energy (eV)
$13a_g$	σ	15.81	13.72	0.87		
$8b_{2u}$	σ	16.34	14.18	0.86	X	13.94
$7b_{3g}$	σ	16.39	14.03	0.86		
$12a_g$	σ	16.64	14.71	0.86		
$10b_{1u}$	σ	17.55	15.43	0.85	XI	15.11
$11a_g$	σ	18.39	16.01	0.84	XII	15.74
$7b_{2u}$	σ	18.68	16.17	0.84		
$10a_g$	σ	19.29	16.83	0.83	XIII	16.34
$6b3_g$	σ	19.37	16.86	0.84		
$9b_{1u}$	σ	20.42	17.69	0.82	XIV	16.94

End of Table D.1

Table D.2: OVGF calculation for fluorene

MO	Type	Koopman theorem value (eV)	OVGF (eV)	Pole strength	label used in figure	Experimental binding energy (eV)
$3a_2$	π	7.73	7.66	0.89	I	7.94
$4b_1$	π	8.85	8.48	0.89	II	8.80 (IIa)
$2a_2$	π	9.13	8.71	0.88		9.10 (IIb)
$3b_1$	π	10.23	9.64	0.88	III	9.85
$20a_1$	σ	12.89	11.29	0.90	IV	11.05
$17b_2$	σ	12.90	11.28	0.90		
$1a_2$	π	13.21	11.74	0.81	V	11.55 (Va)
$19a_1$	σ	13.60	11.92	0.89		
$16b_2$	σ	13.62	12.17	0.82		11.95 (Vb)
$2b_1$	π	13.68	11.99	0.89		
$18a_1$	σ	15.12	13.41	0.88	VI	13.20
$15b_2$	σ	15.41	13.58	0.88		
$17a_1$	σ	15.86	14.01	0.87	VII	13.75
$14b_2$	σ	16.12	14.00	0.87		
$1b_1$	π	16.39	14.80	0.84	VIII	14.45
$13b_2$	σ	16.59	14.79	0.87		
$16a_1$	σ	17.03	15.05	0.86		
$15a_1$	σ	17.84	15.59	0.86	IX	15.45
$12b_2$	σ	18.16	16.05	0.85		
$14a_1$	σ	19.01	16.82	0.85	X	16.45

APPENDIX E

FRANCK-CONDON FACTORS CALCULATIONS FOR VIBRATIONAL PROGRESSION

Calculated frequencies and relative intensities (with HWHM 5 cm^{-1}) for different modes of vibration:

Table E.1: Franck-Condon factors calculation for pyrene

Wavenumber		Relative Intensity
(in cm^{-1})	(in microns)	
0	0	0.435
421	23.75	0.031
601	16.64	0.007
832	12.02	0.008
1187	8.42	0.008
1280	7.81	0.048
1430	6.99	0.036
1660	6.02	0.077
2081	4.81	0.005
2709	3.69	0.005
2939	3.40	0.009
3090	3.24	0.006
3319	3.01	0.007

Table E.2: Franck-Condon factors calculation for fluorene

Wavenumber		Relative Intensity	Wavenumber		Relative Intensity
(in cm^{-1})	(in microns)		(in cm^{-1})	(in microns)	
0	0	0.198	1524	6.56	0.005
223	44.84	0.051	1574	6.35	0.004
428	23.36	0.057	1602	6.24	0.003
446	22.42	0.007	1657	6.04	0.037
649	15.41	0.016	1680	5.95	0.003
747	13.39	0.055	1717	5.82	0.003
856	11.68	0.010	1881	5.32	0.012
970	10.31	0.015	1922	5.20	0.002
1024	9.77	0.005	1964	5.09	0.004
1069	9.35	0.005	2085	4.80	0.012
1175	8.51	0.015	2103	4.76	0.003
1195	8.37	0.003	2204	4.54	0.002
1217	8.22	0.017	2307	4.33	0.004
1378	7.26	0.002	2404	4.16	0.010
1390	7.19	0.004	2513	3.98	0.002
1396	7.16	0.004	2627	3.81	0.003
1422	7.03	0.005	2832	3.53	0.003
1440	6.94	0.005	2874	3.48	0.003
1457	6.86	0.010	3114	3.21	0.002
1494	6.69	0.009	3314	3.02	0.004

Table E.3: Franck-Condon factors calculation for naphthalene

Wavenumber		Relative Intensity
(in cm^{-1})	(in microns)	
0	0	0.447
523	19.12	0.022
1069	9.35	0.008
1232	8.12	0.013
1407	7.11	0.114
1518	6.59	0.012
1621	6.17	0.085
1931	5.18	0.005
2144	4.66	0.004
2639	3.79	0.004
2815	3.55	0.015
2853	3.51	0.003
2926	3.42	0.002
3028	3.30	0.021
3139	3.19	0.002
3242	3.08	0.009

Table E.4: Franck-Condon factors calculation for anthracene

Wavenumber		Relative Intensity
(in cm^{-1})	(in microns)	
0	0	0.478
1232	8.12	0.012
1293	7.73	0.010
1413	7.08	0.082
1547	6.46	0.025
1597	6.26	0.061
2645	3.78	0.002
2706	3.70	0.003
2826	3.54	0.008
2889	3.46	0.001
2960	3.38	0.004
3010	3.32	0.010
3095	3.23	0.001
3144	3.18	0.003
3194	3.13	0.004

APPENDIX F

NON-INTRUSIVE DIAGNOSTICS FOR XENON ION THRUSTER

Introduction to thruster

For space programs, the electric propulsion is a primary contributor as an alternative to chemical propulsion used in spacecraft. It is already used in LEO satellite constellations and small Earth-orbiting satellites (Azziz, 2003). The idea is to provide more thrust at reduced weight of payload and low cost. Hence worldwide several academic as well as industrial research is going on for the enhancement in work-efficiency of the thruster used in space agencies (Boyd and Dressler, 2002; Fife, 1999; Oh, 1996; Azziz, 2003). Out of different type of thrusters, the Indian Space Research Organization (ISRO), India uses Hall thrusters or Hall Effect thrusters (HET), a special class of electric thrusters (see reference(Goebel and Katz, 2008) for working principle). This section deals with the experiments conducted with 18mN thruster (Xe gas as the propellant) used in Liquid Propulsion Systems Center (LPSC) of ISRO at Valiamala using their facility. This collaborative experimental work between IIST, Trivandrum and LPSC, valiamala was initiated to study the characteristics of thruster as well as plume dynamics, discharge current oscillation which are critical to thruster stability.

Three main parameters namely breathing mode oscillation of plasma, UV-Vis-IR emission spectra and UV-Vis multi spectral imaging are studied by varying the external parameters like Xe flow rate, cathode temperature, anode voltage, magnetic field etc. to understand the behavior of plasma and to relate them with the stability of thruster. To study these properties experiments were conducted at LPSC facility.

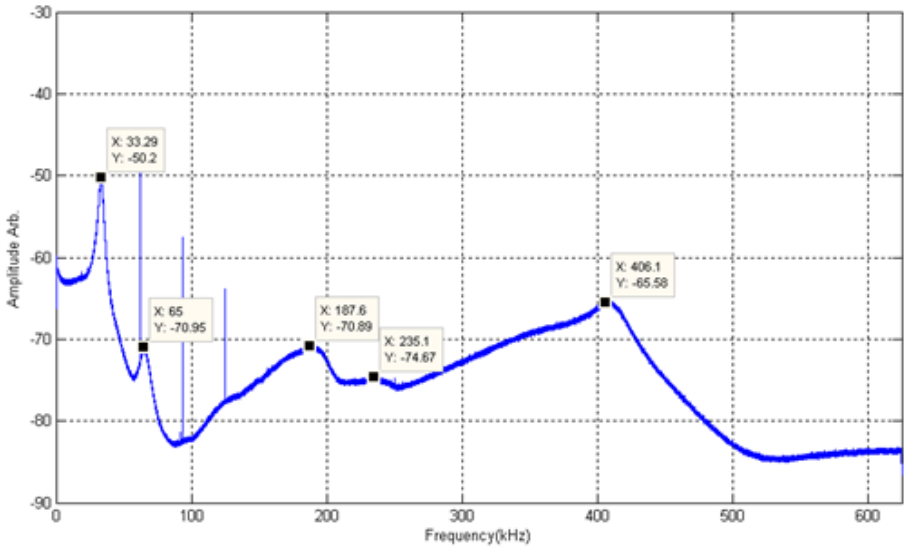

Figure F.1: Breathing oscillation in FFT data of 18mN thruster at operation with Xe flow rate 1.2 mg/sec.

The anode current oscillation study was performed by analyzing the plume spectra and their Fast Fourier Transform (FFT) components (recorded using an oscilloscope of bandwidth 200 MHz and sampling rate 2.5 Gs/sec) which showed the presence of so-called "breathing mode" oscillations (at $\sim$ 33 kHz followed by a weak feature at 65 kHz) during the 18mN thruster at operation with Xe flow rate 1.2 mg/sec (see figure F.1). It is well known that the stability of thruster, i.e; the plasma behavior is closely related to the frequency and amplitude of anode current oscillation.

The presence of impurity in plasma (either due to erosion from the surface of several components used in thruster or due to poor vacuum inside the chamber), the proportion of Xe neutral to ion (due to recombination probability near the cathode: source of electron) is studied by identifying the lines (NISTa, June 2014) in the optical emission spectrum (OES). The measurements conclusively identified the role of various secondary emissions and degassing from the thruster components. A conditioning protocol is developed for the anode unit and implemented successfully, leading to stable long duration operation of the 18mN thruster. The OES can be obtained using a CCD camera infront of a spectrometer containing a high resolution diffraction grating

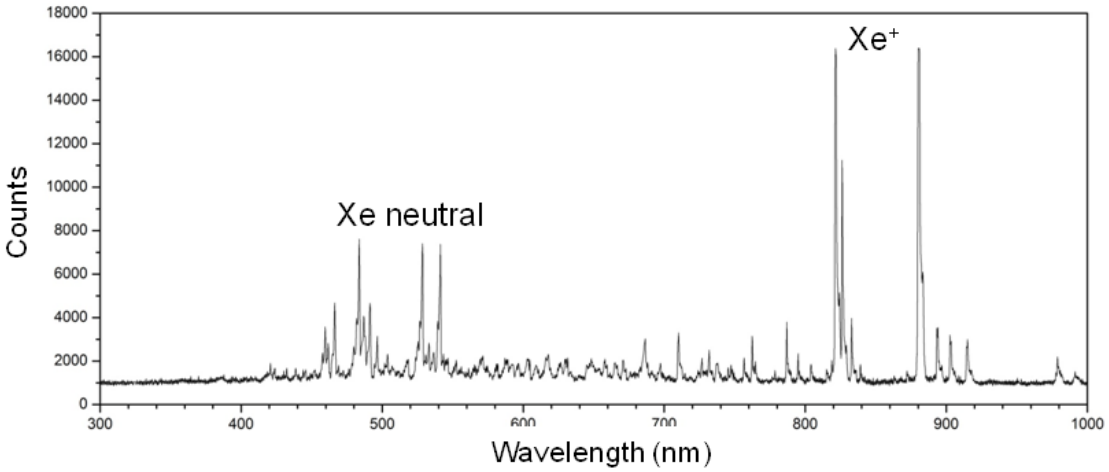

Figure F.2: Line identification using OES data obtained from fibre optic spectrometer.

(in visible range). The field of view for the spectrometer was set for the first order diffraction with the center wavelength at 480 nm (to mainly probe singly charge Xe). These images requires post analysis to obtain the OES. For the real time analysis a fiber optic spectrometer is used (see figure F.2).

With the help of different narrow band filters in a high sensitivity CCD camera to select a narrow range in wavelength, the thruster plume was imaged. The filters were chosen for the characteristic wavelength of boron, silicon, Xe neutral as well as mono-cation. Since the liner material on anode is boron nitride and silicon dioxide, these elements are expected to be present as impurity in the plume. Figure F.3a shows the 2D profile of these impurities showing that a sharp plume is dominated by Xe^{+} followed by a diffused distribution of Xe neutral. Whereas the boron and silicon impurities are much less in impurities and localized close to the exit of the thruster. Figure F.3b shows the CCD images are converted into relative intensity numbers which can then be analyzed in a selective manner for the particle distribution in the plasma.

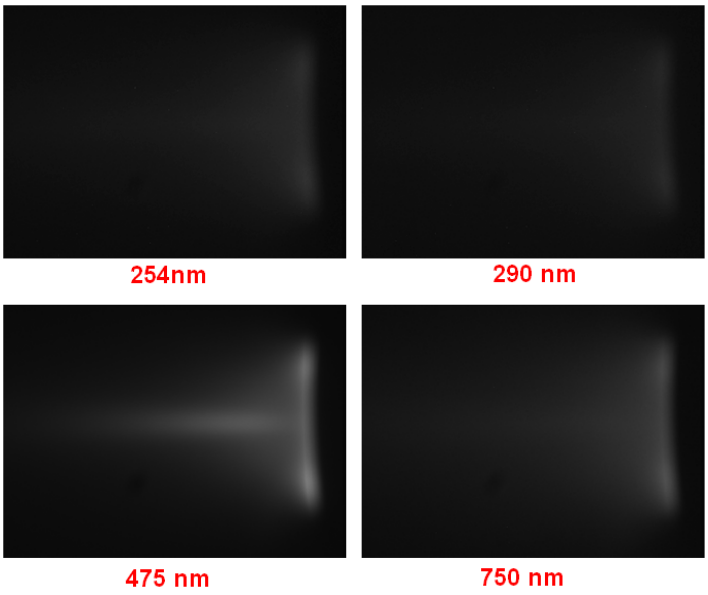

(a)

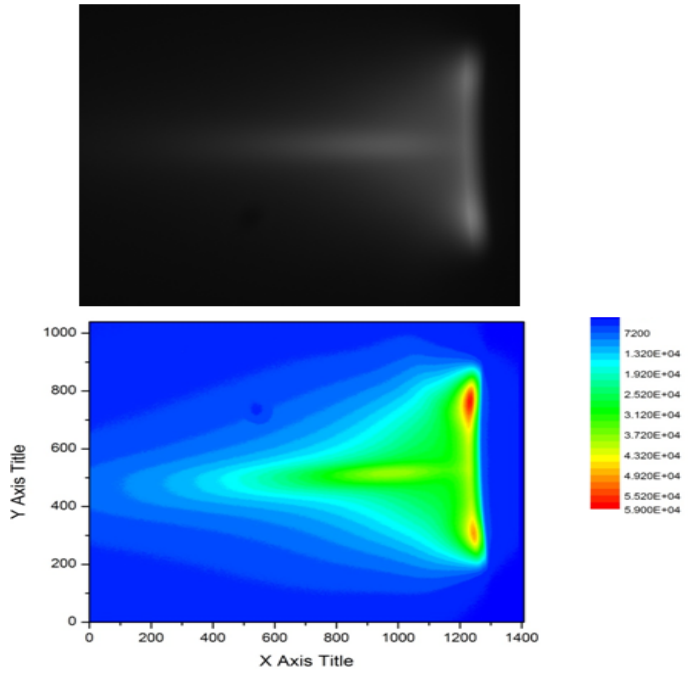

(b)

Figure F.3: (a) Multispec data obtained using high sensitivity CCD camera with specific filters, (b) image converted to numbers showing the intensity profile of the plume coming from different elements within plasma.

LIST OF PAPERS BASED ON THESIS

Papers in Refereed International Journals

1. **Mishra, P. M.**, Rajput, J., Safvan, C. P., Vig, S. and Kadhane, U. (2013). Electron emission and electron transfer processes in proton-naphthalene collisions at intermediate velocities. ***Physical Review A***, 88, 052707.

2. **Mishra, P. M.**, Rajput, J., Safvan, C. P., Vig, S. and Kadhane, U. (2014). Velocity dependence of fragmentation yields in proton-naphthalene collision and comparison with electronic energy loss calculation. ***Journal of Physics B: Atomic, Molecular and Optical Physics***, 47, 085202 (9pp).

3. **Mishra, P. M.**, Avaldi, L., Bolognesi, P., Prince, K. C., Richter, R. and Kadhane, U. (2014). Valence shell photoelectron spectroscopy of pyrene and fluorene: photon energy dependence in the far ultraviolet region. ***Journal of Physical Chemistry A***, 118, 3128-3135.

4. **Mishra, P. M.** and Kadhane, U. (2014). *Monte Carlo* simulation of electronic energy loss for proton impact on nucleobases. ***Nuclear Instruments and Methods in Physics Research Section B***, 336, 12-18.

5. **Mishra, P. M.**, Avaldi, L., Bolognesi, P., Prince, K. C., Richter, R. and Kadhane, U. (2014). Plasmon excitation in valence shell photoelectron spectroscopy for PAHs. *accepted in* ***Journal of Physics: Conference Series***.

6. **Mishra, P. M.** and Kadhane, U. (2014). Modeling of ion-molecule collision using *Monte Carlo* simulation. *accepted in* ***Journal of Physics: Conference Series***.

7. **Mishra, P. M.**, Avaldi, L., Bolognesi, P., Prince, K. C., Richter, R., Vig, S. and Kadhane, U. Franck-Condon factor for photoionization of PAHs: A comparison between theory and experiment. ***Communicated***.

8. **Mishra, P. M.** and Kadhane, U. Electron affinity of selected PAHs using DFT: effect of cyclopenta ring fusion and aromaticity. ***Under preparation***.

9. **Mishra, P. M.**, Rajput, J., Safvan, C. P., Vig, S. and Kadhane, U. Kinetic release from energetic proton emission in proton-naphthalene collision,. ***Under preparation***.

Chapters in Book

1. **Mishra, P. M.**, Rajput, J., Safvan, C. P., Vig, S. and Kadhane, U. (2012). In book "Electron collision processes in atomic and molecular physics", edited by Prof Vinodkumar, P. C. M., Publisher: Narosa publishing house Pvt Ltd. ISBN-978-81-8487-343-6.

2. Three abstracts of COSmIC dust, in "AstroPAH, A News Letter on Astronomical PAHs", issue 8, number 8, June 2014.

Oral Presentations in Conferences/ Symposiums

1. **Mishra, P. M.** and Kadhane, U. (2010). Simulation of "Linear Time of Flight Mass Spectrometer" for better resolution, V^{th} *In house symposium on atomic and molecular physics.* IITM, Chennai, India, January 09-10.

2. **Mishra, P. M.**, Rajput, J., Safvan, C. P., Vig, S. and Kadhane, U. (2013). Exploring Plasmon excitation in PAHs as a consequence of proton collision, *DST-SERC School on Physics of Highly Charged Ions.* TIFR, Mumbai, India, February 10-March 03.

3. **Mishra, P. M.**, Rajput, J., Safvan, C. P., Vig, S. and Kadhane, U. (2013). Collision of naphthalene with energetic protons, *Electron collision processes in Atomic and Molecular*

Physics. Gujarat, India, March 07-09.

4. **Mishra, P. M.**, Avaldi, L., Bolognesi, P., Prince, K. C., Richter, R. and Kadhane, U. (2014). Franck-Condon factors calculation for vibrational progression seen in photoelectron spectrum of PAHs, *International Conference on photoelectron and vibrational spectroscopy.* Thiruvananthapuram, India, July 08-12.

5. **Mishra, P. M.**, Avaldi, L., Bolognesi, P., Prince, K. C., Richter, R. and Kadhane, U. (2014). Plasmon excitation in valence shell photoelectron spectroscopy for PAHs, *17th International Conference on Highly Charged Ions.* San Carlos de Bariloche, Argentina, August 31-September 05.

Poster Presentations in Conferences/ Symposiums

1. **Mishra, P. M.**, Maryam, N. and Kadhane, U. (2010). Design and Simulation of Electrostatic and RF handling devices and mass spectrometer, *Topical Conference on Interaction of EM Radiation with Atoms, Molecules and Clusters.* RRCAT, Indore, India, March 03-06.

2. **Mishra, P. M.** and Kadhane, U. (2012). Investigation of structural and dynamical properties of PAH molecules and molecular ions, *Conference on Highly Charged Ions and Atomic Collisions.* TIFR, Mumbai, India, March 28-31.

3. **Mishra, P. M.**, Avaldi, L., Bolognesi, P., Prince, K. C., Richter, R. and Kadhane, U. (2012). Photoelectron spectroscopy of pyrene and fluorene in extreme UV range, *Twelfth International Conference on Electron Spectroscopy and Structure.* France, September 16-21.

4. **Mishra, P. M.**, Rajput, J., Safvan, C. P., Vig, S. and Kadhane, U. (2012). 1) Photoelectron Spectroscopy features as a function of photon energy for Pyrene & Fluorene using Synchrotrone source, 2) Probing H-loss mechanism in collision with energetic protons & its

implications to PAH stability, 3) Franck Condon Factors for photoionisation of Pyrene & Fluorene: Comparison between theory & experiment, *DAE-BRNS Symposium on Atomic, Molecular and Optical Physics.* IISER, Kolkata, India, December 14-17.

5. **Mishra, P. M.**, Rajput, J., Safvan, C. P., Vig, S. and Kadhane, U. (2013). 1) Exploring Plasmon excitation in PAHs as a consequence of proton collision, 2) Modeling Ion-PAH collision using *Monte Carlo* simulation, *Topical conference on atomic processes in plasmas.* IPR, Gandhinagar, India, November 18-20.

6. **Mishra, P. M.** and Kadhane, U. (2014). 1) Coupling of Plasmon excitation in collision of proton and photon with PAHs, 2) Modelling ion-PAH collision using *Monte Carlo* simulation, *Stored particle atomic physics research collaboration.* TIFR, Mumbai, India, January 28-29.

7. **Mishra, P. M.**, Avaldi, L., Bolognesi, P., Prince, K. C., Richter, R., Vig, S. and Kadhane, U. (2014). 1) Valence shell photoelectron spectroscopy for PAHs and its significance, 2) Energetics of intermediate velocity proton collision with naphthalene, *46th Conference on European group on Atomic Systems.* France, June 30-July 04.

8. **Mishra, P. M.**, Avaldi, L., Bolognesi, P., Prince, K. C., Richter, R., Vig, S. and Kadhane, U. (2014). Photoelectron spectroscopy and vibrational progression analysis for PAHs, *International workshop on photoionization and Resonant inelastic X-ray scattering.* Ettore Majorana foundation and centre for scientific culture, Erice, Italy, August 26-September 01.

9. **Mishra, P. M.**, Avaldi, L., Bolognesi, P., Prince, K. C., Richter, R. and Kadhane, U. (2014). 1) Plasmon excitation in intermediate velocity proton collisions with naphthalene, 2) Modeling of Ion-molecule collisions using *Monte Carlo* simulation, *17th International Conference on Highly Charged Ions.* San Carlos de Bariloche, Argentina, August 31-September 05.

Awards and Achievements

1. Proposal for an experiment titled " **Photo-fragmentation and photo-ionization of PAH molecules using photoelectron-photoion coincidence**" was accepted and the experiment was done at GASPHASE photoemission beam line at the Elettra Sincrotrone Laboratory, Trieste, Italy on March 16-24, 2012.

2. Proposal for an experiment titled "**Fragmentation and ionisation of PAH molecules due to collision with slow highly charged ions**" was accepted and the experiment was done at Inter University Accelerator centre, New Delhi, India on June 01-10, 2012.

3. **Best Poster Award** by Indian Society of Atomic and Molecular Physics-2013 in a conference for the poster titled 'Exploring Plasmon excitation in PAHs as a consequence of proton collision', at Institute for Plasma Research, Gandhinagar, India, on November 18âĂŞ20, 2013.